## BOSTON UNIVERSITY GRADUATE SCHOOL OF ARTS AND SCIENCES

#### Dissertation

# METER-SCALE WAVES IN THE E-REGION IONOSPHERE: CROSS-SCALE COUPLING AND VARIATION WITH ALTITUDE.

by

#### MATTHEW A. YOUNG

B.S., University of New Hampshire, 2012

Submitted in partial fulfillment of the requirements for the degree of

Doctor of Philosophy

2019

### Approved by

First Reader

Meers M. Oppenheim, PhD Professor of Astronomy

Second Reader

Joshua L. Semeter, PhD Professor of Electrical and Computer Engineering

Ionosphere? Witches did that. So you have them to thank. For the ionosphere.

Griffin McElroy

#### Acknowledgments

Although my name will be on the diploma, this degree required the support and patience of many people.

My parents have been my foundation throughout my entire life. They've cheered me when I've succeeded and comforted me when I've failed, and will do so many more times, I'm sure. They also knew me when I "wasn't a math or science person", yet encouraged me to pursue my newfound interest in both when I went back to school.

I could not have survived the past few years without the day-to-day, hour-to-hour, and sometimes minute-to-minute support from Madeleine. They have been my partner, my best friend, my compass, and my bub.

Normie, Mermie, and Annie always check my work and make sure I'm awake in time for breakfast.

Steph and Derrek have provided not only a house in which to live while I finished this degree, but a home in which to thrive. Leanora has made every day brighter and constantly reminds me of what's important.

Meers took a chance on me as an incoming grad student even though I knew just enough about computer programming to not realize how little I knew. He taught me how to avoid the many potential pitfalls inherent to high-performance computing, how to balance thinking about the numerical model with thinking about the physics, and how to write for a scientific audience. Beyond that, he gave me a lot of space to learn on my own. He was also tremendously supportive of my music.

Yakov offered much guidance on the history of our field and provided invaluable mentoring on developing a physical intuition for complicated processes. Above all, he taught me to "feel the instability."

Before I even thought about grad school, Marc Lessard gambled on me as an

undergraduate research assistant and gave me my start in space science.

I am grateful to Dan Clemens for timely, tough, and ultimately inspiring conver-

sations about the path to a PhD, and to Josh Semeter for reminding me to pick up

a guitar and consider the absurdity of the universe now and then.

I am grateful to everyone in the department who encouraged me to keep playing

music despite the academic rigor of grad school. Thanks, especially, to Al Marscher

for organizing "Astronomy Unplugged!" and to Ken Brecher for asking "Are You

Happy?"

This list would be weefully incomplete if I didn't thank Quinn, Damean, David,

Anne, Mary, Erin, and Tom, as well as many past Astronomy/CSP/IAR staff mem-

bers, for all the problems of varying size and severity that they fixed for me without

complaint. Thanks, too, to the custodial staff that takes such good care of CAS.

Thanks to past and present grad students for conversations, camaraderie, and

desk whisk(e)v; thanks to my Seacoast friends who have been patient with me while

I followed this dream.

Last, but not least: Thanks to the giants upon whose shoulders I have stood.

Matt Young

December 2018

Department of Astronomy/Center for Space Physics

vi

METER-SCALE WAVES IN THE E-REGION

IONOSPHERE: CROSS-SCALE COUPLING AND

VARIATION WITH ALTITUDE.

MATTHEW A. YOUNG

Boston University, Graduate School of Arts and Sciences, 2019

Major Professor: Meers M. Oppenheim, PhD

Professor of Astronomy

Center for Space Physics

ABSTRACT

The Sun ionizes a small fraction of Earth's atmosphere above roughly 60 km, pro-

ducing the plasma that constitutes the ionosphere. Radio signals passing through the

ionosphere scatter off of plasma density structures created by the Farley-Buneman

instability (FBI). While numerous studies have characterized the FBI's intrinsic na-

ture, its evolution within the broader context of the surrounding plasma remains

enigmatic. This dissertation answers two fundamental questions about the FBI: How

does it interact with density gradients? How does its non-linear evolution depend on

the background plasma?

The fourth chapter examines the combined development of the FBI and the gra-

dient drift instability (GDI) using a 2-D simulation of the equatorial ionosphere. A

half-kilometer wave perturbs a plasma layer perpendicular to the ambient magnetic

field, causing the perturbed layer to develop GDI waves along the gradient aligned

with the ambient electric field, as well as FBI waves in a region where the total

electric field exceeds a certain threshold. Early radar observations suggested that

vii

these two instabilities were distinct phenomena; the reported results illustrate their coupled nature.

The fifth chapter presents 2-D simulations in which a one-kilometer plasma wave develops an electric field large enough to trigger meter-scale waves. Such large-scale waves arise via the GDI within the daytime ionospheric gradient around 100-110 km. Typical ionospheric radars only observe meter-scale irregularities but observations show meter-scale waves tracing out larger structures. Simulated meter-scale FBI in the troughs and crests of kilometer-scale GDI matches radar observations of the daytime equatorial ionosphere, answers a question about electric-field saturation raised by rocket observations in the 1980s, and predicts an anomalous cross-field conductivity important to magnetosphere-ionosphere (M-I) coupling.

The sixth chapter of this dissertation presents 3-D simulations of the FBI at a range of altitudes and driving electric fields appropriate to the auroral ionosphere, where it plays a role in M-I coupling. Research has thoroughly established the linear theory of FBI but rigorous analysis of radar measurements requires an understanding of the turbulent stage. These simulations explain the change in instability flow direction with altitude, with regard to the direction of background plasma flow.

## Contents

Li	st of	Tables	XIII
Li	st of	Figures	xiv
Li	st of	Abbreviations x	xiv
1	Intr	roduction	1
	1.1	Overview	1
	1.2	The Ionospheric Canvas	1
	1.3	Motivation	2
	1.4	Earth's Global Ionosphere and Thermosphere	3
		1.4.1 Fundamental concepts	5
		1.4.2 Ionospheric structure and composition	7
		1.4.3 Ionospheric observation techniques	12
	1.5	Review of relevant literature	15
	1.6	Theory of E-region instabilities	34
		1.6.1 The Farley-Buneman instability (FBI)	36
		1.6.2 The gradient drift instability (GDI)	37
2	The	eoretical Framework	39
	2.1	Linear Fluid Theory	39
	2.2	Linear Kinetic Theory	49
	2.3	Quasi-Neutral Potential Equation	54

3	Nur	merical Framework	60
	3.1	The Particle-In-Cell (PIC) Method	60
	3.2	The Hybrid Approach	63
	3.3	Finite-Difference Scheme for the Potential Equation	65
	3.4	Matrix Inversion Methods	70
	3.5	Hybrid EPPIC Development	71
		3.5.1 Electron distribution	71
		3.5.2 One-step hybrid gather	72
		3.5.3 Using PETSc for potential	72
		3.5.4 Efficient PETSc setup	73
		3.5.5 Running PETSc on a subset of communicators	73
4	Inst	upled Growth and Evolution of Farley-Buneman/Gradient Drift tabilities on Meter and Decameter Scales in a Common Plasma ume	
	4.1	Introduction	75
	4.2	Theory	77
	4.3	Numerical Model	79
	4.4	Results	81
		4.4.1 Density and electric field	82
		4.4.2 Spectra	87
	4.5	Discussion	94
		4.5.1 Connection with observations	94
		4.5.2 Dispersion relation	97
	4.6	Conclusion	99
5		ondary Farley-Buneman Instability Driven by a Kilometer-Scale mary Wave: Anomalous Transport and Formation of Flat-Topped	

	Ele	ctric Fields. 10	2
	5.1	Introduction	)2
	5.2	Theory	)4
	5.3	Numerical Model	)6
	5.4	Results	.3
		5.4.1 Meter-scale irregularity amplitudes	4
		5.4.2 Average zonal electric field	6ء
		5.4.3 Relative perturbed density	8
		5.4.4 Density irregularity spectra	22
	5.5	Discussion	26
	5.6	Conclusion	31
6	Var	iation of the Farley-Buneman Spectrum with Altitude 13	3
	6.1	Introduction	33
	6.2	Simulation Methods and Limitations	35
	6.3	Irregularity growth at meter and decameter scales	38
	6.4	Average Temperatures	<b>!</b> 1
	6.5	Ion Density Perturbations	13
	6.6	Perturbed Ion Density Spectra	51
	6.7	Thermal Instability Effects	59
	6.8	Instability Flow Angle	39
	6.9	Conclusion	76
7	Cor	nclusion 18	<b>0</b>
	7.1	Summary of the Dissertation	30
		7.1.1 Summary of Chapter 4	30
		7.1.2 Summary of Chapter 5	31
		7.1.3 Summary of Chapter 6	32

	7.2	Future Work	182
	7.3	Final Remarks	184
$\mathbf{A}$	Pro	of of xyz	186
Li	List of Journal Abbreviations		
$\mathbf{R}$	References		188
$\mathbf{C}_1$	urric	ulum Vitae	198

## List of Tables

4.1	Simulation Parameters for Chapter 4	81
5.1	Simulation Parameters for Chapter 5	109
6.1	Simulation Parameters for Chapter 6	138

## List of Figures

1.1	Altitude profiles of (a) MSIS neutral temperature from 0 to 300 km $$	
	and (b) IRI electron density from 0 to 1000 km at the magnetic equa-	
	tor. Solid lines correspond to daytime and dashed lines correspond to	
	nighttime	7
1.2	Altitude profiles of density of (a) neutral species and (b) charged	
	species from 0 to 1000 km at the magnetic equator. Individual species	
	names are placed as close as possible to the corresponding profile.	
	The neutral-species densities from from MSIS and the charge-species	
	densities come from IRI	Ĝ
1.3	Canonical type-I (left) and type-II spectra (right). The left panel is	
	from Cohen and Bowles (1967), showing a composition of spectra taken	
	near noon at Jicamarca, during relatively strong electrojet. The top	
	two panels show echoes from $70^{\circ}$ west and east, the middle panel shows	
	echoes from vertical, and the bottom two panels show echoes from	
	$45^{\circ}$ west and east. The right panel is from Balsley (1969), showing	
	simultaneous spectra taken near 18:00 at Jicamarca. The top panel	
	shows echoes at $11^{\circ}$ west, the middle panel shows echoes at $26^{\circ}$ west,	
	and the bottom panel shows echoes at $51^{\circ}$ west	19
1.4	Cartoon of electrostatic E-region instability formation	35
1.5	Cartoon of the Farley-Buneman instability mechanism	37
1.6	Cartoon of the gradient drift instability mechanism	38

$2 \cdot 1$	The geometry that gives rise to the combined FBI and GDI dispersion	
	relation in the E region. The background electric field, $\mathbf{E}_0$ , and plasma-	
	density gradient, $\nabla n_0$ , point vertically. The background magnetic	
	field, $\mathbf{B}_0$ , points out of the page. The electron drift velocity, $\mathbf{u}_e$ , points	
	predominantly in the $\mathbf{E}_0 \times \mathbf{B}_0$ direction, the ion drift velocity, $\mathbf{u}_i$ , points	
	predominantly in the $+\mathbf{E}_0$ direction, and $\mathbf{u}_d \equiv \mathbf{u}_e - \mathbf{u}_i$ is the relative	
	drift velocity. The directions of $\mathbf{u}_i$ , $\mathbf{u}_e$ , and $\mathbf{u}_d$ have been exaggerated	
	to show altitudinal range, and are not necessarily consistent with ${\bf k}.$ .	58
2.2	A plot of one-dimensional motion in phase space, with examples of	
	single-particle motions	59
4.1	Initial configurations of relative perturbed density $(\delta n/n_0; \text{ color})$ and	
	electrostatic potential ( $\phi$ ; contours). The initial density consists of a	
	Gaussian bump centered at $z=128~\mathrm{m}$ and modulated by a 512-m	
	wave. The electrostatic potential is the result of solving equation 4.3	
	at the first time step	83
4.2	Final relative perturbed density for each run: (a) $E_{0z}=6~\mathrm{mV/m},$	
	(b) $E_{0z}=9~{\rm mV/m},$ (c) $E_{0z}=12~{\rm mV/m}.$ In all runs, gradient-drift	
	instability develops along the positive vertical gradient. For $E_{0z}$ =	
	9 mV/m and 12 mV/m, Farley-Buneman instability develops in the	
	central density trough, with faster growth for $E_{0z}=12~\mathrm{mV/m.}$	85

4.3	Final total electric field (grayscale) and potential (color contours) for	
	each run: (a) $E_{0z} = 6 \text{ mV/m}$ , (b) $E_{0z} = 9 \text{ mV/m}$ , (c) $E_{0z} = 12$	
	mV/m. The grayscale bar shows values in multiples of the threshold	
	electric field for Farley-Buneman instability, $E_c \approx 11.2 \text{ mV/m}$ . In all	
	runs, the total electric field peaks in the central density trough. For	
	$E_{0z} = 9 \text{ mV/m}$ and $12 \text{ mV/m}$ , the total electric field is well above $E_c$ .	
	The contours span $\pm \max( \phi )$ , red to blue, where $\max( \phi )$ is (a) 0.28	
	V, (b) 0.45 V, (c) 0.54 V	86
4.4	Average electric-field magnitude in the central $64 \times 64$ m for the	
	first 25.6 ms. For $E_{0z}=6~\mathrm{mV/m}$ (black trace), the average electric	
	field does not rise above the threshold for Farley-Buneman instability,	
	whereas it does for $E_{0z}=9~\mathrm{mV/m}$ and 12 mV/m (blue and green	
	traces)	88
4.5	Spectral power and width at 3 m as a function of phase velocity $(V_{ph})$	
	and angle from $+\hat{x}$ , (i.e. $\mathbf{E}_0 \times \mathbf{B}_0$ ): (a) & (d) $E_{0z} = 6$ mV/m, (b)	
	& (e) $E_{0z}=9~\mathrm{mV/m},$ (c) & (f) $E_{0z}=12~\mathrm{mV/m}.$ The white line in	
	(a)-(c) shows the mean phase velocity and the sign convention is such	
	that negative velocities imply waves traveling away from an observer	
	with line-of-sight $\theta$	90
4.6	Spectral power and width at 8 m as a function of phase velocity $(V_{ph})$	
	and angle from $+\hat{x}$ . See description of Figure 4.5 for individual panels.	91
4.7	Spectral power and width at 2 m as a function of phase velocity $(V_{ph})$	
	and angle from $+\hat{x}$ . See description of Figure 4.5 for individual panels.	93
4.8	Phase-velocity spectra at $\theta=15^\circ$ : (a) Power in 2-m waves normalized	
	to the spectrum of the $12\text{-mV/m}$ run; (b) Self-normalized power in	
	2-m, 3-m, and 8-m waves for the 12-mV/m run	95

4.9	Local linear growth from equation 4.4 for waves traveling at $\theta = 15^{\circ}$	
	from $+\hat{x}$ . Rows (top to bottom): $\lambda = 2$ m, $\lambda = 3$ m, and $\lambda = 8$ m.	
	Columns (left to right): $E_{0z} = 6 \text{ mV/m}$ , $E_{0z} = 9 \text{ mV/m}$ , and $E_{0z} = 12$	
	$mV/m. \ . \ . \ . \ . \ . \ . \ . \ . \ . \$	99
5.1	Initial plasma density configuration for all runs. Density is a sine	
	about $n_0 = 10^{10} \text{ m}^{-3}$ in the east-west direction, with an amplitude of	
	$\pm 5\%$ or $\pm 10\%$ . This configuration mimics a single period of a large-	
	scale GDI wave. The white box represents a 128-m $\times$ 128-m patch	
	shown in Figures 5.6 and 5.7	110
5.2	Total electric field at $t \approx 1/\nu_i$ for all runs. The solid traces corre-	
	spond to ten-percent runs; the dashed lines correspond to five percent	
	runs. For both amplitudes, red represents 96 km, black represents 98	
	km, green represents 100 km, blue represents 102 km, and magenta	
	represents 104 km. Panel a: The magnitude of the total electric field,	
	$ \mathbf{E}_I  = \sqrt{E_{z0}^2 + \delta E_x^2}$ . Panel b: The angle from due west of the total	
	field, $\theta(\mathbf{E}_I) = \tan^{-1}(E_{z0}/\delta E_x)$ . In case the reader is unable to dis-	
	tinguish colors: the text labels in panel b indicate the order of lines	
	in both panels. In panel a, the 96-km trace nearly covers the 98-km	
	trace; in the panel b, they are indistinguishable	111

5.3	Spectral power in 2-m to 6-m density (top) and electric-field (bottom)	
	perturbations propagating within $30^{\circ} \leq \theta \leq 50^{\circ}$ west of zenith, nor-	
	malized to the $t \approx 1/\nu_i$ value in each run. Colors and line styles are	
	the same as in Figure $5.2$ . Dashed vertical lines mark three fiducial	
	times for later analysis: The first (20.48 ms) corresponds to growth in	
	ten-percent runs, the second (40.96 ms) corresponds to growth in five-	
	percent runs, and the third (245.76 ms) corresponds to a saturated	
	state in all runs	115
5.4	Vertical average of the zonal electric field at three moments during	
	each ten-percent run: the initial step (solid), during growth (dotted),	
	and in saturation (dashed)	117
5.5	Vertical average of the zonal electric field at three moments during	
	each five-percent run: the initial step (solid), during growth (dotted),	
	and in saturation (dashed)	118
5.6	Snapshots of relative perturbed density, $\delta n/n_0$ , and self-normalized	
	spectral power, $P$ , during ten-percent runs. Each density panel rep-	
	resents the 128 m $\times$ 128 m box outlined in white in Figure 5·1 after	
	filtering out wavelengths greater than 100 m. Each spectrum cov-	
	ers $(k_x, k_z) \in [0, +\pi] \times [-\pi, +\pi]$ . White circles show values from	
	$k=2\pi/2~\mathrm{m}^{-1}$ (largest) to $k=2\pi/7~\mathrm{m}^{-1}$ (smallest) and white radii	
	show values of $\theta$ from $-90^{\circ}$ (bottom) to $+90^{\circ}$ (top)	119
5.7	Same as Figure 5.7 but for five-percent runs	191

5.8	Spectral power as a function of zenith angle and phase velocity during
	the second half of all ten-percent runs. Columns, from left to right,
	correspond to the runs at 102 km, 100 km, 98 km, and 96 km. Rows,
	from top to bottom, show power in 3-m, 5-m, and 10-m waves. The
	color scale runs from 0 dB to -30 dB. White dotted lines mark $\pm C_s.$ . 123
5.9	Same as Figure 5.8 but for five-percent runs
6.1	Figure 2 from Dimant and Oppenheim (2004), showing theoretical
	altitudinal profiles of $\psi$ and $\kappa_i$ at equatorial and high magnetic latitudes.136
6.2	Comparison of amplitude in meter-scale density perturbations (solid
	lines) to amplitude in decameter-scale density perturbations (dashed
	lines), in both 2-D and 3-D runs. The meter-scale amplitude com-
	prises amplitude in all available modes with 1 m $\leq \lambda \leq$ 4 m. The
	decameter-scale amplitude comprises amplitude in all available modes
	with 10 m $\leq \lambda \leq$ 40.96 m. In both panels, the blue trace corresponds
	to the 107-km run, the green trace to the 110-km run, and the red
	trace to the 113-km run. Note the difference in time ranges between
	2-D and 3-D runs

6.3	Average electron and ion temperatures, computed as functions of time	
	from the respective velocity distributions, for each run. Rows corre-	
	spond to altitude, from 107 km (bottom) to 113 km (top). The left	
	column shows temperatures in 2-D runs and the right column shows	
	temperatures in 3-D runs. In each panel, the solid traces correspond	
	to electron temperature and the dotted traces correspond to ion tem-	
	perature. For each species, the blue trace gives the Hall temperature	
	(aligned with $\mathbf{E}_0 \times \mathbf{B}_0$ ), the green trace gives the parallel temperature	
	(aligned with ${f B}_0$ ) and the red trace gives the Pedersen temperature	
	(aligned with $\mathbf{E}_0$ ). As in Figure 6.2, the time ranges significantly differ	
	between 2-D and 3-D runs	142
6.4	Relative perturbed ion density, $\delta n_i/n_0$ , at sixteen time steps through-	
	out the 2-D run at 107 km. The time stamp of each panel is in the	
	upper left corner. Each panel spans 40.96 m $\times$ 40.96 m, covering the	
	entire physical area perpendicular to ${f B}_0$ . The color scale for all panels	
	ranges from $-0.2$ to $+0.2$ , or $-20\%$ of $n_0$ to $+20\%$ of $n_0$	144
6.5	Relative perturbed ion density, $\delta n_i/n_0$ , at sixteen time steps through-	
	out the 2-D run at 110 km. The layout is identical to that of Figure	
	6.4	145
6.6	Relative perturbed ion density, $\delta n_i/n_0$ , at sixteen time steps through-	
	out the 2-D run at 113 km. The layout is identical to that of Figure	
	6.4	146
6.7	Relative perturbed ion density, $\delta n_i/n_0$ , at sixteen time steps through-	
	out the 3-D run at 107 km. The layout is identical to that of Figure	
	6.4 except that the time steps are different, since the 3-D runs cover	
	a quarter as much time as do the 2-D runs	148

6.8	Relative perturbed ion density, $\delta n_i/n_0$ , at sixteen time steps through-	
	out the 3-D run at 110 km. The layout is identical to that of Figure	
	6.7	149
6.9	Relative perturbed ion density, $\delta n_i/n_0$ , at sixteen time steps through-	
	out the 3-D run at 113 km. The layout is identical to that of Figure	
	6.7	150
6.10	Self-normalized log squared spectral amplitude in relative ion density	
	perturbation, $\langle \delta n_i/n_0 \rangle^2$ , during the 2-D run at 107 km. Panel times	
	correspond to the sixteen time steps shown in Figure 6.4. Each panel	
	spans slightly more than $-\pi$ to $+\pi$ in $k_x$ and $k_y$ . The color scale for	
	all panels ranges from -20 dB to 0 dB, or two orders of magnitude in	
	power	152
6.11	Self-normalized log squared spectral amplitude in relative ion density	
	perturbation, $\langle \delta n_i/n_0 \rangle^2$ , during the 2-D run at 110 km. The layout is	
	identical to that of Figure 6·10	153
6.12	Self-normalized log squared spectral amplitude in relative ion density	
	perturbation, $\langle \delta n_i/n_0 \rangle^2$ , during the 2-D run at 113 km. The layout is	
	identical to that of Figure 6·10	154
6.13	Self-normalized log squared spectral amplitude in relative ion density	
	perturbation, $\langle \delta n_i/n_0 \rangle^2$ , during the 3-D run at 107 km. Panel times	
	correspond to the sixteen time steps shown in Figure 6.7. The layout	
	is otherwise identical to that of Figure 6·10	156
6.14	Self-normalized log squared spectral amplitude in relative ion density	
	perturbation, $\langle \delta n_i/n_0 \rangle^2$ , during the 3-D run at 110 km. The layout is	
	identical to that of Figure 6.13	157

6.15	Self-normalized log squared spectral amplitude in relative ion density	
	perturbation, $\langle \delta n_i/n_0 \rangle^2$ , during the 3-D run at 113 km. The layout is	
	identical to that of Figure 6.13	158
6.16	Phase offset of relative ion temperature perturbations, $\delta T_{i\mathbf{k}}/T_{i0}$ , from	
	relative ion density perturbations, $\delta n_i/n_0$ , during the 2-D run at 107	
	km. Panel times correspond to the sixteen time steps shown in Figure	
	6.4. Each panel spans slightly more than $-\pi$ to $+\pi$ in both $k_x$ and	
	$k_y$ . The color scale for all panels is periodic and ranges from $-180^{\circ}$ to	
	+180°	162
6.17	Phase offset of relative ion temperature perturbations, $\delta T_{i\mathbf{k}}/T_{i0}$ , from	
	relative ion density perturbations, $\delta n_i/n_0$ , during the 2-D run at 110	
	km. The layout is identical to that of Figure 6·16	163
6.18	Phase offset of relative ion temperature perturbations, $\delta T_{i\mathbf{k}}/T_{i0}$ , from	
	relative ion density perturbations, $\delta n_i/n_0$ , during the 2-D run at 113	
	km. The layout is identical to that of Figure 6-16	164
6.19	Phase offset of relative ion temperature perturbations, $\delta T_{i\mathbf{k}}/T_{i0}$ , from	
	relative ion density perturbations, $\delta n_i/n_0$ , during the 3-D run at 107	
	km. Panel times correspond to the sixteen time steps shown in Figure	
	6.7. The layout is otherwise identical to that of Figure $6.16$	166
6.20	Phase offset of relative ion temperature perturbations, $\delta T_{i\mathbf{k}}/T_{i0}$ , from	
	relative ion density perturbations, $\delta n_i/n_0$ , during the 3-D run at 110	
	km. The layout is identical to that of Figure 6·19	167
6.21	Phase offset of relative ion temperature perturbations, $\delta T_{i\mathbf{k}}/T_{i0}$ , from	
	relative ion density perturbations, $\delta n_i/n_0$ , during the 3-D run at 113	
	km. The layout is identical to that of Figure 6.19	168

6.22	RMS squared spectral amplitude in $\delta n_i/n_0$ during growth and after	
	saturation in 2-D runs. Each panel spans 0 to $+2\pi$ in $k_x$ and $-\pi$ to $+\pi$	
	in $k_y$ . Rows correspond to altitude, from 107 km (bottom) to 113 km	
	(top). The left column shows the growth stage and the right column	
	shows the saturation stage. In each panel, a magenta line indicates	
	the drift angle, $\beta$ , a cyan line indicates the optimal flow angle for the	
	combined FBI+ITI, $\theta_{\rm opt}$ , and white lines indicate the centroid angle,	
	$\langle \theta \rangle$ , with $\pm \sigma$ uncertainties. The top of each panel lists the centroid	
	angle. The color scale is identical to Figures 6·10 through 6·15	173
6.23	RMS squared spectral amplitude in $\delta n_i/n_0$ during growth and after	
	saturation in 3-D runs. The figure layout is identical to that of Figure	
	6.22	174

## List of Abbreviations

1D (1-D)		One dimension (one-dimensional)
2D (2-D)		Two dimensions (two-dimensional)
3D (3-D)		Three dimensions (three-dimensional)
DC		Direct Current
$\mathrm{EM}$		Electromagnetic
ESF		Equatorial spread F
EUV		Extreme Ultraviolet
FAC		Field-Aligned Current
FAI		Field-Aligned Irregularities
FD		Finite Difference (numerical method)
FFT		Fast Fourier Transform
FBI		Farley-Buneman Instability
FWHM		Full-Width at Half Maximum
GDI		Gradient Drift Instability
GMRES		Generalized Minimal RESidual
GIIII		(numerical method)
GPS		Global Positioning System
HF		High Frequency
IRI2016 (IRI)		International Reference Ionosphere,
11(12010 (11(1)		2016 version
ISR		Incoherent Scatter Radar
JRO		Jicamarca Radio Observatory
LOS		Line of Sight (also Line-of-Sight)
MFP		Mean Free Path
NRLMSISE-00	• • • • • • • • • • • • • • • • • • • •	Mean Free Fam
		Nevel Descend Laboratory
(MSIS)		Naval Research Laboratory
		Mass Spectrometer Incoherent Scatter
		radar model
DDMG		extending to the Exobase, 2000 version
PETSc		The Portable, Extensible,
DIG		Toolkit for Scientific computing
PIC		Particle-In-Cell (numerical method)
RHS		Right-Hand Side
LHS		Left-Hand Side

SNR	 Signal-to-Noise Ratio
UV	 Ultraviolet
UHF	 Ultra High Frequency
VHF	 Very High Frequency

#### Chapter 1

#### Introduction

#### 1.1 Overview

This dissertation addresses the role of a particular type of density wave in the electrically charged upper atmosphere of Earth. These waves, described in detail below, are especially common around 100 km during the daytime, but have also been observed at night. Many places in the solar system meet the conditions for their existence, and recent theoretical research has even invoked them to explain heating in the solar chromosphere (Fontenla, 2005; Fontenla et al., 2008; Madsen et al., 2014; Fletcher et al., 2018). We know they exist in the Earth's atmosphere because they strongly scatter very high frequency (VHF) radio waves, which made them obvious to the first radio operators as far back as the 1940s. We also know, through both theory and observations, that they grow most readily at wavelengths of a few meters. What we do not know is how they interact with larger-scale structures, including other types of waves, and how their saturated, turbulent behavior changes with altitude.

#### 1.2 The Ionospheric Canvas

Earth's atmosphere above roughly 60 km is partially ionized during the day by solar EUV and soft X-ray radiation. The resultant plasma is called the ionosphere and comprises three main regions: the D region from 60 km to 90 km, the E region from 100 km to 150 km, and the F region from 150 km to several thousands of km.

Studying the motion of the plasma in the ionosphere, including plasma instabilities, is crucial to knowing how electromagnetic (EM) energy passes through and couples into the upper atmosphere. This dissertation focuses on plasma instabilities in the lower to middle E-region, spanning roughly 90 km to 115 km. There, Earth's magnetic field ( $\mathbf{B}_0$ ) and ambient electric fields ( $\mathbf{E}_0$ ) dominate electron motion while collisions with neutral particles dominate ion motion — in other words, electrons are magnetized and ions are unmagnetized. In addition, ionization layers and the increasing background plasma density provide medium- to large-scale density gradients.

Two instabilities that generate waves and, ultimately, turbulence in such a plasma have garnered significant attention since the advent of radar: A two-stream instability called the Farley-Buneman instability (FBI) that derives its free energy from ion inertia when magnetized electrons stream supersonically through unmagnetized ions, and the gradient drift instability (GDI), which derives its free energy from an ionization gradient aligned with an electric field. The two instabilities are special cases of one dispersion relation and may therefore occur in the same volume of plasma, provided appropriate fields and gradients exist. Furthermore, large GDI waves can create polarization electric fields high enough to trigger FBI waves in a parametric instability.

The FBI and GDI produce waves at various wavelengths but the observations that motivate their analysis come from radars that are sensitive to wavelengths of a few meters or less. At the heart of this dissertation is a desire to understand how, to adapt a phrase from Hysell et al. (2018), meter-scale waves produced by the FBI and GDI paint the natural "canvas" of the E-region ionosphere.

#### 1.3 Motivation

The following questions motivate the work presented in this dissertation:

- 1. How do density irregularities from co-evolving Farley-Buneman (FBI) and gradient drift instabilities (GDI) relate to historical classifications of radar spectra?

  Chapter 4 addresses this question.
- 2. How does a kilometer-scale wave give rise to vertically propagating meter-scale waves and how do those meter-scale waves feed back to their kilometer-scale driver?

Chapter 5 addresses these questions.

3. How does the spectrum of FBI turbulence change with altitude and how well do two-dimensional (2-D) simulations model the three-dimensional (3-D) dynamics?

Chapter 6 addresses these questions.

#### 1.4 Earth's Global Ionosphere and Thermosphere

This section describes the global structure of Earth's thermosphere and ionosphere, filling in and expanding upon the picture sketched out in §1.2. The main goals are to allow the reader to appreciate the body of previous research described in §1.5 and to accept the body of new research described in Chapters 4, 5, and 6. The excellent texts by Rishbeth and Garriott (1969); Schunk and Nagy (2004); Prölls (2004); Kelley (2009) provide historical introductions to ionospheric research, instruction in the relevant mathematical concepts, and explanations of the fundamental physical and chemical processes in the upper atmosphere and ionosphere.

The ionosphere makes up a tiny fraction of the Earth's atmosphere – compositionally, it is a collection of trace species embedded in the neutral gas above roughly 60 km. Nonetheless, it supports strong currents and large-scale electric fields, it interacts with the surrounding neutral species, and it affects EM waves that pass through it.

A London-based watchmaker named George Graham provided the first account of daily fluctuations in Earth's magnetic field as recorded by a compass needle, and published his findings in the Royal Society of London's *Philosophical Transactions*, in 1724. In 1839, Friedrich Gauss proposed that currents in the upper atmosphere caused such observed fluctuations of the geomagnetic field on the ground. In 1860, Lord Kelvin echoed Gauss's conclusion and Elias Loomis made the first connection between the aurora and Earth's magnetic field. Balfour Stewart built on the ideas of Gauss and Kelvin to further conjecture, in 1882, that tidal winds drive a dynamo which produces the currents responsible for geomagnetic fluctuations. Guglielmo Marconi made the first demonstration of transatlantic radio communication by bouncing an EM signal off of a conducting layer in the upper atmosphere in 1901; while Marconi and his contemporaries did not understand the nature of that conducting layer, those transmissions set the stage for modern ionospheric research.

The original physicists and radio operators who followed Marconi's successful transatlantic transmission called the reflecting layer the Kennelly-Heaviside (or simply Heaviside) layer, after Arthur Kennelly and Oliver Heaviside proposed in 1902 that free charges in the upper atmosphere were responsible for reflecting Marconi's radio waves. In the same year, Oliver Lodge put forth the pioneering physical theory that the influence of solar radiation increases the conductivity of the air by producing free electrons. In 1924, two teams of researchers – Edward Appleton and Miles Barnett in England, and Gregory Breit and Merl Tuve in the USA – made what the aeronomy community generally accepts as the first measurements of height of Marconi's reflecting layer. In fact, Appleton originated the D/E/F nomenclature scheme by marking the observed conducting layer with an E in his notes to signify that it supports electric fields. Upon observing a second layer at higher altitude, he had the presence of mind to mark that layer with an F, as well as to denote a conjectured

lower layer with a D.

#### 1.4.1 Fundamental concepts

Before delving into more detailed descriptions of ionospheric dynamics, it is important to understand the ionosphere and the atmosphere that hosts it. First, a few general definitions:

#### 1. Debye length and Debye sphere

The Debye length is the fundamental length of plasma physics. It is essentially the length at which the inward electrostatic pull of a charged particle on a more mobile, oppositely charged particle balances the outward thermal motion of the more mobile particle. Mathematically, its expression is

$$\lambda_{Dj} \equiv \sqrt{\frac{\epsilon_0 k_B T_j}{n_j q_j^2}}$$
 in meters,

where j stands for any charged species (e.g., j = e for electrons),  $\epsilon_0$  is the permittivity of free space,  $k_B$  is Boltzmann's constant, and  $T_j$ ,  $n_j$ , and  $q_j$  are the temperature, density, and charge of species j. On spatial scales much larger than the Debye length, the lighter particles shield the charge of the heavier particle. A Debye sphere is simply a sphere with radius  $\lambda_{Dj}$ .

#### 2. Plasma

A plasma is an ionized gas that is electrically neutral on large scales and that behaves collectively. The first criterion means that, on average, particles in a given region shield particles farther away from the electrostatic force of their nearby neighbors. More concisely: there are many particles in a Debye sphere (defined above). The second criterion means that when there *is* a charge imbalance in a particular region, it has long-range EM effects for which there are no parallels in a neutral gas. For example: In space, no one can hear you

scream because the density of neutral particles is negligibly small, precluding the inter-particle collisions that comprise sound waves. However, moving charged particles can create magnetic fields that stretch to infinity and beyond.

#### 3. Weakly, partially, and fully ionized plasmas

All ionospheres comprise a plasma embedded in a neutral gas. The role of collisions between two charged species versus collisions between charged and neutral species determines whether a plasma is weakly, partially, or fully ionized. In a weakly ionized plasma, the neutral density is many orders of magnitude larger than the ionized density, so collisions between charged species and neutral species dominate. The D and E regions of Earth's ionosphere are weakly ionized. In a partially ionized plasma, the neutral density is a few orders of magnitude larger than the ionized density, so both charged-charged and charged-neutral collisions are important. The F region of Earth's ionosphere is a partially ionized plasma. In a fully ionized plasma, neutral species may still exist but collisions between charged species and neutral species are negligible. The topside ionosphere is a fully ionized plasma.

#### 4. Plasma frequency

The plasma frequency is the most fundamental oscillation in a plasma. Given two oppositely charged species, one lighter than the other, any separation between the two will create a restorative electrostatic force. The lighter species will respond to this force by moving toward the heavier species but its inertia will cause it to overshoot and move away in the opposite direction. This oscillatory behavior will continue until some outside force, such as a collision, stops it. The oscillation frequency is the plasma frequency.

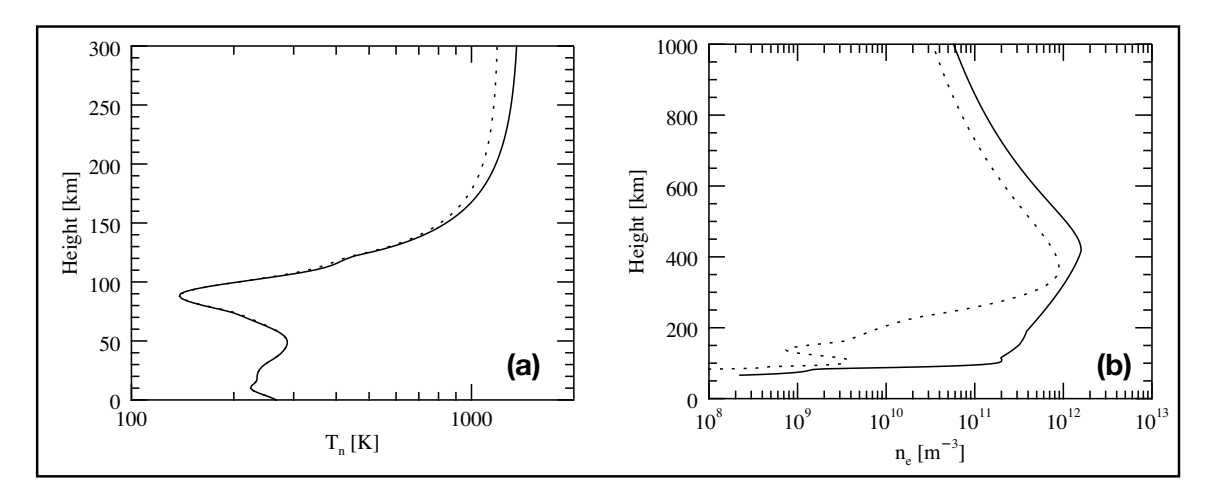


Figure 1·1: Altitude profiles of (a) MSIS neutral temperature from 0 to 300 km and (b) IRI electron density from 0 to 1000 km at the magnetic equator. Solid lines correspond to daytime and dashed lines correspond to nighttime.

#### 1.4.2 Ionospheric structure and composition

Taking a cue from Kelley (2009), the altitudinal profiles of neutral temperature and electron density in Figure 1·1 gives a cursory description of the neutral atmosphere and the ionosphere, respectively. The temperature profile comes from the 2000 version of the Naval Research Laboratory Mass Spectrometer Incoherent Scatter radar model extending to the Exobase (NRLMSISE-00 or simply MSIS) (Picone et al., 2002) and the electron density profile comes from the 2016 version of the International Reference Ionosphere (IRI2016, or simply IRI) (Bilitza et al., 2017). Moving up from sea level, the daytime temperature in the troposphere drops exponentially until it reaches the tropopause at  $h \approx 10$  km. Above the tropopause, ozone in the stratosphere absorbs ultraviolet (UV) radiation and causes the temperature to increase with altitude until the stratopause at  $h \approx 50$  km. The stratopause marks a transition from UV heating to radiative cooling, and the temperature drops precipitously through the mesosphere. The temperature hits its minimum at the mesopause, around 90 km, at which point extreme ultraviolet (EUV) and soft X-ray photons heat

the neutral gas from roughly 130 K to 1000 K or more over 100 km. This region of intense heating is aptly called the thermosphere. The nighttime temperature profile follows the daytime profile fairly closely at the magnetic equator; it only diverges by a modest amount above  $h \approx 150$  km due to the lack of solar irradiation. Neither daytime nor nighttime profile change much above 300 km.

The electron density profile serves as a measure of total ionization as a result of the quasi-neutrality assumption. Note that even though the vertical axis extends to sea level, appreciable ionization (and hence the ionosphere) starts at around 60 km. From 60 km to 90 km, the daytime electron density climbs from effectively zero to about 10<sup>9</sup> m<sup>-3</sup>. This is the D region ionosphere. It disappears at nighttime. The electron density increases even more quickly until about 100 km, where it reaches a local peak. Although the nighttime E-region density is more than an order of magnitude lower, the peak is far more noticeable. The E-region peak exists because of the specific neutral composition, which the following section will describe in more detail. Above the E-region peak and corresponding "valley region", the electron density again increases, this time up to its maximum. The F region begins around 150 km – the distinction is again more obvious at night – and the F-region peak is also the global ionization peak in the atmosphere.

Figure 1·2 shows the composition of charged and neutral species from IRI and MSIS, respectively. Neutral density for  $N_2$ ,  $O_2$ , and Ar in Figure 1·2a decrease exponentially with altitude at about the same rate up to the turbopause around 100 km, where turbulent mixing stops. Above the turbopause, they separate out based on masses, according to hydrostatic equilibrium. The profiles of atomic oxygen, atomic nitrogen, and atomic hydrogen differ from the simple exponential fall-off because of chemical interactions in the upper atmosphere. Most of the O is bound up in  $O_2$  below 100 km or so, but as altitude increases, there is more solar radiative flux, which

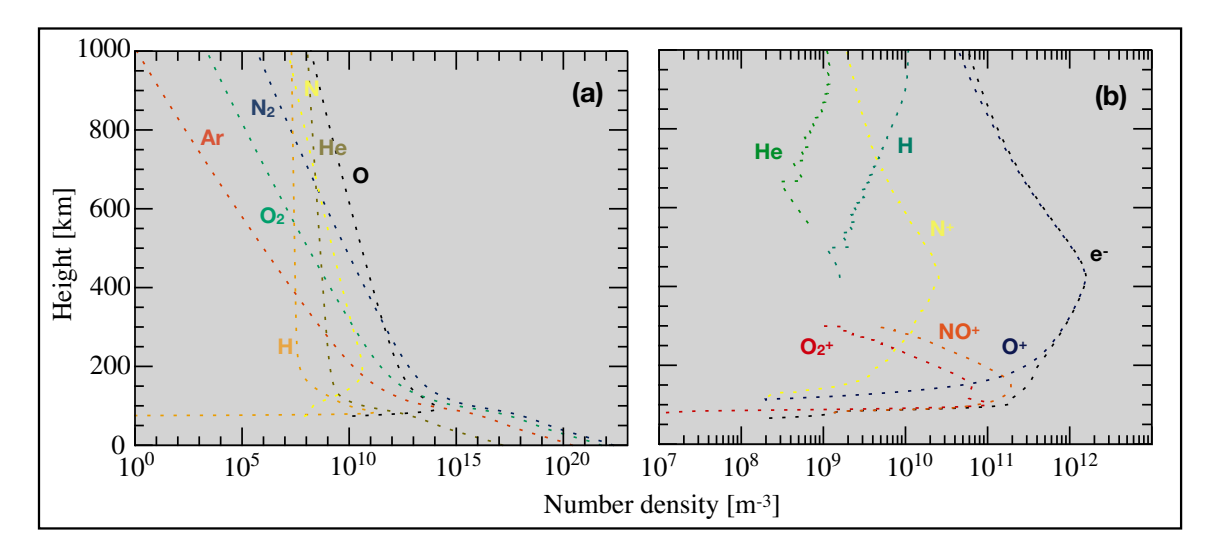


Figure 1·2: Altitude profiles of density of (a) neutral species and (b) charged species from 0 to 1000 km at the magnetic equator. Individual species names are placed as close as possible to the corresponding profile. The neutral-species densities from from MSIS and the charge-species densities come from IRI.

causes some  $O_2$  molecules to dissociate into O. Above the turbopause, the density of O will naturally decrease more slowly than the density of  $O_2$  due to their different scale heights.

The electron profile in Figure 1·2b is identical to the daytime profile in Figure 1·1b. Figure 1·2b shows that the E region consists mainly of  $NO^+$  and  $O_2^+$  ions, while  $O^+$  gradually increases to provide most of the plasma in the F region. The difference between molecular ions in the E region and atomic ions in the F region accounts for the difference between daytimes and nighttime electron profiles in Figure 1·1b. At E-region altitudes,  $N_2$ , O, and  $O_2$  absorb photons with wavelengths less than 790 Å, 910 Å, and 1030 Å, respectively, to produce  $N_2^+$ ,  $O^+$ , and  $O_2^+$ . Although neither O nor  $O^+$  constitute major species in the E region, both can act as a catalyst to form  $NO^+$  from  $N_2^+$ , and even though the density of O is less than the densities of  $N_2$  and  $O_2$ , it is still far greater than any of the ion densities. Likewise, the E region nearly disappears at night because recombination works much more efficiently for

molecular ions than for atomic ions and because the higher neutral density makes collisions much more frequent.

There are also phenomenological distinctions between different regions in the ionosphere. The D region ionosphere is very weakly ionized and it supports more exotic ions, including negatively-charged water-cluster ions, and charged dust. Throughout most of the D region, ions and electrons collide so frequently with neutral species that neutral dynamics significantly influence their behavior. The D region has colloquially developed the nickname "the ignorosphere" because its ionization is too low to produce the density irregularities that radars typically observe and because it is difficult to measure in situ. However, it can significantly impact radio-wave propagation because of its high electron-neutral collision frequency,  $\nu_e$ , since a plasma will attenuate EM waves when the wave frequency is near  $\nu_e$ . More precisely, the product  $n_e\nu_e$  is what matters for absorption, since the EM wave passes straight through the neutral atmosphere. The neutral density, and therefore  $\nu_e$ , is roughly constant at D-region altitudes, so increasing  $n_e$  leads to increased absorption. For that reason, the daytime D region heavily attenuates short-wave radio signals in the 1-8 MHz range, whereas those signals propagate with significantly reduced attenuation after the D region disappears at night. X-ray flares can produce severe attenuation at HF frequencies (3-30 MHz) by drastically increasing the electron density. Naturally, the D region has recently garnered increase attention precisely because the aeronomy community knows so little about it, not to mention the fact that the mesosphere hosts interesting neutral phenomena which may have charged counterparts. New observational techniques and the push to understand energy transfer throughout the whole atmosphere-ionosphere system will almost certainly lead to increased interest in the D region.

The E region was the first known ionosphere region because it reflects radio

waves. It also supports appreciable electric fields and strong currents, the latter of which deflect ground-based magnetometers and compasses. It is weakly ionized in the sense of the definition above, but there is an important distinction between ions and electrons. In the low to middle E region, ions typically collide with neutral particles more frequently than they complete a gyro-orbit in the Earth's magnetic field, meaning that they tend to follow neutral dynamics. Electrons, on the other hand, respond to the magnetic field more than to the neutral dynamics. This dynamical difference leads to the plasma instabilities that are at the heart of this dissertation, which section 1.6 will describe in detail.

The equatorial and auroral E regions host strong currents called electrojets. The equatorial electrojet arises because of tidal motions of the neutral atmosphere and the auroral electrojet arises because of strong magnetospheric currents that flow along field lines and close in the ionosphere. In the equatorial case, the energy in solar radiation that does not go into ionizing neutral particles goes into heating the neutral gas. This heating causes an upward (vertical) neutral wind that drags ions across magnetic field lines. The primary neutral wind component is the migrating diurnal tide – migrating meaning that the effect moves with the Sun and diurnal meaning that the effect has a daily period. This wind produces an east-west (zonal) dynamo electric field on the order of 1 mV/m (Schunk and Nagy, 2004). The zonal electric field drives a small Pedersen current,  $\mathbf{J}_{zonal}$ , but that current is not the equatorial electrojet. Rather, the  $\mathbf{J}_{zonal} \times \mathbf{B}_0$  force due to the zonal current moves electrons upward and ions downward.

The plasma conductivity significantly drops off below 90 km, due to the decrease in ionization, and again above 120 km, due to increased ion magnetization; the combined effect produces a vertical electric field to cancel the charge polarization and maintain quasi-neutrality. That vertical polarization electric field is larger than the

zonal field by a factor of  $\sigma_H/\sigma_P \approx 10$ , where  $\sigma_H$  and  $\sigma_P$  are the Hall and Pedersen conductivities. The total zonal current is  $J_{zonal} = \sigma_H E_{vertical} + \sigma_P E_{zonal} = \left[ (\sigma_H/\sigma_P)^2 + 1 \right] \sigma_P E_{zonal} = \sigma_c E_{zonal}$ , where  $\sigma_c \equiv \sigma_H^2/\sigma_P$  is called the Cowling conductivity (Kelley, 2009). This total current comprises the equatorial electrojet. In the auroral zone geomagnetic storms produce strong electric fields that map along highly conducting magnetic field lines until they reach the E region, where they drive Pedersen and Hall currents that close the field-aligned currents (FACs). The resultant Hall current comprises the auroral electrojet.

Near the top of the E region, the ion collisions become less important than ion motion in the Earth's magnetic field and the F region consists of a partially ionized plasma that responds mostly to EM forces. The electrostatic instabilities of the E region give way to new instabilities, including huge plasma bubbles and plumes that create the radar phenomenon known as equatorial spread F (ESF) and that cause scintillation of global positioning satellite (GPS) signals. The F region extends up to the exobase, where the mean free path (MFP) becomes larger than the scale height (this applies in an average sense, since both quantities differ among species). At that point, particles can escape the atmosphere before colliding with other particles, so the exobase effectively represents the edge of space.

### 1.4.3 Ionospheric observation techniques

The aeronomy community observes the ionosphere using both remote sensing and in situ observations. We perform remote sensing with radars across a wide range of radio frequencies: Coherent scatter radars in the HF (3-30 MHz), VHF (30-300 MHz), and UHF (300-3000 MHz) bands reflect from ionospheric irregularities with sizes ranging from a few centimeters to tens of meters, providing information about plasma density irregularities; incoherent scatter radars (ISRs) typically operating at hundreds of MHz reflect from a sea of thermal electrons, providing information

about density, temperature, and composition. The term coherent scatter refers to the coherent return signal that builds up after many partial reflections from wave fronts spaced out at half the wavelength of the radar beam. The term incoherent scatter refers to the reflection of the radar beam from many electrons in a common volume, whose motions are not organized into coherent wave fronts. A special class of ISRs, called phased-array radars, produce volumetric images of ionospheric state parameters through sophisticated electronic steering and data-analysis software; and active heating experiments perturb small patches of the ionosphere while measuring the effect with other instruments. We also perform remote sensing with lidar. Lidar instruments operate on principles similar to radars (in fact, the term "lidar" is an extension of the term "radar"), except instead of reflecting or scattering off collections of free electrons in the ionosphere, they can reflect off of ions, neutral atoms and molecules, or more complex particles such as dust grains. All-sky images provide a way to passively observe naturally occurring ionospheric processes that emit light, including aurora and air glow – they are often very sensitive and may collect light over a range of wavelengths or at one particular wavelength. Remote sensing was once primarily a ground-based approach, but space craft now routinely fly radars, lidars, and cameras as part of their instrument packages.

Of course, those same space craft also provide valuable in situ data. That data may include measurements of ion and neutral species composition, ambient magnetic and electric field strength and orientation, or electrostatic and electromagnetic waves. Most standard satellite orbits have perigees no closer than a few hundred kilometers, meaning they do not sample the E-region ionosphere on a regular basis, though some satellites have taken data during their final descent. Small satellites (e.g., cubesats, nanosatellites, etc.) may pass below a few hundred kilometers on dedicated missions, but atmospheric drag limits the lifetime of any such orbit. Balloons provide in situ

data of the lower atmosphere, but the loss of buoyancy as atmospheric density drops exponentially with altitude limits their maximum height to around 40 km – too low to probe the ionosphere directly.

Rockets have proven to be a reliable method for directly observing the ionosphere, especially the E region, but they provide only one shot at getting a set of measurements. Rocket payloads often carry instruments similar to those on satellite payloads – instruments designed to measure electromagnetic fields, neutral and charged particles, and plasma waves. While rockets are likewise bound to follow laws of orbital motion, a particular mission design may allow a rocket to spend more time at a target altitude, or sample all altitudes up to apogee. A mission may even feature multiple rockets with various trajectories. Finally, rockets can also modify the ionosphere via chemical release. Explosive injection of a chemical such as barium produces an isolated plasma which responds to local winds and electromagnetic fields, and whose gradients can produce confined density irregularities.

Radar and rocket data provide the observational basis for the work presented in this dissertation because radars have been measuring coherent scatter from the E region since the 1930s, beginning with radar aurora, and rockets have been a consistent vehicle for *in situ* measurement of the E region since around the same time. The advent of small satellites provides an exciting new avenue for directly probing the low ionosphere.

Numerical modeling has benefited immensely from recent (and on-going) revolutions in computing technology and power. Thanks to Moore's Law, along with the increasing commercial market for computer scientists and IT specialists, numerical modeling is widely accessible to the scientific community. Modern supercomputers allow researchers to easily run simulations on tens of thousands of nodes.

Analytic theory produces rigorous explanations of observed and simulated data

within the scope of physical laws. Even as computers grow more powerful and as artificial intelligence becomes a more robust method for sussing out physical patterns, mathematical theory provides rigorous insight and makes predictions that lead to further research.

#### 1.5 Review of relevant literature

Researchers have studied radio-frequency echoes from the E-region ionosphere since at least the 1940s; as a result, the body of potentially "relevant" literature is substantial. This section will provide adequate background on the general research related to E-region instabilities, and chapters 4, 5, and 6 will fill in more specific information as necessary. For excellent reviews, see Fejer (1979); Fejer and Kelley (1980); Forbes (1981); Farley (1985, 2009). For the most part, this section progresses historically.

The characterization of E-region irregularities began in earnest in the early 1960s, when research teams from the National Bureau of Standards, lead by Dr. Kenneth Bowles, fixed their radars on the ionosphere above the magnetic equator (Bowles et al., 1960, 1963). Earlier observations of "radar aurora", beginning with an employee in the Research and Development Department of Marconi's Wireless Telegraph Co., Ltd. (Eckersley, 1937), showed that a sufficiently strong HF radio apparatus could observe radar echoes associated with the visible aurora. A little less than two decades later, Bowles (1954) used a 25.4 MHz radar to study the auroral echoes and determine that the radar aurora is highly aspect sensitive – that is, it only reflects radio-frequency waves when the transmitter and receiver are oriented close to perpendicular to the magnetic field. Two years later, Booker (1956) established that auroral radar echoes come from field-aligned irregularities (FAI) in the electron density, with scale sizes on the order of a meter perpendicular to  $\mathbf{B}_0$  and five to ten meters parallel to  $\mathbf{B}_0$ .

These and other observations inspired the move to the geomagnetic equator, where the relative quiescence of the ionosphere makes it an excellent natural plasma laboratory. Those observational campaigns of the early 1960s at Jicamarca Radio Observatory (JRO) included the work by Bowles et al. (1960, 1963). The first – a two-and-a-half-page letter – took the crucial step of proposing that auroral and equatorial electrojet irregularities were not quite Booker's field-aligned ellipsoidal density structures, but rather plane waves propagating perpendicular to  $\mathbf{B}_0$  with field-aligned wave fronts. They also made the prescient assertion that these VHF echoes may result from longitudinal waves of electron density. Farley (1963b) responded with a brief note of his own, outlining a theoretical description of the irregularities that Bowles et al. (1960) had observed. In that note, he showed that by extending the existing kinetic theory of two-stream plasma waves to include the effect of the background magnetic field and charge-neutral collisions, he could explain the electrojet observations as long he used a collision term that only affects the charged species' velocity distributions (not their distributions in space). In the same published volume, Buneman (1963) outlined a simplified fluid version of the modified two-stream instability in the E-region ionosphere. As a result, the aeronomy community has come to call this process the Farley-Buneman instability (FBI).

Shortly after Farley and Buneman published their theoretical outlines, Bowles et al. (1963) expanded on the work of Bowles et al. (1960), summarizing the nature of aspect-limited E-region echoes as distinct from other phenomena observed at VHF, describing additional observations at the magnetic equator, and placing both observations and theory in the context of the equatorial and auroral electrojets. In the same volume, Cohen and Bowles (1963) explain more thoroughly how the observed irregularities are embedded in the electrojet, and demonstrate that irregularities only occur when the electrojet exceeds a certain strength. Finally, Farley (1963a) pub-

lished the detailed version of the kinetic theory he had outlined in Farley (1963b) and showed that it explained the recent observations. In particular, he noted that Buneman (1963) assumed that fluid theory sufficiently described electron and ion behavior in the modified two-stream instability, but that that assumption breaks down for short enough wavelengths. The kinetic description is crucial to ion dynamics when the wave oscillation frequency,  $\omega$ , is on the order of the ion collision frequency,  $\nu_i$  – for the parameters he used, that occurs at wavelengths around 1.5 m. Farley's theory also explains that the previously observed threshold condition of electrojet irregularities arises from the need for electrons to stream through ions faster than the plasma acoustic speed. Some authors argue that this threshold criterion is the only robust prediction that linear theory has to offer (e.g., (Hysell et al., 2012)).

Balsley (1965) performed two subsequent VHF experiments at JRO. The first experiment showed that the E-region echoing layer is bifurcated before and after local noon, but converges to a single layer slightly thicker than the sum of the two layers around noon. The second experiment showed that there exist a class of echoes that the two-stream plane-wave theory cannot explain. Notably, the unexplained echoes traveled at speeds slower than the plasma acoustic speed. Cohen and Bowles (1967) corroborated the observations of slower echoes with a more sensitive VHF system. They also reported weak echoes in radar beams pointed vertically and obliquely, and described a power asymmetry in vertical echoes. Dougherty and Farley (1967) attempted to attribute the second class of echoes to the natural result of mode-coupling of modified two-stream modes as part of a nonlinear inverse cascade. However, such a model fails to account for the presence of such irregularities when the electrojet is not strong enough to trigger the modified two-stream instability.

The end of 1967 saw the first self-consistent 2-D model of the dynamo theory for the equatorial region, by Untiedt (1967), who constructed a meridional model of the electrojet which neglects local winds and local time variations but which allows for vertical current flow. Additional observations by Balsley (1969) established that there are, in fact, two distinct types of spectra in VHF observations of the equatorial electrojet: type-I spectra produced by the modified two-stream instability, and type-II spectra, produced by some other mechanism. In response, Rogister and D'Angelo (1970) produced a fluid treatment of electrojet irregularities including gradients with an emphasis on explaining type-II irregularities. After discarding a few likely but ultimately insufficient instability candidates, they declared that the type-II mechanism requires an ionization gradient. They identified a high-frequency version of a gradient-driven instability first studied in the laboratory by Simon (1963) and Hoh (1963), and applied to the ionospheric case by Maeda et al. (1963), as the culprit. The aeronomy community now commonly knows this instability as the gradient-drift instability (GDI). Although these pioneering researchers had not adopted the terms FBI and GDI to describe the mechanisms behind type-I and type-II irregularities, respectively, the remainder of this presentation will employ those terms. Figure 1.3 shows canonical type-I spectra from Cohen and Bowles (1967) and type-II spectra from Balsley (1969). Both sets of observations are from JRO.

Rockets as a tool for ionospheric study matured in the late 1960s/early 1970s, providing a new perspective to compliment radar spectra and suss out irregularity mechanisms. Prakash et al. (1969) recorded irregularities in three altitude ranges: 97-106 km, 142-155 km, and around 170 km and reported that the spectral indices of irregularities, which describe the change of irregularity amplitude with wavelength, in the lower range suggested two distinct types of spectra. They also acknowledged that electric fields, more than neutral turbulence, must play an important role. From a second rocket flight, Prakash et al. (1970) reported density irregularities with scale sizes in the ranges 1-15 m and 30-300 m. All irregularities occurred in regions where

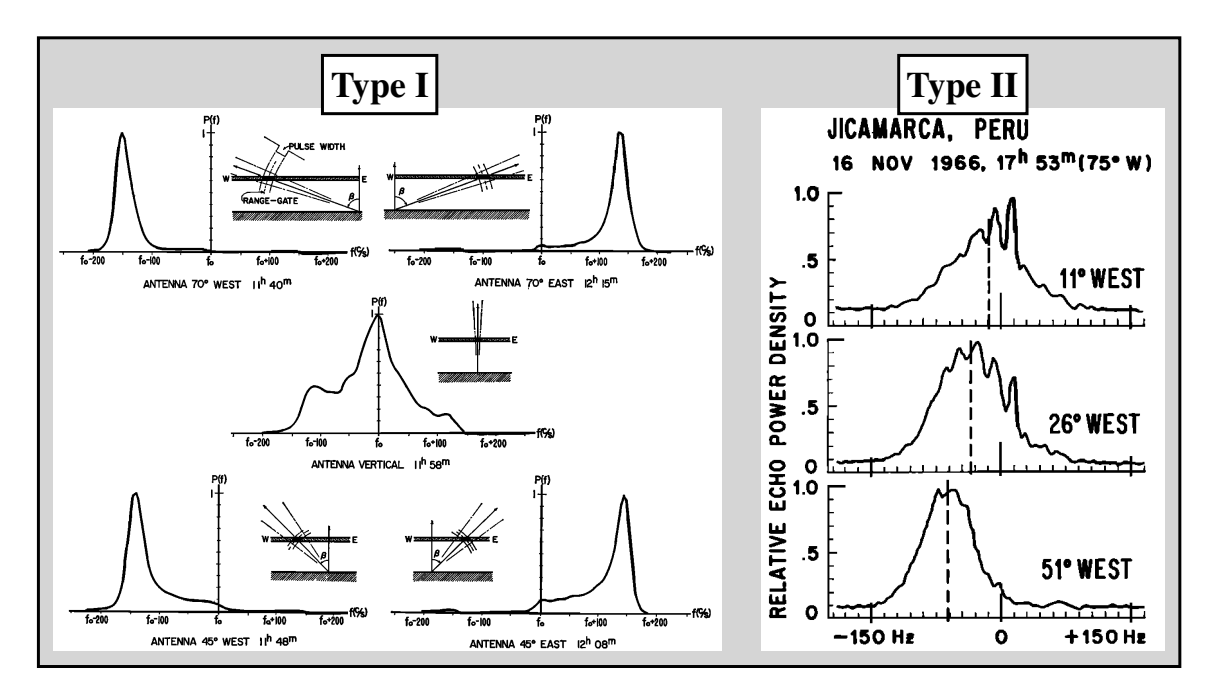


Figure 1·3: Canonical type-I (left) and type-II spectra (right). The left panel is from Cohen and Bowles (1967), showing a composition of spectra taken near noon at Jicamarca, during relatively strong electrojet. The top two panels show echoes from 70° west and east, the middle panel shows echoes from vertical, and the bottom two panels show echoes from 45° west and east. The right panel is from Balsley (1969), showing simultaneous spectra taken near 18:00 at Jicamarca. The top panel shows echoes at 11° west, the middle panel shows echoes at 26° west, and the bottom panel shows echoes at 51° west.

the background density gradient was favorable to the GDI, but the GDI can only account for the those in the 30-300 m range. The authors seem to consider that the FBI may play a role in generating the small-scale instabilities but they suggested further study.

Balsley and Farley (1971) investigated the wavelength dependence of the properties of type-I and type-II equatorial electrojet irregularities at three frequencies: 16.25 MHz, 49.92 MHz, and 146.25 MHz. They found that when type-I echoes are present, they dominate the 50-MHz spectrum more than they dominate the 16-MHz spectrum, and type-II echoes are always important at 16 MHz but are absent at 146

MHz. They also noticed that type-I echoes show up more or less simultaneously in all three frequencies, after the flow speed crosses the two-stream threshold while smaller drift velocities produce type-II echoes only at lower frequencies. Overall, the type-I mechanism appeared to efficiently generate irregularities over a wide range of wavelengths, whereas the efficiency of the type-II mechanism dropped off rapidly as wavelength decreases. The authors certainly understood the type-I mechanism but the manifestation of gradient-driven turbulence in radar spectra remained unclear. They suggested that the irregularities at 16 and 50 MHz arise from nonlinear interactions between directly gradient-driven modes (i.e., a turbulent cascade) and that those at 146 MHz were in the diffusive subrange. As the community wrestled with type-II spectra, Rogister (1972) published a theoretical analysis of one-dimensional gradient-driven turbulence in the equatorial electrojet, showing that linearly unstable long-wavelength modes transfer energy to short-wavelength modes which are stabilized by classical diffusion, supporting the conclusions of Balsley and Farley (1971).

Shortly thereafter, Sudan et al. (1973) published a 2-D model that accounts for short-wavelength electrojet irregularities when the drift speed is below the FBI threshold. Their 2-D model allows long-wavelength waves produced by the background plasma gradient to drive obliquely propagating meter-scale irregularities. A companion paper by Farley and Balsley (1973) presented the observational evidence for that proposed mode-coupling scheme and concluded, in part, that the electrojet is highly turbulent over hundreds of meters, the local drift velocity within large-scale structures controls production of small-scale structures, and the local drift velocity may differ substantially from the mean drift velocity. They also offered the hypothesis that type-I spectra saturate at the acoustic speed because the observations represent waves that have had time to grow to relatively large amplitudes, and are traveling at the threshold speed as they leave the unstable region.

Later that year, Balsley and Farley (1973) published radar observations with improved spatial and temporal resolution that gave strong support to the proposal that large-scale irregularities generated by GDI produce small-scale GDI and FBI irregularities. They believed that, while one-dimensional wave steepening and turbulence may play some role in generating type-II spectra, its effect is weaker than that of 2-D coupling between large and small structures. Schmidt and Gary (1973) then presented the first kinetic derivation of a linear dispersion relation for FBI including gradients by deriving a solution to the kinetic equation in the  $\mathbf{E}_0 \times \mathbf{B}_0$  frame, where  $\mathbf{E}_0$  disappears. They compared their kinetic treatment to the fluid theory of Rogister and D'Angelo (1970) and showed that a fluid approximation is valid for electrons in the region of interest. They also showed that a gradient increases the growth rate at  $k \ll 10^{-2}$  m<sup>-1</sup> and that ion fluid theory is valid for  $\omega < \nu_i/10$ .

A short theoretical work by Farley and Fejer (1975) lead those authors to suggest that large-scale waves directly excite type-I irregularities when the local plasma meets threshold conditions, which could explain the rocket observations by Prakash et al. (1970). Fejer et al. (1975a,b) presented JRO observations of the E-region at oblique angles, with roughly 1.1-km altitude resolution, during daytime and dusk. Fejer et al. (1975a) observed type-I echoes only above about 105 km and noted that the width of type-II echoes becomes large before type-I echoes appear. They saw no echoes above the daytime type-I power peak at about 107 km and observed a peak in phase velocity at about 104 km. Fejer et al. (1975b) presented observations during dusk and noted that the observed switch in echoing regions was consistent with reversal of electrojet, with its attendant reversal in direction of favorable gradient. Both works provided strong evidence that the GDI produces type-II irregularities, as long as the linear theory includes recombination.

Daytime JRO observations at vertical incidence by Fejer et al. (1976) contained

no sign of type-I echoes above 108.25 km, with a peak in power at around 104 km. Their most notable observation was an up/down asymmetry in the power of type-I echoes despite the fact that the relative Doppler shift was the same. They found that vertically propagating type-I irregularities could change direction in a matter of seconds and they also observed that the asymmetry reversed at night. Knowing that previous measurements had shown an east-west power asymmetry, they proposed that the two asymmetries are related and that both arise from an asymmetry in nonlinear limiting processes that depend on the direction of electrojet current. This evidence, as well as the fact that type-II echoes dominated the spectra during longer integration times, fortified the picture of a highly turbulent electrojet scattering region. Similar nighttime observations by Farley et al. (1978) showed that type-I power could dominate the spectrum at times and could occur over a wider range of altitudes than during the day, with evidence of structures on the scales of kilometers to tens of meters in addition to the meter-scale irregularities that the radar observed directly.

Around this time period, a small group of researchers began publishing observations of irregularities in the equatorial electrojet above Africa, using an HF system in Ethiopia. Hanuise and Crochet (1977) used measurements at 5, 7, and 10 m to show that irregularities appear at longer wavelengths sooner than at smaller wavelengths and that type-II phase velocity is constant across frequencies whereas type-I increases with frequency. The latter conclusion is consistent with theories that include a gradient in electron density, since the density gradient affects the threshold phase velocity (Farley and Fejer, 1975). They also confirmed that the echoing laying bifurcates during daytime at all frequencies. Crochet et al. (1979a,b) reported observations during counter-electrojet conditions, when the electrojet reverses direction. Their observations that type-II echoes disappear during counter-electrojet were con-

sistent with linear theory, since the electric field and plasma gradient were no longer favorably aligned. They observed oblique type-I echoes above 105 km but noted that the type-I Doppler shift followed a cosine law with zenith angle, unlike typical type-I echoes. They also took advantage of HF refraction in the E region to observe horizontally propagating echoes, which they call "type H" at 100-105 km.

A few years later, Crochet and Hanuise (1981) introduced a new multiple-scatter technique to probe the k spectrum at multiple angles with a single radar, using the F region and the ground as reflecting surfaces. A subsequent three-paper series outlined important results of HF observations with the Ethiopia system: Hanuise and Crochet (1981b) presented observations of backscatter from irregularities with phase velocities below 200 m/s. The measured phase velocity of irregularities varied with wavelength from 5 m to 50 m, and with elevation angle, and the spectral width was on the order of the Doppler shift, indicating strong turbulence. Hanuise and Crochet (1981c) presented observations of type-I irregularities at intermediate wavelengths (tens of meters). The phase velocity was near the instability threshold value and was constant with elevation angle. The spectral width increased with wave number, was constant with elevation angle, and was on the order of the Doppler shift at the longest wavelength observed. Hanuise and Crochet (1981a) presented observations during counter-electrojet observations of two-stream spectra with phase velocities that follow the linear-theory expression – that is, they have a cosine dependence on the angle between the radar line-of-sight (LOS) and the background plasma convection. This angle is important to radar observations and is called the "flow angle". They called these "type 0" irregularities to distinguish them from type-I irregularities observed during normal electrojet times, since the later appear to have roughly constant phase speed near the acoustic speed.

Computers became more useful in the 1960s and 1970s for calculating numerical

solutions to some theoretical problems, though self-consistent computer simulations of ionospheric phenomena still lagged radar, rocket, and laboratory observations as a scientific tool. Newman and Ott (1981) produced the first numerical simulations of nonlinear two-stream instability by using modeling electrons and a single species of ions with the two-fluid equations. Their simulations had constant  $\mathbf{B}_0$  and orthogonal  $\mathbf{E}_0$ , collisions between charged and neutral particles, and a viscous term to mimic the ion Landau damping that a fluid model lacks. The background plasma was homogeneous and isothermal. They presented results from two models: Model A used a constant-direction electric field source; Model B assumed the spatial average of the vertical current density to be zero. Model A showed horizontal waves dominating the spectrum whereas Model B showed a more isotropic distribution of phase velocities. In Model B, phase velocity of the dominant modes tends to the acoustic velocity. They found that Model A best explained the behavior of type I irregularities in the absence of type II irregularities while Model B acted like a stable system that had been hit by an impulsive force. Model B was less physical in that it required an external field to vary as irregularities grew in a local region, but it exhibited a rotation in angular spectrum with respect to the current density, indicating a stabilization mechanism responsible for deactivating the two-stream instability.

ISR measurements by Schlegel and St.-Maurice (1981) showed anomalous electron heating in the polar E region. Previous work had reported some cases of enhanced electron temperatures but this is the first to identify it as a feature of the E region that can not be due to classical heat sources. Comparison of temperature and drift data led the authors to conclude that heating is due to plasma waves in a region of large Hall currents and low collision frequencies – in other words, FBI waves. The observed electron temperatures correlate well with the DC (direct current – that is, constant) electric field. implications to the polar E region include increased chemical

reaction rates and modified energy budget. The results also have implications for ISR measurements, which typically assume equal electron and ion temperatures. A companion paper by St.-Maurice et al. (1981) contained a theoretical analysis of anomalous electron heating by plasma waves and produced theoretical temperature profiles similar to observed profiles. They found that the single most important factor is DC electric field strength, with electric fields below 45 mV/m producing little heating. They concluded that the amount of wave heating may equal as much as half of the Joule heating for electric fields above that threshold.

Kudeki et al. (1982) Showed existence of kilometer-scale, horizontally propagating waves during type-I conditions with an interferometry technique at JRO. This work also showed that the frequency and growth rate typically cited for meter-scale waves do not apply to wavelengths on the order of a kilometer. A companion paper by Pfaff et al. (1982) presented *in-situ* rocket observations of "intense electrostatic waves" on the upward electron gradient during the day and downward electron gradient during the night, at the magnetic equator. Their observations were consistent with the gradient drift instability explanation of wave generation.

Sudan (1983) reviewed then-known characteristics of type-I and type-II echoes before applying a theory of plasma turbulence, partially developed by the author, to the equatorial electrojet. The theory predicted an irregularity power spectrum for both the absolute magnitude and variation with k, without recourse to any empirical laws. The author claimed that the theory predicts every feature of type-II irregularities; he also provided a rational explanation of why type-I irregularities appear to be isotropic in azimuthal angle and limited to phase velocities near  $C_s$ . He developed a nonlinear model of an isothermal, electrostatic, quasi-neutral plasma with the heuristic assumption that the electron fluid contains the principle nonlinearity. This approach included augmenting the electron collision frequency,  $\nu_e \rightarrow \nu_e + \nu_*$ , where

the second term represents an electron collision frequency driven by wave-induced electron diffusion. According to Sudan and Keskinen (1984), the theory predicted the magnitude of the wave-power spectrum as a function of wavelength in terms of a strength parameter similar to a Reynold's number that defines the level of turbulence.

Fejer et al. (1984) developed a general theory for electrojet waves (e.g., FBI and GDI) and waves observed at higher altitudes (e.g., ion-cyclotron and current convective waves). Their theory neglects electron inertia, neutral winds, and electric field shear effects and assumes quasi-neutrality and an isothermal plasma. It is valid for wavelengths much larger than the ion MFP or the ion Larmour radius, whichever is smaller. Depending on wavelength, the electron density gradients, electron-ion collisions, and recombination can substantially affect the threshold drift velocity. They derived a dispersion relation (their Equation 4) of which the typically cited relations for the  $\gamma \ll \omega_r$ ,  $kL \gg [\kappa_i (1 + \psi_\perp)]$  limit, and the  $\gamma \sim \omega_r$ ,  $kL < [\kappa_i (1 + \psi_\perp)]$  limit are special cases. They note that the general instability criterion for gradient-driven turbulence is that  $\mathbf{k} \cdot \mathbf{V}_d$  and  $\mathbf{k} \cdot (\nabla n \times \mathbf{B}_0)$  have the same sign, but they consider only waves propagating parallel to  $\mathbf{k} \cdot (\nabla n \times \mathbf{B}_0)$ .

Kudeki et al. (1985) proposed, on theoretical grounds, that up–down asymmetry is a result of nonlinear development of the primary GDI wave. Before developing the theory, they discarded various previously suggested mechanisms including the following: different up/down propagation at different altitudes (later observations with higher resolution showed that up-going and down-going waves can exist at the same altitude), nonlinear rotation of the angular spectrum due to effects of type-I waves (the rotation angle is insufficient), the primary-scale waves simply are not sinusoidal (the authors didn't rule this out directly, but said there is no evidence of it occurring in the E region), and the unequal effect on up-going and down-going type-I threshold velocities due to density gradients in the primary-scale wave (the largest

perturbations occur where primary-wave density gradients are small). They note that a purely sinusoidal primary wave drives a net downward electron flux during the daytime (upward during the nighttime) due to the basic GDI process, and assert that if there were a balancing asymmetry in the vertical velocity waveform of the primary wave, that asymmetry would have the correct sense to match observations.

The Condor rocket campaign in 1983 produced a host of publications, three of which are especially relevant here. Kudeki et al. (1987) showed radar interferometer observations at JRO of the unstable equatorial electrojet during the rocket flights. Major results relevant to the daytime electrojet include simultaneous radar and rocket observations of kilometer-scale plasma waves, a "remarkable consistency" between radar/rocket observations of wave parameters and theory, identification of a top-side pure two-stream layer above 108 km, and the implication that nonlinear mode coupling could compete with the anomalous diffusion described in Sudan (1983) to saturate two-stream waves in the topside layer.

Pfaff et al. (1987a) presented rocket data that showed three irregularity regions: a two-stream region between 103 km and 111 km, a gradient-drift region between 90 km and 106.5 km, and an interaction region between 103 km and 106.5 km. They also found that kilometer-scale waves dominated the *in-situ* spectrum despite the fact that the linear growth rate predicted a large-scale peak at a few hundred meters. Measurements of kilometer-scale  $\delta E$  and  $\delta n/n_0$  verified the predicted in-phase relationship and amplitudes of the kilometer-scale waves were 10-15 mV/m – strong enough to drive vertical two-stream secondary waves. Large-scale waveforms in the vicinity of two-stream activity displayed remarkable steepening and theretofore unobserved flat-top structures. Irregularity power showed a broad range of wavelengths in the lower electrojet, with a peak near tens to hundreds of meters and a rapid decay toward smaller scales.

Pfaff et al. (1987b) focused on the two-stream waves, both in the interaction region from 103 km to 106.5 km and in the top-side region above 106.5 km. The top-side region coincides with the portion of observations where the large-scale gradient was stabilizing (i.e., the gradient drift condition was zero or negative), and contained a laminar, horizontal two-stream flow. The two-stream flow was strongest near 108 km, coincident with the altitude of strongest electrojet current in previous observations. Waves had phase velocities comparable to the electron drift velocity of 500 m/s, and peak wavelengths of 2-3 m. The rocket also observed distinct vertically oriented waves that the authors attribute to a mode-coupling process with waves that originated in the interaction region. Two-stream waves appeared to have wavelengths as short as 50 cm.

St.-Maurice et al. (1989) reported the first observations of coherent backscatter with the 440-MHz steerable radar at Millstone Hill. That radar frequency, which is in the ultra high frequency (UHF) band, is sensitive to irregularities with a 34-cm wavelength. They observed echoes within one half degree of perpendicular to  $\mathbf{B}_0$ , at a mean height varying between 105 km and 115 km. The layer could be as thin as 4-5 km at times, and that the scattering occasionally split into two layers. They also observed that the Doppler shift of 34-cm irregularities corresponded to the electron drift, up to a limiting value at the ion acoustic speed, and found the strength of echoes to increase with ambient electric field strength. Note, however, that Foster and Tetenbaum (1992) point to an error in the phase-velocity analysis that St.-Maurice et al. (1989) used.

The work by St.-Maurice et al. (1989) leveraged the power of an ISR to observe coherent scatter from irregularities probably produced by the FBI. They comment that the Millstone Hill 440-MHz radar had much greater power and sensitivity in comparison to other coherent scatter radars in operation at the time, was the only

UHF radar with which to study coherent E-region echoes at aspect angles perpendicular to  $\mathbf{B}_0$ , had excellent spatial resolution due to its narrow beam, could also observe F-region incoherent scatter, and routinely observed the E region at lower latitudes than similar radars. It continues to provide unique insight to sub-auroral ionospheric processes.

Foster and Tetenbaum (1991) extended the work of St.-Maurice et al. (1989) by using the Millstone Hill 440-MHz radar to provide observations at higher spatial and temporal resolution. The higher resolution allowed them to address variability of UHF echoes on spatial scales of 6-10 km and on temporal scales of 20-60 s. They observed echoing events that lasted for around 30 minutes, during which backscatter amplitude oscillated with the period of ultra low frequency geomagnetic micropulsations. Interspersed throughout these events were intense bursts of backscatter lasting for a few minutes. Foster and Tetenbaum (1992) found that the phase speed of 34-cm echoes increased with increasing backscatter amplitude, indicating no limit such as the ion acoustic speed. On the other hand, their observations did suggest a direct relation between changes in irregularity phase speeds and changes in ambient E-region electric field.

In a seminal paper, Foster and Erickson (2000) showed that the phase speed of 34-cm irregularities is limited by the ion acoustic speed after accounting for the effect of wave heating on electron temperature,  $T_e$ , which in turn increases the ion acoustic speed. Those observations were the result of an experimental setup in which the main beam of the Millstone Hill 440-MHz radar measured  $\mathbf{E}_0 \times \mathbf{B}_0$  drift velocity from the F region while side-lobe contamination yielded E-region irregularity strength. Those combined measurements showed an excellent agreement between  $\mathbf{E}_0$  and  $T_e$ . Erickson et al. (2002) used the linear relationship between backscattered power at 440 MHz and  $\mathbf{E}_0$ , along with a detailed model of the radar response to irregularities

generated by the FBI, to provide insight into the fine-scale structure of a mid-latitude polarization jet and sub-auroral ion drift (SAID) event – both signatures of sub-auroral magnetosphere-ionosphere coupling.

Ronchi et al. (1989) performed a nonlocal linear analysis of the GDI in the daytime equatorial electrojet. The main feature of their analysis was the inclusion of the altitude dependence of ion-neutral and electron-neutral collisions. They numerically integrated the nonlocal linear equations and interpreted the results via an eikonal analysis of wave packets. They found that the major characteristics of the unstable modes were not sensitive to the details of the equilibrium plasma density profile, but rather to the average gradient value and to the profiles of the Pedersen and Hall conductivity, which ultimately determine ion and electron mobilities.

Ronchi et al. (1991) presented two-fluid numerical simulations of the GDI in the daytime equatorial electrojet. Their grid supported wavelengths from about 100 m to 10 km and incorporated the effects of smaller scales via anomalous electron diffusion and mobility terms. They simulated both *in-situ* rocket and remote radar observations. In the former case, they were able to reproduce some power spectra similar to observations, while in the latter case, they found that spectral features of 3-m type-II echoes acted as tracers for large-scale dynamics. The authors make particular note of the fact that a purely linear nonlocal analysis predicts that all kilometer-scale perturbations will eventually be damped through velocity shear whereas the non-linear effects present in their simulation, including energy coupling from intermediate wavelengths back to long wavelengths, can overcome the linear damping and maintain instability.

Ronchi et al. (1991) and similar work in the early 1990s mark the emergence of numerical simulations as a mature tool for studying electrojet irregularities. Janhunen (1994b) reported results from a particle-in-cell (PIC) simulation of FBI in the

plane perpendicular to  $\mathbf{B}_0$ . He found that phase did not saturate at the acoustic speed and he observed waves propagating at nonzero flow angle for  $\mathbf{E}_0$  clearly above the FBI threshold. He also reported no perpendicular wave heating, and concluded that if waves heat electrons in the ionosphere, heating must be due to the parallel component. Janhunen (1994a) used the results of Janhunen (1994b), which were in press at the time, to develop a formalism for FBI saturation based on flow-angle stabilization, rather than the anomalous collision theory that Sudan (1983) proposed.

Oppenheim et al. (1995) reported results from hybrid simulations in 2.5 dimensions of FBI in the topside equatorial electrojet. They drew four principle conclusions from their simulations: First, wave growth propagates at an angle offset from  $\mathbf{E}_0 \times \mathbf{B}_0$  (i.e., at a nonzero flow angle) and the angle depends on the strength of the driving electric field,  $\mathbf{E}_0$ . Second, primary FBI modes couple nonlinearly to modes that propagate perpendicular to the local primary wavefronts. Third, waves propagate at or above the acoustic speed but well below the speed predicted by linear theory. Fourth, primary-wave phase velocities remain nearly constant when the authors scanned a simulated radar over the simulation volume.

Oppenheim et al. (1996) added to these results the conclusion that nonlinear  $\delta \mathbf{E} \times \mathbf{B}_0$  motion dominates the behavior of saturated waves. Their analysis of this nonlinear effect in FBI waves was similar to those of Sudan et al. (1973) and Kudeki et al. (1985) for coupling large-scale GDI waves to small-scale FBI waves. Oppenheim and Otani (1996) published additional results from the simulations described in Oppenheim et al. (1996), this time focused on the wave spectra of the saturated state. They reported that 1) saturated two-stream waves produce type-I spectra over a broad range of elevation angles, 2) the phase velocity of two-stream waves is below that predicted by linear theory, 3) mode-coupling leads to type-II spectra even in the absence of a density gradient, 4) mode-coupling also leads to long wave-

lengths, and 5) the spectral power decreases at a rate of 0.3 dB/degree of elevation angle. Oppenheim (1996) extended the argument of Kudeki et al. (1985) to show that a large-scale wave-driven current arises from FBI waves and predicted that it would also arise from GDI waves. The nonlinear  $\delta \mathbf{E} \times \mathbf{B}_0$  drift of electrons in the wave troughs and crests produces a net current because electrons drift at the same speed in roughly opposite directions. Since there are more electrons in crests than in troughs, the process produces a net current. The wave-driven current should reduce the wave polarization electric field, which could limit the speed of irregularities to the threshold speed – namely, the ion acoustic speed. This applies especially to oblique FBI driven by large-scale GDI in the equatorial ionosphere.

Oppenheim (1997) applied the results of Oppenheim (1996) to a 1-D slab model of the electrojet and showed that a parameterized nonlinear current that reproduces the large-scale effects of nonlinear  $\delta \mathbf{E} \times \mathbf{B}_0$  from saturated FBI waves reduces the electrojet current closer to, but still greater than, the FBI threshold. That work also reiterated the point from Oppenheim (1996) that nonlinear drift effects can create flat-top waveforms in large-scale wave electric fields similar to those observed by Pfaff et al. (1987a,b).

At the same time as the simulation work by Oppenheim and collaborators, Dimant and Sudan (1995a) developed a kinetic theory for electron dynamics in low-frequency  $\mathbf{E} \times \mathbf{B}$  instabilities that carefully considered various effects related to electron-neutral collisions. They first considered the asymptotic short-wavelength case and showed how the new theory can significantly alter results in the lower ionosphere, then used the new theory to derive the general dispersion relation for FBI in the whole wavelength band in the low-frequency limit Dimant and Sudan (1995b).

Dimant and Sudan (1995c) applied the theory of Dimant and Sudan (1995a,b) to low-frequency instabilities in ionosphere and showed that it predicts long-wavelength

waves at low altitudes. The predicted waves travel along the bisector between the  $\mathbf{E}_0$  and  $\mathbf{E}_0 \times \mathbf{B}_0$  directions due to perturbations in the electron current as a result of the modified Pedersen conductivity. They authors propose that waves with wavelengths around ten meters can be excited at altitudes too low for the standard FBI, assuming the electric field is strong enough. Fortuitously, a rocket campaign in 1991 designed to study dynamics and chemistry of sodium and iron layers in the upper mesosphere/lower thermosphere carried plasma instruments.

Blix et al. (1996) showed observations from the METAL rocket campaign of plasma waves with characteristics that matched those predicted by Dimant and Sudan (1995c). Dimant and Sudan (1997) followed those rocket observations with a simplified fluid analysis of the low-frequency, long-wavelength instability mechanism. They explained that the new instability draws its free energy from Ohmic heating of electrons by a perturbed electric field and operates efficiently in the upper D/lower E regions, where related instabilities like the FBI and GDI do not. The low-altitude preference comes from the attendant increase in electron Pedersen conductivity. The instability arises due to two mechanisms: The first is due to the sign of plasma pressure perturbations being opposed to the density perturbations; the second mechanism results from thermal perturbations of the electron Pedersen conductivity, which increases monotonically with temperature via  $\nu_{en}$ . The first mechanism is stabilizing at positive flow angle  $(\mathbf{k} \cdot \mathbf{E}_0 > 0)$  and destabilizing at negative flow angle  $(\mathbf{k} \cdot \mathbf{E}_0 < 0)$ ; the second mechanism is always destabilizing. The pressure-perturbation (i.e. first) mechanism maximizes along the bisector between  ${\bf k}$ and  $-\mathbf{E}_0$  because that is where the projection of  $\mathbf{E}_0$  has the same sign as the perturbed electric field,  $\delta \mathbf{E}$ . Strong enough drift velocities can also excite the instability via the electron-Pedersen-conductivity (i.e. second) mechanism.

### 1.6 Theory of E-region instabilities

The FBI and GDI both arise from a warm, weakly ionized plasma. They both require that electrons are magnetized while ions are demagnetized via collisions with surrounding neutral particles. The magnetization parameter of a charged species quantifies these requirements:  $\kappa_j \equiv \Omega_j/\nu_j$ , where  $\Omega_j \equiv q_j B_0/m_j$  is the gyrofrequency (or cyclotron frequency) of species j with charge  $q_j$  and mass  $m_j$  in a magnetic field of strength  $B_0$ , and  $\nu_j$  is that species' collision frequency. The analysis in this section will apply to a plasma consisting of electrons and one species of ions, denoted by subscripts e and i, respectively. In plasmas that are more than weakly ionized (i.e. partially or fully ionized), collisions between charged particles are important. However, "collisions" in this dissertation shall imply collisions between charged particles and neutral particles unless otherwise specified. In the lower- to middle- E-region ionosphere,  $\kappa_e \gg 1$  and  $\kappa_i < 1$ ; this is what it means for electrons to be magnetized and ions to be (collisionally) demagnetized.

The difference between  $\kappa_e$  and  $\kappa_i$  is crucial to both the FBI and GDI because it causes electrons to separate from ions in the frame of reference of natural perturbations. Figure 1.4 shows a cartoon of how electrostatic instabilities form in a warm, collisional plasma. For the sake of specificity, suppose the background magnetic field,  $\mathbf{B}_0$ , points out from the page and that there is a vertical background electric field,  $\mathbf{E}_0$ . We can define a right-handed coordinate system in which  $\hat{x}$  points to the right,  $\hat{y}$  points up, and  $\hat{z}$  points out of the page, so that  $\mathbf{E}_0 = E_0 \hat{y}$ ,  $\mathbf{B}_0 = B_0 \hat{z}$ , and  $\mathbf{E}_0 \times \mathbf{B}_0 = E_0 B_0 \hat{x}$ . In a frame of reference fixed to the neutral atmosphere, the predominant electron motion is a Hall drift in the  $\mathbf{E}_0 \times \mathbf{B}_0$  direction whereas the predominant ion motion is to follow the neutrals with which they frequently collide. In the frame of reference of a small, naturally arising perturbation, that discrepancy manifests as an electron drift in  $\hat{x}$  and an ion drift in  $-\hat{x}$ . Since there are more

electrons and ions in regions of high relative perturbed density, where  $\delta n/n_0 > 0$ , the adjacent regions of low relative perturbed density,  $\delta n/n_0 < 0$ , cannot neutralize the separation of electrons from ions. That separation produces a polarization electric field,  $\delta E_x/E_0$ , whose sign is in phase with the sign of  $\delta n/n_0$ . Another way to think about this field is that it is the plasma's attempt to get rid of any flux divergence that would drive it away from quasi-neutrality. The polarization electric field plays a role in both the Farley-Buneman and gradient drift instabilities, though the roles are different. Sections 1.6.1 and 1.6.2 describe the physical nature of these two instabilities.

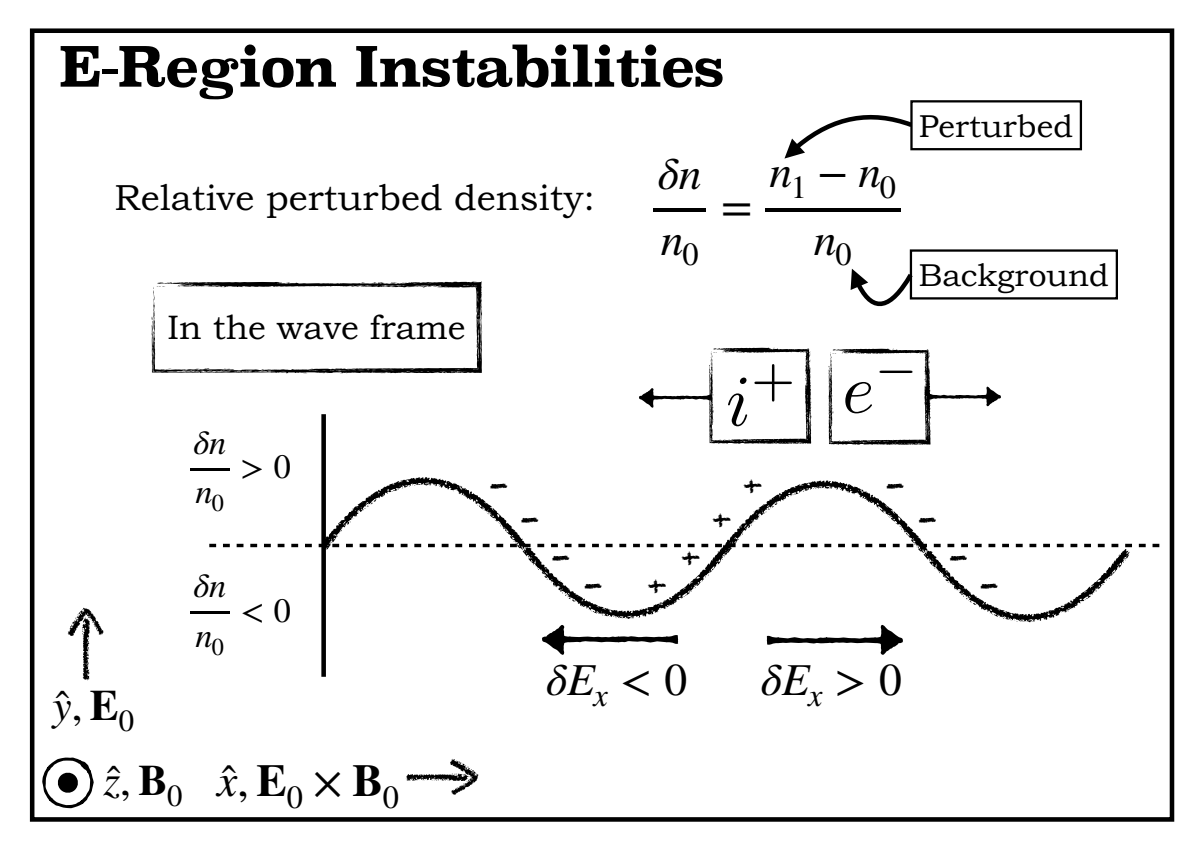


Figure 1.4: Cartoon of electrostatic E-region instability formation.

#### 1.6.1 The Farley-Buneman instability (FBI)

The Farley-Buneman instability (FBI) arises when the electron drift speed exceeds the plasma acoustic speed by a small factor of order unity, typically labeled  $\psi$ . Chapter 2 describes the parameter  $\psi$  in greater detail – it suffices to say at this point that  $\psi$  is a measure of how much more mobile electrons are when compared to ions. Figure 1.5 shows the physical setup leading to the FBI, with alternating bright  $(\delta n/n_0 > 0)$ and dark  $(\delta n/n_0 < 0)$  regions representing the seed perturbation from Figure 1.4. The supersonic electron drift imparts kinetic energy to the ions through the polarization electric field. Since ions drift in the  $-\hat{x}$  direction in the wave frame,  $\delta E_x/E_0$ tends to slow them down at wave crests and speed them up at wave troughs. Under conditions of subsonic electron flow, the attendant increase in thermal pressure would smooth out the resulting density gradients. As the electron drift speed approaches the threshold  $C_s(1+\psi_{\perp})$ , which is roughly equal to the plasma acoustic speed, ion inertia overcomes plasma pressure and relative density perturbations grow, leading to instability. The ion inertial represents a gradient in the ion kinetic energy. Under sub-threshold conditions, increased pressure in the regions of relatively high perturbed density – where  $\delta n/n_0 > 0$  – smooths out density perturbations. Increasing the electric field causes electrons to stream more quickly through ions and the electrostatic attraction forces ions to follow. In order to conserve flux, the ion velocity is largest where  $\delta n/n_0$  is smallest; therefore, the kinetic energy they gain from the electrostatic force is also largest where  $\delta n/n_0$  is smallest. When this new energy overcomes the plasma pressure, ions move out of regions of  $\delta n/n_0 < 0$  and into regions of  $\delta n/n_0 > 0$ . These amplifications of  $|\delta n/n_0|$  drive the FBI. See also Dimant and Sudan (1995c).

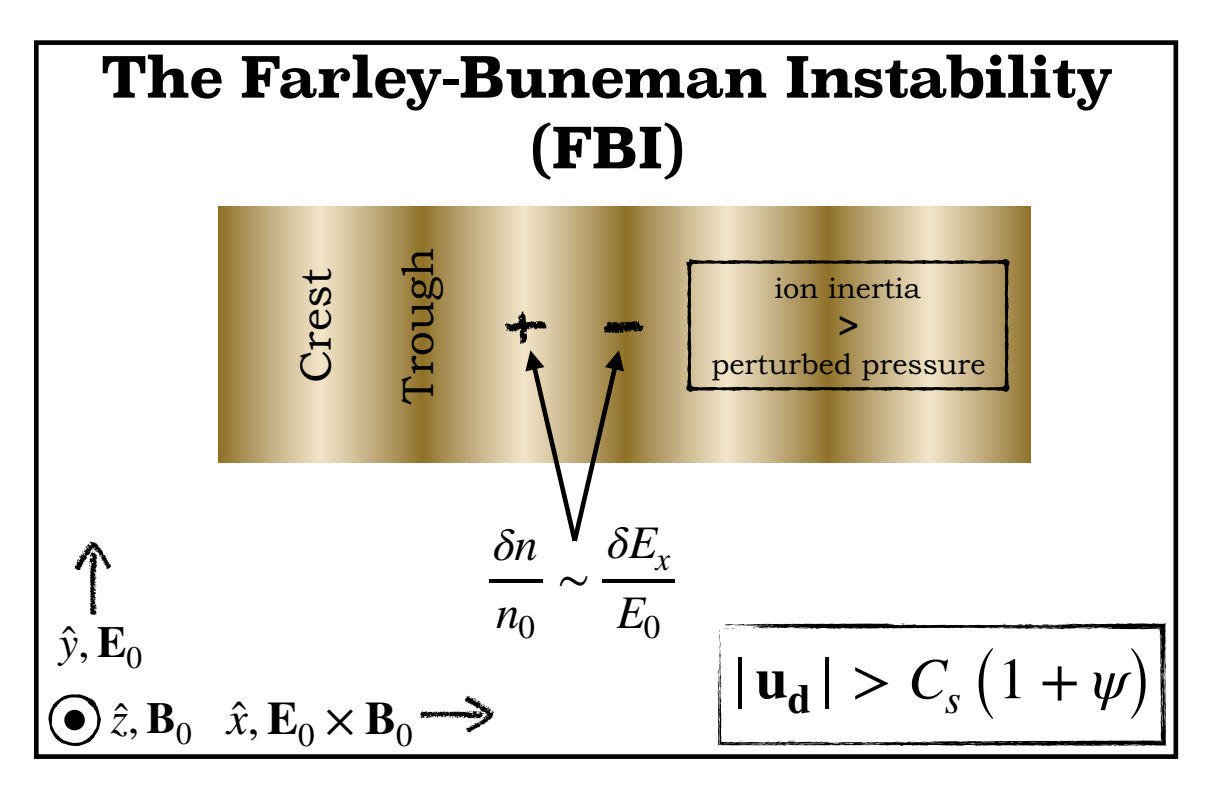


Figure 1.5: Cartoon of the Farley-Buneman instability mechanism.

#### 1.6.2 The gradient drift instability (GDI)

The gradient drift instability arises from a perturbed Hall drift of both ions and electrons in the seed-wave troughs and crests. Figure 1.6 shows the physical setup leading to the GDI, with alternating bright  $(\delta n/n_0 > 0)$  and dark  $(\delta n/n_0 < 0)$  regions again representing the seed perturbation. The difference is that now there is an additional background density gradient,  $\nabla n_0$ . In the case of the GDI, the relative drifts that lead to  $\delta E_x/E_0$  are still important but a supersonic electron drift is no longer necessary. Instead, the polarization field leads to a  $\delta \mathbf{E} \times \mathbf{B}_0$  drift directed parallel to  $\nabla n_0$  in the troughs and anti-parallel in the crests. The fact that there is relatively more plasma in the crests and less in the troughs (by definition) means that a region of  $\delta n/n_0 > 0$  flows into a region where  $n_0$  is even smaller, so that  $\delta n/n_0$  increases further. Likewise, regions of  $\delta n/n_0 < 0$  decrease further. These

amplifications of  $|\delta n/n_0|$  drive the GDI. See also Dimant and Sudan (1997).

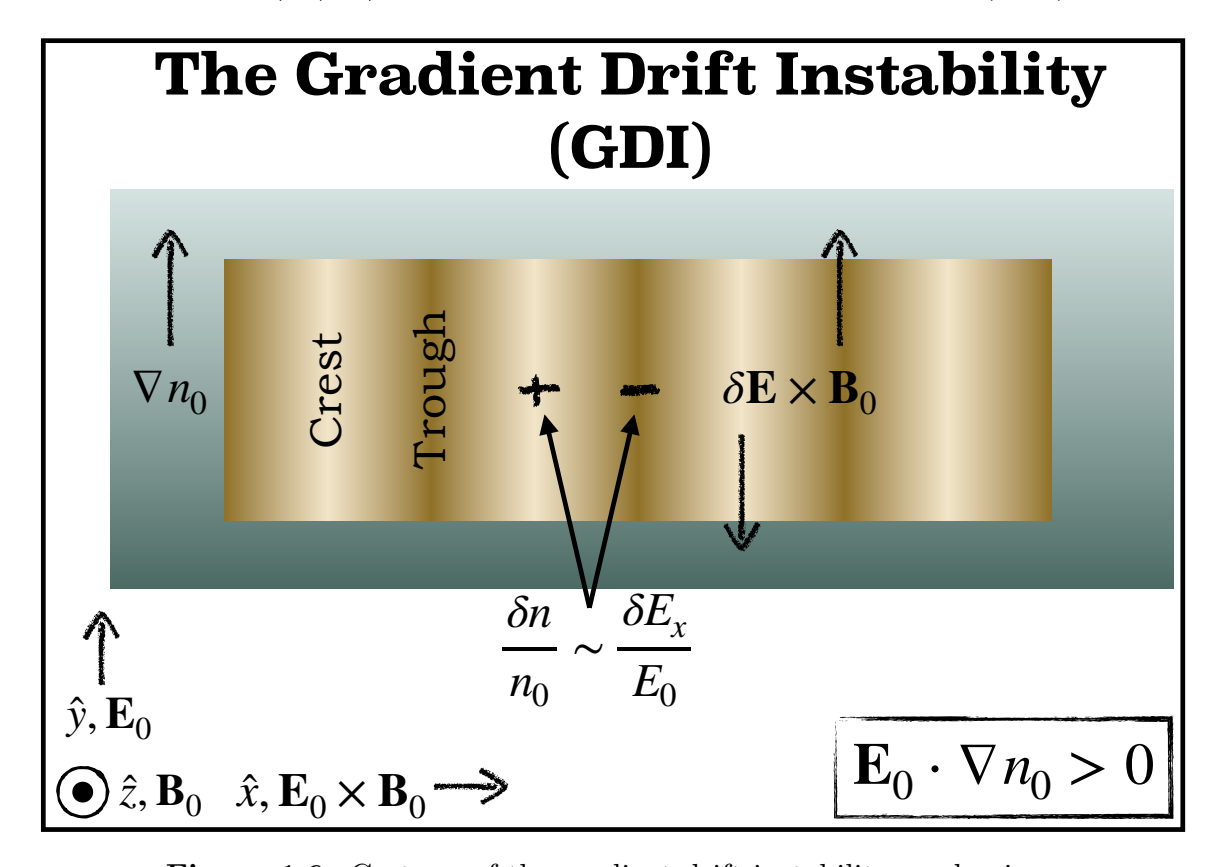


Figure 1.6: Cartoon of the gradient drift instability mechanism.

# Chapter 2

### Theoretical Framework

Section 1.6 elucidated the physical mechanisms behind the FBI and GDI in a qualitative manner. This chapter delves more deeply into the quantitative underpinnings of both instabilities and demonstrates how they may arise simultaneously if the plasma meets certain criteria. Section 2.1 begins the description by developing the fluid theory relevant to a warm, electrostatic plasma. It proceeds through an introduction to linear instability analysis, followed by a derivation of the general dispersion relation that captures both FBI and GDI. Finally, it identifies the short-comings of the fluid approach, most notably in the case of FBI wave growth. Section 2.2 introduces the fundamental concepts of kinetic plasma theory, then picks up where section 2.1 left off by showing how a kinetic approach overcomes the difficulty faced by a fluid treatment of the FBI. The hybrid numerical simulations at the heart of much of this dissertation treat electrons as a fluid and ions as particles (i.e., kinetically). Section 2.3 derives the electrostatic potential equation that ties the dynamics of those two species together.

## 2.1 Linear Fluid Theory

On scales much larger than the Debye length and much slower than the plasma frequency, the ionospheric plasma behaves as a quasi-neutral fluid comprising electrons, multiple species of ions, and perhaps even charged dust or ice. Plasma fluid theory in the context of the ionosphere seeks to understand the dynamics of those individ-

ual species' self-consistent evolution as they react to ambient electromagnetic and gravitational fields and interact with the neutral gas in which they are embedded while simultaneously gaining or losing constituent particles due to ionization and recombination. The following analysis applies to any single plasma species treated as a fluid, here denoted by subscript s.

The primary equation of interest in studying a plasma species' dynamics is the momentum equation:

$$\frac{\partial \mathbf{u}_s}{\partial t} + (\mathbf{u}_s \cdot \nabla)\mathbf{u}_s = \frac{q_s}{m_s} \left( \mathbf{E} + \mathbf{u}_s \times \mathbf{B} \right) - \frac{\nabla \cdot \mathsf{P}_s}{n_s m_s} - \mathbf{u}_s \left( \nu_{sn} - \alpha_s \right) - \mathbf{g}, \tag{2.1}$$

where  $\mathbf{u}_s$  denotes the fluid velocity,  $q_s$  denotes the charge,  $m_s$  denotes the mass,  $\mathbf{E}$  and  $\mathbf{B}$  are the total electric and magnetic fields,  $\mathsf{P}_s$  is the pressure tensor,  $n_s$  denotes the number density,  $\nu_{sn}$  represents the average frequency of collisions with neutral particles,  $\alpha_s$  represents the rate at which various methods (sources and sinks) produce or destroy particles of this species, and  $\mathbf{g}$  is the acceleration due to gravity. The second term on the left-hand side (LHS) describes changes in momentum due to gradients in the fluid flow.

Equation 2.1 is essentially an application of Newton's Second Law to a weakly ionized gas. The first term on the right-hand side (RHS) is the Lorentz force. The total electric and magnetic fields comprise background terms,  $\mathbf{E}_0$  and  $\mathbf{B}_0$ , as well as any fields that the plasma self-consistently generates. The second term, containing the pressure tensor, captures the effects of density and temperature gradients. Section 2.2 will demonstrate the potential complexity of this term; for now, a convenient form of P that applies to many ionospheric phenomena is  $P_s = n_s k_b T_s I$ , where I is the identity tensor,  $k_B$  is the Boltzmann constant, and  $T_s$  is the plasma temperature. This form of the pressure tensor simplifies when the plasma is isothermal, so that  $\nabla T_s = 0$ . The third RHS term contains the combined effects of collisions, particle

production, and particle loss on altering the momentum of the overall fluid. In the simplest sense, the effect of collisions with neutral particles is intuitive: more collisions will slow the fluid. To understand the effect of production and loss in an equivalently simple sense, consider what would happen if an ionization source were to create a bunch of new species-s particles: the existing fields and gradients would accelerate them in the same manner that those fields and gradients had accelerated the existing species-s particles. Now, the fluid has more mass moving at the same velocity, and thus greater momentum. The magnitude of the Lorentz force is roughly ten-thousand times greater than that of the gravitational force for even modest E-region parameters and, whereas gravity has a pronounced influence on the neutral atmosphere and on large-scale, slowly evolving F-region instabilities, its effect on the FBI and GDI is negligible. Therefore, the remainder of this analysis will ignore the effect of gravity on ions and electrons.

A general treatment of Equation 2.1 requires Maxwell's equations for  $\mathbf{E}$  and  $\mathbf{B}$ . However,  $\mathbf{B}$  is effectively constant in the E-region ionosphere, especially on time scales appropriate to the FBI and GDI, so it will suffice to know  $\mathbf{E}_0$ ,  $\mathbf{B}_0$ , and any electric fields that develop due to plasma inhomogeneities. After specifying an appropriate form for  $\mathbf{P}_s$  and appropriate values for physical constants (e.g.,  $q_s$  and  $m_s$ ), all that remains is to determine how  $n_s$  evolves. The relevant equation is the continuity equation:

$$\frac{\partial n_s}{\partial t} = -\nabla \cdot (n_s \mathbf{u}_s) + \alpha_s. \tag{2.2}$$

Equation 2.2 states that two factors determine the time rate of change of species-s number density: 1) the flux out of the volume of interest and 2) the creation or destruction of species-s particles.

Equations 2.2 and 2.1 include terms related to the production and loss of particles of a given species; the remainder of this analysis will neglect them. Though their

effect is more relevant than, say, that of gravity, the simulations presented in chapters 4, 5, and 6 are concerned more with the evolution of an existing plasma on time scales shorter than those of ionization and recombination in the E region.

The following linear fluid instability analysis of a plasma consisting of a electrons and ions explains how even the relatively simple system embodied by equations 2.1 and 2.2, under the aforementioned assumptions, gives rise to both the FBI and GDI. The first step is to identify the dynamic variables.

Linear analysis begins by assuming that all dynamic variables consist of a zerothorder background term and first-order perturbations that are small in magnitude compared to the background term. In the case of density, for example,  $n(\mathbf{r},t) \approx$  $n_0 + n_1(\mathbf{r},t)$  with  $n_0 \gg n_1$ . The next assumption is that all first-order quantities vary as complex exponentials:  $n_1(\mathbf{r},t) = n' \exp [-i(\omega t - \mathbf{k} \cdot \mathbf{r})]$ . The second assumption effectively converts differential equations into algebraic equations, which tremendously simplifies the math. Specifically, taking the time derivative of  $n_1(\mathbf{r},t)$ is equivalent to multiplying by  $-i\omega$  and taking the spatial gradient is equivalent to multiplying (in an appropriate way) by  $\mathbf{k}$ . Symbolically,

$$\frac{\partial}{\partial t} \to -i\omega \quad \nabla \to i\mathbf{k} \quad \nabla \to i\mathbf{k} \cdot \quad \nabla \times \to i\mathbf{k} \times .$$

The goal of linear perturbation analysis is to derive a dispersion relation, which is a function that expresses the frequency,  $\omega$ , as a function of wave number,  $\mathbf{k}$ .

Given the electrostatic nature of the FBI and GDI, there is only a background magnetic field. On the other hand, the electric field consists of both zeroth- and first-order quantities. The first-order quantities comprise the electrostatic perturbations of interest, so  $\mathbf{E}(\mathbf{r},t) = \mathbf{E}_0 - \nabla \phi(\mathbf{r},t)$ . This linear analysis also explicitly assumes  $P_s = n_s k_B T_s$  with  $\nabla T_s \equiv \mathbf{0}$  and it wraps  $k_B$  into  $T_s$  so that temperature has units of energy. This is partially a matter of convenience but it also reduces the likelihood of

confusion between the Boltzmann constant,  $k_B$ , and the wave number, k.

In general, vector quantities can have components in all three directions. Chapters 4 and 5 present results from 2-D simulations while Chapter 6 presents results from both 2-D and 3-D simulations. The following analysis applies to 3-D dynamics but starts from the following additional assumptions for the sake of clarifying the underlying physics: 1)  $\mathbf{B}_0 = B_0 \hat{z}$  and  $\mathbf{E}_0 = E_0 \hat{y}$ ; 2) ions Pedersen predominantly drift in the direction of  $+\mathbf{E}_0$  but have a small component in the  $\mathbf{E}_0 \times \mathbf{B}_0$  at higher altitudes, where  $\nu_i$  is small; 3) electrons Hall predominantly drift in the  $\mathbf{E}_0 \times \mathbf{B}_0$  direction but have a small Pedersen component in the  $-\mathbf{E}_0$  direction at lower altitudes, where  $\nu_e$  is large; 4) the background gradient,  $\nabla n_0$ , points parallel to  $\mathbf{E}_0$ ; 5) waves propagate orthogonal to  $\nabla n_0$  (i.e.  $\mathbf{k} = k_x \hat{x} + k_y \hat{y}$ ); 6) the background ion drift is negligible; 7) the background electron drift is not negligible but it is divergence free (i.e.,  $\nabla \cdot \mathbf{u}_e = 0$ ). Figure 2·1 shows the relative directions of relevant quantities in the plane perpendicular to  $\mathbf{B}_0$ .

The linearized inertialess electron momentum is

$$0 = -\frac{e}{m_e} \left( -i\mathbf{k}\phi' + \mathbf{u}'_e \times \mathbf{B}_0 \right) - \frac{iT_e}{m_e} \mathbf{k} \frac{n'_e}{n_0} - \nu_e \mathbf{u}'_e.$$

$$(\hat{x}) \quad 0 = \frac{iek_x \phi'}{m_e} - \Omega_e u'_{ey} - \frac{ik_x T_e n'_e}{m_e n_0} - \nu_e u'_{ex}$$

$$(\hat{y}) \quad 0 = \Omega_e u'_{ex} - \nu_e u'_{ey}$$

$$(\hat{z}) \quad 0 = \frac{iek_z \phi'}{m_e} - \frac{ik_z T_e n'_e}{m_e n_0} - \nu_e u'_{ez}$$

Solving the  $\hat{y}$  equation for  $u'_{ey}$  in terms of  $u'_{ex}$  and plugging into the  $\hat{x}$  equation yields

$$0 = \frac{iek_x\phi'}{m_e} - \frac{\Omega_e^2}{\nu_e}u'_{ex} - \frac{ik_xT_en'_e}{m_en_0} - \nu_eu'_{ex}$$
$$u'_{ex} = \frac{ik_x}{m_e\nu_e\left(1 + \kappa_e^2\right)} \left(e\phi' - \frac{T_en'_e}{n_0}\right).$$

Solving the  $\hat{z}$  term for  $u'_{ez}$  yields

$$u'_{ez} = \frac{ik_z}{m_e \nu_e} \left( e\phi' - \frac{T_e n'_e}{n_0} \right)$$

Note that  $u'_{ex}$  contains all the effects of gyromotion in the  $\kappa_e$  and that  $u'_{ez} > u'_{ex}$  by a factor of  $(k_z/k_x)(1 + \kappa_e^2)$ . Even with  $k_z/k_x \sim 0.01$  typical of the FBI, the fact that  $\kappa_e \sim 100 - 200$  in the E region means that electron perturbations move much more quickly along  $\mathbf{B}_0$ , as one should expect.

The linearized electron continuity equation is

$$\omega n'_{e} = u_{e0}k_{x}n'_{e} + n_{0}k_{x}u'_{ex} + n_{0}k_{z}u'_{ez} - iu'_{ey}\frac{dn_{e}}{dy}$$
$$= u_{e0}k_{x}n'_{e} + n_{0}k_{x}u'_{ex} + n_{0}k_{z}u'_{ez} - i\kappa_{e}u'_{ex}\frac{dn_{e}}{dy}$$

Solving for  $u'_{ex}$  yields

$$u'_{ex} = (k_x - i\kappa_e G)^{-1} \left[ (\omega - k_x u_{e0}) \frac{n'_e}{n_0} - k_z u'_{ez} \right]$$
$$= (k_x - i\kappa_e G)^{-1} \left[ (\omega - k_x u_{e0}) \frac{n'_e}{n_0} - \frac{ik_z^2}{\nu_e m_e} \left( e\phi' - \frac{T_e n'_e}{n_0} \right) \right]$$

where  $G \equiv n_0^{-1} dn_e/dy$  measures the gradient strength and the second line uses  $u'_{ez}$  from the momentum equation. The remainder of this analysis will assume that  $G \geq 0$ , which implies that  $\mathbf{u}'_{ey} \cdot (dn_e/dy) \,\hat{y} > 0$ , corresponding to an electric field parallel to the electron density gradient.

Plugging this expression back into the equation for electron momentum perpendicular to  $\mathbf{B}_0$  eliminates  $u'_{ex}$ :

$$(k_x - i\kappa_e G)^{-1} \left[ (\omega - k_x u_{e0}) \frac{n'_e}{n_0} - \frac{ik_z^2}{\nu_e m_e} \left( e\phi' - \frac{T_e n'_e}{n_0} \right) \right] = \frac{ik_x}{m_e \nu_e \left( 1 + \kappa_e^2 \right)} \left( e\phi' - \frac{T_e n'_e}{n_0} \right)$$

The linearized ion momentum equation is

$$-i\omega \mathbf{u}_{i}' = +\frac{e}{m_{i}}\left(-i\mathbf{k}\phi' + \mathbf{u}_{i}' \times \mathbf{B}_{0}\right) - \frac{iT_{i}}{m_{i}}\mathbf{k}\frac{n_{i}'}{n_{0}} - \nu_{i}\mathbf{u}_{i}'.$$

Ions are unmagnetized for much of the altitude range of interest to this dissertation. At upper-electrojet altitudes, the ion drift component in the Hall direction grows to an appreciable fraction of the electron Hall component but the present analysis will still capture the interesting physics while assuming that ions are unmagnetized. Under that assumption, the ion momentum equation has no component in the  $\hat{y}$  direction.

$$-i\omega \mathbf{u}_{i}' = -\frac{ie\mathbf{k}\phi'}{m_{i}} - \frac{iT_{i}\mathbf{k}n_{i}'}{m_{i}n_{0}} - \nu_{i}\mathbf{u}_{i}'$$
$$\mathbf{u}_{i}' = \frac{\mathbf{k}}{m_{i}(\omega + i\nu_{i})} \left(e\phi' + \frac{T_{i}n_{i}'}{n_{0}}\right)$$

The linearized ion continuity equation, under the assumption that ions are stationary in the neutral frame, yields an expression for  $\mathbf{k} \cdot \mathbf{u}_i'$ 

$$\mathbf{k} \cdot \mathbf{u}_i' = \frac{\omega n_i'}{n_0}.$$

Dotting  $\mathbf{k}$  into the ion moment equation leads to

$$\mathbf{k} \cdot \mathbf{u}_{i}' = \frac{\omega n_{i}'}{n_{0}} = \frac{k^{2}}{m_{i} (\omega + i\nu_{i})} \left( e\phi' + \frac{T_{i}n_{i}'}{n_{0}} \right)$$

The next step is to couple the ion and electron momentum through the perturbed potential,  $\phi'$ . From the ion equation,

$$e\phi' = \left[\frac{m_i\omega\left(\omega + i\nu_i\right)}{k^2} - T_i\right] \frac{n_i'}{n_0}$$

Inserting this into the electron equation and rearranging terms gives

$$\left[ \frac{m_{i}\omega\left(\omega + i\nu_{i}\right)}{k^{2}} - T_{i} \right] \frac{n'_{i}}{n_{0}} = \frac{n'_{e}}{n_{0}} \left[ \frac{m_{e}\nu_{e}\left(1 + \kappa_{e}^{2}\right)}{ik_{x}^{2} + \kappa_{e}k_{x}G + ik_{z}^{2}\left(1 + \kappa_{e}^{2}\right)} \right] \times \left\{ \omega - k_{x}u_{e0} + \frac{iT_{e}}{m_{e}\nu_{e}} \left[ \frac{ik_{x}^{2} + \kappa_{e}k_{x}G + ik_{z}^{2}\left(1 + \kappa_{e}^{2}\right)}{1 + \kappa_{e}^{2}} \right] \right\}$$

This analysis has thus far used four equations – electron and ion momentum and continuity – in five dynamical variables – the perturbed electron and ion densities, the perturbed ion and electron velocities, and the perturbed potential. It requires an additional equation to fully eliminate all perturbed quantities. The final necessary assumption is that this plasma is quasi-neutral. That means that  $n_i \approx n_e \equiv n$ , so that the perturbed densities are equal. Under this assumption,

$$\omega - k_x u_{e0} = \left[ \frac{ik_x^2 + \kappa_e k_x G + ik_z^2 (1 + \kappa_e^2)}{k^2 \nu_e (1 + \kappa_e^2)} \right] \frac{m_i}{m_e} \left[ \omega (\omega + i\nu_i) - k^2 C_s^2 \right]$$

$$\approx \left( \frac{\psi}{\nu_i} - i \frac{\psi_\perp \kappa_e k_x G}{k^2 \nu_i} \right) \left[ \omega (i\omega - \nu_i) - ik^2 C_s^2 \right]$$
(2.3)

where

$$\psi_{\perp} \equiv \frac{\nu_e \nu_i}{\Omega_e \Omega_i}, \qquad \psi \equiv \psi_{\perp} \left[ \left( \frac{k_x}{k} \right)^2 + \left( \frac{\kappa_e k_z}{k} \right)^2 \right]$$

and  $C_s \equiv \sqrt{(T_i + T_t)/m_i}$  is the isothermal sound speed. The final step in deriving Equation 2.3 took advantage of the fact that  $\kappa_e^2 \gg 1$ .

All that remains is to rearrange Equation 2.3 to get an expression for the complex frequency,  $\omega$ , in terms of the wavenumbers,  $(k_x, k_z)$ . After carrying out some algebra,

$$\omega^2 + i\omega\nu_i \left(1 + \frac{\eta_{\mathbf{k}}}{\delta_{\mathbf{k}}}\right) - ik_x u_{e0}\nu_i \left(\frac{\eta_{\mathbf{k}}}{\delta_{\mathbf{k}}}\right) - k^2 C_s^2 \approx 0, \tag{2.4}$$

where

$$\eta_{\mathbf{k}} \equiv k \left( k \psi + i \psi_{\perp} \kappa_e k_x G / k \right)$$
 and  $\delta_{\mathbf{k}} \equiv \left( k \psi \right)^2 + \left( \psi_{\perp} \kappa_e k_x G / k \right)^2$ 

When there is no gradient, G = 0,  $\eta_{\mathbf{k}} = 1/\psi$ , and Equation 2.4 reduces to

$$\omega^2 + i\omega\nu_i \left(1 + \frac{1}{\psi}\right) - i\frac{k_x u_{e0}\nu_i}{\psi} - k^2 C_s^2 \approx 0.$$

The roots of Equation 2.4 give the wave frequency as a function of wave number, as required. These roots are complex in general. The usual analytic approach is to write  $\omega = \omega_r + i\omega_i$ , where  $\omega_r$  is the real wave frequency and  $\omega_i$  is the growth or damping rate. To understand these quantities in a physical sense, remember that this derivation began by assuming quantities vary as  $\exp[-i(\omega t - \mathbf{k} \cdot \mathbf{r})]$ . Plugging  $\omega = \omega_r + i\omega_i$  in gives  $\exp(\omega_i) \exp[-i(\omega_r t - \mathbf{k} \cdot \mathbf{r})]$ . Clearly, if  $\omega_i < 0$ , perturbations will decay exponentially whereas if  $\omega_i > 0$ , perturbations will grow exponentially. Next, we can factor out the wave-number magnitude, k, from the argument of the complex exponential and define the phase velocity,  $V_{ph} \equiv \omega_r/k$ , to get  $\exp(\omega_i) \exp[-ik(V_{ph}t - \mathbf{k} \cdot \mathbf{r}/k)]$ . This form more makes the notion of plane waves more apparent.

The standard approach in the literature to determining  $\omega_r$  (or  $V_{ph}$ ) and  $\omega_i$  is to assume  $|\omega_r| \gg |\omega_i|$ , which is to say that perturbations undergo many oscillations in the time it takes their amplitude to increase by a factor of  $e \approx 2.7$ . What this approximation really comes down to is assuming  $\omega^2 \approx \omega_r^2$  while  $\omega \approx \omega_r + i\omega_i$ . With these assumptions, Equation 2.4 becomes

$$\left(\frac{\omega_r^2 - k^2 C_s^2}{\nu_i}\right) \delta_{\mathbf{k}} - \omega_i \left[\delta_{\mathbf{k}} + \Re(\eta_{\mathbf{k}})\right] - \Im(\eta_{\mathbf{k}}) \left(\omega_r - k_x u_{e0}\right)$$

$$= i \left\{-\omega_r \left[\delta_{\mathbf{k}} + \Re(\eta_{\mathbf{k}})\right] + \omega_i \Im(\eta_{\mathbf{k}}) + k_x u_{e0} \Re(\eta_{\mathbf{k}})\right\} \tag{2.5}$$

The real and imaginary parts must each vanish independently. The imaginary part of Equation 2.5 reads

$$\omega_r \left[ \delta_{\mathbf{k}} + \Re(\eta_{\mathbf{k}}) \right] - \omega_i \Im(\eta_{\mathbf{k}}) - k_x u_{e0} \Re(\eta_{\mathbf{k}}) = 0$$

We can assume that the term  $\sim \omega_i$  is negligible compared to the other terms. For wavelengths of a few meters and gradient scale lengths of a kilometer or more,  $\delta_{\mathbf{k}} \gg \Re(\eta_{\mathbf{k}})$  and the imaginary-part equation yields an expression for the real frequency:

$$\omega_r = \frac{k_x u_{e0}}{1 + \psi} \tag{2.6}$$

In general, ions have some degree of magnetization and the phase velocity is not parallel to the Hall direction. In that more general case,  $k_x u_{e0} \to \mathbf{k} \cdot \mathbf{u}_d$  in Equation 2.6, where  $\mathbf{u}_d \equiv \mathbf{u}_{e0} - \mathbf{u}_{i0}$  is the relative drift velocity.

This equation predicts that the phase velocity during linear instability growth should be proportional to the electron drift velocity but less than it by a factor slightly greater than unity. However, much of the research cited in §1.5 has established that FBI perturbations propagate with a phase speed close to the plasma acoustic speed,  $C_s$ .

The real part of Equation 2.5 reads

$$\left(\frac{\omega_r^2 - k^2 C_s^2}{\nu_i}\right) \delta_{\mathbf{k}} - \omega_i \left[\delta_{\mathbf{k}} + \Re(\eta_{\mathbf{k}})\right] - \Im(\eta_{\mathbf{k}}) \left(\omega_r - k_x u_{e0}\right) = 0$$

Again, assuming perturbation wavelengths of a few meters and a gradient scale length of a kilometer or more,  $\delta_{\mathbf{k}} \approx (k\psi)^2$  and  $\delta_{\mathbf{k}} + \Re(\eta_{\mathbf{k}}) \approx k^2\psi(1+\psi)$ . Taking advantage of these approximations and Equation 2.6 yields an expression for the growth rate:

$$\omega_i = \frac{\psi}{1+\psi} \left[ \frac{\omega_r^2 - k^2 C_s^2}{\nu_i} + \omega_r G \left( \frac{\kappa_e k_x}{k_x^2 + \kappa_e^2 k_z^2} \right) \right]$$
 (2.7)

The term proportional to  $\omega_r^2$  describes the ion inertial energy that powers the FBI, as described in §1.6.1. The term proportional to  $k^2C_s^2$  describes diffusive damping. The term proportional to  $\omega_r G$  describes the additional ion inertial provided by the zeroth-order electron density gradient. Instability growth occurs when  $\omega_i > 0$ . In order for that to happen, both terms containing  $\omega_r$  must combine to overcome  $-k^2C_s^2$ . Note

that if this analysis had not assumed  $G \ge 0$ , a negative value would flip the sign of the  $\omega_r G$  term and inhibit instability.

Both Equations 2.6 and 2.7 are equivalent to standard expressions for the real frequency and growth rate as reported in the literature, after accounting to notational differences. See, for example, Fejer and Kelley (1980). One important aspect of Equation 2.7 is that it increases monotonically with  $k_x$ . In physical terms, this means that the growth rate increases without bound as the wavelength decreases toward zero. Since an infinite growth rate is unphysical, there must be something missing. What is missing is a kinetic effect called "ion Landau damping" in which ions steal energy from waves with wavelengths shorter than a few ion MFPs. The next section explains how kinetic plasma physical differs from fluid plasma physics.

# 2.2 Linear Kinetic Theory

At its root, plasma kinetic theory is a statistical description of the position and velocity of a collection of particles over time. At a particular moment in time, a distribution of particles – having three position coordinates and three velocity coordinates, in general – exists in a six-dimensional space called "phase space". Figure 2·2 shows phase space for one-dimensional motion. It depicts changes in particle trajectories along one spatial axis (r) and the corresponding velocity axis (v). A straight line parallel to the r axis, in the +v half-plane, represents a particle moving with constant positive velocity in the +r direction. Likewise, a straight line parallel to the r axis, in the -v half-plane, represents a particle moving with constant negative velocity in the -r direction. A closed circle in phase space represents a particle trajectory that always returns to the same position and velocity after a fixed amount of time – in other words, a periodic orbit. More complex trajectories may combine elements of constant velocity and changing velocity (i.e., acceleration) as long as their

changes in position are self-consistent, and a single phase-space plot like that shown in Figure 2·2 may contain multiple trajectories, each corresponding to an individual particle. Unfortunately, representing phase space in higher dimensions presents a graphical challenge, since it requires at least four coordinate axes.

One cubic meter of E-region plasma contains tens of billions of particles, each with their own six-dimensional phase-space trajectories, so the task of visualizing a plasma at this fundamental level quickly becomes impossible. Instead of following every particle in a plasma, it is convenient to consider all the particles in a small volume of phase space bounded by  $(r_{x0}, r_{y0}, r_{z0}, v_{x0}, v_{y0}, v_{z0})$  and  $(r_{x0} + dr_x, r_{y0} + dr_y, r_{z0} + dr_z, v_{x0} + dv_x, v_{y0} + dv_y, v_{z0} + dv_z)$ , and written  $d^3rd^3v$ . The density of particles of species s in this small volume is  $f_s(\mathbf{r}, \mathbf{v}) = N_s(\mathbf{r}, \mathbf{v})/d^3rd^3v$ ; this phase-space density,  $f_s$ , is called the distribution function of species s. The task of understanding the dynamics of species s now manifests as the task of deducing the time evolution of  $f_s$  through phase space. Since  $\mathbf{r} = \mathbf{r}(t)$  and  $\mathbf{v} = \mathbf{v}(t)$ , the total time derivative of  $f_s(\mathbf{r}, \mathbf{v})$  is

$$\frac{df_s(\mathbf{r}, \mathbf{v})}{dt} = \frac{\partial f_s}{\partial t} + \frac{d\mathbf{r}}{dt} \cdot \nabla_r f_s + \frac{d\mathbf{v}}{dt} \cdot \nabla_v f_s,$$

where  $\nabla_r$  and  $\nabla_v$  are the total gradients in configuration and velocity space, respectively. The analysis thus far has not considered any way to add or remove particles from  $d^3rd^3v$ , so  $df_s/dt = 0$  by Liouville's Theorem. One major element missing is the effect of collisions. Since collisions may change a particle's position and velocity, they simply alter that particle's trajectory through phase space, thereby altering  $f_s$  in time. Therefore, a full treatment requires additional term that removes particles from  $d^3rd^3v$  when it increases. This additional term, nominally representing collisions, balances  $df_s/dt$ . In fact, even production and loss of plasma particles simply add or subtract particles at a certain location in phase space, so they, too enter into the (as yet unspecified) collision term. This final form is called the Boltzmann

equation:

$$\frac{\partial f_s}{\partial t} + \frac{d\mathbf{r}}{dt} \cdot \nabla_r f_s + \frac{d\mathbf{v}}{dt} \cdot \nabla_v f_s = \left[ \frac{\delta f_s}{\delta t} \right]_c \tag{2.8}$$

The simplest collision operator is

$$\left[\frac{\delta f_s}{\delta t}\right]_c = -\nu_i f_s$$

This exponentially damps out perturbations in  $f_s$  with a time scale of  $\nu_i^{-1}$ . The main short-coming of this form is that the number of particles in phase space is conserved on average but not locally; it exaggerates the collisional damping of longitudinal waves (Farley, 1963a). A slightly more complex collision operator, known as the BGK collision operator after Bhatnagar, Gross, and Krook (Bhatnagar et al., 1954), has the form

$$\left[\frac{\delta f_s}{\delta t}\right]_c = -\nu_s \left(f_s - \frac{n_s}{n_0} f_{s0}\right),\,$$

where  $f_{s0}$  is the zeroth-order distribution function, and  $n_s$  and  $n_0$  are the number densities corresponding to  $f_s$  and  $f_0$ . Farley (1963a) showed that this term is sufficient to account for collisional processes in electrostatic turbulence.

Equation 2.8 for the ion distribution, with the BGK collision operator, and under the influence of an ambient magnetic field, is

$$\frac{\partial f_i}{\partial t} + \frac{d\mathbf{r}}{dt} \cdot \nabla_r f_i + \frac{e}{m_i} \left( \mathbf{E} + \mathbf{v}_i \times \mathbf{B}_0 \right) \cdot \nabla_v f_i = -\nu_i \left( f_i - \frac{n_i}{n_0} f_{i0} \right)$$

To develop an expression similar to that describes FBI ion dynamics kinetically, we can assume that the ion Hall drift is negligible ( $\mathbf{v}_i \times \mathbf{B}_0 \to 0$ ) and linearize:

$$-i\left(\omega - \mathbf{k} \cdot \mathbf{v} + i\nu_i\right) f_{i1} + \frac{e}{m_i} \left(\mathbf{E}_0 \cdot \nabla_v f_{i1} + \mathbf{E}_1 \cdot \nabla_v f_{i0}\right) = \nu_i \frac{n_{i1}}{n_{i0}} f_{i0}$$

It is reasonable to assume that  $\mathbf{E}_0$  only has a component in the Pedersen direction, so that  $\mathbf{E}_0 \cdot \nabla_v f_{i1} \to 0$ . Conveniently, this also makes the problem analytically tractable.

This analysis will also assume that  $\mathbf{k} = k_x \hat{x}$ , in order to prevent the mathematical development from obscuring the crucial physics, which occur in the Hall direction.

Assuming  $(\omega - k_x v_x + i\nu_i) \neq 0$  almost everywhere, we can normalize by that term and integrate over all velocities to get an expression that depends only on space and time.

$$i \int_{-\infty}^{+\infty} f_{i1} d^{3}v = \frac{eE_{1}}{m_{i}} \int_{-\infty}^{+\infty} \frac{1}{\omega - k_{x}v_{x} + i\nu_{i}} \frac{\partial f_{i0}}{\partial v_{x}} d^{3}v - \frac{\nu_{i}n_{i1}}{n_{i0}} \int_{-\infty}^{+\infty} \frac{f_{i0}}{\omega - k_{x}v_{x} + i\nu_{i}} d^{3}v$$

$$i n_{i1} = \frac{eE_{1}}{m_{i}} \int_{-\infty}^{+\infty} \frac{\partial f_{i0}}{\partial v_{x}} \left[ \frac{1}{\omega + i\nu_{i} - k_{x}v_{iD} - k_{x}(v_{x} - v_{iD})} \right] d^{3}v$$

$$- \frac{\nu_{i}n_{i1}}{n_{i0}} \int_{-\infty}^{+\infty} f_{i0} \left[ \frac{1}{\omega + i\nu_{i} - k_{x}v_{iD} - k_{x}(v_{x} - v_{iD})} \right] d^{3}v$$

$$= \frac{eE_{1}}{m_{i}\sqrt{2}kv_{ith}} \int_{-\infty}^{+\infty} \frac{\partial f_{i0}}{\partial v_{x}} \left[ \frac{\omega + i\nu_{i} - k_{x}v_{iD}}{\sqrt{2}kv_{ith}} - \frac{k_{x}(v_{x} - v_{iD})}{\sqrt{2}kv_{ith}} \right]^{-1} d^{3}v$$

$$- \frac{\nu_{i}n_{i1}}{n_{i0}\sqrt{2}kv_{ith}} \int_{-\infty}^{+\infty} f_{i0} \left[ \frac{\omega + i\nu_{i} - k_{x}v_{iD}}{\sqrt{2}kv_{ith}} - \frac{k_{x}(v_{x} - v_{iD})}{\sqrt{2}kv_{ith}} \right]^{-1} d^{3}v$$

where  $v_{ith} \equiv \sqrt{T_i/m_i}$  is the ion thermal speed and  $v_{iD} = eE_0/m_i\nu_i$  is the ion drift speed. At this point, it is helpful to define the following auxiliary variables

$$t \equiv \frac{k_x (v_x - v_{iD})}{\sqrt{2}kv_{ith}} \qquad \zeta \equiv \frac{\omega + i\nu_i - k_x v_{iD}}{\sqrt{2}kv_{ith}}$$

Note that the first definition implies  $dv_x = \sqrt{2}v_{ith}dt$ . Substituting those auxiliary variables gives

$$in_{i1} = \frac{eE_1}{m_i\sqrt{2}kv_{ith}} \iiint \frac{\partial f_{i0}(t)}{\partial t} \frac{1}{\zeta - t} dt dv_y dv_z - \frac{\nu_i n_{i1}}{kn_{i0}} \iiint f_{i0}(t) \frac{1}{\zeta - t} dt dv_y dv_z$$

The integrals imply integration over  $(-\infty, +\infty)$  in all three coordinates. Having an equation for  $f_{i0}$  would help here. Having an equation for  $f_{i0}$  whose function

and first derivative both have well-behaved integrals would really help. Fortunately, assuming  $f_{i0}$  is a Maxwellian is pretty reasonable since we assume that these linear perturbations grow out of thermal noise. In that case the first integral on the RHS becomes

$$\iiint \frac{\partial f_{i0}(t)}{\partial t} \frac{1}{\zeta - t} dt dv_y dv_z = \frac{1}{2\sqrt{\pi}v_{ith}} \int \frac{\partial e^{-t^2}}{\partial t} \frac{1}{\zeta - t} dt$$

and the second becomes

$$\iiint f_{i0}(t) \frac{1}{\zeta - t} dt dv_y dv_z = \frac{1}{\sqrt{2\pi}} \int e^{-t^2} \frac{1}{\zeta - t} dt$$

There is a special function in plasma physics called the plasma dispersion function. Its definition is

$$Z(\zeta) \equiv \frac{1}{\sqrt{\pi}} \int \frac{e^{-t^2}}{t - \zeta} dt$$

Conveniently, we can write its first derivative as

$$Z'(\zeta) \equiv \frac{1}{\sqrt{\pi}} \int \frac{\partial e^{-t^2}}{\partial t} \frac{1}{t - \zeta} dt$$

These special functions, together with the integrated Maxwellians, allow us to write the ion response in its final compact form:

$$in_{i1} = \frac{n_{i0}eE_{1}}{2m_{i}\sqrt{\pi}kv_{ith}^{2}} \left(-\sqrt{\pi}\right)Z'(\zeta) + \frac{\nu_{i}n_{i1}n_{i0}}{\sqrt{2\pi}n_{i1}kv_{ith}} \left(-\sqrt{\pi}\right)Z(\zeta)$$

$$= -\frac{n_{i0}eE_{1}}{2m_{i}kv_{ith}^{2}}Z'(\zeta) + \frac{\nu_{i}n_{i1}}{\sqrt{2}n_{i0}kv_{ith}}Z(\zeta)$$

$$\frac{n'_{i}}{n_{i0}} = \frac{e}{m_{i}}\frac{E'Z'(\zeta)}{\sqrt{2}\nu_{i}v_{ith}}Z(\zeta) - i2kv_{ith}^{2}$$
(2.9)

In the final line, primes again represent the amplitude of Fourier-transformed quantities.

At this point, we need a way to relate  $n'_i$  to E', so that the final expression does not depend on perturbed quantities. The electric field couples ion behavior to electron

behavior, so the natural next step is to relate Equation 2.9 to the electron response due to E'. Since the kinetic ion development neglected the component parallel to  $\mathbf{B}_0$ , a2-D version of the electron response from §2.1 will suffice:

$$\frac{\omega - ku_{e0}}{k - i\kappa_e G} \frac{n'_e}{n_0} = \frac{ik\nu_e}{m_e \left(\Omega_e^2 + \nu_e^2\right)} \left(e\phi' - \frac{T_e n'_e}{n_0}\right).$$

Recalling that  $E' = -ik\phi'$ , we can solve this for the electron fluid response:

$$\frac{n_e'}{n_0} = -eE' \left[ \left( \frac{\omega - ku_{e0}}{k - i\kappa_e G} \right) \left( 1 + \kappa_e^2 \right) m_e \nu_e + ikT_e \right]^{-1}$$
(2.10)

After solving both Equations 2.9 and 2.10 for eE', invoking quasineutrality, equating the resultant expressions, and rearranging terms, we get

$$\omega - k u_{e0} = \frac{1}{\nu_e (1 + \kappa_e^2)} \frac{m_i}{m_e} \left[ \frac{\sqrt{2}\nu_i k v_{ith} Z(\zeta) - i2k^2 v_{ith}^2}{Z'(\zeta)} - \frac{ik^2 T_e}{m_i} \right] \left( 1 - \frac{i\kappa_e G}{k} \right) \tag{2.11}$$

This equation has a form similar to Equation 2.3. The difference is that the ion contribution contains  $\omega$  via  $\zeta$ . The analytic approaches that transformed Equation 2.3 into Equations 2.6 and 2.7 are no longer available. Equation 2.11 requires a sophisticated root solver to handle  $Z(\zeta)$  and  $Z'(\zeta)$ . Xie (2013) describes an example of such a sophisticated algorithm.

# 2.3 Quasi-Neutral Potential Equation

The hybrid plasma model at the heart of much of the work in this dissertation treats electrons as an inertialess fluid and ions as kinetic particles. Chapter 3 describes the hybrid model in greater detail; this section is concerned with deriving the electrostatic potential equation that couples electrons and ions. Despite the fact that this work treats ions kinetically, a fluid description of ion dynamics will suffice to derive an appropriate expression for the potential. The inertialess fluid treatment for electrons

is predicated on the assumption that their relatively small mass lets them respond essentially instantaneously to any accumulation of positive charge – NO<sup>+</sup> is the dominant ion species in the E-region ionosphere, so the ion to electron mass ratio is  $m_i/m_e \approx 55,000$ .

The inertialess electron momentum equation is

$$\frac{D\mathbf{v}_e}{Dt} \approx 0 = -\frac{e}{m_e} \left( \mathbf{E} + \mathbf{u}_e \times \mathbf{B} \right) - \frac{\nabla \cdot \mathbf{P}_e}{n_e m_e} - \nu_e \mathbf{u}_e, \tag{2.12}$$

where the LHS represents the full convective derivative of the electron fluid velocity, and all other terms have the meaning of those in section 2.1 applied to electrons. A modest amount of algebra transforms Equation 2.12 into

$$\mathbf{u}_e = -(1 + \kappa_e^2)^{-1} \epsilon \left( \frac{e\mathbf{E}}{m_e \nu_e} + \frac{\nabla \cdot \mathsf{P}_e}{n_e m_e \nu_e} \right), \tag{2.13}$$

where

$$\epsilon \equiv \begin{pmatrix} 1 & -\kappa_e & 0 \\ +\kappa_e & 1 & 0 \\ 0 & 0 & 1 + \kappa_e^2 \end{pmatrix} \qquad \kappa_e \equiv \frac{|\Omega_e|}{\nu_e}$$

Section 1.6 introduced the magnetization parameter of a plasma species,  $\kappa_s$ , defined as the ratio of cyclotron frequency to collision frequency. Similarly, the  $\epsilon$  tensor captures the effects of electromagnetic Hall drift and collisions with neutrals on the electron fluid momentum.

The continuity equation relates a species velocity to its density. For electrons, using Equation 2.13 for  $\mathbf{v}_e$  gives

$$\frac{\partial n_e}{\partial t} = \nabla \cdot \left[ (1 + \kappa_e)^{-1} \epsilon \left( \frac{e n_e \mathbf{E}}{m_e \nu_e} + \frac{\nabla \cdot \mathbf{P}_e}{m_e \nu_e} \right) \right] + S_e$$

This dissertation considers electrostatic plasma processes that occur on time scales for which  $\partial \mathbf{B}/\partial t \approx 0$ . Faraday's Law then states that  $\nabla \times \mathbf{E} \approx 0$ . Because the curl of the gradient of a scalar function vanishes identically, the solution to

 $\nabla \times \mathbf{E} = 0$  for an arbitrary electric field is  $\mathbf{E} = -\nabla \phi$ . For the cases of interest here, it is convenient to split the total electric field into a constant background component,  $\mathbf{E}_0$ , and a spatiotemporally varying component,  $-\nabla \phi(x, y, z, t)$ . Since the magnetic field does not vary, it is also convenient to write  $\mathbf{B} = \mathbf{B}_0$ . Plugging these new field expressions into the electron continuity equation and solving for  $\phi$  yields

$$\nabla \cdot (n_e \epsilon \nabla \phi) = \nabla \cdot \left[ n_e \epsilon \left( \mathbf{E}_0 + \frac{\nabla \cdot \mathsf{P}_e}{e n_e} \right) \right] + (1 + \kappa_e^2) \frac{m_e \nu_e}{e} \left( S_e - \frac{\partial n_e}{\partial t} \right)$$

Up to this point, this treatment has allowed electron and ion densities to differ. However, the plasma processes of interest occur on temporal scales much slower than the plasma frequency and on spatial scales much larger than the Debye length. Therefore, the plasma is quasi-neutral and  $n_e \approx n_i \equiv n$ . In light of quasi-neutrality, the ion continuity equation reads

$$\frac{\partial n}{\partial t} = -\nabla \cdot (n\mathbf{u}_i) + S_i$$

and since quasi-neutrality implies  $\partial n_e/\partial t = \partial n/\partial t$ , the potential equation becomes

$$\nabla \cdot (n\epsilon \nabla \phi) = \nabla \cdot \left[ n\epsilon \left( \mathbf{E}_0 + \frac{\nabla \cdot \mathsf{P}_e}{en} \right) \right] + (1 + \kappa_e^2) \frac{m_e \nu_e}{e} \left[ S_e + \nabla \cdot (n\mathbf{u}_i) - S_i \right]$$

This equation suffices to describe the potential that couples inertialess electrons to ions in a quasi-neutral plasma, given background electric and magnetic fields, a quasi-neutral density, an expression for the electron pressure, an electron-neutral collision frequency, and an expression for the ion (fluid) velocity. However, this dissertation is concerned with the FBI and GDI in the absence of plasma production and loss, so  $S_e = 0$  and  $S_i = 0$ . Finally, writing the ion flux as  $n\mathbf{u}_i \equiv \mathbf{\Gamma}_i$  and collecting divergence terms leads to the following flux-conserving form of the potential equation:

$$\nabla \cdot (n\epsilon \nabla \phi) = \nabla \cdot \left[ n\epsilon \left( \mathbf{E}_0 + \frac{\nabla \cdot \mathsf{P}_e}{en} \right) + \left( 1 + \kappa_e^2 \right) \frac{m_e \nu_e}{e} \mathbf{\Gamma}_i \right]. \tag{2.14}$$

Ion dynamics only appear in the flux term,  $\Gamma_i$ . The first velocity moment of the ion distribution gives the average flux:

$$\langle n\mathbf{u}_i\rangle = \iiint vf_i\,d^3v$$

and this quantity is easy to calculate in a PIC simulation. Therefore, despite the foregoing fluid development, Equation 2.14 applies readily to hybrid simulations.

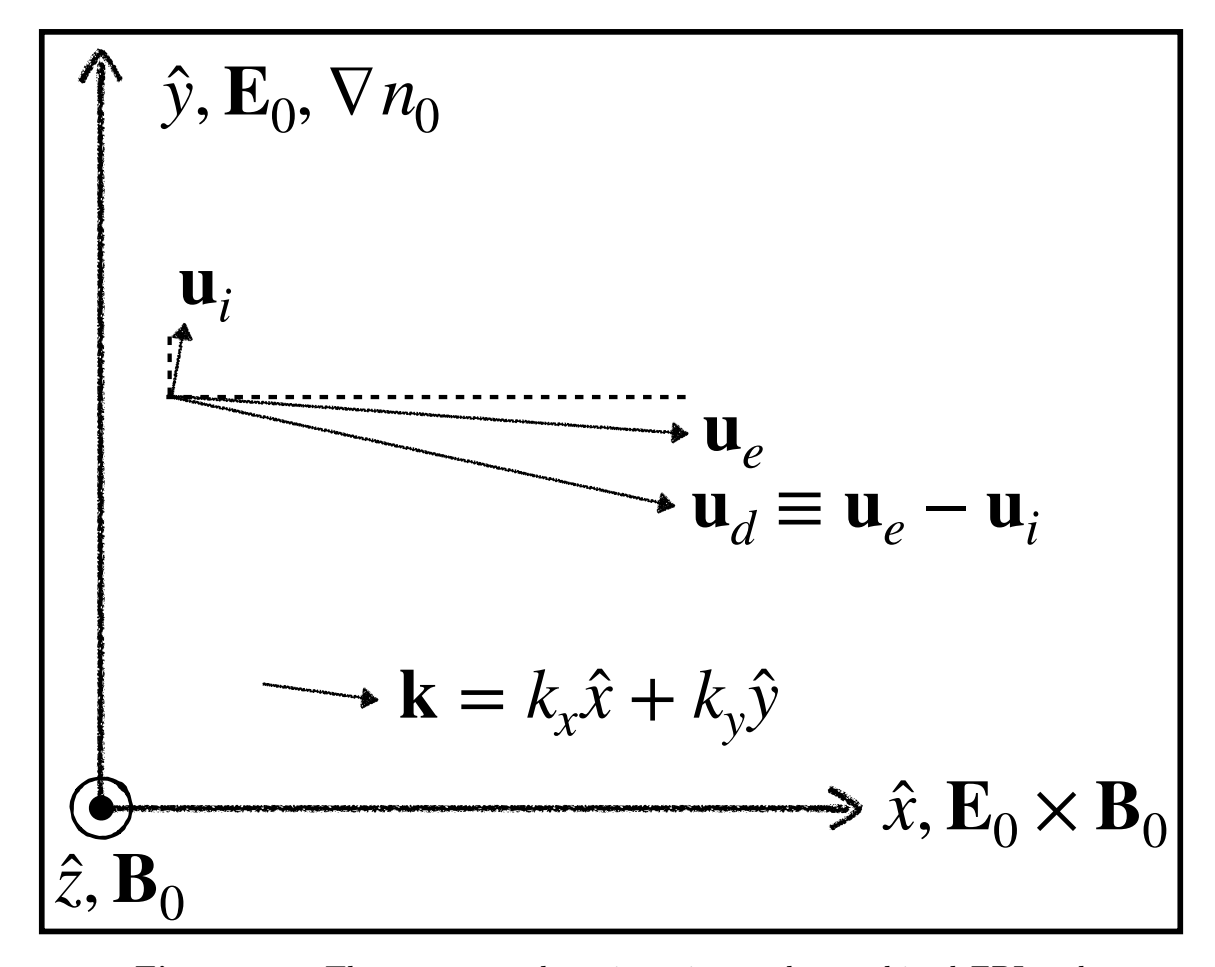


Figure 2·1: The geometry that gives rise to the combined FBI and GDI dispersion relation in the E region. The background electric field,  $\mathbf{E}_0$ , and plasma-density gradient,  $\nabla n_0$ , point vertically. The background magnetic field,  $\mathbf{B}_0$ , points out of the page. The electron drift velocity,  $\mathbf{u}_e$ , points predominantly in the  $\mathbf{E}_0 \times \mathbf{B}_0$  direction, the ion drift velocity,  $\mathbf{u}_i$ , points predominantly in the  $+\mathbf{E}_0$  direction, and  $\mathbf{u}_d \equiv \mathbf{u}_e - \mathbf{u}_i$  is the relative drift velocity. The directions of  $\mathbf{u}_i$ ,  $\mathbf{u}_e$ , and  $\mathbf{u}_d$  have been exaggerated to show altitudinal range, and are not necessarily consistent with  $\mathbf{k}$ .

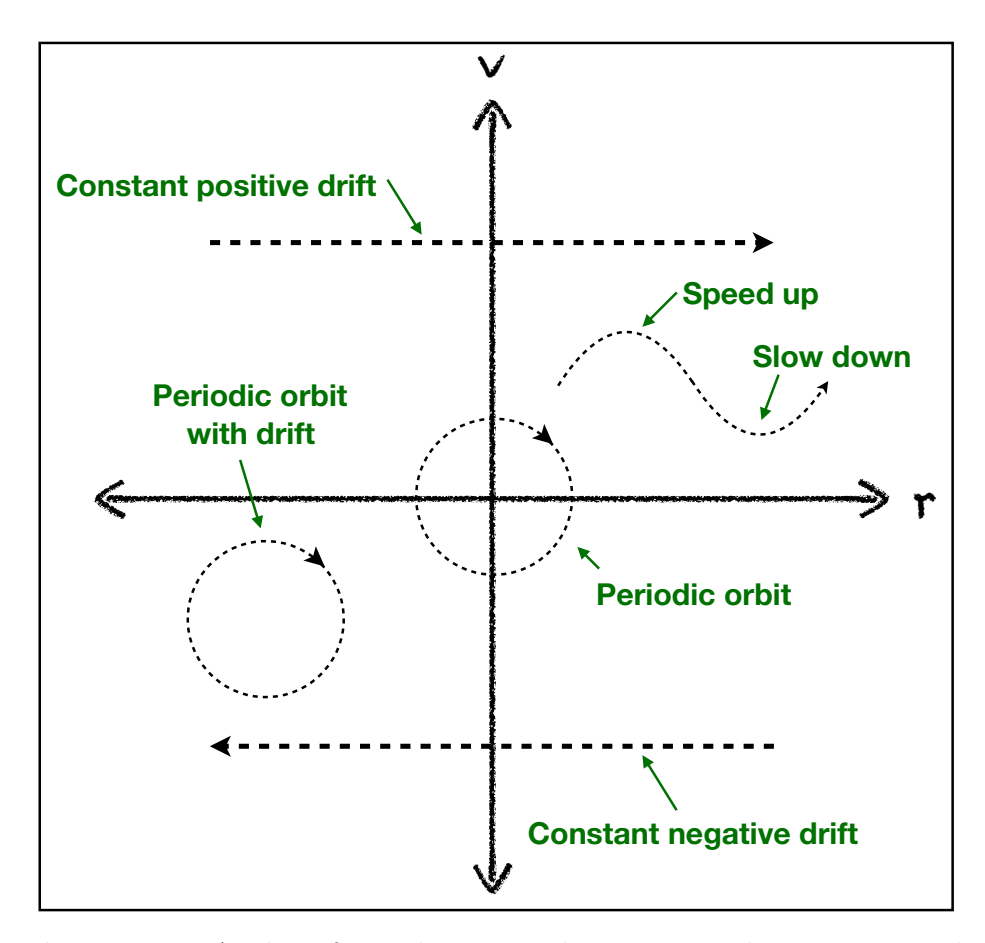


Figure  $2 \cdot 2$ : A plot of one-dimensional motion in phase space, with examples of single-particle motions.

# Chapter 3

# Numerical Framework

# 3.1 The Particle-In-Cell (PIC) Method

The Boltzmann equation introduced in Chapter 2 describes the time evolution of a single particle species distribution. Ostensibly, one could simulate the evolution of Equation 2.8 by approximating the second and third terms (i.e., the phase-space derivatives) at each time step, prescribing a numerical form of the right-hand-side collisional term, and using an appropriate time-stepping scheme to evolve the particle distribution. A popular alternative to following individual particles is to follow "macro-particles" that each represent millions of physical particles. The macro-particles have a prescribed shape that determines their charge density, which the model weights to a grid at each time step. The model can then derive a self-consistent electric field value at each grid point at each time step simply by knowing each particle's position. The complexity of this approach increases in proportion to the number of particles, N; for contrast, the complexity of calculating the electric field by evaluating Coulomb's Law for each pair of particles would increase in proportion to  $N^2$ . The method of calculating field quantities by extrapolating particle positions to a grid is called the particle-in-cell (PIC) method (Birdsall and Langdon, 1991).

The Electrostatic Parallel PIC (EPPIC) code, designed by Professor Meers Oppenheim, employs a PIC approach with additional collision routines to simulate the sort of weakly ionized plasma found in the Earth's E-region ionosphere. Developing a hybrid extension of EPPIC, which treats electrons as an inertialess, isothermal

fluid in quasi-neutrality with ions, has been a major component of this dissertation research. A description of EPPIC, with an emphasis on the hybrid extension, follows.

EPPIC begins by initializing the particles based on a given distribution. A natural initial distribution is to have spatially homogeneous particle positions and a Gaussian distribution of velocities. Such a simple initial condition can nonetheless address many fundamental aspects of kinetic plasma physics. The simulations presented in Chapter 6 initialized particles homogeneously with special modifications designed to reduce the noise inherent in approximating a continuous distribution on a discrete grid. Should the physical model require a more complex initial distribution, the user must chose an algorithm that defines particle positions and velocities in a physically realistic way. One method for defining particle positions is the "transformation method". The transformation method assigns particle positions based on the inverse of the integral of the target distribution. It is efficient but it clearly requires that the distribution have a finite, invertible integral. The simulations presented in Chapter 4 initialized particles via the transformation method. Another method for defining particle positions is called the "rejection method". The rejection method is not specific to the PIC method nor even to plasma models – it is a general technique for generating random deviates from a known distribution function (Press et al., 2007). The simulations presented in Chapter 5 initialized particles via the rejection method.

Following the particle-initialization stage, as well as other setup tasks, EPPIC proceeds to "gather" the particle positions into either quasi-neutral density,  $n(\mathbf{r})$ , and ion flux,  $\Gamma_i(\mathbf{r}) = n(\mathbf{r})v_i(\mathbf{r})$ , or into charge density,  $\rho_c(x, y, z) = \sum_j q_j n_j(\mathbf{r})$ , where the  $q_j$  are the species' charges and the  $n_j$  are the individual species' densities. In either case,  $\mathbf{r}$  represents whatever positional coordinates are appropriate for modeling the system of interest. The choice of n and  $\Gamma_i$  or  $\rho_c$  depends on whether the

physical model assumes quasi-neutrality or not. Given gathered quantities, the general PIC method would calculate the electric field,  $\mathbf{E}(\mathbf{r})$ , and magnetic field,  $\mathbf{B}(\mathbf{r})$ , on the grid. For a fully electromagnetic system, it would use a gathered current density, J(r), to derive E(r) and B(r) from Maxwell's equations. However, the simulations presented in this dissertation assume the plasma is electrostatic. Under the electrostatic assumption, magnetic perturbations are negligible and Faraday's Law reads  $\nabla \times \mathbf{E} = 0$ . General rules of vector calculus state that the curl of the gradient of a scalar function is identically zero, meaning that the electrostatic statement of Faraday's Law implies  $\mathbf{E} = -\nabla \phi$ ; here,  $\phi(\mathbf{r})$  is the electrostatic potential and the negative sign ensures that ions and electrons move in the correct directions. The pure-PIC version of EPPIC does not assume quasi-neutrality, and can therefore use Gauss's Law in the form of Poisson's equation,  $\nabla^2 \phi = -\rho_c/\epsilon_0$ , to calculate the potential. The scientific computing community has a wealth of experience solving Poisson's equation; the solution is particularly simple for simulations with periodic boundary conditions. The results presented in Chapter 6 employed a fast spectral method for solving Poisson's equation with periodic boundary conditions. Quasi-neutrality, on the other hand, assumes by definition that  $\rho_c \approx 0$ . Such a model cannot take advantage of the the nice properties inherent in Poisson's equation and must calculate the potential by an alternative approach. The results presented in Chapters 4 and 5 employed the quasi-neutral hybrid version of EPPIC, which solves Equation 2.14 for the potential via a finite difference method.

EPPIC uses a particle parallelization scheme in which multiple processors essentially run independent PIC simulations that come together to compute the electric field. Each processor updates particle velocities and positions independently, using the existing electric field, then gathers the positions as described above. Next, EPPIC uses the Message Passing Interface (MPI) to calculate an average density (and

ion flux, if applicable) across processors, which it passes to the field-solver routine. This parallelization scheme allows EPPIC to run efficiently on up thousands to tens of thousands of processors.

## 3.2 The Hybrid Approach

Given the success of PIC simulations in plasma physics, it is natural to ask: Why bother with the hybrid approach? The more rigorous way to model electrons and ions would be to treat them both as particles; even with the assumptions inherent in the PIC scheme, this seems like the best approach. The FBI is an ion instability and requires a kinetic treatment of ions but the fully kinetic code also accounts for electrons heating effects that the hybrid code can not capture in its current state. It also does not suffer from the same limitations as the quasi-neutral code because it does not have to solve Equation 2.14 at each time step. One major limitation of the quasi-neutral solver was its inability to handle electron magnetizations much larger than  $\kappa_e = 150$ . Since magnetization increases with altitude, that makes altitudes in the middle-to-upper electrojet inaccessible. The drawbacks to using the pure-PIC version of EPPIC are that it must resolve the electron Debye length,  $\lambda_{De}$ , in space and (the inverse of) the electron plasma frequency,  $\omega_{pe}$ , in time.

The electron Debye length is the length beyond which electrons shield the positive charge of ions, producing a quasi-neutral plasma. The pure-PIC version of EPPIC typically sets and maintains an equal total number of electrons and ions but does not assume quasi-neutrality. Therefore, it must resolve electron-ion separation on scales smaller than the Debye length in order to calculate the electrostatic potential via Poisson's equation. The Debye length varies as  $\sqrt{T_e/n_0}$ , where  $T_e$  is the electron temperature and  $n_0$  is the background plasma density. That means that lowering  $n_0$  or raising  $T_e$  would make it easier for the simulation to resolve  $\lambda_{De}$ . The first option

is feasible to a degree, but Rosenberg and Chow (1998) showed that a simulation requires  $\omega_{pi:sim}/\nu_{i:sim} > 1$  for quasi-neutrality, where  $\omega_{pi:sim}$  and  $\nu_{i:sim}$  are the simulated values of ion plasma frequency and ion-neutral collision frequency, respectively. Raising  $T_e$  is a reasonable aid because the FBI typically heats electrons anyway. In practice, we have used a combination of both approaches.

The electron plasma frequency – the fundamental oscillation that electrons make in a neutralizing background of a positively charged species – depends on the electron mass. In the E-region ionosphere, the positively charged species may be  $NO^+$  or  $O_2^+$ , both of which are more than  $5 \times 10^4$  times more massive than an electron. The code can save some time by evolving electron dynamics on a time scale of  $1/\omega_{pe}$  while "subcycling" ions on a time scale of  $1/\omega_{pi}$ . However, the FBI is an ion instability, meaning that the code needs to ultimately resolve ion dynamics. In order to resolve both electron dynamics and ion dynamics, the code needs to take  $\sqrt{m_i/m_e}$  electron time steps for each ion time step. For E-region ions, that means taking nearly 250 electron time steps for each ion time step. One common approach to this problem is to artificially inflate the electron mass, thereby lowering  $\sqrt{m_i/m_e}$ . This leads to problems in defining other parameters that depend on the electron mass, notably the electron-neutral collision frequency. EPPIC conserves momentum and energy during electron-neutral collisions by artificially inflating the neutral mass specifically during that collision process while using the true neutral mass during ion collisions. Note that even though  $\omega_{pe}$  depends on  $n_0$  – a parameter that is arguably more flexible than  $m_e$  – the challenge is in the ratio of time scales. Unlike the case of resolving  $\lambda_{De}$ , changing  $n_0$  does not help here. Furthermore, changing  $n_0$  in one direction for either  $\omega_{pe}$  or  $\lambda_{De}$  makes the problem worse for the other quantity. See Oppenheim and Dimant (2004) for more details about the limitations of pure-PIC EPPIC.

## 3.3 Finite-Difference Scheme for the Potential Equation

We can write electron pressure tensor on the RHS of Equation 2.14 as  $P_e = nk_BT_e$ I, where I is the identity tensor. Assuming isothermal electrons, we get  $\nabla \cdot P_e = k_BT_e\nabla n$ , so the RHS depends only on quasi-neutral density, ion flux, and constant parameters. Suppose we split the physical domain into a 2-D grid of discrete points. Each point has an index, (i, j). We know the value of the RHS after gathering ions into density and flux as described above. We want to know the potential at each point, so we need to discretize the LHS. The centered finite-difference (FD) approach in 1 D computes the difference between a function at neighboring half grid steps. For some arbitrary function, f(x), first and second derivatives become

$$\begin{split} \frac{df}{dx} &\approx \frac{f^{(i+1/2)} - f^{(1-1/2)}}{\Delta x} \\ \frac{d^2f}{dx^2} &= \frac{d}{dx} \left(\frac{df}{dx}\right) \approx \frac{f^{(i+1)} - 2f^{(i)} + f^{(i-1)}}{(\Delta x)^2}, \end{split}$$

where  $\Delta x$  is the grid-step size and parenthetical superscripts denote grid locations. Note that the half-cell locations do not actually exist on the computational grid – if we were to halve the grid-cell size, we would have better resolution but we would still label each point (i, j). The FD approach requires a method for evaluating functions at half-cell points, but we will deal with that later. For the sake of clarity, we can define the intermediate variable  $\mathbf{L} \equiv n\epsilon \nabla \phi$ .

$$\nabla \cdot \mathbf{L} = \frac{\partial L_x}{\partial x} + \frac{\partial L_y}{\partial y} \approx \frac{L_x^{(i+1/2,j)} - L_x^{(i-1/2,j)}}{\Delta x} + \frac{L_y^{(1,j+1/2)} - L_y^{(i,j-1/2)}}{\Delta y}$$
(3.1)

This contains four terms in L, each evaluated at a grid point neighboring (i, j). Expanding the first  $L_x$  term yields

$$\begin{split} L_x^{(i+1/2,j)} &= n^{(i+1/2,j)} \left( \epsilon \nabla \phi \right)_x^{(i+1/2,j)} \\ &= n^{(i+1/2,j)} \left[ \partial_x \phi^{(i+1/2,j)} - \kappa_e \partial_y \phi^{(i+1/2,j)} \right] \\ &\approx n^{(i+1/2,j)} \left[ \frac{\phi^{(i+1,j)} - \phi^{(i,j)}}{\Delta x} - \kappa_e \frac{\phi^{(i+1/2,j+1/2)} - \phi^{(i+1/2,j-1/2)}}{\Delta y} \right], \end{split}$$

where  $\partial_x$  and  $\partial_y$  denote partial derivatives in x and y, respectively. The second-order differential operator has taken care of the half-cell terms that behave like  $\partial_{xx}\phi$  and  $\partial_{yy}\phi$ , which is not surprising, given the FD expression for  $d^2f/dx^2$  above. To deal with n and the remaining  $\phi$  terms at half-cell locations, we will assume that they change smoothly from one cell to the next that a simple average will suffice:

$$\begin{split} n^{(i+1/2,j)} &= \frac{n^{(i+1,j)} + n^{(i,j)}}{2} \\ \phi^{(i+1/2,j+1/2)} &= \frac{\phi^{(i+1,j+1)} + \phi^{(i+1,j)} + \phi^{(i,j)} + \phi^{(i,j+1)}}{4} \\ \phi^{(i+1/2,j-1/2)} &= \frac{\phi^{(i+1,j)} + \phi^{(i+1,j-1)} + \phi^{(i,j-1)} + \phi^{(i,j)}}{4}. \end{split}$$

Note that evaluating the  $\phi$  terms at half-cell locations in both directions requires an average of four neighboring points. Cancelling terms and dividing by  $\Delta x$  leads to

$$\frac{L_x^{(i+1/2,j)}}{\Delta x} \approx \frac{n^{(i+1,j)} + n^{(i,j)}}{2} \times \left[ \frac{\phi^{(i+1,j)} - \phi^{(i,j)}}{(\Delta x)^2} - \kappa_e \frac{\phi^{(i+1,j+1)} + \phi^{(i,j+1)} - \phi^{(i+1,j-1)} - \phi^{(i,j-1)}}{4\Delta y \Delta x} \right].$$

The process for expanding the three other L terms is identical and it yields

$$\begin{split} \frac{L_x^{(i-1/2,j)}}{\Delta x} &\approx \frac{n^{(i,j)} + n^{(i-1,j)}}{2} \\ &\times \left[ \frac{\phi^{(i,j)} - \phi^{(i-1,j)}}{(\Delta x)^2} - \kappa_e \frac{\phi^{(i,j+1)} + \phi^{(i-1,j+1)} - \phi^{(i,j-1)} - \phi^{(i-1,j-1)}}{4\Delta y \Delta x} \right] \\ \frac{L_y^{(i,j+1/2)}}{\Delta y} &\approx \frac{n^{(i,j+1)} + n^{(i,j)}}{2} \\ &\times \left[ \kappa_e \frac{\phi^{(i+1,j+1)} + \phi^{(i+1,j)} - \phi^{(i-1,j+1)} - \phi^{(i-1,j)}}{4\Delta x \Delta y} + \frac{\phi^{(i,j+1)} - \phi^{(i,j)}}{(\Delta y)^2} \right] \\ \frac{L_y^{(i,j-1/2)}}{\Delta y} &\approx \frac{n^{(i,j)} + n^{(i,j-1)}}{2} \\ &\times \left[ \kappa_e \frac{\phi^{(i+1,j)} + \phi^{(i+1,j-1)} - \phi^{(i-1,j)} - \phi^{(i-1,j-1)}}{4\Delta x \Delta y} + \frac{\phi^{(i,j)} - \phi^{(i,j-1)}}{(\Delta y)^2} \right] \end{split}$$

All that remains is to plug these expressions back into Equation 3.1 and rearrange in terms of  $\phi$  at the nine relevant grid points. After an appropriate amount of algebra,

the FD expression for the LHS of Equation 2.14 is

$$\nabla \cdot (n\epsilon \nabla \phi) \approx \\ \phi^{(i,j)} \left\{ -\left[ \frac{n^{(i+1,j)} + 2n^{(i,j)} + n^{(i-1,j)}}{2(\Delta x)^2} \right] - \left[ \frac{n^{(i,j+1)} + 2n^{(i,j)} + n^{(i,j-1)}}{2(\Delta y)^2} \right] \right\} \\ + \phi^{(i+1,j)} \left\{ \frac{n^{(i+1,j)} + n^{(i,j)}}{2(\Delta x)^2} + \kappa_e \frac{n^{(i,j+1)} - n^{(i,j-1)}}{8\Delta x \Delta y} \right\} \\ + \phi^{(i-1,j)} \left\{ \frac{n^{(i,j)} + n^{(i-1,j)}}{2(\Delta x)^2} + \kappa_e \frac{n^{(i,j-1)} - n^{(i,j+1)}}{8\Delta x \Delta y} \right\} \\ + \phi^{(i,j+1)} \left\{ \frac{n^{(i,j+1)} + n^{(i,j)}}{2(\Delta y)^2} + \kappa_e \frac{n^{(i-1,j)} - n^{(i+1,j)}}{8\Delta x \Delta y} \right\} \\ + \phi^{(i,j-1)} \left\{ \frac{n^{(i,j)} + n^{(i,j-1)}}{2(\Delta y)^2} + \kappa_e \frac{n^{(i+1,j)} - n^{(i-1,j)}}{8\Delta x \Delta y} \right\} \\ + \phi^{(i+1,j+1)} \left\{ \kappa_e \frac{n^{(i,j+1)} - n^{(i,j+1)}}{8\Delta x \Delta y} \right\} \\ + \phi^{(i-1,j+1)} \left\{ \kappa_e \frac{n^{(i-1,j)} - n^{(i,j+1)}}{8\Delta x \Delta y} \right\} \\ + \phi^{(i+1,j-1)} \left\{ \kappa_e \frac{n^{(i+1,j)} - n^{(i,j-1)}}{8\Delta x \Delta y} \right\} \\ + \phi^{(i-1,j-1)} \left\{ \kappa_e \frac{n^{(i,j-1)} - n^{(i,j-1)}}{8\Delta x \Delta y} \right\} . \tag{3.2}$$

Note that  $\kappa_e \to 0$  reduces Equation 3.2 to

$$\begin{split} \nabla \cdot (n \nabla \phi) \approx \\ \phi^{(i,j)} \left\{ - \left[ \frac{n^{(i+1,j)} + 2n^{(i,j)} + n^{(i-1,j)}}{2 \left( \Delta x \right)^2} \right] - \left[ \frac{n^{(i,j+1)} + 2n^{(i,j)} + n^{(i,j-1)}}{2 \left( \Delta y \right)^2} \right] \right\} \\ + \phi^{(i+1,j)} \left\{ \frac{n^{(i+1,j)} + n^{(i,j)}}{2 \left( \Delta x \right)^2} \right\} \\ + \phi^{(i-1,j)} \left\{ \frac{n^{(i,j)} + n^{(i-1,j)}}{2 \left( \Delta x \right)^2} \right\} \\ + \phi^{(i,j+1)} \left\{ \frac{n^{(i,j+1)} + n^{(i,j)}}{2 \left( \Delta y \right)^2} \right\} \\ + \phi^{(i,j-1)} \left\{ \frac{n^{(i,j)} + n^{(i,j-1)}}{2 \left( \Delta y \right)^2} \right\}, \end{split}$$

which is diagonally dominant and is therefore relatively simple to solve numerically. The physical significance of this limit is that, as electrons become unmagnetized, they Pedersen drift with the ions and there is no Hall contribution to the potential. In the further limit of homogeneous density, Equation 3.2 becomes

$$n\nabla^{2}\phi \approx \\ n\left[\frac{\phi^{(i+1,j)} - 2\phi^{(i,j)} - \phi^{(i-1,j)}}{\left(\Delta x\right)^{2}} + \frac{\phi^{(i,j+1)} - 2\phi^{(i,j)} - \phi^{(i,j+1)}}{\left(\Delta y\right)^{2}}\right]$$

This is just Poisson's equation and is, as mentioned above, very computationally friendly.

The immediate advantage of writing Equation 3.2 in the form given is that it allows for easy translation it into a matrix system of the form  $A\phi = \rho$ . At each grid point, Equation 3.2 provides represents the product  $A\phi$  and the RHS of Equation 2.14, evaluated at the grid point of interest, provides a single numerical value for  $\rho$ . The numerical challenge to invert the matrix equation to provide  $\phi = A^{-1}\rho$ .

It may be tempting to first expand the divergence operator in Equation 3.2 as

$$\nabla \cdot (n\epsilon \nabla \phi) = \nabla \cdot [n (\partial_x \phi - \kappa_e \partial_y \phi) \hat{x} + n (\kappa_e \partial_x \phi + \partial_y \phi) \hat{y}]$$
$$= n\nabla^2 \phi + \nabla n \cdot \nabla \phi + \kappa_e (\nabla n \times \nabla \phi) \cdot \hat{z}$$

and apply centered FD expressions directly to  $\nabla n$ ,  $\nabla \phi$ , and  $\nabla^2 \phi$ . However, this approach yields incorrect results when density perturbations grow large. The reason is that the matrix A is singular, since adding any constant to  $\phi$  is also a solution to  $\nabla \cdot (n\epsilon \nabla \phi) = f$ . The iterative-inversion approach to solving the potential equation in EPPIC projects out the nullspace of A in order to eliminate the singularity; the direct-inversion approach applies a method originally described in Oppenheim et al. (1996) which implicitly sets the DC component of  $\phi$  and solves a reduced linear system with one fewer row and one fewer column. The latter approach retains the advantages of a centered FD scheme to accurately capture the divergence-free nature of Equation 2.14.

#### 3.4 Matrix Inversion Methods

The hybrid EPPIC results presented in Chapter 4 used an iterative-inversion approach that combined Hypre's algebraic multigrid (AMG) method, BoomerAMG (Falgout and Yang, 2002), with the generalized minimal residual (GMRES) method (Saad and Schultz, 1986). Algebraic multigrid is an extension of geometric multigrid. Geometric multigrid approximates a numerical problem on coarser and coarser meshes, finds a solution (usually via a direct-inversion method) to the simplified problem on the coarsest grid, then interpolates that solution back to the fine grid. Algebraic multigrid arose as a response to problems without a well-defined grid. It takes advantage of algebraic connections between matrix elements rather than spatial proximity on a physical grid (Briggs et al., 2000).

The hybrid EPPIC results presented in Chapter 5 used a direct-inversion numerical library called MUltifrontal Massively Parallel Solver (MUMPS) (Amestoy et al., 2001, 2006). Frontal solvers, in general, use a variant of Gaussian elimination that avoids having to handle many terms that equal zero. A multifrontal method is simple an extension of the frontal method that can run efficiently on parallel systems. The general multifrontal method (Liu, 1992) performs a Cholesky matrix decomposition (A = LL\*) but Cholesky decomposition only applies to symmetric matrices. The quasi-neutral potential equation produces an unsymmetric matrix, so MUMPS must perform a Gaussian decomposition (A = LU). superLU\_DIST(Li et al., 1999) is an alternative numerical library for directly inverting large parallel matrices. The work presented in Chapter 5 used MUMPS because it employs very efficient memory usage and because MUMPS ran faster than superLU\_DIST in identical EPPIC test runs.

## 3.5 Hybrid EPPIC Development

This section describes significant contributions to EPPIC that I implemented while developing the hybrid version, but which are not immediately relevant to the presentations in Chapters 4, 5, and 6.

#### 3.5.1 Electron distribution

EPPIC allows the user to declare what type of distributions they want to simulate. The most common and well-supported option is to simulate multiple particle distributions (i.e., the pure-PIC version of EPPIC) but routines exist to handle various types of fluid distributions. The isothermal, quasi-neutral, inertialess hybrid approach evolves a particle distribution of ions but it need not actually follow a distribution of electrons. The work presented in Chapters 4 and 5 focuses on ion dynamics, with electrons providing a quasi-neutralizing background that couples to

ions via the potential equation. That fact allowed me to streamline hybrid EPPIC by creating a new type of distribution, which is simply a set of constant parameters. Using that method for hybrid electrons, EPPIC simply reads in electron parameters (e.g., mass, charge, collision frequency) from an input file and passes them to the potential equation. Doing so precludes the need to set up a dynamic distribution that the rest of the code will never use.

#### 3.5.2 One-step hybrid gather

The standard PIC approach only gathers particle positions into charge density but Equation 2.14 requires number density and ion flux. I extended the pure-PIC gather routine to compute both number density and flux components in one pass. Number density is trivial: It simply involves interpolating particle positions to the grid without weighting each distribution by its respective charge. The extension to flux components is also natural, since the routine will have already calculated the interpolation factors – all that remains is to multiply each particle by its velocity in each direction to compute each flux component. This approach requires storing an additional array for each dimension of the physical system, but it requires only one pass through each particle distribution. Memory is inexpensive and computational efficiency is of primary concern for EPPIC. Each particle distribution can consist of millions of PIC particles on each processor, so favoring algorithmic efficiency over memory efficiency makes sense.

#### 3.5.3 Using PETSc for potential

Hybrid EPPIC leverages the Portable, Extensible Toolkit for Scientific Computation (PETSc) (Balay et al., 2018, 2015, 1997) to switch between solution methods for the linear system given by  $A\phi = \rho$ . PETSc provides data structures and algorithms for the scalable parallel solution of PDEs, exposing an effective "algebra of composi-

tion" that lets the easily user experiment with different iterative and direct methods. Adding PETSc functionality to the existing version of EPPIC was a fundamental component of the research presented in this dissertation and will allow future users to test other methods for solving Equation 2.14

#### 3.5.4 Efficient PETSc setup

I initially put all the PETSc code into the potential-solver routine, which EPPIC calls at each time step. That meant that EPPIC asked PETSc to create and destroy data structures at each time step. That was fine for an iterative method such as BoomerAMG+GMRES but it made direct methods such as MUMPS seem prohibitively slow. Removing the routines that create and destroy data structures and placing them in EPPIC's main procedure allowed PETSc to reuse existing structures. This is crucial to efficient use of a direct method because the setup processes, in which the algorithm factors the matrix, is often the most time consuming. Moving the data-structure creation to the main procedure meant that MUMPS could perform that factorization once and reuse it, making direct solution of  $A\phi = \rho$  much more efficient over multiple time steps.

#### 3.5.5 Running PETSc on a subset of communicators

EPPIC exhibits nearly perfect weak scaling with respect to particle-related routines. Weak scaling measures the ability of a parallel numerical algorithm to complete a large version of a given problem in the same time as it would take to compute a smaller version, provided it can use more parallel processors. Weak scaling differs from strong scaling in that the later measures how much an algorithm speeds up when it can use more processors. EPPIC's nearly perfect weak scaling for particles arises from the previously described particle parallelization scheme in which each process handles its own PIC distribution. A global operation like the potential solver should exhibit at

least good strong scaling if it is to be useful. The biggest pitfall is inter-processor communication – the user must look for a sweet spot between providing enough processors to divide the problem into manageable chunks but not so many that inter-processor communication dominates the algorithm. For the research presented in Chapter 5, the efficiency of MUMPS appeared to decrease for processor counts larger than 256. However, keeping the processor count at or below 256 meant either assigning more particles to each processor than it could fit in memory, or settling for low particle counts. The first option is clearly unfeasible and the second option resulted in systems with too much particle noise to discern the relevant physics. The solution was to implement the ability to run PETSc on a subset of the total number of processors. This allowed me to rerun the simulations presented in Chapter 5 with much lower particle noise, and was fundamental to producing the results of that chapter.

# Chapter 4

# Coupled Growth and Evolution of Farley-Buneman/Gradient Drift Instabilities on Meter and Decameter Scales in a Common Plasma Volume

### 4.1 Introduction

Type-I irregularities exhibit a narrow spectrum. The early observations by Cohen and Bowles (1967) led researchers to conclude that Type-I irregularities have a Doppler shift that is constant with zenith angle, but more recent work suggests that their Doppler shift varies with the cosine of elevation angle (Woodman and Chau, 2002; Hysell et al., 2007). They occur due to the Farley-Buneman instability (FBI) when the total electric field rises above a threshold level and causes the relative  $\mathbf{E} \times \mathbf{B}$  drift speed to exceed the acoustic speed by a factor slightly larger than unity. The electrons Hall drift through collisionally demagenitized ions, which are Pedersen drifting much more slowly than the electron Hall drift, and pull ions in the  $\mathbf{E} \times \mathbf{B}$  direction in the presence of density perturbations. The influence of supersonic electron drift causes ion inertia to overcome plasma thermal pressure, causing areas of relative density enhancement  $(\delta n/n_0 > 0)$  or depletion  $(\delta n/n_0 < 0)$  to become respectively more enhanced or depleted, leading to instability. The instability threshold criterion is that the wave phase-speed component parallel to the background electron drift exceed the plasma acoustic speed by the factor  $1 + \psi_{\perp}$ , where  $\psi_{\perp}$  is the ratio of electron

to ion mobilities and is typically 0.2 to 0.3 in the lower equatorial E-region (Dimant and Oppenheim, 2004). Since this instability develops in the absence of background density gradients, the electron drift speed is  $|\mathbf{V}_{e0}| = |\mathbf{E}_0 \times \mathbf{B}_0|/B_0^2$  and the instability criterion is equivalently a criterion on the background electric field. Although theory predicts that type-I irregularities should have a phase speed proportional to the electron drift speed, observations show that they saturate at the ion acoustic speed,  $C_s$ . A kinetic treatment shows that the FB instability has a maximum growth rate at a wavelength of a few meters (Oppenheim et al., 1996).

Type-II irregularities exhibit a broad spectrum at small Doppler shifts that increase with zenith angle. They do not have a threshold electric field predicted by linear theory in the way that type-I irregularities do, but they do require that magnetized electrons drift through collisional ions fast enough to produce the polarization electric field that drives electrostatic irregularities. Type-II irregularities occur in the presence of background density gradients when  $\mathbf{E} \cdot \nabla n_0 > 0$ . A small perturbation electric field  $(\delta E/E_0 \propto \delta n/n_0)$  causes regions of  $\delta n/n_0 < 0$  to  $\delta \mathbf{E} \times \mathbf{B}$  drift into regions of higher background density and regions of  $\delta n/n_0 > 0$  to drift into regions of lower background density.

Ronchi et al. (1991) asked what role large-scale waveforms play in the dynamics of meter-scale irregularities and suggested that 3-m irregularities detected in radar backscatter experiments may be passively advected with kilometer-scale waves. They note "considerable experimental evidence that the characteristics of the short wavelength two-stream irregularities depend upon the presence or absence of long wavelength activity". With the advent of improved radar technology at Jicamarca and the new imaging techniques described in Hysell and Chau (2006), Hysell et al. (2007) identified 3-m waves generated by, and advecting with, kilometer-scale gradient-drift waves, consistent with the predictions of Ronchi et al. (1991). Hassan et al. (2015)

presented a fluid model of the E-region designed to reproduce Type-I and Type-II irregularities, but their simulation box extended only  $100 \text{ m} \times 100 \text{ m}$ , and did not show the effect of large-scale waves on the generation of meter-scale irregularities.

The work presented in this chapter and the next shows numerical simulation results that support the conclusions of Ronchi et al. (1991) and observations of Hysell et al. (2007), and provide a connection between meter-scale density irregularities and larger background wave perturbations. It shows that such large-scale density waves must give rise to the meter-scale irregularities routinely observed by VHF radars in the E-region equatorial ionosphere, even when the measured ambient electric field is too small to drive pure two-stream turbulence.

This chapter is organized as follows: Section 4.2 provides background on the theory of coupled FBI/GDI, section 4.3 describes the numerical model and simulation methods, section 4.4 describes the simulation results, section 4.5 discusses the results within the context of observations and theory, and section 4.6 concludes the chapter.

# 4.2 Theory

The production of meter-scale irregularities from large-scale perturbations can be understood from linear theory. Consider a quasi-neutral, electrostatic, isothermal plasma with inertialess electrons propagating perpendicular to the background magnetic field. In the E-region, around 100 km, electrons are magnetized while ions are collisionally demagnetized. In terms of the gyrofrequency,  $\Omega_j \equiv |q_j|B/m_j$ , and collision frequency,  $\nu_j$ , of electrons (j=e) and ions (j=i), that means  $\kappa_e \equiv \Omega_e/\nu_e \gg 1$  while  $\kappa_i \equiv \Omega_i/\nu_i < 1$ . This work assumes geomagnetically quiet conditions with a static vertical background electric field,  $\mathbf{E}_0 = E_0 \hat{z}$ , and meridional magnetic field,  $\mathbf{B}_0 = -B_0 \hat{y}$ . All dynamics occur in the plane perpendicular to  $\mathbf{B}_0$ . Linearizing the fluid equations for electrons and a single ion species in the rest frame of the ions and in

the presence of a simple vertical density gradient with scale length  $L = n_0 (dn_0/dz)^{-1}$  leads to the dispersion relation

$$\omega - \mathbf{k} \cdot \mathbf{V}_{e0} = \frac{\psi_{\perp}}{\nu_i} \left[ \omega \left( i\omega - \nu_i \right) - ik^2 C_s^2 \right] \left( 1 - \frac{i\Omega_e}{\nu_e k L} \right), \tag{4.1}$$

where  $\mathbf{V}_{e0}$  is the total electron drift velocity and  $C_s^2 = K_b(T_i + \gamma_e T_e)/m_i$  is the plasma acoustic speed. Writing  $\omega(\mathbf{k}) = \omega_r(\mathbf{k}) + i\omega_i(\mathbf{k})$  and assuming  $|\omega_i(\mathbf{k})| \ll |\omega_r(\mathbf{k})|$ , the oscillation frequency and linear growth rate are given by

$$\omega_r(\mathbf{k}) = \frac{\mathbf{k} \cdot \mathbf{V}_{e0}}{1 + \psi_{\perp}} \tag{4.2a}$$

$$\omega_i(\mathbf{k}) = \frac{\psi_{\perp}}{1 + \psi_{\perp}} \left[ \frac{\Omega_e}{\nu_e} \frac{\omega_r}{kL} + \left( \omega_r^2 - k^2 C_s^2 \right) \frac{1}{\nu_i} \right], \tag{4.2b}$$

where  $\psi_{\perp} \equiv \nu_e \nu_i / \Omega_e \Omega_i$  (Sudan et al., 1973; Rogister and D'Angelo, 1970). The system will be unstable when  $\omega_i(\mathbf{k}) > 0$ .

Table 4.1 gives the parameter values used in this work, which presents three simulations of the equatorial E-region ionosphere at 100 km altitude. All runs used a constant horizontal magnetic field  $\mathbf{B}_0 = -2.5 \times 10^{-5} \hat{y}$  T. The threshold electric field magnitude for pure-FB instability in the absence of gradients is  $E_c = B_0 C_s (1 + \psi_{\perp}) \approx 11.2 \text{ mV/m}$ . Pfaff et al. (1997) measured vertical DC electric field values of approximately 9 mV/m in situ during a sounding rocket campaign and Moro et al. (2016) inferred vertical DC electric field values in the range 0.51 to 20.67 mV/m, with a mean diurnal value of  $8.12\pm1.51$  mV/m, from radar data. One goal of the hybrid simulations was to examine the effects of the vertical background electric field, so the three runs presented here are sorted by background vertical electric field. One run used  $E_{0z} = 9$  mV/m, consistent with the Pfaff et al. (1997) measurement around 100 km and the average value inferred by Moro et al. (2016); a second run used  $E_{0z} = 12$  mV/m, just above the threshold for FB instability; and a third run used  $E_{0z} = 6$  mV/m, a value far too low to trigger FB turbulence but still reasonable for

the equatorial E region. This work ignores the zonal electric field, which is typically an order of magnitude smaller than the vertical field. The geometry causes the zeroth-order electron  $\mathbf{E}_0 \times \mathbf{B}_0$  drift to point from east to west (in the  $\hat{x}$  direction). All runs were seeded by the same initial density wave, as described in §4.4.1. The initial density wave has a more complex structure than that which equation 4.1 assumes; §4.5.2 will address the more complex density gradient structure. The NRL MSIS Atmosphere Model (Picone et al., 2002) provides neutral temperatures and densities, and the following formulas from Schunk and Nagy (2004) provide the ion and electron collision frequencies:

$$\nu_i = 4.34 \times 10^{-10} n_{N_2}$$

$$\nu_e = 2.33 \times 10^{-11} n_{N_2} \left( 1 - 1.21 \times 10^{-4} T_e \right) T_e,$$

where  $n_{N_2}$  is the  $N_2$  density in cm<sup>-3</sup> and the constants have appropriate units to make the units of  $\nu_i$  and  $\nu_e$  both s<sup>-1</sup>. Because this work does not attempt to simulate a particular event, it uses parameters from 01 January 2000, 12:00 UT as a representative case.

#### 4.3 Numerical Model

This work employs a numerical code similar to the Electrostatic Parallel Particle-In-Cell (EPPIC) code described in Oppenheim et al. (2008) and Oppenheim and Dimant (2004). It incorporates a novel parallelized electrostatic potential solver based on theory described in Oppenheim et al. (1996). This section first describes the evolution of the collisional ion distribution, then describes the electrostatic potential equation that arises due to quasi-neutrality with inertialess electrons.

For ion dynamics, this code follows the standard particle-in-cell (PIC) approach (Birdsall and Langdon, 1991), solving the collisional ion momentum equation in two

stages: Particles first move under the influence of the electric and magnetic fields, using a standard Boris mover. They then collide with neutral particles, using the statistical characteristics of a given neutral distribution with a prescribed collisional algorithm to change the ion momentum. The simulation runs presented here used a single ion species,  $NO^+$ , and a single neutral species,  $N_2$ , since those are the dominant species in the E-region ionosphere. Unlike the pure-PIC version of EPPIC, the quasi-neutral version does not use an artificially inflated electron mass to relax the time-step constraints set by the ion-to-electron mass ratio. It also takes ion dynamics to be representative of overall plasma dynamics since  $n_i \approx n_e \equiv n$ , but requires a new approach to calculating the perturbed electric field via the electrostatic potential. A description of that approach follows.

The hybrid PIC code treats electrons as an inertialess thermal fluid with temperature  $T_e$  and either an isothermal or linearly adiabatic equation of state. Treating electrons as inertialess relaxes the pure-PIC requirement of resolving electron dynamics on a time scale  $\sim 1/f_{pe}$  and on spatial scales  $\sim \lambda_{De}$ , and allows the simulation to use the true value of the electron mass as a parameter. The assumption of inertialess fluid electrons, coupled with the quasi-neutral condition  $(\nabla \cdot \mathbf{J} = 0)$ , leads to an equation for the electrostatic potential in terms of density, n, ion flux,  $\Gamma_i = n\mathbf{v}_i$ , and parameters of the electron fluid (e.g.  $\nu_e$  and  $m_e$ ):

$$\nabla \cdot [n\epsilon \nabla \phi] = \nabla \cdot \left[ n\epsilon \left( \mathbf{E}_0 + \frac{k_b T_e}{e} \frac{\nabla n}{n} \right) + \left( 1 + \kappa_e^2 \right) \frac{m_e \nu_e}{e} \Gamma_i \right], \tag{4.3}$$

where

$$\epsilon \equiv \left( \begin{array}{cc} 1 & -\kappa_e \\ \kappa_e & 1 \end{array} \right) \quad \text{and} \quad \kappa_e \equiv \frac{\Omega_e}{\nu_e}$$

The hybrid model casts equation 4.3 as a linear system of centered finite-difference equations which can be converted to a matrix equation of the form  $A\phi = f(n, \Gamma_i)$ . The simulation solves the matrix equation for  $\phi$  at each time step using routines from

Table 4.1: Simulation Parameters for Chapter 4

Symbol Value

Symbol	Value
$m_i$	$5.0 \times 10^{-26} \text{ [kg]}$
$m_e$	$9.1 \times 10^{-31}  [kg]$
$m_n$	$4.6 \times 10^{-26}  [\text{kg}]$
$T_i = T_e = T_n$	220 [K]
$ u_i$	$3.0 \times 10^3  [\mathrm{s}^{-1}]$
$ u_e$	$3.0 \times 10^4  [s^{-1}]$
$B_{y0}$	$-2.5 \times 10^{-5} \ [\text{T}]$
$E_{z0}^{\sigma}$	6.0, 9.0, 12.0  [mV/m]
$n_0$	$10^{10}  [\mathrm{m}^{-3}]$
$N_x$	2048 [cells]
dx	0.25[m]
$N_z$	1024 [cells]
dz	$0.25[\mathrm{m}]$
$N_t$	8192 [steps]
dt	$5 \times 10^{-5} [s]$

the Portable Extensible Toolkit for Scientific Computing (PETSc) (Balay et al., 2015, 1997). The specific numerical approach involves preconditioning the linear system with *hypre*'s BoomerAMG algebraic multigrid method (Falgout and Yang, 2002), then performing the actual solve with the restarted generalized minimal residual (GMRES) method (Saad and Schultz, 1986).

Table 4.1 lists the cell width in each direction, dx and dz, the number of cells,  $N_x$  and  $N_z$ , the the time step, dt, and the number of time steps,  $N_t$ . The simulation spans 512 m in zonal (east-west) distance, 256 m in vertical distance, and 409.6 ms in real time. The simulation used periodic boundary conditions. The following section describes the initial density condition.

#### 4.4 Results

This section presents the results of the three simulation runs, with background vertical electric fields  $E_{0z} = 6 \text{ mV/m}$ , 9 mV/m, and 12 mV/m. It first describes the initial imposed density configuration and resultant potential, then shows snapshots of the perturbed density and total electric field at the end of each run. Following

those results, it describes the spectral power as a function of line-of-sight (LoS) angle and phase velocity for 2-m, 3-m, and 8-m waves.

#### 4.4.1 Density and electric field

Figure 4.1 shows the initial relative perturbed density  $(\delta n/n_0)$  in color with electrostatic potential  $(\phi)$  contours for all runs. The initial density consists of a Gaussian bump with a full width at half maximum (FWHM) of 146 m, ranging from  $8 \times 10^9$  ${\rm m}^{-3}$  to  $1.2 \times 10^{10}~{\rm m}^{-3}$ . The bump is uniformly perturbed by a single period of the function  $z(x) = -z_0 \sin(2\pi x/L_x)$ , where  $z_0 = 32$  m and  $L_x = 512$  m. This serves to mimic a large-scale wave seeding the system. The results presented here show density and electrostatic potential shifted vertically by  $N_z/2$  because the interesting dynamics develop along the positive vertical density gradient and in the density trough. The electrostatic potential results from solving equation 4.3; its shape is determined by density gradients (second term in the RHS of equation 4.3), and the relative drifts of electrons and ions (first and third terms in the RHS of equation 4.3). The density gradients lead to ambipolar electric fields that add to or subtract from the vertical polarization electric field. The shape of the large-scale seed wave creates a zonal polarization that modifies ion and electron drifts to enforce  $\nabla \cdot \mathbf{J} = 0$ . The precise shape of  $\phi$  for each run depends on  $E_{0z}$ , but for the early stages of each run (i.e. before turbulence develops), all the runs appear similar.

Figure 4·2 shows the final  $\delta n/n_0$  for each run. In all panels, waves with wavelengths on the order of ten meters grow along the positive vertical density gradient. This result is consistent with local linear theory, which predicts that gradient-drift waves will grow when  $\mathbf{E}_0 \cdot \nabla n > 0$ . The most obvious difference among these three figures is the increasing growth of small-scale density perturbations in the central density trough with increasing  $E_{0z}$ . Here, "small-scale" implies perturbations on the order of a few meters as opposed to both the ubiquitous tens-of-meter gradient-drift

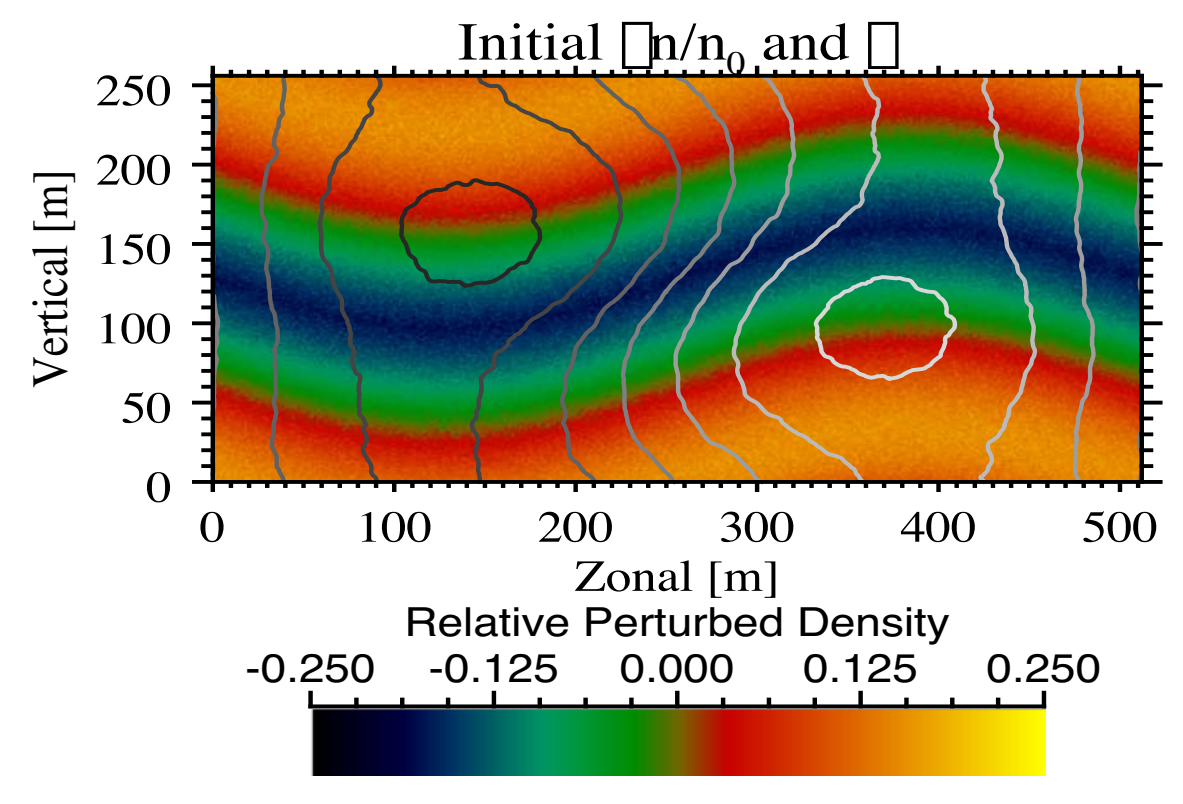


**Figure 4.1:** Initial configurations of relative perturbed density  $(\delta n/n_0$ ; color) and electrostatic potential  $(\phi)$ ; contours). The initial density consists of a Gaussian bump centered at z=128 m and modulated by a 512-m wave. The electrostatic potential is the result of solving equation 4.3 at the first time step.

waves that grow along the positive vertical density gradient and the 512-m seed wave. Movies included as supplemental information show the evolution of relative perturbed density for each simulation run.

Figure 4·3 shows the final total electric-field magnitude  $(E_T = |\mathbf{E}_0 - \nabla \phi|)$  in grayscale for each run, with contours of electrostatic potential  $(\phi)$  overlaid in color. The grayscale range is the same for all plots and spans 0 to twice  $E_c \approx 11.2 \text{ mV/m}$ . The color contours span  $\pm \max(|\phi|)$ , with the  $+\max(|\phi|)$  in red and  $-\max(|\phi|)$  in blue; the actual values are  $\max(|\phi|) = 0.28 \text{ V}$  for  $E_{0z} = 6 \text{ mV/m}$ ,  $\max(|\phi|) = 0.45 \text{ V}$  for  $E_{0z} = 9 \text{ mV/m}$ , and  $\max(|\phi|) = 0.54 \text{ V}$  for  $E_{0z} = 12 \text{ mV/m}$ . In all three runs, the electric field peaks near the center of the simulation domain, within the density trough, coincident with small-scale wave growth in the  $E_{0z} = 9 \text{ mV/m}$  and 12 mV/m runs. Although the peak value of  $E_T$  changes with different values of  $E_{0z}$ , the shape of  $\phi$  determines the location of the peak. The exact values of  $\phi$  depend on  $\mathbf{E}_0$  via the ion and electron drifts, so the overall shape differs among runs, but the location of the peak in  $-\nabla \phi$  lies in roughly the same place for all three runs. This suggests that the large-scale density configuration plays a more important role in determining the peak location than do the relative drifts.

When FB irregularities develop for  $E_{0z} = 9$  mV/m and 12 mV/m, they develop in the center of the simulation, in the density trough at the western edge of the upper large-scale density wave. In this region,  $-\nabla \phi$  has its greatest magnitude and points from lower-right to upper-left. Note that, due to periodic boundary conditions, the right edge of the simulation box wraps around to the left edge. Shifting the domain zonally (x direction) by 256 m would represent a reversal of the perturbing sine wave that effectively places the density trough at the *eastern* edge of center. In that way, these runs also account for the case in which the large-scale density wave is reversed.

Figure 4.4 shows the average total electric field within a 64 m  $\times$  64 m box in the

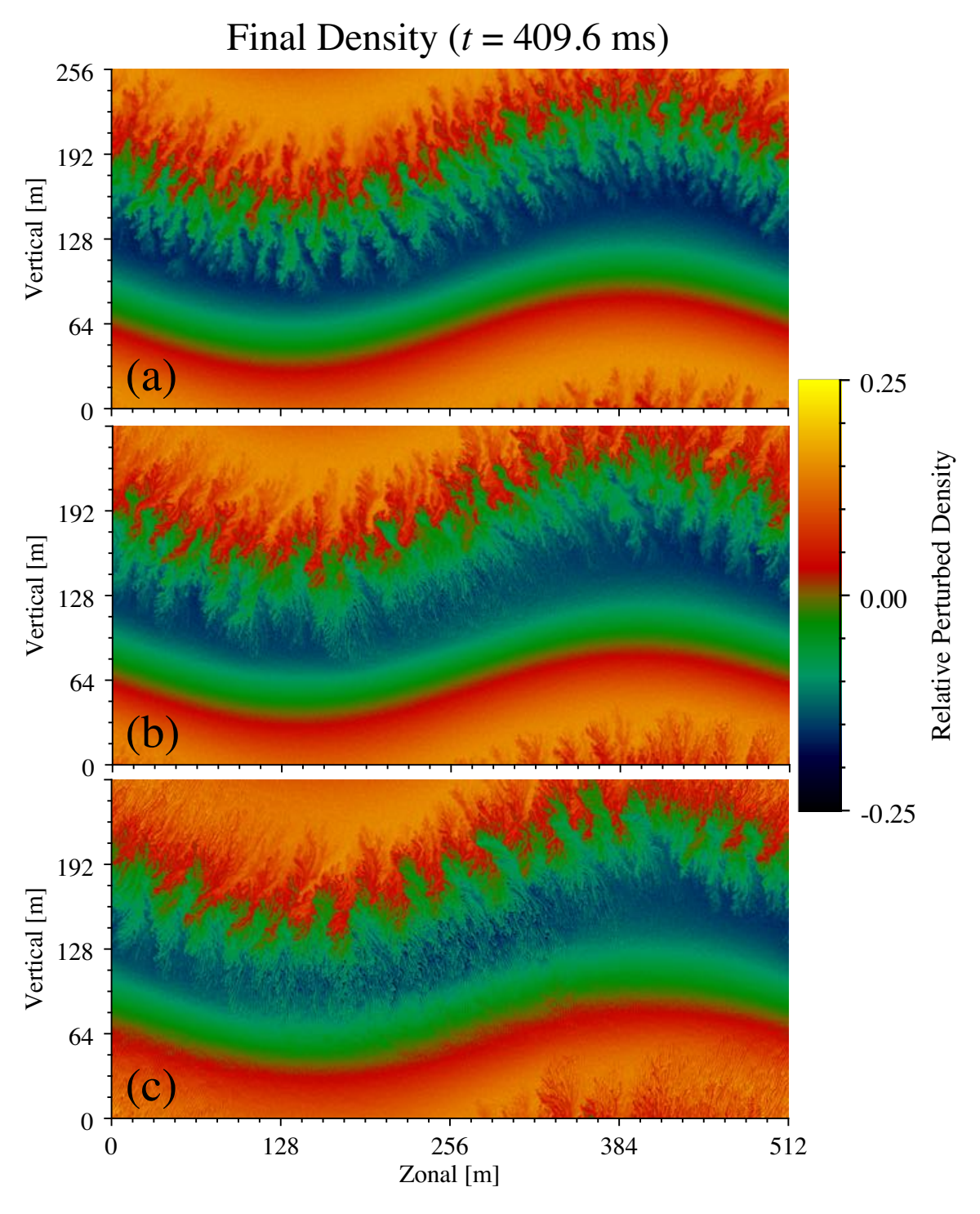


Figure 4.2: Final relative perturbed density for each run: (a)  $E_{0z} = 6$  mV/m, (b)  $E_{0z} = 9$  mV/m, (c)  $E_{0z} = 12$  mV/m. In all runs, gradient-drift instability develops along the positive vertical gradient. For  $E_{0z} = 9$  mV/m and 12 mV/m, Farley-Buneman instability develops in the central density trough, with faster growth for  $E_{0z} = 12$  mV/m.

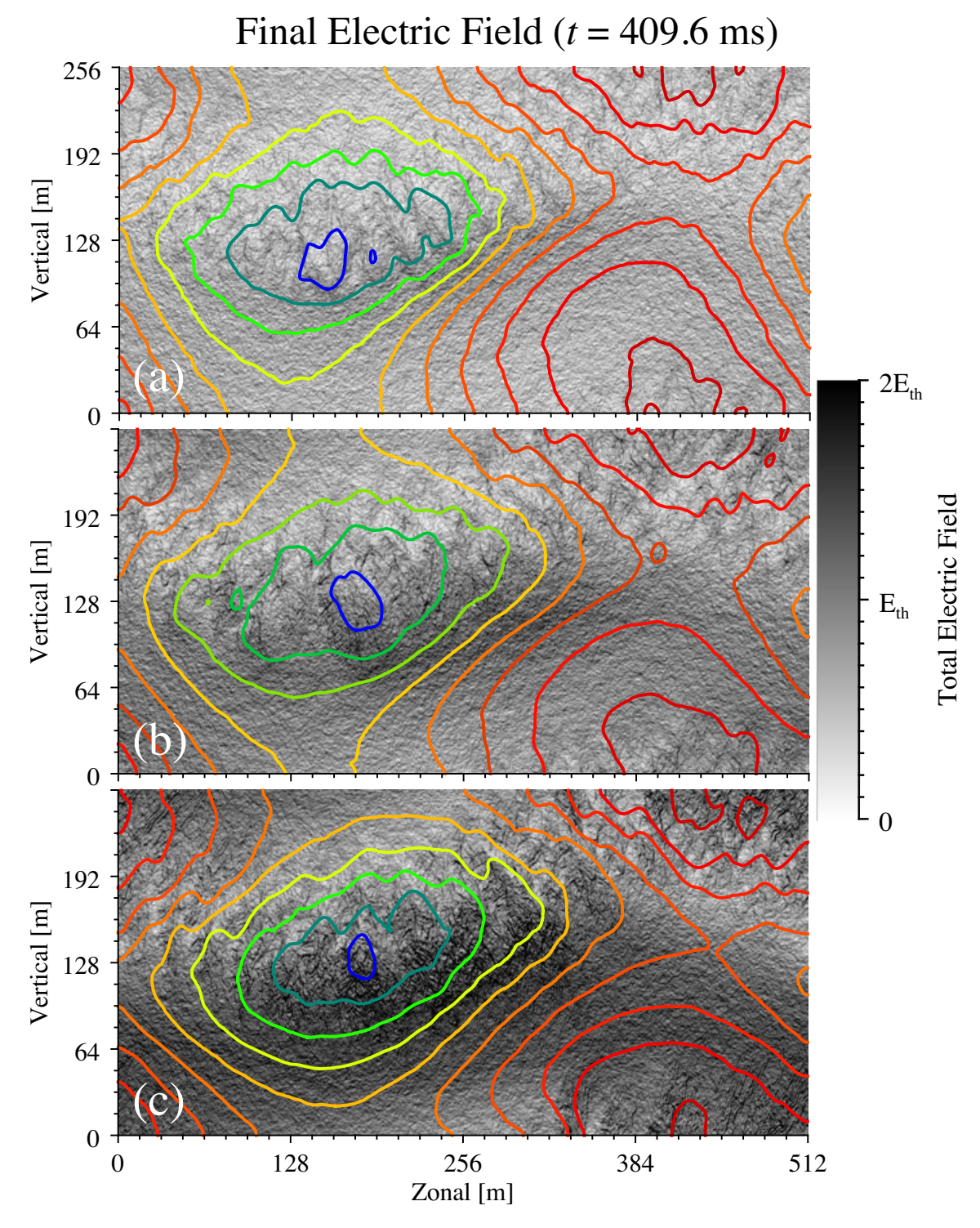
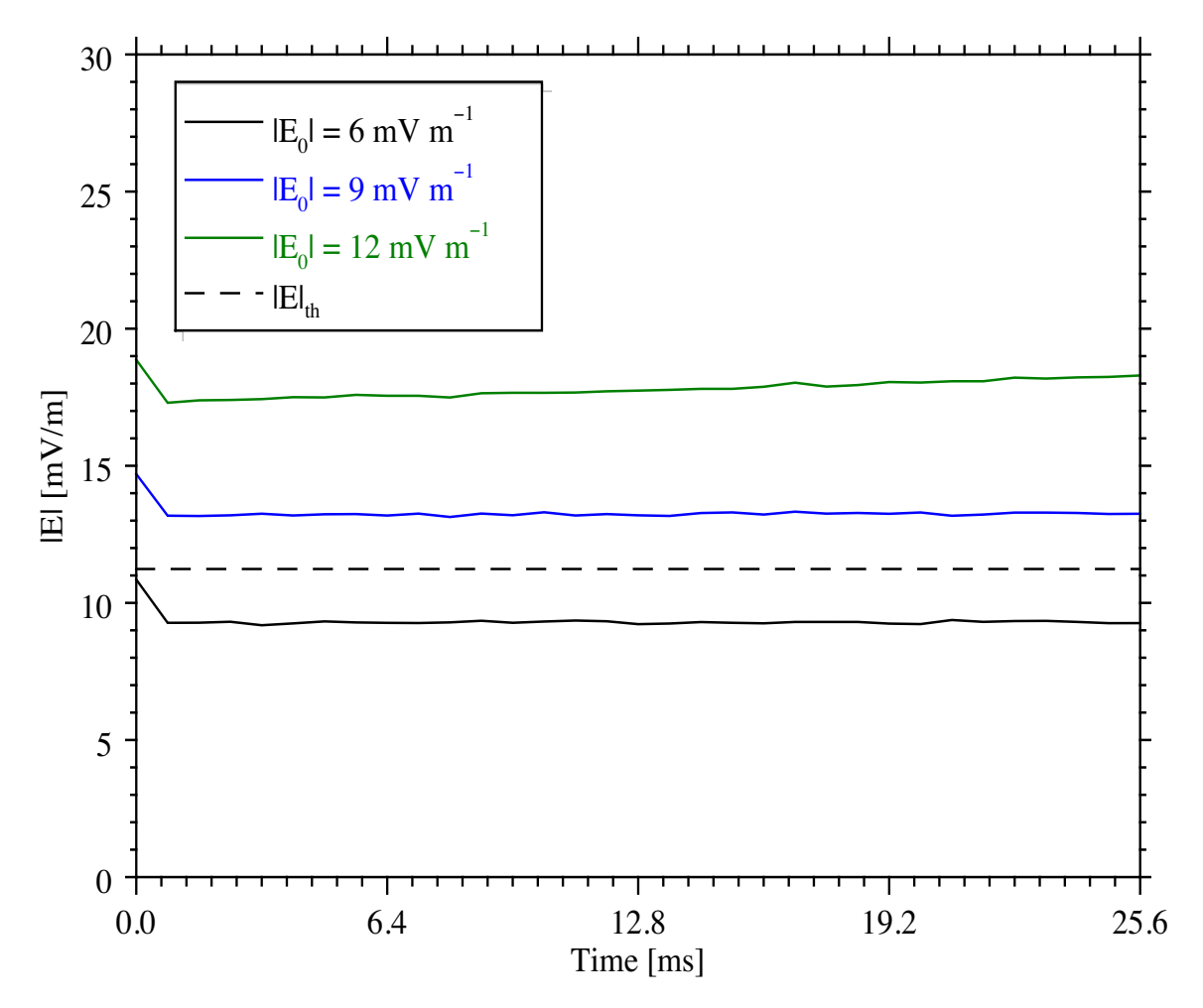


Figure 4.3: Final total electric field (grayscale) and potential (color contours) for each run: (a)  $E_{0z}=6$  mV/m, (b)  $E_{0z}=9$  mV/m, (c)  $E_{0z}=12$  mV/m. The grayscale bar shows values in multiples of the threshold electric field for Farley-Buneman instability,  $E_c\approx 11.2$  mV/m. In all runs, the total electric field peaks in the central density trough. For  $E_{0z}=9$  mV/m and 12 mV/m, the total electric field is well above  $E_c$ . The contours span  $\pm \max(|\phi|)$ , red to blue, where  $\max(|\phi|)$  is (a) 0.28 V, (b) 0.45 V, (c) 0.54 V.

center of the simulation domain as a function of time for the first 25.6 ms of each run. This box captures the area where  $|\nabla\phi|$ , and thus  $E_T$ , is greatest during the beginning of each run. The initial drop in average electric field is an artifact of start-up. The plot shows that  $E_T < E_c$  for the  $E_{0z} = 6$  mV/m run whereas  $E_T > E_c$  for both the  $E_{0z} = 9$  mV/m and  $E_{0z} = 12$  mV/m runs. Note that  $E_T$  is still growing at 25.6 ms in the  $E_{0z} = 12$  mV/m run whereas it levels off almost immediately in the other two runs. The direction of  $E_T$  for each run, which is given by the counterclockwise angle from  $+\hat{x}$  (i.e.  $\tan^{-1}(E_y/E_x)$ ) and is nearly constant over the time span of Figure 4·4, is  $101^{\circ}$  (6 mV/m),  $107^{\circ}$  (9 mV/m), and  $107^{\circ}$  (12 mV/m). Thus a super-threshold total electric field arises very quickly in the density trough along the rising edge of the density wave for  $E_{0z} > 9$  mV/m, causing electrons in that region to  $\mathbf{E} \times \mathbf{B}_0$  drift at super-threshold speeds at approximately 17° from purely westward, thereby triggering FB turbulence in the density trough.

#### 4.4.2 Spectra

This section presents results from a spectral analysis of each run, at three wavelengths: 3, 8, and 2 m. The first wavelength corresponds to what the 50-MHz radar at Jicamarca should observe via coherent back scatter. The second wavelength represents Type-II irregularities driven directly by the 512-m initial density perturbation and is near the wavelength observed by Patra et al. (2005) with the 18-MHz radar at Trivandrum, India. The third wavelength corresponds to peak growth of Type-I turbulence due to pure FB instability in the 9-mV/m and 12-mV/m runs. Although this wavelength does not lend itself immediately to comparison with observations (the authors are not aware of a 75-MHz E-region radar), it is an interesting case because it represents the combined growth of Type-I and Type-II irregularities. Though all simulations show characteristics of Type-II irregularities at all wavelengths, the 12-mV/m run develops a primary high-speed population of Type-I irregularities at



**Figure 4.4:** Average electric-field magnitude in the central  $64 \times 64$  m for the first 25.6 ms. For  $E_{0z} = 6$  mV/m (black trace), the average electric field does not rise above the threshold for Farley-Buneman instability, whereas it does for  $E_{0z} = 9$  mV/m and 12 mV/m (blue and green traces).

2 m and a secondary high-speed population at 3 m. The end of this section briefly discusses these high-speed populations.

Figure 4.5 shows the normalized spectral power as a function of LoS angle,  $\theta$ , (counterclockwise from  $+\hat{x}$ ) and phase velocity,  $V_{ph} = \omega/k$ , for 3-m waves. The color in panel (a) shows the spectral power normalized to the peak value at each angle for the  $E_{0z} = 6$  mV/m run and the white line indicates the mean phase velocity,  $\langle V_{ph} \rangle$ . Panel (d) shows spectral width,  $\Delta V_{ph}$  (i.e. FWHM), for the same run. Panels (b) and (e) show the same quantities for the  $E_{0z} = 9$  mV/m run, and panels (c) and (f) show those quantities for the  $E_{0z} = 12$  mV/m run. In all runs, the mean phase velocity varies approximately as  $\langle V_{ph} \rangle \sim -E_{0z} \cos \theta$ . For  $E_{0z} = 6$  mV/m,  $-0.5C_s \lesssim \langle V_{ph} \rangle \lesssim 0.5C_s$ ; for  $E_{0z} = 9$  mV/m,  $-0.7C_s \lesssim \langle V_{ph} \rangle \lesssim 0.7C_s$ ; and for  $E_{0z} = 12$  mV/m,  $-0.9C_s \lesssim \langle V_{ph} \rangle \lesssim 0.9C_s$ . The spectral width approximately equals  $\langle V_{ph} \rangle$  near  $\theta = 0^{\circ}$  and  $\theta = 180^{\circ}$ , and increases as  $\theta$  approaches  $90^{\circ}$ .

Figure 4.6 shows the normalized spectral power as a function of angle for 8-m waves, with panels corresponding to the same quantities as in Figure 4.5. The trends are similar to those of 3-m waves:  $\langle V_{ph} \rangle \sim -E_{0z} \cos \theta$ ,  $\Delta V_{ph} \approx \langle V_{ph} \rangle$  near  $\theta = 0^{\circ}$  and  $\theta = 180^{\circ}$ , and  $\Delta V_{ph}$  increases as  $\theta$  approaches 90°. For  $E_{0z} = 6$  mV/m,  $-0.4C_s \lesssim \langle V_{ph} \rangle \lesssim 0.4C_s$ ; for  $E_{0z} = 9$  mV/m,  $-0.5C_s \lesssim \langle V_{ph} \rangle \lesssim 0.6C_s$ ; and for  $E_{0z} = 12$  mV/m,  $-0.8C_s \lesssim \langle V_{ph} \rangle \lesssim 0.7C_s$ .

The fact that  $\langle V_{ph} \rangle < V_{e0}/(1+\psi_{\perp})$  when  $\theta=0^{\circ}$  in Figures 4.5 and 4.6 represents a departure from linear theory (equation 4.2a). A likely explanation for the relatively low mean phase velocities is that the simulated observer with LoS at  $\theta$  sees a mix of linearly growing waves and nonlinear turbulence, including mode coupling and wave broadening effects. A full description of the turbulent state of combined FBI/GDI is beyond the scope of this chapter; instead, the authors refer the reader to St.-Maurice and Hamza (2001), Drexler et al. (2002), and references therein. Regardless of the

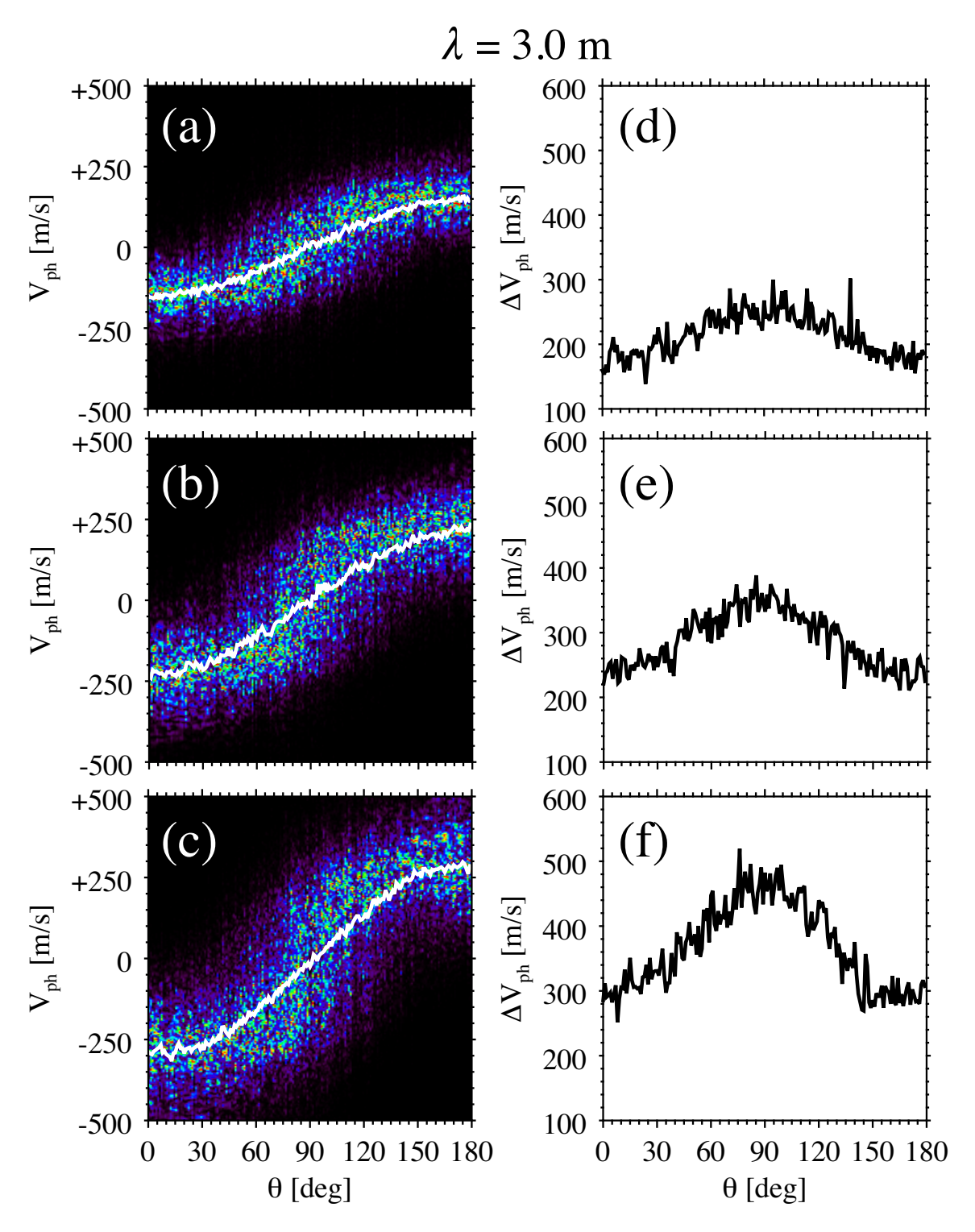
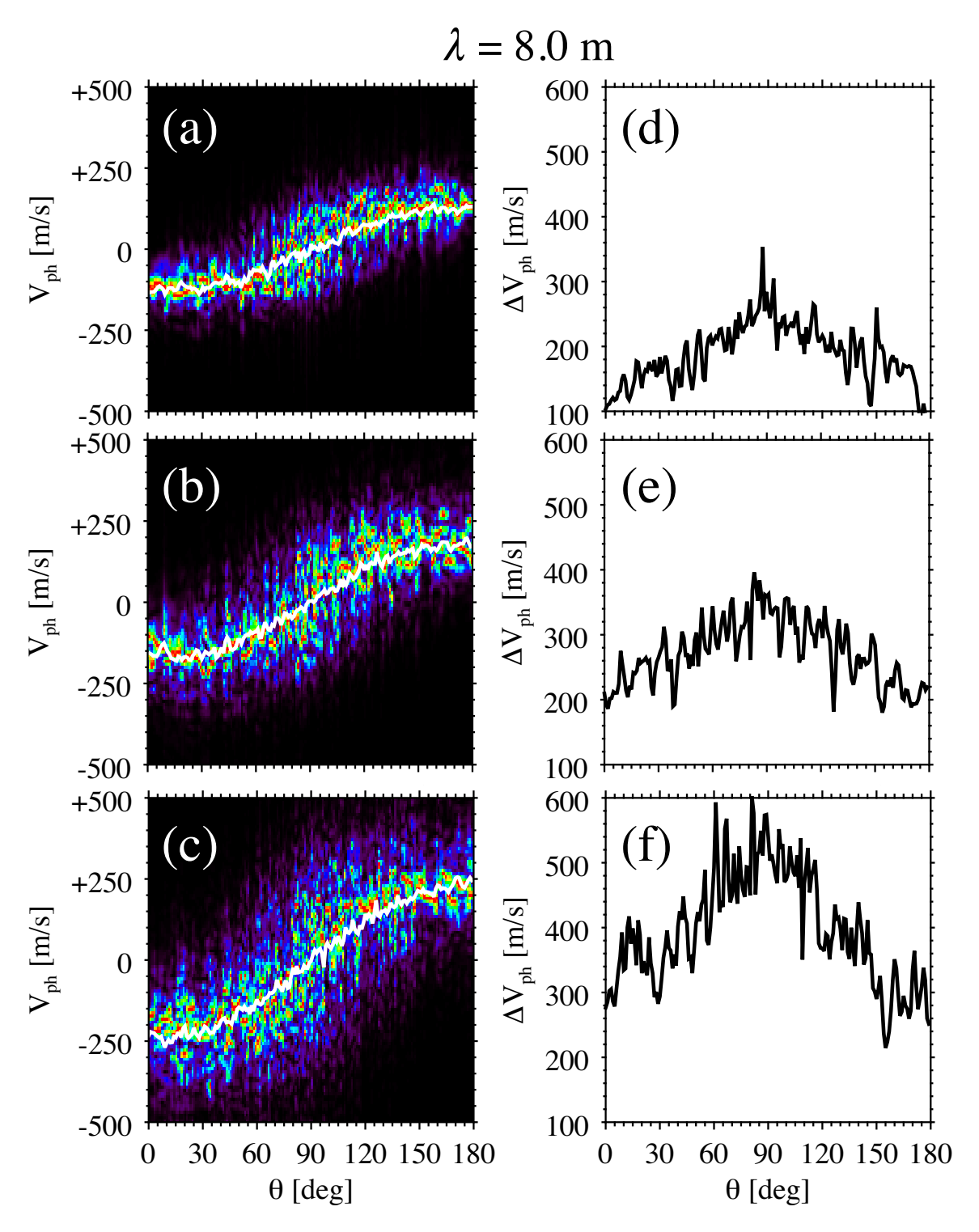


Figure 4.5: Spectral power and width at 3 m as a function of phase velocity  $(V_{ph})$  and angle from  $+\hat{x}$ , (i.e.  $\mathbf{E}_0 \times \mathbf{B}_0$ ): (a) & (d)  $E_{0z} = 6$  mV/m, (b) & (e)  $E_{0z} = 9$  mV/m, (c) & (f)  $E_{0z} = 12$  mV/m. The white line in (a)-(c) shows the mean phase velocity and the sign convention is such that negative velocities imply waves traveling away from an observer with line-of-sight  $\theta$ .



**Figure 4.6:** Spectral power and width at 8 m as a function of phase velocity  $(V_{ph})$  and angle from  $+\hat{x}$ . See description of Figure 4.5 for individual panels.

nonlinear mechanisms at work, turbulent perturbations should not travel significantly faster than the linear phase velocity predicted by equation 4.2a, so any contributions from nonlinear effects only act to decrease the mean value.

The fact that  $\langle V_{ph} \rangle$  differs in magnitude between 3-m and 8-m waves represents an additional departure from linear theory, which predicts a phase velocity independent of wavelength. This is not surprising, since Figure 4·2 clearly shows a turbulent system. The trend toward lower peak  $\langle V_{ph} \rangle$  continues to longer wavelengths (not shown), suggesting that as waves grow to the scale size of the gradient, they interact directly with the slowly moving large-scale wave rather than propagating perpendicular to the local gradient. This non-local interaction slows waves as a function of wavelength.

Figure 4·7 shows the normalized spectral power as a function of angle for 2-m waves, again in the style of Figure 4·5. These waves differ substantially from 3-m and 8-m waves in that, for  $E_{0z} = 12 \text{ mV/m}$ , the spectral-power distribution in panel (c) skews toward  $V_{ph} \approx -425 \text{ m/s}$  for  $\theta \in [0^{\circ}, 30^{\circ}]$ . Beyond  $\theta = 30^{\circ}$ ,  $\langle V_{ph} \rangle$  increases linearly until  $\theta \approx 150^{\circ}$ , at which point it is nearly constant over  $\theta \in [150^{\circ}, 180^{\circ}]$ . Likewise, panel (f) shows that  $\Delta V_{ph}$  is not symmetric about  $\theta = 90^{\circ}$ , with the steeper slope for  $0 < \theta < 90$  caused by the fact that the spectral-power distribution skews toward the narrow high-speed component up to  $\theta \approx 30^{\circ}$ . The next paragraph further discusses the asymmetric behavior of 2-m waves in this simulation.

Figure 4.8 illustrates the asymmetry in Figure 4.7: Panel (a) shows the spectral power in 2-m waves for each run, at  $\theta = 15^{\circ}$ , averaged over a 2-degree beam. The angle  $\theta = 15^{\circ}$  corresponds to roughly the direction of  $\mathbf{E} \times \mathbf{B}_0$  in the central density trough, where  $\mathbf{E}$  is the total electric field (cf. the discussion of Figure 4.4 in §4.4.1). Each curve was normalized to the peak power of the 12-mV/m curve. Note that the horizontal axis is not symmetric about  $V_{ph} = 0$  m/s. The relative amplitudes

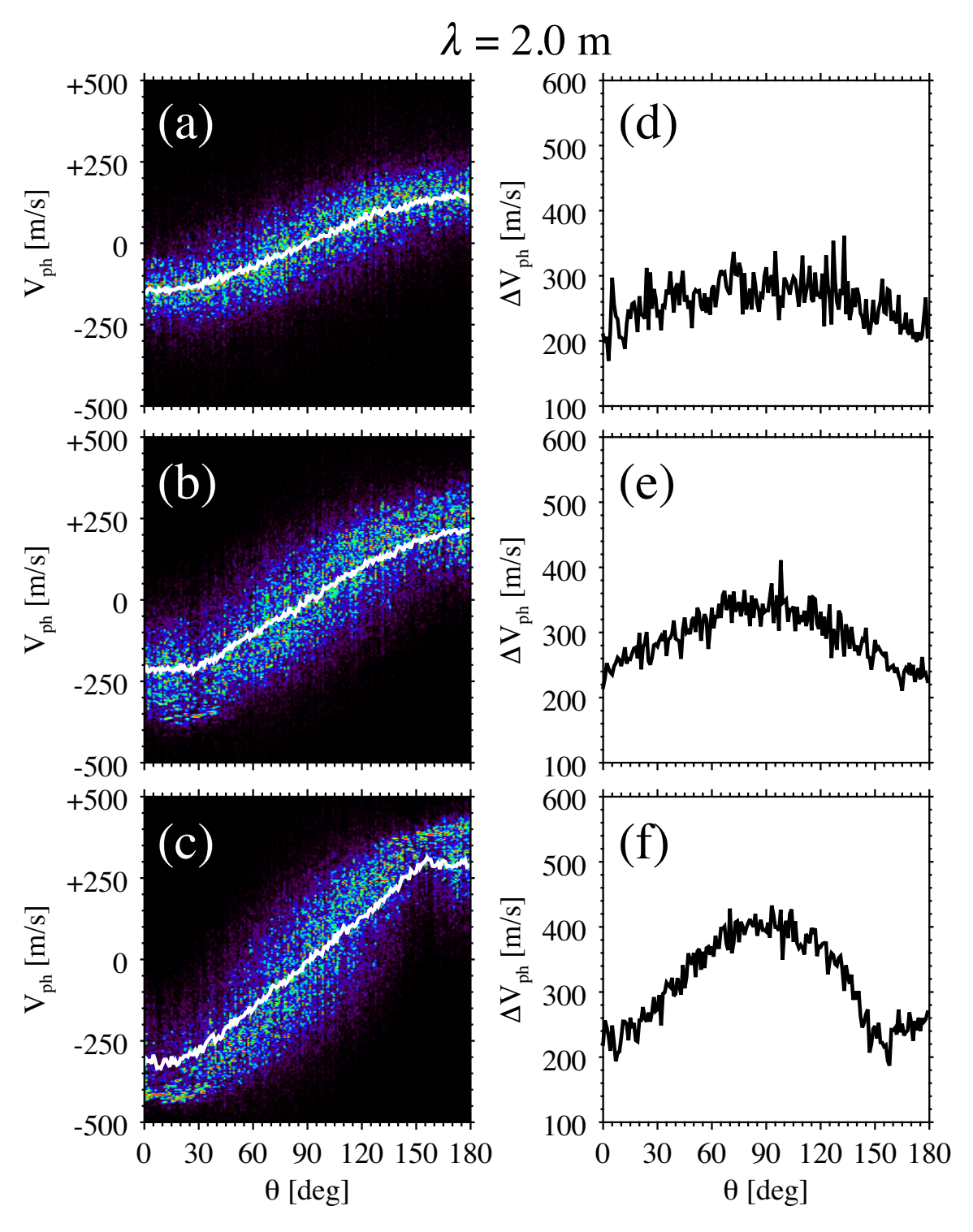


**Figure 4.7:** Spectral power and width at 2 m as a function of phase velocity  $(V_{ph})$  and angle from  $+\hat{x}$ . See description of Figure 4.5 for individual panels.

of 2-m waves in the 6-mV/m and 9-mV/m runs are less than 10% of the 12-mV/m run and the skewed shape of the 12-mV/m run is clear. Unlike the broad spectra in the 6-mV/m and 9-mV/m runs, the 12-mV/m run generates a broad component centered near -300 m/s and a narrow component centered near -425 m/s. Panel (b) shows the spectral power of 2-m, 3-m, and 8-m waves for the 12-mV/m run. The 8-m curve is broad and nearly symmetric, but the 2-m and 3-m curves show an asymmetry that is not clear in Figure 4.5, namely, an inflection point near 400 m/s. This suggests a second distribution with higher negative velocity. The high-speed 3m population may result from the locally enhanced electric field or it may result from mode coupling. Such mode coupling probably takes the form of an inverse cascade process (Oppenheim et al., 2008) in the region where the pure FB instability creates 2-m waves, but may also include contributions from a forward cascade process related to the gradient-drift instability. The growth of 2-m Type-I irregularities represents a parametric instability in which the large-scale seed wave drives meter-scale turbulence by enhancing the electric field. In a larger simulation (beyond the capabilities of the present simulator), we expect that a similar parametric instability could generate 3-m waves, as observed as Type-I echoes (Hysell et al., 2007).

# 4.5 Discussion

This section first describes similarities between simulation results and observations of coherent echoes reported in the literature, then connects results to a more general theory of coupled FBI/GDI growth than that presented in §4.2.

#### 4.5.1 Connection with observations

This work not only represents the first kinetic simulations of coupled FBI/GDI but also lends insight to observations of E-region plasma irregularities observed by radars.

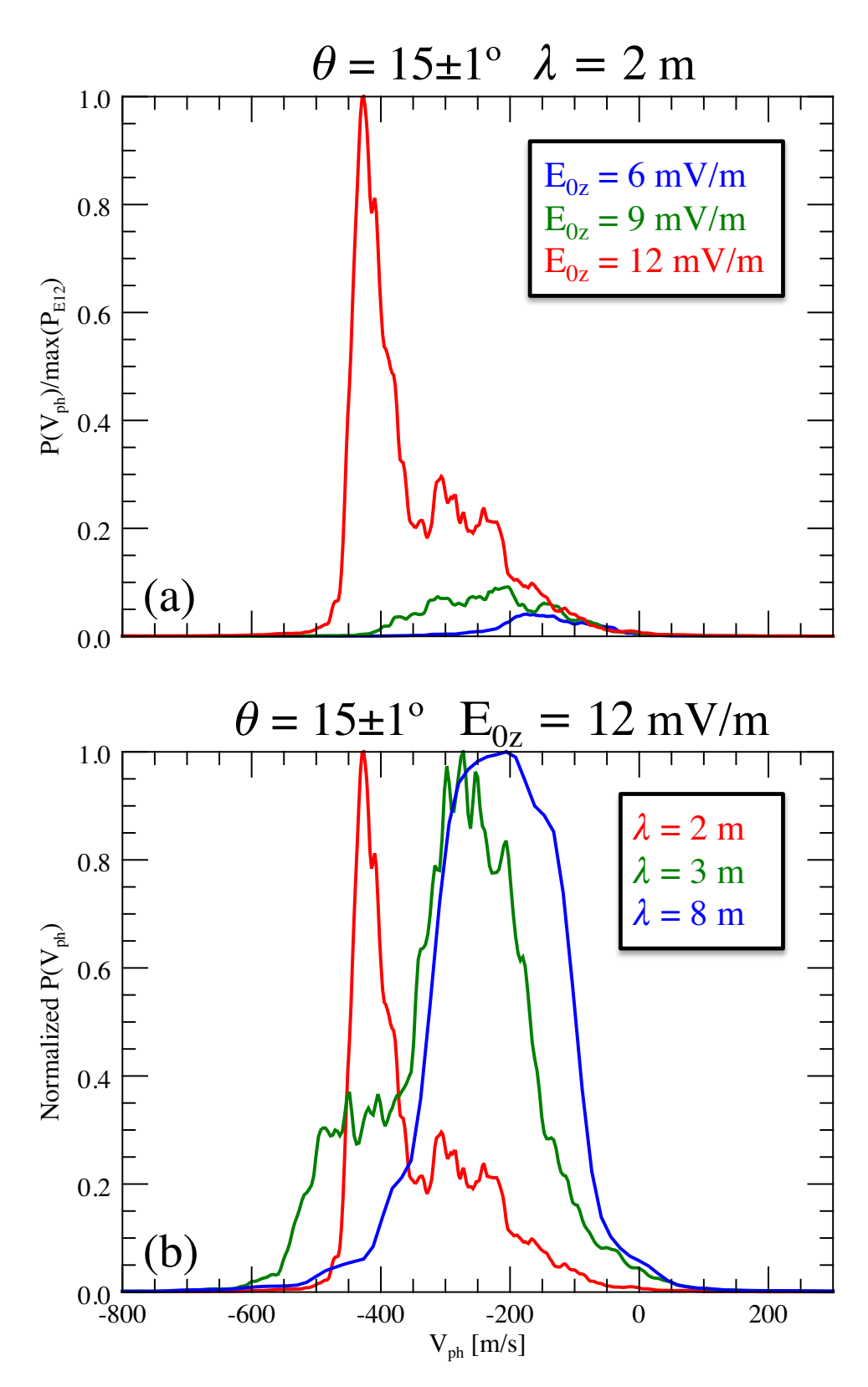


**Figure 4-8:** Phase-velocity spectra at  $\theta = 15^{\circ}$ : (a) Power in 2-m waves normalized to the spectrum of the 12-mV/m run; (b) Self-normalized power in 2-m, 3-m, and 8-m waves for the 12-mV/m run.

Patra et al. (2005) reported east-west asymmetries in Type II irregularities observed with an 18-MHz radar located near the magnetic equator, and attributed the asymmetry to the tilt in kilometer-scale primary waves at E-region altitudes. Hysell et al. (2007) connected east-west asymmetries with up-down Type I asymmetries observed with a 50-MHz radar and noted that the depleted phases (i.e. troughs) of kilometer-scale primary waves should have larger electric fields than the corresponding enhanced phases (i.e. crests), leading to observations of larger line-of-sight drifts and preponderance of Type I echoes in westward-aligned beams. The density results presented in Figure 4.2, while not directly comparable to kilometer-scale processes, are consistent with those observations and the total electric field results presented in Figure 4.3 account for the development of Type-I irregularities within the depleted region westward of a large-scale wave. In that region, the positions of density troughs and crests modifies the electrostatic potential in a manner that enhances the polarization electric field. This adds to the background and ambipolar electric fields within the density trough between the two large-scale density crests. These results also support the conclusion by Ronchi et al. (1991) that long wavelength activity affects the characteristics of short wavelength two-stream irregularities. In the work presented here, long wavelength activity creates the electrostatic potential field that drives short-wavelength two-stream irregularities within the density trough between long wavelength waves Sudan et al. (1973). It is worth noting again that Figure 4.7c shows a thin band of relatively high normalized power near  $V_{ph} \approx -425$  m/s for  $0^{\circ} < \theta < 30^{\circ}$ , suggesting that two-stream irregularities have a constant  $V_{ph}$  over this range. This result is consistent with early claims that the phase speed of Type-I irregularities is constant with zenith angle (Cohen and Bowles, 1967). Furthermore,  $\langle V_{ph} \rangle$  (the white line) never exceeds  $\pm C_s \approx 350$  m/s, suggesting that the mean phase speed saturates at  $C_s$ . This claim is also consistent with observations (Sudan, 1983).

### 4.5.2 Dispersion relation

An analysis of instability growth in these simulations must account for magnetized electrons and unmagnetized ions with arbitrary wavevector in the presence of a 2-D background gradient. Sudan et al. (1973) derived the two-fluid dispersion relation for an isothermal, electrostatic, quasi-neutral plasma with a strictly vertical background gradient and static horizontal background magnetic field. The appendix of Fejer et al. (1975b) shows the derivation of a similar two-fluid dispersion relation, allowing for plasma production and an arbitrary wavevector. Sudan (1983) developed a nonlinear theory of Type II irregularities from which he obtained a linear dispersion relation similar to that given by Sudan et al. (1973). Dimant and Oppenheim (2011b) derived a fluid dispersion relation for the combined FBI/GDI with arbitrary magnetization, gradients, and wavevector, including production and recombination effects. Makarevich (2016) presents a general dispersion relation for E- and F-region instabilities that makes no assumptions about altitude, wavevector, or background density gradient.

Equation A29 with equations A34 and A35 in Dimant and Oppenheim (2011b), under the additional assumptions  $k_{\parallel} = 0$  and  $\kappa_i \ll 1$ , yield a local linear growth rate appropriate to the present work:

$$\omega_i(\mathbf{k}) = \frac{\psi_{\perp}}{1 + \psi_{\perp}} \left[ \frac{1}{\nu_i} \left( \omega_r^2 - k^2 C_s^2 \right) - \frac{\Omega_e \left( \mathbf{k} \times \hat{b} \right) \cdot \mathbf{G}}{\nu_e k_{\perp}^2} \omega_r \right], \tag{4.4}$$

The symbols  $\psi_{\perp}$ ,  $\nu_{e}$ ,  $\Omega_{e}$ ,  $\omega_{r}$ , and  $C_{s}$  have the same meanings as in equations 4.2;  $\hat{b}$  is a unit vector parallel to the magnetic field  $(-\hat{y})$  in the present geometry) and  $\mathbf{G} \equiv n_{0}^{-1} \nabla n_{0}$ . Note that some of the notation used here differs from that used in Dimant and Oppenheim (2011b) for the sake of consistency.

Figure 4.9 shows  $\omega_i(\mathbf{k})$  from equation 4.4 evaluated numerically for 2-m, 3-m,

and 8-m waves propagating at  $\theta = 15^{\circ}$ , given the initial density and total electric field in each run. In the calculation of  $\omega_r(\mathbf{k})$  for  $\omega_i(\mathbf{k})$ ,  $\mathbf{V}_{e0}$  includes the Hall drift and the diamagnetic drift. Panels (a), (b), & (c) show that  $\omega_i(\mathbf{k})$  is non-positive everywhere for 2-m waves when  $E_{0z} = 6 \text{ mV/m}$ , and becomes increasingly positive with increasing  $E_{0z}$ , as expected. The location of  $\omega_i(\mathbf{k}) > 0$  is not exactly cospatial with the peak in FB irregularities in Figure 4-2c, which coincide with a more localized region centered on the peak in  $E_T$ . The reason is two-fold: First, 2-m waves develop quickly along the entire positive vertical density gradient of the background wave and are less severely damped near the central trough than longer-wavelength waves. Nonlinear wave interaction along the density gradient produces cascading features composed of a range of wavelengths from a few to tens of meters, effectively washing out the 2-m waves. Second, the preceding fluid analysis does not capture the fact that the kinetic FB growth rate peaks at a few meters. In the region of enhanced electric field, the true growth rate (i.e. including kinetic effects) will be higher for waves with wavelengths of a few meters.

There are also trends for fixed  $E_{0z}$  and varying wavelength. Panels (a), (d), & (g) show that, in the run with  $E_{0z} = 6 \text{ mV/m}$ ,  $\omega_i(\lambda = 8 \text{ m}) > \omega_i(\lambda = 3 \text{ m}) > \omega_i(\lambda = 2 \text{ m})$  with  $\omega_i(\lambda = 2 \text{ m}) \leq 0$ . This is consistent with Figure 4·2a, in which long-wavelength gradient-drift turbulence grows along the positive vertical density gradient of the background wave. For  $E_{0z} = 9 \text{ mV/m}$ , panels (b), (e), & (h) show that  $\omega_i(\lambda = 8 \text{ m}) \approx \omega_i(\lambda = 3 \text{ m}) \approx \omega_i(\lambda = 2 \text{ m}) > 0$  along the positive gradient near the central region but  $\omega_i(\lambda = 8 \text{ m}) > \omega_i(\lambda = 3 \text{ m}) > \omega_i(\lambda = 2 \text{ m}) \approx 0$  away from the center. This is consistent with the increased growth of meter-scale waves in the central region and the predominance of longer wavelengths near the edges, but does not exactly predict the smallest-scale wave growth in the central trough for the reasons described above. For  $E_{0z} = 12 \text{ mV/m}$ , panels (c), (f), & (i) show

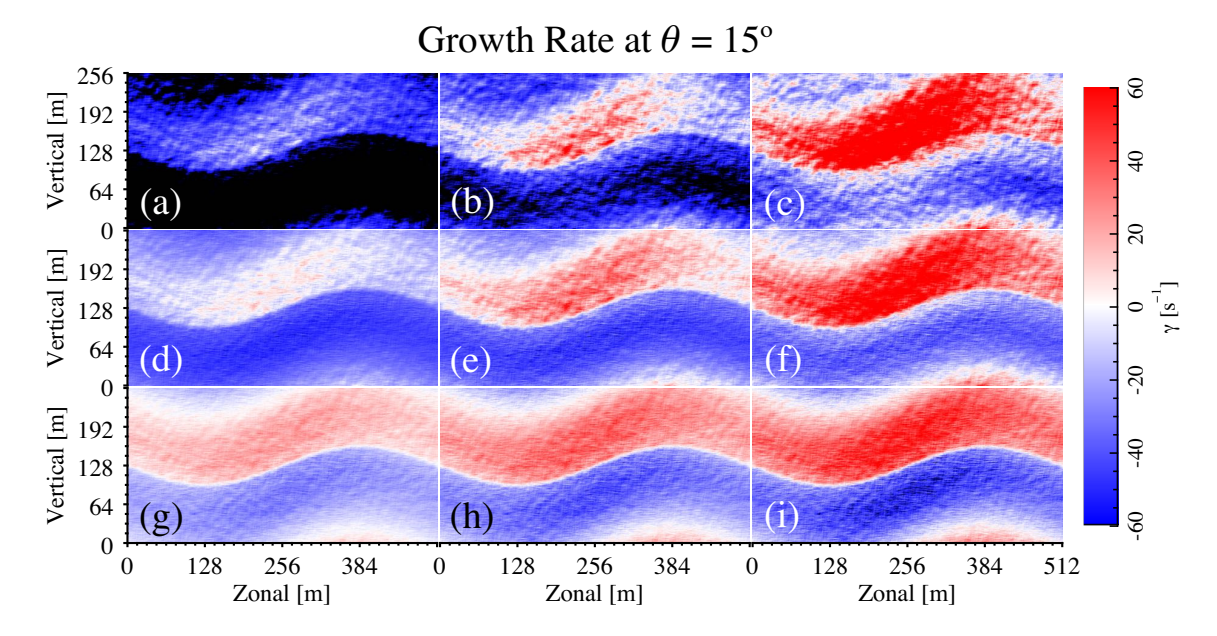


Figure 4.9: Local linear growth from equation 4.4 for waves traveling at  $\theta = 15^{\circ}$  from  $+\hat{x}$ . Rows (top to bottom):  $\lambda = 2$  m,  $\lambda = 3$  m, and  $\lambda = 8$  m. Columns (left to right):  $E_{0z} = 6$  mV/m,  $E_{0z} = 9$  mV/m, and  $E_{0z} = 12$  mV/m.

that  $\omega_i(\lambda = 2 \text{ m}) > \omega_i(\lambda = 3 \text{ m}) > \omega_i(\lambda = 8 \text{ m}) > 0$  along the positive gradient. Again, the prediction made by the fluid growth rate is consistent with wave growth along the positive density gradient but does not predict meter-scale FB turbulence in the central trough. The reader may benefit from comparing Figure 4.9 to the supplemental movies of relative perturbed density for each simulation run.

# 4.6 Conclusion

This chapter presents a novel parallelized hybrid quasi-neutral plasma simulation designed to simulate E-region turbulence. The numerical model treats ions as particles via a PIC method while treating electrons as an inertialess thermal fluid, which precludes the need for an artificially large electron-to-ion mass ratio. The model does not keep track of a distribution of electrons. Therefore, it cannot capture kinetic effects of electron wave-particle coupling but does not need to resolve the Debye

length or the inverse plasma frequency. It does not currently include electron thermal physics, but future versions will. The chief advantage of this simulation is that it is well suited to studying meter- and decameter-scale turbulence in the presence of hundred-meter- to kilometer-scale density waves. The results of this work represent the first simulations of the coupled Farley-Buneman/gradient-drift instability in the equatorial E-region ionosphere. While the simulations presented here span only 512 m  $\times$  256 m, they attempt to reproduce VHF radar observations of backscatter from meter-scale density irregularities in the presence of background waves that span a few kilometers. This work also introduces an electrostatic potential solver that uses algebraic multigrid to precondition an iterative method capable of handling the large off-diagonal elements caused by electron magnetization.

#### The main results are:

- Simulations with zeroth-order vertical electric fields of 6 mV/m, 9 mV/m, and 12 mV/m produce gradient-drift turbulence in regions that satisfy the linear condition for instability.
- 2. The total electric field in the density minimum is large enough to drive Farley-Buneman turbulence even when the zeroth-order vertical field is below the turbulent threshold.
- 3. Waves develop in all runs and travel westward along the background positive density gradient with phase velocities below the plasma acoustic speed.
- 4. Wave power spectra of 2-m, 3-m, and 8-m waves show characteristics of Type-II irregularities in all runs.
- 5. When the background electric field is 12 mV/m, wave spectra at 15° from  $\mathbf{E}_0 \times \mathbf{B}_0$  show a distinct Type-I population at 2 m and a secondary Type-I-like population at 3 m.

6. The Type-I population has roughly constant phase velocity over a 30° range in LoS angle and the mean phase velocity peaks at the plasma acoustic speed.

The results of this hybrid simulation can be used to interpret radar observations of meter-scale density irregularities propagating with a vertical component and an east-west asymmetry. The east-west asymmetry arises as a combination of the density gradients introduced by the background density wave and the electron-drift effects caused by the total electric field and ambient magnetic field in the background density minima, embodied in the quasi-neutral electrostatic potential equation. The presence of density crests and troughs produces a polarization electric field that adds to the background and ambipolar electric fields, driving FB turbulence.

# Chapter 5

# Secondary Farley-Buneman Instability Driven by a Kilometer-Scale Primary Wave: Anomalous Transport and Formation of Flat-Topped Electric Fields.

# 5.1 Introduction

Chapter 4 and Young et al. (2017) presented numerical simulation results showing the coupled growth of FBI and GDI in a plasma characteristic of the equatorial E-region at 100 km altitude during daytime. Those results demonstrate the interplay between both instabilities in the presence of ionization gradients and a background electric field, as well as how a large-scale density perturbation can create a polarization electric field that drives the total electric field above the threshold for FBI.

Although Young et al. (2017) showed that the same zeroth-order plasma attributes (e.g., large-scale wave, background fields, and charged-neutral collision frequencies) can produce spectra exhibiting both types of irregularities defined by early researchers, it did not fully explain observations of meter-scale irregularities presumably produced by secondary FBI in the presence of kilometer-scale primary GDI waves (Hysell et al., 2007). Sudan et al. (1973) proposed a theoretical mechanism for generating meter-scale waves from kilometer-scale GDI waves, via excitation of secondary GDI and FBI in the frame of the primary wave. Kudeki et al. (1982) demonstrated the clear presence in Jicamarca data of kilometer-scale structures despite

the fact that the Jicamarca 50-MHz radar observes only 3-m waves. Those authors showed that it is not unreasonable to observe east-west drift velocities much smaller than the ion acoustic velocity while simultaneously observing vertically propagating type I echoes. They also discussed how the linear theory differs for long wavelength waves.

Rocket observations by Pfaff et al. (1987b) showed density irregularities around 103-106 km in altitude consistent with vertically propagating 2- to 3-m FBI waves driven by a large-scale wave electric field. They found that their in situ observations were consistent with both the Sudan et al. (1973) theory and concurrent ground-based observations with the Jicamarca 50-MHz radar. Kinetic simulations and a simplified fluid simulation by Oppenheim (1997) demonstrated how wave-driven currents from the FBI can modify large-scale GDI and reproduce the in-situ electric fields measured by Pfaff et al. (1987b). Two-fluid simulations by Ronchi et al. (1991) produced evidence that the electric fields in kilometer-scale waves dominates meter-scale dynamics so that the 3-m waves observed in radar backscatter experiments essentially trace out the kilometer-scale dynamics.

This chapter presents results from a numerical simulation of E-region plasma in which a primary 1024-m wave, meant to mimic a single GDI wave, gives rise to secondary FBI waves with wavelengths of a few meters. The meter-scale waves drive a non-linear plasma transport that significantly reduces the large-scale wave electric field. The presentation proceeds as follows: Section 5.2 outlines the linear local theory relevant to the FBI and GDI, Section 5.3 describes the numerical model underlying the simulations, Section 5.4 shows results from the simulations, Section 5.5 discusses the physical implications of the simulation results and their connections to observations, and Section 5.6 concludes the chapter.

# 5.2 Theory

The FBI and GDI are collisional electrostatic plasma instabilities that propagate nearly perpendicular to the background magnetic field. The FBI, also called the modified two-stream instability, derives its free energy from the increased ion inertia that results when electrons stream through ion density perturbations faster than the local plasma acoustic speed. At subsonic electron drift speeds, ion thermal pressure smooths out any localized density perturbations; above a critical threshold drift speed, ion inertia imparted by the streaming electrons overcomes thermal pressure and causes density perturbations to steepen. See Dimant and Sudan (1995c) for a more detailed description of the physical nature of the FBI.

The GDI derives its free energy from the presence of density gradients aligned with the ambient electric field. In the frame of a naturally occurring density perturbation, the polarization electric field,  $\delta \mathbf{E}$ , points parallel or antiparallel to the direction of propagation, depending upon whether the relative perturbed density,  $\delta n/n_0$ , is positive or negative. The presence of the magnetic field,  $\mathbf{B}_0$ , causes plasma in wave crests to  $\delta \mathbf{E} \times \mathbf{B}_0$  drift into regions of lower background density while plasma in wave troughs drifts into regions of higher background density. Both processes lead to an increase in the magnitude of  $\delta n/n_0$ , producing the instability. See, for example, Section 2 of Dimant and Sudan (1997) for a more detailed description of the physical nature of the GDI.

These two instabilities arise in collisional E-region plasmas and their threshold criteria – a supersonic electron drift for the FBI and a gradient parallel to the ambient electric field for the GDI – can easily occur in the same plasma volume. The standard linear analysis of the combined FBI/GDI assumes a quasineutral, isothermal plasma with inertialess, magnetized electrons and collisionally demagnetized ions. In keeping with standard development of FBI/GDI theory, this work will employ the

magnetization parameter for species j,  $\kappa_j \equiv \Omega_j/\nu_j$ , where  $\Omega_j$  is the absolute value of the cyclotron frequency and  $\nu_j$  is the average frequency of collisions with neutral particles. The assumptions on electron and ion magnetization in the E-region ionosphere correspond to  $\kappa_e \gg 1$  and  $\kappa_i < 1$ .

Linearizing the continuity and momentum equations for electrons and a single species of ions, both subject to the above assumptions and in the presence of a vertical density gradient with scale length  $L \equiv n_0(z) \left[ dn_0(z)/dz \right]^{-1}$ , leads to the following dispersion relation:

$$\omega - \mathbf{k} \cdot \mathbf{u}_d = \frac{\psi_{\perp}}{\nu_i} \left[ \omega \left( i\omega - \nu_i \right) - ik^2 C_s^2 \right] \left( 1 - \frac{i\kappa_e}{kL} \right)$$
 (5.1)

where  $\mathbf{u}_d = \mathbf{u}_{i0} - \mathbf{u}_{e0}$  is the zeroth-order plasma drift, with  $\mathbf{u}_{(i,e)0}$  representing the ion and electron drift velocities,  $\psi_{\perp} \equiv (\kappa_i \kappa_e)^{-1}$  is the anisotropy factor, and  $C_s \equiv \sqrt{K_B (T_i + T_e)/m_i}$  is the plasma acoustic speed. Writing  $\omega = \omega_r + i\omega_i$  and assuming  $|\omega_i| \ll |\omega_r|$  yields expressions for the phase frequency and growth rate:

$$\omega_r = \frac{\mathbf{k} \cdot \mathbf{u}_d}{1 + \psi_\perp} \tag{5.2a}$$

$$\omega_i = \frac{\psi_{\perp}}{1 + \psi_{\perp}} \left[ \omega_r \frac{\kappa_e}{kL} + \left( \omega_r^2 - k^2 C_s^2 \right) \frac{1}{\nu_i} \right], \tag{5.2b}$$

See Rogister and D'Angelo (1970) and Sudan et al. (1973) for more thorough developments of similar expressions. Fejer et al. (1975b) developed a two-fluid dispersion relation that allows for plasma production and an arbitrary wave vector. Dimant and Oppenheim (2011b) derived a general fluid FB/GD dispersion relation for arbitrarily magnetized plasmas (i.e., at arbitrary altitude), including arbitrary wave vector, gradients, and production and recombination. Makarevich (2016) developed a similar dispersion relation as that derived in Appendix A of Dimant and Oppenheim (2011b) without assuming the same long-wavelength, low-frequency limit. However,

a two-fluid dispersion relation becomes inappropriate as the wavelength approaches the ion mean-free-path, where ion Landau damping becomes significant.

Dimant and Sudan (1995a,b, 1997) also predicted an electron thermal instability (ETI) using a fully kinetic approach and Dimant and Oppenheim (2004) extended that theory to explain ion thermal instability (ITI) effects in simulations by Oppenheim and Dimant (2004). The ETI produces waves with wavelengths of tens of meters in the upper D/lower E region (cf Blix et al. (1996)), where the plasma does not favor FBI and GDI growth. The ITI, on the other hand, produces waves with wavelengths of a few meters in the same regime as the FBI, leading to interaction between the two. The most notable effect of the combined FBI/ITI instabilities is in waves turning away from the  $\mathbf{E}_0 \times \mathbf{B}_0$  direction, which is the most favorable for pure FBI growth.

Equations 5.2a and 5.2b provide a sufficient starting point for analysis of the present work because the present work ignores production and recombination, assumes a vertical background density gradient, and, to first order, comprises two essentially one-dimensional systems at right angles to each other. This work also assumes isothermal fluid electrons and does not produce significant zeroth-order heating in the (kinetic) ions. The absence of thermal effects in equations 5.2a and 5.2b only fails to capture small corrections to ion dynamics, mostly related to wave turning.

# 5.3 Numerical Model

The simulations presented in this chapter employed a hybrid version of the Electrostatic Parallel Particle in Cell (EPPIC) code described in Oppenheim and Dimant (2004); Oppenheim et al. (2008), using the parallel potential solver described in Young et al. (2017). The hybrid version of EPPIC improves on the simulation code described in that work by taking full advantage of EPPIC's domain decomposition

scheme. The model assumes quasineutrality between inertialess electrons and one species of ions. In the absence of sources and sinks, the quasineutrality assumption implies that the current,  $\mathbf{J}$ , must be divergence free  $(\nabla \cdot \mathbf{J} = 0)$ . For singly ionized ions, this simplifies to  $\nabla \cdot (\mathbf{\Gamma}_i - \mathbf{\Gamma}_e) = 0$ , where  $\mathbf{\Gamma}_{i,e}$  are the ion and electron. In other words, the flux divergences of the two species balance, leading to an equation for the electrostatic potential:

$$\nabla \cdot [n\epsilon \nabla \phi] = \nabla \cdot \left[ n\epsilon \left( \mathbf{E}_0 + \frac{k_b T_e}{e} \frac{\nabla n}{n} \right) + \left( 1 + \kappa_e^2 \right) \frac{m_e \nu_e}{e} \mathbf{\Gamma}_i \right], \tag{5.3}$$

where  $\kappa_e$  is the electron magnetization and  $\epsilon$  is a tensor that captures the effect of electron magnetization on the plasma drift:

$$\kappa_e \equiv \frac{\Omega_e}{\nu_e} \quad \text{and} \quad \epsilon \equiv \begin{pmatrix} 1 & -\kappa_e \\ \kappa_e & 1 \end{pmatrix}$$

The numerical model discretizes Equation 5.3 using finite differences and solves it on a Cartesian grid subject to periodic boundary conditions. The current version of hybrid EPPIC employs the MUltifrontal Massively Parallel Solver (MUMPS) (Amestoy et al., 2001, 2006) within the Portable Extensible Toolkit for Scientific Computing (PETSc) (Balay et al., 2015, 1997) to solve the resultant linear system.

Table 5.1 gives the values of relevant parameters used in this work. The simulation treats both ion-neutral and electron-neutral collisions elastically. The former acts approximately as a Maxwell molecule interaction, with the relevant collision frequency,  $\nu_i$ , from Equation 4.146 (and Table 4.4) in Schunk and Nagy (2004). The latter contributes to the RHS of Equation 5.3 as a constant fluid parameter, with the relevant collision frequency,  $\nu_e$ , from Table 4.6 in Schunk and Nagy (2004). The dimensionless parameter  $\psi_{\perp}$ , which affects both phase speed and growth rate, varies with altitude primarily due to the dependence of  $\nu_e$  and  $\nu_i$  on neutral density (Dimant and Oppenheim, 2004).

The simulation runs presented here span roughly 1 km by 250 m in the plane perpendicular to  $B_0$  at the magnetic equator. They have an initial density in the form  $n(x,z) = n_0 \left[1 + A\cos\left(2\pi x/L_x\right)\right]$ , where  $n_0$  is the ambient plasma density and A is an amplitude relative to  $n_0$ . In other words, density is uniform in the vertical direction  $(\hat{z})$  and sinusoidal in the zonal direction  $(\hat{x})$ , representative of a single period of a large-scale wave typical of the linear-stage GDI.

The work by Kudeki et al. (1982) determined the dominant wavelength of km-scale waves to be in the range 2-6 km, based on measurement of the east-west drift velocity, combined with the observed period of oscillation. The roughly 1-km primary waves used in this work represent the current spatial limit of our simulations, which required 15 hours on 1024 cores for each run. Since the perturbed electric field of the primary wave depends predominantly on the amplitude of perturbed density, using a 1-km primary wave suffices to elucidate the cross-scale coupling at the heart of this analysis, despite falling short of the range of observed wavelengths.

This work presents ten runs at five effective altitudes. At each altitude, one run had a primary-wave amplitude of five percent of the background plasma density (collectively, "the five-percent runs") and the other had a primary-wave amplitude of ten percent of the background plasma density (collectively, "the ten-percent runs"). The simulated  $\psi_{\perp}$  parameter determines the effective altitude of each pair of runs (Dimant and Oppenheim, 2004). Formally, the value of  $\psi_{\perp}$  depends on collision and cyclotron frequencies of all plasma species in the system of interest (cf. Madsen et al. (2014)); in these runs, all relevant parameters except the ion collision frequency,  $\nu_i$ , are constant. This work uses a set of five baseline simulation runs with no density gradients and an ambient electric field of 6 mV/m – too low to drive the FBI – to determine the effective ion collision frequency from ion Pedersen and Hall drifts. The psuedo-randomness inherent in the PIC collision algorithm results in a simulated

**Table 5.1:** Simulation Parameters for Chapter 5

Symbol	Value	Unit	Name
$m_i$	$5.0 \times 10^{-26}$	kg	ion mass
$m_e$	$9.1 \times 10^{-31}$	kg	electron mass
$m_n$	$4.6 \times 10^{-26}$	kg K	neutral mass
$T_i$ $T_e$ $T_n$	220		ion temperature
$\underline{T_e}$	220	K	electron neutral temperature
$T_n$	220	K	neutral temperature
$n_0$	$10^{10}$	$\mathrm{m}^{-3}$	plasma density
$ u_i$	5900, 5100, 4200, 3400, 2500	$s^{-1}$	ion-neutral coll. freq.
$ u_e$	$6.0, 5.0, 4.0, 3.0, 2.0 \times 10^4$	$s^{-1}$	electron-neutral coll. freq.
h	96,98,100,102,104	$\mathrm{km}$	effective altitude
$ B_{y0} \\ E_{z0} \\ L_x \\ dx \\ L_z $	$-2.5 \times 10^{-5}$	${ m T}$	magnetic field
$E_{z0}^{"}$	9.0	$\mathrm{mV/m}$	vertical electric field
$L_x$	$\approx 1$	m km	zonal box length
dx	0.5	$\mathbf{m}$	zonal cell size
$L_z$	$\approx 0.25$	${ m km}$	vertical box length
az	0.5	$\mathbf{m}$	vertical cell size
$L_t$	$\approx 0.3$	$\mathbf{S}$	real-time span
$\underline{}$ $dt$	$10^{-5}$	S	time step

value of  $\nu_i$  is not necessarily equal to the input value for a given run. This work reports the simulated values of  $\nu_i$ , and the resultant simulated values of  $\psi_{\perp}$ , because they better represent the physical system of interest. The simulated  $\psi_{\perp}$  values for the five sub-threshold runs are approximately 1.01, 0.72, 0.48, 0.29, 0.14. Following Figure 2 of Dimant and Oppenheim (2004), these values of  $\psi_{\perp}$  set the effective altitudes of each pair of runs at 96 km, 98 km, 100 km, 102 km, and 104 km, respectively.

Figure 5·1 shows the initial plasma density configuration for all runs. The simulation uses a particle rejection method to distribute ions so that their initial condition mimics one period of a kilometer-scale wave. This kilometer-scale primary wave represents a simplified version of GDI growth in the daytime E-region plasma gradient. The quasineutral model assumes  $n_e \approx n_i \equiv n$  and thus treats the ion density as the total density. The white square demarcates a 128 m × 128 m box in the primary-wave trough. Figures 5·6 and 5·7 will refer to these boxes. The simulation outputs density as relative perturbed density,  $\delta n/n_0 \equiv \left[n_1(x,z,t) - n_0\right]/n_0$ , where  $n_1(x,z,t)$  is the dynamic density that the simulation PIC method calculates at each time step

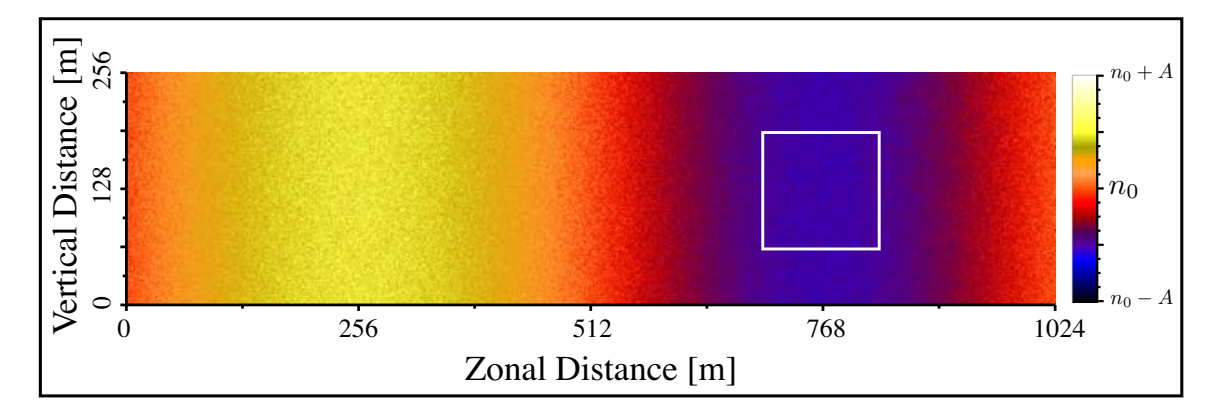


**Figure 5·1:** Initial plasma density configuration for all runs. Density is a sine about  $n_0 = 10^{10} \text{ m}^{-3}$  in the east-west direction, with an amplitude of  $\pm 5\%$  or  $\pm 10\%$ . This configuration mimics a single period of a large-scale GDI wave. The white box represents a 128-m  $\times$  128-m patch shown in Figures 5·6 and 5·7.

and  $n_0$  is a fixed input value. The FBI growth does not depend on the total density, provided the density satisfies the condition  $\omega_{pi}/\nu_i > 1$  (Rosenberg and Chow, 1998).

The background electric field,  $E_{z0} = 9 \text{ mV/m}$ , is vertical and the background magnetic field,  $B_{y0} = 2.5 \times 10^{-5} \text{ T}$ , points out of the page. The zonal direction points from east on the left to west on the right. Linear theory predicts that a polarization electrostatic field,  $\delta \mathbf{E}$  will develop in phase with the perturbed density. Given the initial density configuration shown in Figure 5·1, this means there will be an eastward  $\delta E_x$  in the central large-scale trough and an westward  $\delta E_x$  in the corresponding crests.

Figure 5·2 shows the initial magnitude of the total electric field,  $|\mathbf{E}_I| = (E_{z0}^2 + \delta E_x^2)^{1/2}$ , and its angle from due west,  $\theta(\mathbf{E}_I) = \tan^{-1}(E_{z0}/\delta E_x)$ , after smoothing density variations smaller than 10 m and averaging vertically. Smoothing brings out the large-scale structure of the initial field components. The vertical average is an appropriate representation of the 2-D initial configuration because the only variation is due to the large-scale density wave. For the purpose of this work, "initial" means the state of the simulation after approximately one collisional time,  $\tau_i \equiv 1/\nu_i$ . The quasineu-

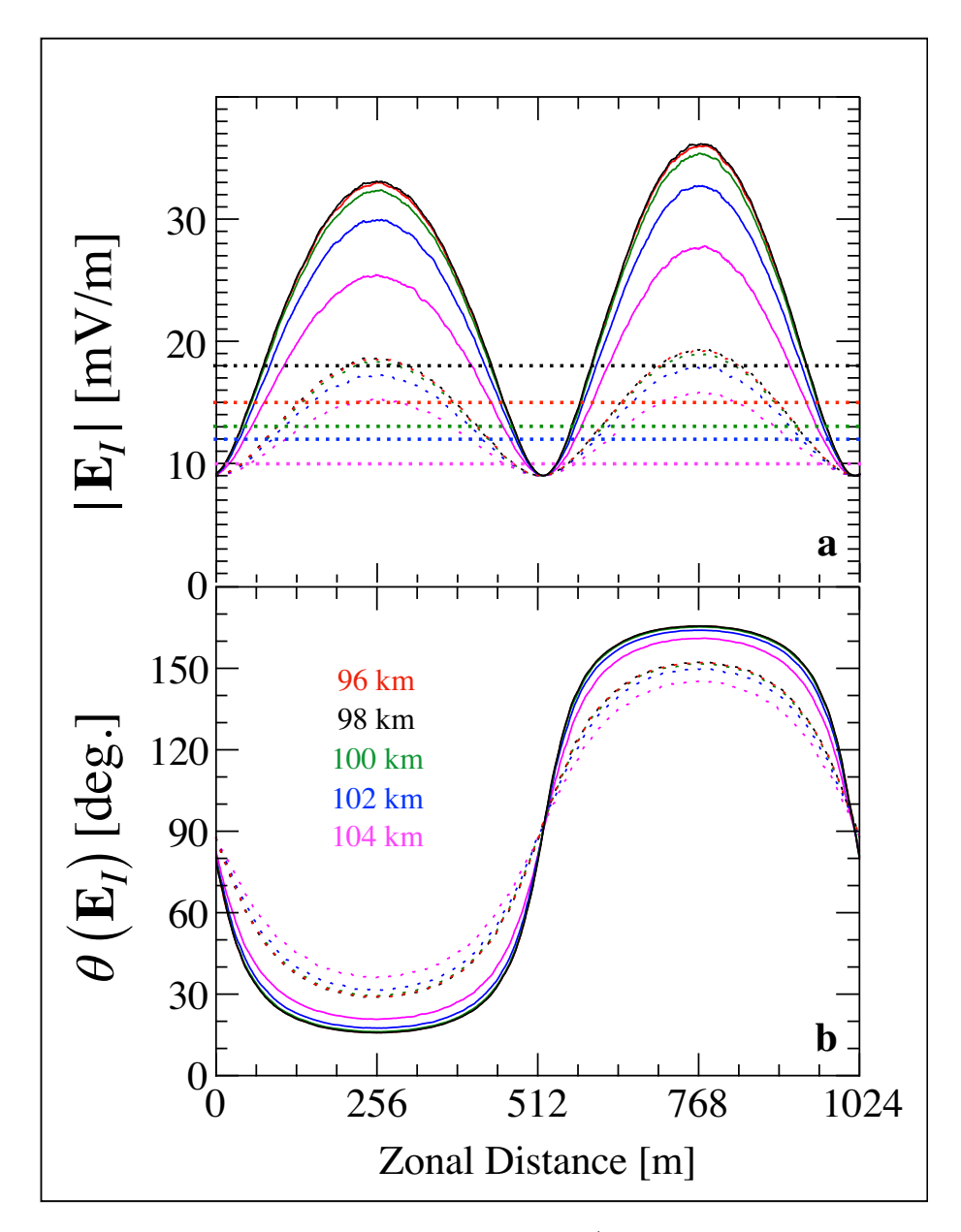


Figure 5.2: Total electric field at  $t \approx 1/\nu_i$  for all runs. The solid traces correspond to ten-percent runs; the dashed lines correspond to five percent runs. For both amplitudes, red represents 96 km, black represents 98 km, green represents 100 km, blue represents 102 km, and magenta represents 104 km. Panel a: The magnitude of the total electric field,  $|\mathbf{E}_I| = \sqrt{E_{z0}^2 + \delta E_x^2}$ . Panel b: The angle from due west of the total field,  $\theta(\mathbf{E}_I) = \tan^{-1}(E_{z0}/\delta E_x)$ . In case the reader is unable to distinguish colors: the text labels in panel b indicate the order of lines in both panels. In panel a, the 96-km trace nearly covers the 98-km trace; in the panel b, they are indistinguishable.

tral hybrid model starts the simulation with artificially high potential unless input parameters are precisely tuned, so showing dynamic quantities after  $t \approx \tau_i$  ensures that the potential has relaxed into a more physically realistic state.

In both panels, the solid lines represent the ten-percent runs and the dashed lines represent the five-percent runs. Color corresponds to altitude, with red at 96 km, black at 98 km, green at 100 km, blue at 102 km, and magenta at 104 km. Both panels indicate that the polarization field dominates the total field and that its overall shape is broadly consistent with zeroth order. Panel a shows that  $|\mathbf{E}|_I$  peaks in the crest and trough, and drops to  $E_{z0}$  in between. Note that the location of  $|\mathbf{E}|_I = E_{z0}$  does not align precisely with the midpoint between crest and trough, where  $n = n_0$ , due to the small ambipolar electric field corresponding to each density gradient. Kudeki et al. (1985) argued that the polarization electric field of the primary wave should develop a natural asymmetry, with higher values in the trough, that counteracts the GDI-induced downward transport of electrons. Since  $E_{z0}$  in this work is homogeneous, the primary-wave polarization field accounts for the asymmetry in Figure 5·2 and is therefore consistent with the results of Kudeki et al. (1985).

The threshold electric field at which FBI turns on is  $E_{th} = B_0 C_s (1 + \psi_{\perp})$ . Using simulation values for  $B_0$ ,  $T_i$ ,  $T_e$ , and  $m_i$ , the value of  $E_{th}$  is approximately 18.0 mV/m at 96 km, 15.0 mV/m at 98 km, 13.0 mV/m at 100 km, 12.0 mV/m at 102 km, and 10.0 mV/m at 104 km. Horizontal dotted lines, color-coded in the same manner as the  $|\mathbf{E}|_I$  traces, show each threshold value. It is clear that  $|\mathbf{E}|_I > E_{th}$  at least somewhere in the simulation domain for all runs.

Panel b shows that the direction of  $\mathbf{E}_I$  in all runs varies continuously from vertical of due west, in the crest, to vertical of due east, in the trough. The peak angle in tenpercent runs varies from roughly  $90 \pm 75^{\circ}$  at the lowest altitudes to roughly  $90 \pm 68^{\circ}$  at 104 km. The angle in five-percent runs varies from roughly  $90 \pm 60^{\circ}$  at the lowest

altitudes to roughly  $90 \pm 53^{\circ}$  at 104 km. The crest-trough asymmetry is also present in this panel, though it is not as obvious as in panel a.

The wave polarization electric field gives rise to a perturbed drift,  $\delta \mathbf{u}_e = \delta \mathbf{E} \times \mathbf{B}_0$ , pointed upward along the trough and downward along the crests. The background vertical electric field,  $E_{z0}$ , is too low to drive the FBI at most altitudes considered here and if it were large enough, it would drive westward waves, not vertical waves. The primary-wave polarization field,  $\delta E_x$ , can be large enough to drive FBI and the waves would propagate vertically – upward in the troughs and downward in the crests. Figure 5·2 shows that the combination of  $E_{z0}$  and  $\delta E_x$  is responsible for driving FBI at an intermediate angle when their total magnitude is above the local threshold value.

# 5.4 Results

This section presents results from eight of the ten simulation runs. Both runs at 104 km failed due to what appears to have been energy in the perturbed electric field increasing without bound, causing particles to jump across the entire simulation domain in one time step. Figure 5·3b, which section ?? describes in detail, shows the perturbed electric field growing very rapidly at the start of the run at 104 km. This is an unfortunate drawback of the quasi-neutral hybrid model with isothermal, inertialess electrons – as  $\kappa_e$  grows with altitude, the linear system representing Equation 5.3 becomes more difficult to solve. Improvements to the code designed to overcome or mitigate this drawback are topics of current and future work. The ten-percent run at 104 km failed just after 1600 time steps and provides information only during early wave growth, to be discussed below. The corresponding five-percent run, on the other hand, failed just before 25000 time steps and therefore provides information on wave growth comparable to the eight successful runs. Due to the inability to

compare the runs at 104 km on the same level as the other eight runs, this report will exclude them from analysis beyond Section 5.4.1.

# 5.4.1 Meter-scale irregularity amplitudes

Figure 5·3 shows the development of 2-m to 6-m density (panel a) and electric-field (panel b) perturbations in each run. The FBI growth rate,  $\omega_i$ , peaks at a few meters, with local plasma parameters controlling the specific peak wavelength, so the chosen wavelength range should capture the relevant instability growth in all simulations. Figure 5·3 therefore represents a proxy for meter-scale irregularity development in each run.

The slope of the traces in Figure 5·3 gives a measure of the normalized growth rate,  $\bar{\gamma}$ . Panel a indicates that  $\bar{\omega_i}$  and the normalized saturated amplitude of density perturbations increases monotonically with altitude in both five- and ten-percent runs. The value of  $\bar{\omega_i}$  among ten-percent runs is approximately 3, 6, and 9 times greater at 98 km, 100 km, and 102 km, relative to its value at 96 km. The growth rate at 104 km appears to be nearly equal to the growth rate at 102 km but the paucity of time steps makes for a tenuous comparison. The saturated amplitude of the four complete ten-percent runs is approximately 3, 4, 5, and 6 times their initial values

In the case of five-percent runs, the small, negative initial value of  $\bar{\omega}_i$  in the runs at 96 km and 98 km, indicated by the fact that amplitude drops below 1, makes comparison with those runs unhelpful. This negative growth rate, which turns positive for the run at 98 km but remains negative for the run at 96 km, is likely a result of initial particle noise seeding the system with artificial spectral power that fades as the runs progresses. In all but the five-percent run at 96 km, the signal from meter-scale irregularities overcomes this particle noise. Comparing the three five-percent runs above 98 km,  $\bar{\omega}_i$  is approximately 4 and 6 times greater at 102 km

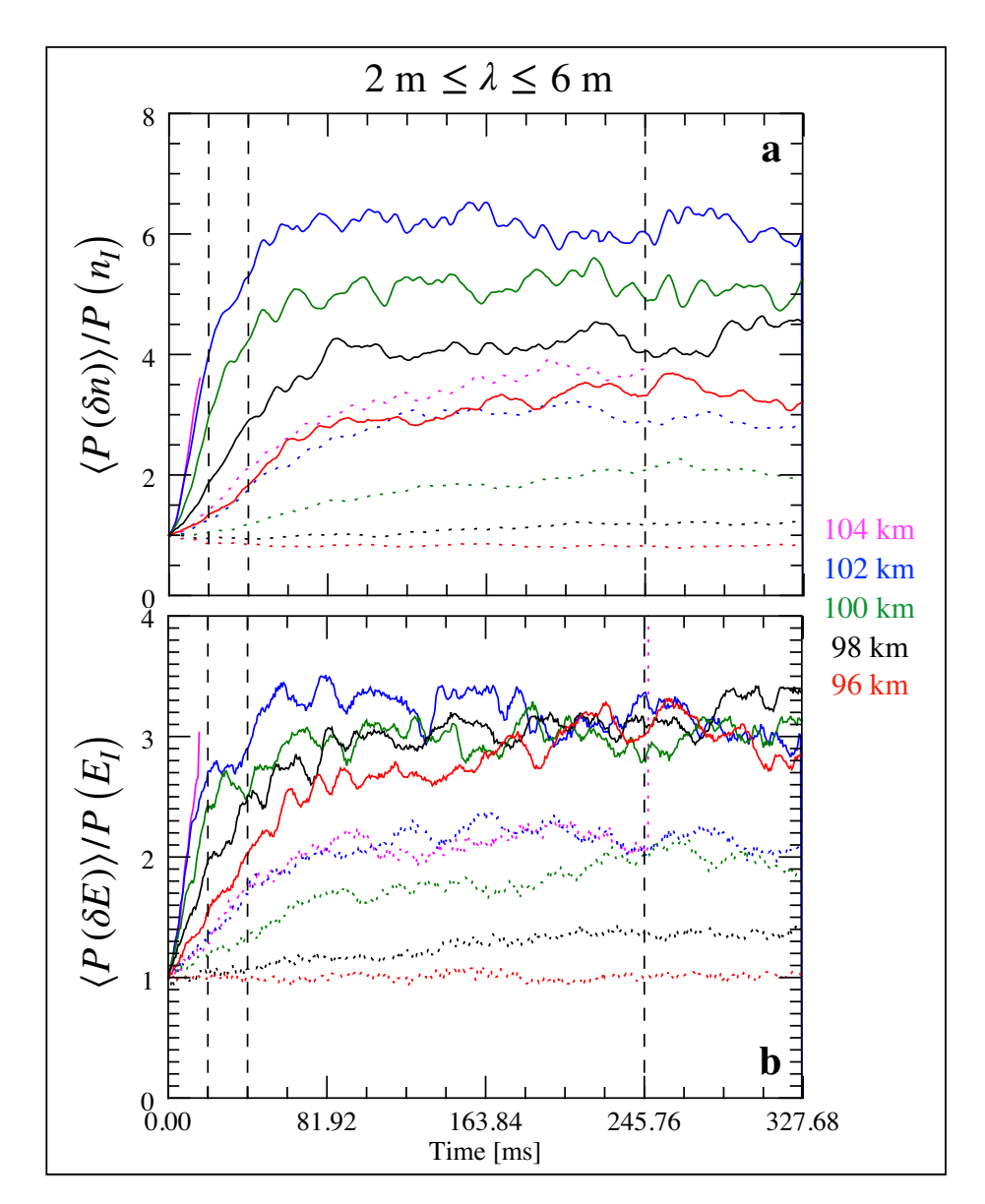


Figure 5·3: Spectral power in 2-m to 6-m density (top) and electric-field (bottom) perturbations propagating within  $30^{\circ} \leq \theta \leq 50^{\circ}$  west of zenith, normalized to the  $t \approx 1/\nu_i$  value in each run. Colors and line styles are the same as in Figure 5·2. Dashed vertical lines mark three fiducial times for later analysis: The first (20.48 ms) corresponds to growth in ten-percent runs, the second (40.96 ms) corresponds to growth in five-percent runs, and the third (245.76 ms) corresponds to a saturated state in all runs.

and 104 km, compared to at 100 km. The "saturated" amplitude of the five-percent run at 96 km is meaningless and the amplitude at 98 km does not grow appreciably above unity. The runs at 100, 102, and 104 km grow to approximately 2, 3, and 3.5 times their initial values, with amplitude in the runs at 102 km and 104 km consistent with that in the ten-percent run at 96 km.

Panel b shows many of the same trends as panel a, but there are notable exceptions. First,  $\bar{\omega}_i$  is much more similar among the ten-percent runs, differing by approximately 3 between 96 km and 102 km. Second, the saturated amplitude of ten-percent runs converges to approximately 3 times the initial value in all four complete runs. Third, the amplitude of the five-percent run at 96 km is consistent with unity because the electric-field spectrum does not suffer from the particle-placement noise that the density spectrum does. Fourth, amplitude in the five-percent runs at 102 km and 104 km, before the latter failed, is nearly identical. Fifth, saturated amplitude of the five-percent runs at 100 km and 102 km converge to approximately 2 times their initial values.

Both panels show vertical dashed lines at 20.48 ms, 40.96 ms, and 245.76 ms. These dashed lines demarcate fiducial time steps for the images of density and electric field shown in the following sections. The line at 20.48 ms represents the growth stage of ten-percent runs. The line at 40.96 ms represents the growth stage of five-percent runs. The line at 245.76 ms represents the saturated stage in all runs. The rest of this work will focus on the eight successful runs.

#### 5.4.2 Average zonal electric field

The most striking result of these simulations is that the polarization electric field of the wave develops a flat-topped nature as meter-scale turbulence develops. This indicates a turbulent mechanism for shorting out the wave electric field and explains rocket observations of large-scale electric field saturation in the equatorial electrojet.

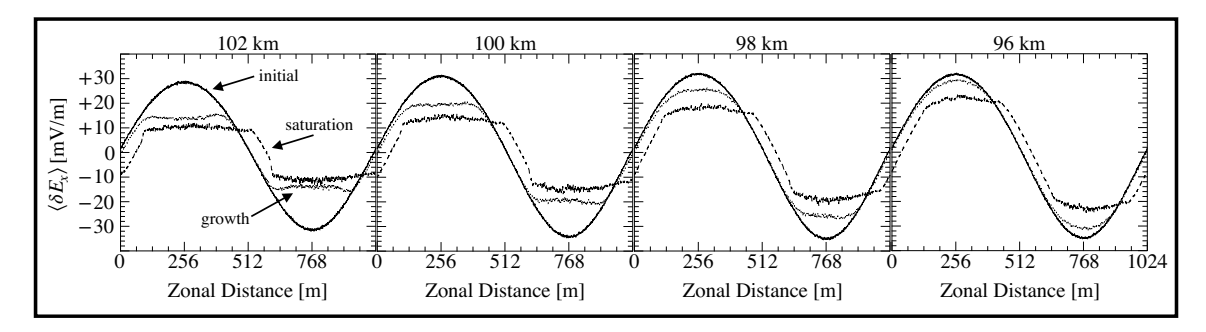


Figure 5.4: Vertical average of the zonal electric field at three moments during each ten-percent run: the initial step (solid), during growth (dotted), and in saturation (dashed).

Figure 5.4 shows the vertically averaged zonal (east-to-west) electric field,  $\langle \delta E_x \rangle$ , during the ten-percent runs. The panels progress from left to right in order of descending altitude. In each panel, the solid trace corresponds to the initial time step, the dotted trace corresponds to the growth-stage time step, and the dashed line corresponds to the saturated time step. The initial trace is nearly identical in all runs, save for an amplitude increase of a few mV/m from 102 km to 96 km, because the primary-wave amplitude largely determines the initial shape of  $\langle \delta E_x \rangle$ . The growthstage shows the greatest variation across altitudes: On one end of the spectrum,  $\langle \delta E_x \rangle$  at 102 km develops a roughly flat top, with an amplitude reduced more than 10 mV/m from its initial value. On the other end,  $\langle \delta E_x \rangle$  at 96 km deviates very little from the initial trace. The growth-rate traces of  $\langle \delta E_x \rangle$  at the intervening altitudes provide intermediate cases. By the saturated time step, the field amplitude develops a relatively flat top in all runs. The saturated amplitude again increases from 102 km to 96 km but the difference is approximately 10 mV/m, meaning that the amplitude reduction due to density irregularities becomes increasingly more drastic from 96 km to 102 km. Finally, the offset between initial and saturated traces indicates that the primary wave drifts westward at a few hundred meters per second.

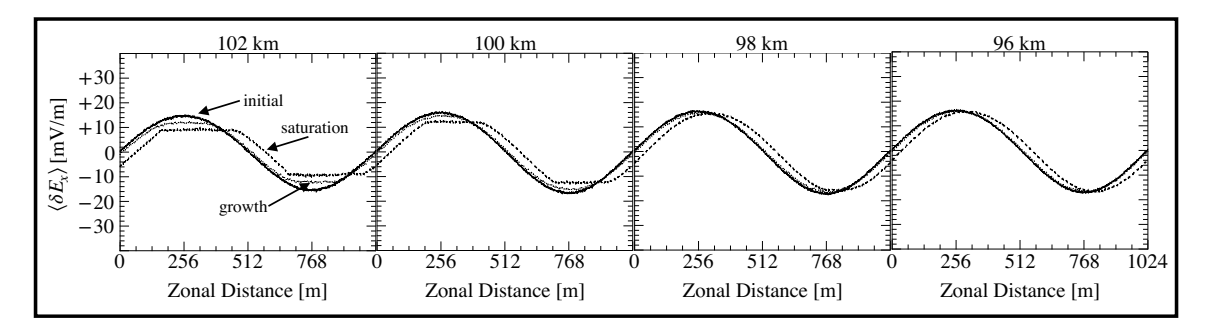


Figure 5.5: Vertical average of the zonal electric field at three moments during each five-percent run: the initial step (solid), during growth (dotted), and in saturation (dashed).

Figure 5.5 shows  $\langle \delta E_x \rangle$  during the five-percent runs, in the same manner as Figure 5.4. The initial trace is again similar in all runs, with an amplitude increase of a few mV/m from 102 km to 96 km. The evolution from initial to saturated  $\langle \delta E_x \rangle$  is far less pronounced that for the ten-percent runs: Only the growth-stage trace at 102 km deviates appreciably from the its initial value, and only the saturated traces at 102 km and 100 km develop flat tops. The saturated trace at 98 km has a slightly reduced amplitude from its initial value while the amplitude of the saturated trace at 96 km is essentially unchanged. Again, the primary wave appears to drift westward at a few hundred meters per second.

### 5.4.3 Relative perturbed density

Images of perturbed density provide insight into irregularity growth and development. This work presents perturbed densities relative to the background plasma density,  $\delta n/n_0 = (n_1 - n_0)/n_0$ , so that a value of 0 represents no deviation from background.

Figure 5.6 shows  $\delta n/n_0$  during ten-percent runs, alongside corresponding self-normalized spatial spectra. The data-analysis routines filtered out wavelengths greater than 100 m in the density panels to effectively de-trend the meter-scale irregularities that are the focus of these snapshots. The amplitude of most perturbations is less than 10% of  $n_0$ , which is consistent with predictions of linear theory for wavelengths

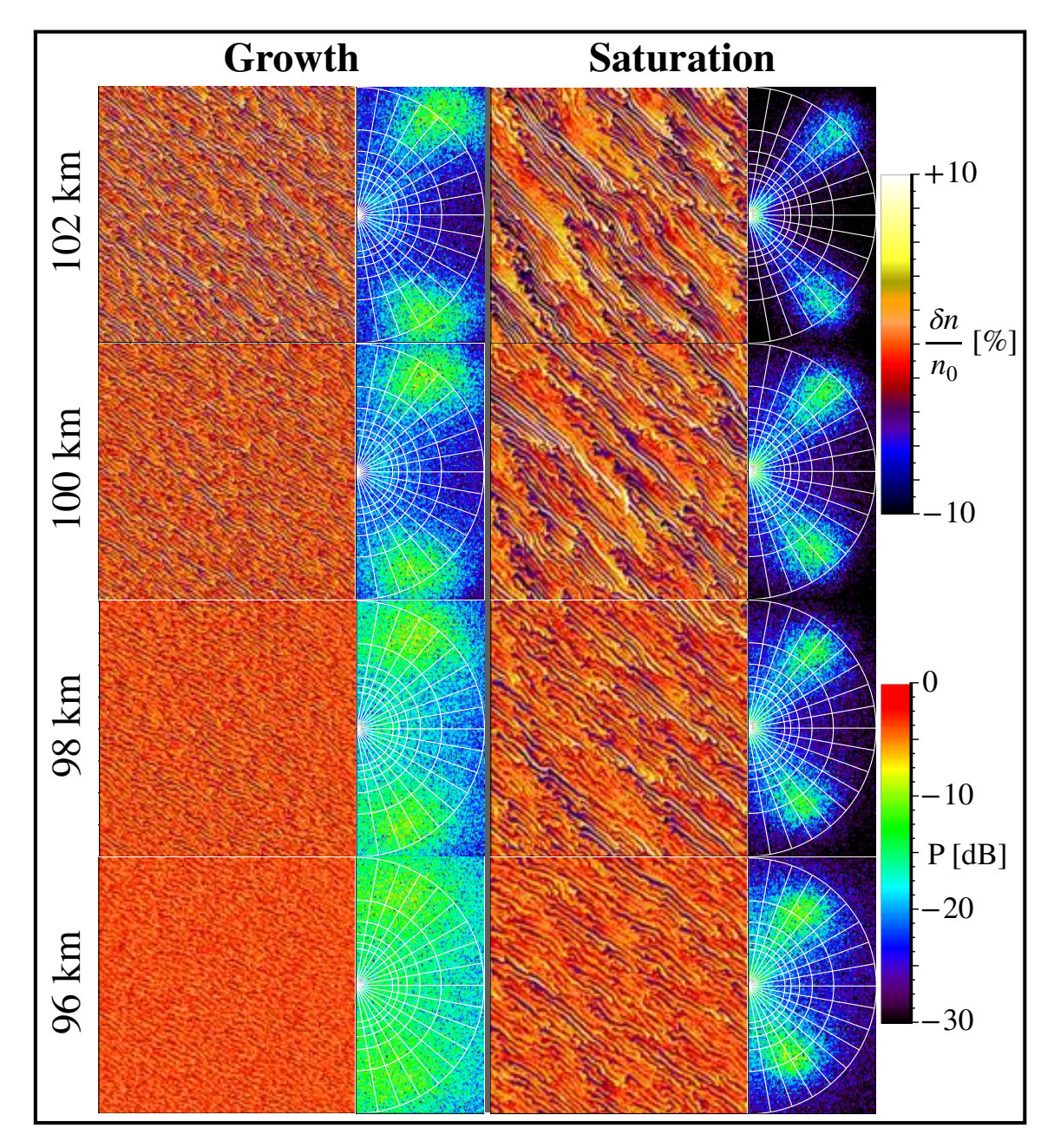


Figure 5·6: Snapshots of relative perturbed density,  $\delta n/n_0$ , and self-normalized spectral power, P, during ten-percent runs. Each density panel represents the 128 m × 128 m box outlined in white in Figure 5·1 after filtering out wavelengths greater than 100 m. Each spectrum covers  $(k_x, k_z) \in [0, +\pi] \times [-\pi, +\pi]$ . White circles show values from  $k = 2\pi/2$  m<sup>-1</sup> (largest) to  $k = 2\pi/7$  m<sup>-1</sup> (smallest) and white radii show values of  $\theta$  from  $-90^{\circ}$  (bottom) to  $+90^{\circ}$  (top).

of roughly half a meter and larger.

Meter-scale irregularity growth is evident at all altitudes, though the wavelength of peak power differs slightly among altitudes and evolves over each run. The peak in the 102-km growth spectrum sits on the  $k = 2\pi/2.0 \text{ m}^{-1}$  circle but moves closer to the  $k = 2\pi/3 \text{ m}^{-1}$  circle at lower altitudes. Growth-stage power is diffuse at 96 km but a cluster of red pixels between  $k = 2\pi/2 \text{ m}^{-1}$  and  $k = 2\pi/3 \text{ m}^{-1}$ , at  $\theta \approx 55^{\circ}$ , corresponds to the weak density irregularities. As each run evolves, the initial clump of power moves toward the center (i.e., to longer wavelengths), and decameter-scale power increases relative to meter-scale power. At 102 km, the meter-scale power remains fairly isolated from the decameter power whereas the space between those two spectral regimes fills in more uniformly as altitude decreases.

The angle of propagation shows in which direction a radar will observe coherent echoes. During irregularity growth at 102 km, waves propagate upward  $(k_z > 0)$  at  $\theta \approx 50^{\circ}$  and downward  $(k_z < 0)$  at a  $\theta \approx 55^{\circ}$ . Moving down in altitude, a trend toward  $\theta = \pm 90^{\circ}$  accompanies the aforementioned trend toward longer wavelengths. At 102 km, 100 km, and 98 km, the propagation angle has a spread of roughly  $10^{\circ}$  during growth; at 96 km, the spectrum appears more diffuse, but the reason may be related to low signal-to-noise ratio rather than a change in physics. In the transition from growth to saturation, the mean propagation angle tends to move approximately  $10^{\circ}$  toward horizontal at all altitudes. The approximately five-degree asymmetry between up-going and down-going waves mentioned for 102 km exists at all altitudes and persists from growth to saturation.

Figure 5.7 shows  $\delta n/n_0$  and corresponding spatial spectra during the five-percent runs, in the same fashion as Figure 5.6. Note that the perturbed density scale now ranges from -5% to +5% of  $n_0$ . Many of the characteristics of density perturbation growth and saturation described for the ten-percent runs apply to the five-percent

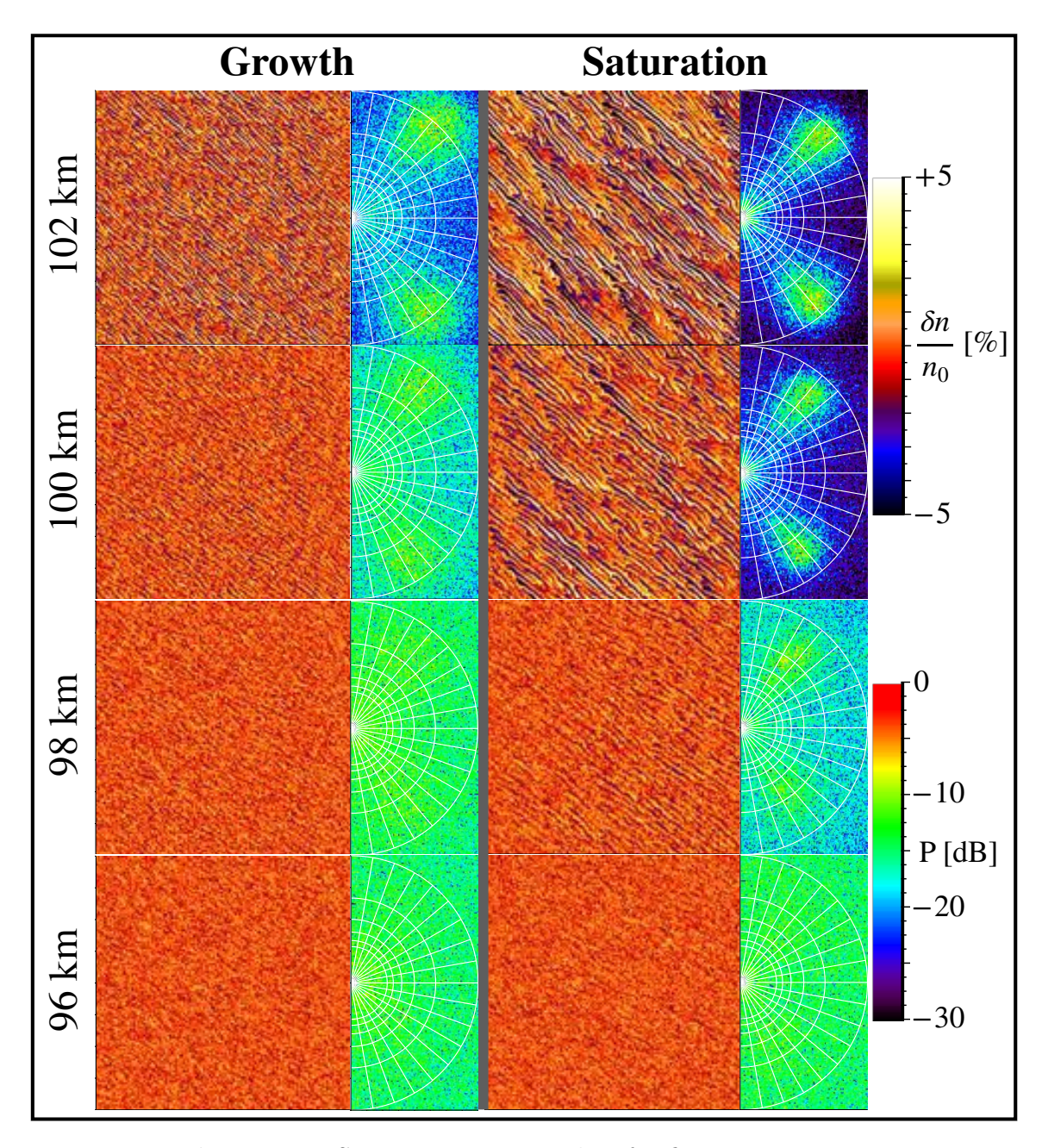


**Figure 5.7:** Same as Figure 5.7, but for five-percent runs.

runs. Wave amplitudes are generally lower in the five-percent runs than in the tenpercent runs, which is consistent with Figure 5·3. The lower amplitude of meter-scale growth at a given altitude is not necessarily obvious in the normalized spectra at 102 km and 100 km, but it should be clear by inspection of  $\delta n/n_0$ , with the knowledge that most density perturbations are less than 5% of  $n_0$ . The lower amplitude of meter-scale growth is evident at 98 km, where waves barely peak out of the noise in the saturated stage, and at 96 km, where both  $\delta n/n_0$  and spectra show noise.

#### 5.4.4 Density irregularity spectra

Radars measure coherent echoes from density irregularities with wavelengths equal to half the radar wavelength. The mean Doppler shift and spectral width of observed echoes distinguish type-I irregularities from type-II irregularities. Simulated radar spectra can thus connect observed irregularity types to the instabilities that create them.

Figure 5·8 shows Fourier spectral power in 3-m, 5-m, and 10-m waves as a function of angle from zenith ( $\vartheta$ ) and phase velocity ( $V_{ph} = \omega_r/k$ ) during the second half of each ten-percent run. The sign convention for  $\vartheta$  is such that positive values denote westward angles and negative values denote eastward angles. Note that  $\vartheta = 90^{\circ} - \theta$ , where  $\theta$  is the angle shown by white radii in Figures 5·6 and 5·7. The sign convention for  $V_{ph}$  follows the standard Doppler convention: positive values denote scatterers moving toward the radar and negative values denote scatterers moving away from the radar. Dotted white lines show  $V_{ph} = \pm C_s$ . As in Figures 5·6 and 5·7, the spectra are normalized to the maximum value in each panel. The purpose is to draw attention to mean frequency and spectral width but this normalization scheme naturally precludes power comparison among frames.

The regions of high power at  $\lambda = 3$  m near  $\vartheta = -40^{\circ}$  and  $\vartheta = +45^{\circ}$  correspond to the spectral features at  $\theta = 50^{\circ}$  and  $\theta = -45^{\circ}$  in Figure 5.6. These primary spectral

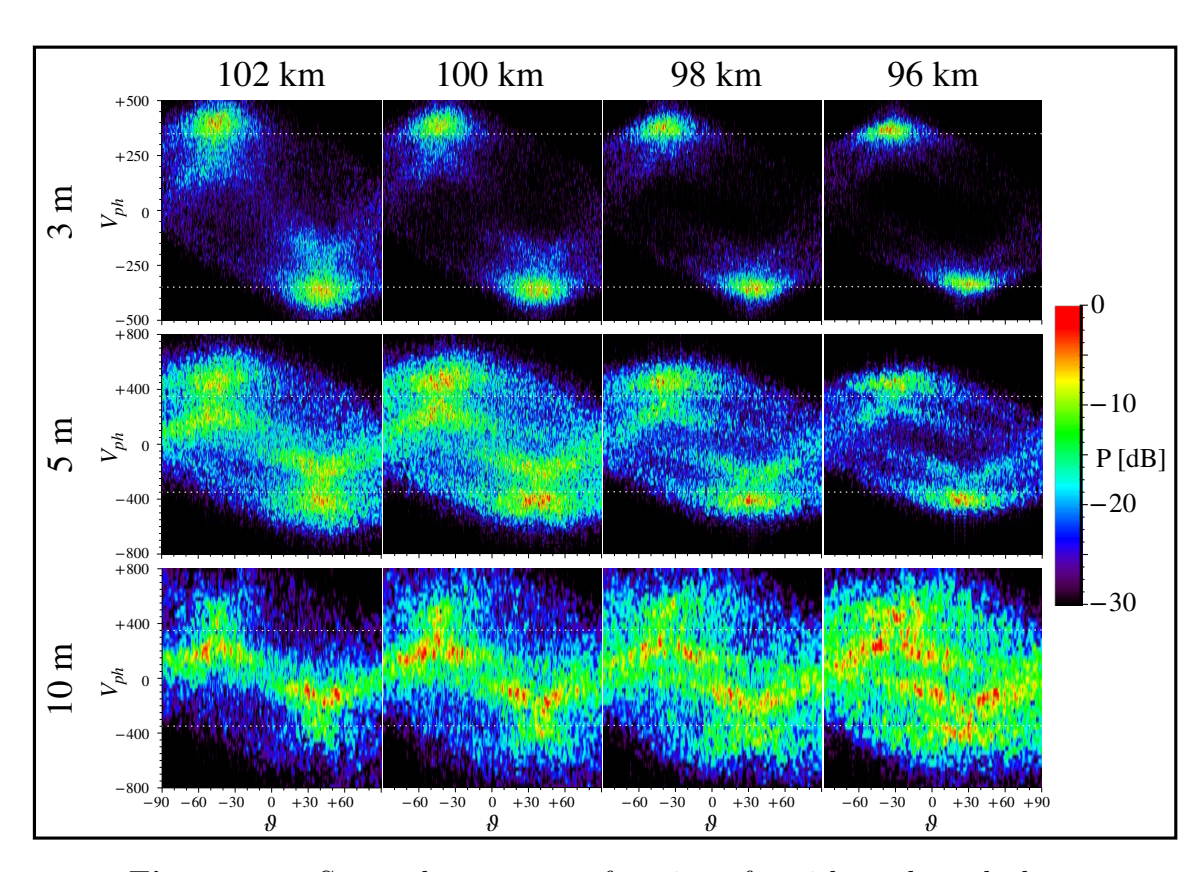


Figure 5.8: Spectral power as a function of zenith angle and phase velocity during the second half of all ten-percent runs. Columns, from left to right, correspond to the runs at 102 km, 100 km, 98 km, and 96 km. Rows, from top to bottom, show power in 3-m, 5-m, and 10-m waves. The color scale runs from 0 dB to -30 dB. White dotted lines mark  $\pm C_s$ .

features exhibit many characteristics of type-I radar spectra. The peaks in 3-m power, where P > -10 dB, are well isolated in angle and their phase velocities deviate from  $C_s$  by less than 50 m/s. Their widths are in the range 50 m/s  $< \Delta \omega_r < 100$  m/s at 102 km and decrease to  $\Delta \omega_r < 50$  m/s at 96 km. At 102 km, a secondary spectral feature below  $|V_{ph}| = 300$  m/s accompanies the peak near  $C_s$  but fades into the background as altitude decreases. The wave frequency of these secondary features appears to have an angular dependence whereas the brighter features do not. Both the lower frequency and angular dependence of these features are reminiscent of type-II radar spectra.

Type-I features are again apparent at  $\lambda = 5$  m. Similarly to 3-m waves, their width narrows with decreasing altitude; however, their mean frequency stays relatively constant at a value just above  $C_s$ , unlike 3-m waves. At 102 km, the spectral power in type-II features competes with the spectral power in type-I features and they exhibit a more obvious angular dependence. The clear angular dependence persists at all altitudes but, as with 3-m waves, the power in type-II features relative to type-I features falls off with altitude.

Slow, type-II features dominate the spectrum of 10-m waves. At 102 km, most of the power propagates with  $V_{ph} < C_s$ ; there are slight increases in power around  $V_{ph} = C_s$  near the angles most favorable for the shorter wavelengths (i.e.,  $45^{\circ} < |\vartheta| < 50^{\circ}$ ), but those features never dominate the spectrum at 10 m. The prevalence of type-II features persists down to 96 km, unlike at shorter wavelengths. Type-I peaks may exist at all altitudes but they become difficult to distinguish below 100 km.

Figure 5.9 shows Fourier spectral power in 3-m, 5-m, and 10-m waves for fivepercent runs in the same manner as Figure 5.8. Many features of Figure 5.9 are similar to Figure 5.8. At 3 m, distinct type-I peaks appear near  $\vartheta = -40^{\circ}$  and  $\vartheta = +45^{\circ}$  with  $V_{ph} \approx C_s$  at 102 km. There are again weak type-II features. The

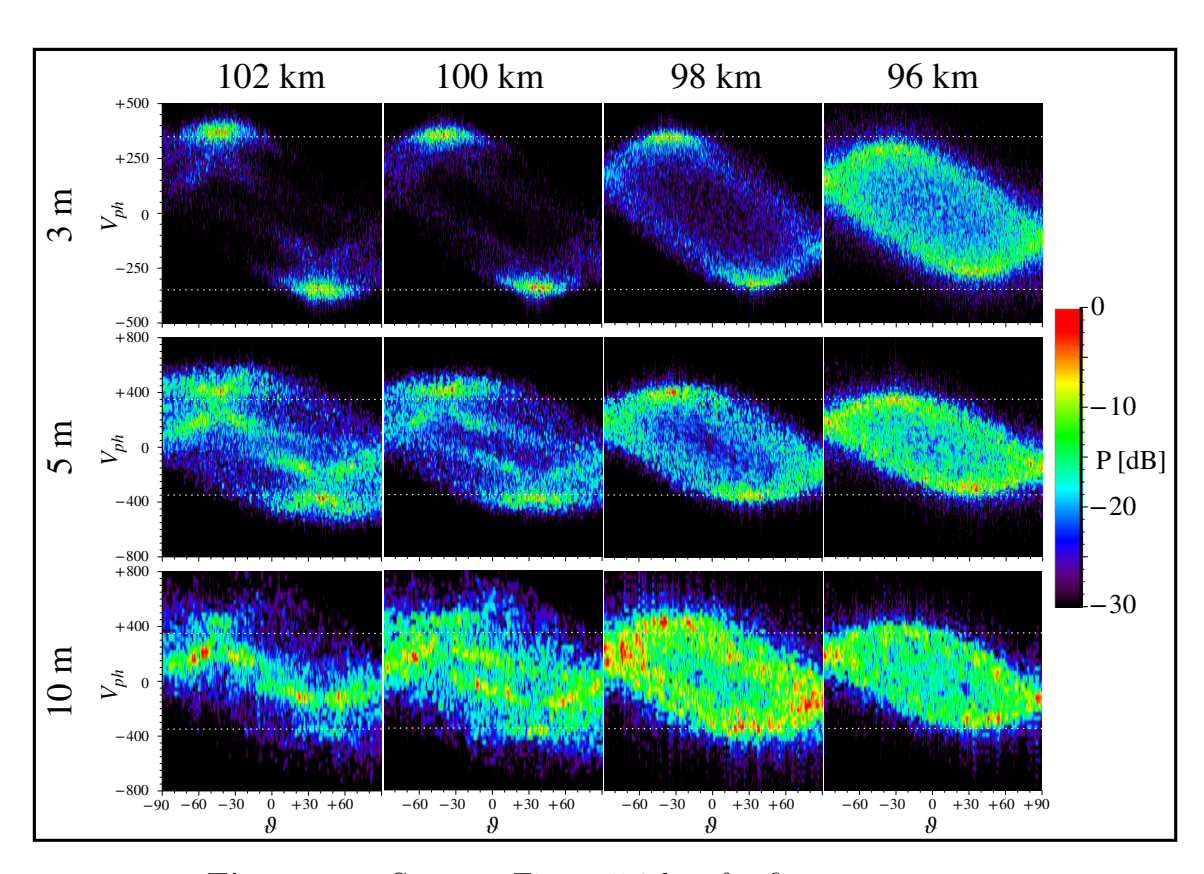


Figure 5.9: Same as Figure 5.8 but for five-percent runs.

type-I spectra are narrower in the five-percent runs than in the ten-percent runs and their mean  $V_{ph}$  value decreases more quickly with altitude. A major distinction between 3-m ten-percent waves and 3-m five-percent waves is that type-I features seem to blend with type-II features as altitude decreases in Figure 5.9.

The spectrum of 5-m waves exhibits both type-I and type-II features, but the peak in spectral power at 102 km shifts from type-II to type-I and back as  $\vartheta$  sweeps past the type-I peak. This trade-off is not apparent in the ten-percent runs. At 100 km, both types still exist and there is again a cut-out in type-II power around the angle of peak type-I power, but type-II power is consistently 10 dB lower than type-I power. Type-I mean  $V_{ph}$  decreases slightly with altitude, dropping below  $C_s$  only at 96 km, and both spectral types blend together below 100 km.

Type-II features again dominate the 10-m spectrum, as in the ten-percent runs. At 10 m, the type-II power cut-out near  $\vartheta = -40^{\circ}$  and  $\vartheta = +45^{\circ}$  is very clear but the corresponding type-I contribution is weak, opposite to the 5-m case. The 10-m spectrum becomes more homogenous in angle as altitude decreases and there is a relatively large amount of power in waves propagating horizontally westward  $(V_{ph} < 0 \text{ at } \vartheta = +90 \text{ and } V_{ph} > 0 \text{ at } \vartheta = -90)$ .

Cut-outs in type-II power are similar to results described in Young et al. (2017), which described the co-evolution of type-I and type-II irregularities. In that work, images of spectral power as a function of zenith angle and phase velocity showed type-II power decreasing where type-I increased. The reason is the the same physical processes govern both types of spectrum, so the competing criteria for FBI and GDI determine the relative power in broad and narrow spectra at meter scales.

#### 5.5 Discussion

Pfaff et al. (1987a,b) reported flat-topped electric fields during a rocket flight through

large-scale waves in the equatorial, daytime E region. They noted that flat-top morphology was not the result of instrumental limitations, and interpreted it instead as evidence that some geophysical process had caused electric-field saturation. The results shown here suggest that electric-field flattening occurs in the presence of FBI turbulence in the crests and troughs of large-scale waves. FBI develops in the regions of the large-scale wave where the plasma drift exceeds the threshold value:  $|\mathbf{u}_d| \equiv |\mathbf{u}_e - \mathbf{u}_i| > C_s (1 + \psi_{\perp})$ . In general, both the zeroth-order and ambipolar electric fields may contribute both Pedersen and Hall components to the ion and electron drift. For the physical situation corresponding to this work,  $\mathbf{u}_d$  is effectively the electron Hall drift due to both the background electric field and the wave polarization electric field.

When secondary FBI waves develop in nature, they are subject to the same electrostatic polarization mechanism as is the primary wave. That means that nonlinear  $\mathbf{E} \times \mathbf{B}_0$  drifts develop in the frame of the meter-scale waves, analogously to the  $\mathbf{E} \times \mathbf{B}_0$  drift that initiated the meter-scale FBI growth (Oppenheim, 1997). However, the FBI growth rate quickly becomes negative for wavelengths below about a meter, so there is no tertiary set of FBI waves propagating perpendicular to the secondary FBI waves. Instead, the meter-scale  $\mathbf{E} \times \mathbf{B}_0$  increases plasma mobility perpendicular to the magnetic field, along meter-scale wave fronts. The increased mobility across the magnetic field represents and anomalous transport. Since there is more plasma in density crests than in density troughs, this anomalous transport produces a nonlinear current (Dimant and Oppenheim, 2011a). It is this nonlinear current that shorts out the primary-wave polarization field and reduces its amplitude to just above the FBI threshold.

The saturated mean polarization electric field in the ten-percent runs noticeably *increases* with decreasing altitude, saturating at a value that sets the total electric

field just above the threshold for FBI. The same is true for the five-percent runs at 102 km and 100 km, though the difference between initial and saturated values is not as stark. In the five-percent run at 98 km the saturated field is barely above the threshold value, so that FBI turbulence does not have time to grow before diffusion reduces the field. At 96 km, the absence of flat-topped saturated fields results from the fact that the initial electric field is simply below the threshold value.

Figures 5.4 and 5.5 also demonstrate that the nonlinear saturation (anomalous transport) mechanism reduces the polarization field to approximately the same value regardless of whether the primary-scale wave amplitude starts at ten or five percent of the background density. This lends credence to the notion that FBI turbulence arises as a way for the primary wave to get rid of the free energy in its polarization field. In nature, of course, the primary wave does not instantaneously appear but, rather, grows in amplitude self-consistently with its driving process (mostly likely the GDI). Thus it should initiate the FBI as it develops, and the actual feedback processes between large-scale growth and meter-scale saturation will necessarily be more complex than the model results presented here. To view the five-percent cases at 98 km and 96 km in this light, the primary wave simply did not need to resort to the FBI to get rid of the free energy in its polarization electric field.

As the primary-wave polarization field decreases, not only does the total-field magnitude decrease but its angle rotates toward vertical. In the crest, the angle rotates away from westward; in the trough, the angle rotates from eastward. This means that the direction of  $\mathbf{E} \times \mathbf{B}_0$  rotates westward in both cases. The linear theory of §5.2 predicts that FBI waves will travel parallel to the relative electron-ion drift, which in these simulations is effectively the  $\mathbf{E} \times \mathbf{B}_0$  direction, so a westward-rotating  $\mathbf{E} \times \mathbf{B}_0$  direction explains the shift in RMS power toward  $\theta = 0$  between growth and saturation shown at all altitudes in Figure 5.6 and at the two highest altitudes in

Figure 5.7. By the same token, the weak waves that grow in the five-percent run at 98 km propagate closer to vertical in the saturated panel than do waves at higher altitudes because the total electric field driving them has not saturated.

The spectra shown in Figures 5.8 and 5.9 represent idealized radar observations at 50 MHz for  $\lambda = 3$  m, 30 MHz for  $\lambda = 5$  m, and 15 MHz for  $\lambda = 10$  m. They predict that a 50-MHz radar should observe type-I echoes propagating with speeds near the plasma acoustic speed,  $C_s$ , at intermediate elevation angles between horizontal and zenith, and that the spectrum should broaden slightly for higher total electric field. The latter result is simply a consequence of more strongly driven turbulence. The simulated spectra further predict that type-II echoes should be stronger in 30-MHz data than in 50-MHz data; more generally, they predict that type-II power will compete with or overwhelm type-I power at wavelengths slightly longer than the wavelength of peak growth, except at the optimum flow angle for the strongest growing waves. At 15 MHz, these spectra predict a broad angular distribution of type-II echoes with possible type-I signatures at the optimum flow angle. Finally, most of the panels in Figure 5.8, as well as the 102-km and 100-km panels in Figure 5.9, imply that the primary wave drives meter-scale irregularities that propagate in multiple distinct eigenmodes. Only at lower altitudes, for lower total electric field, and at longer wavelength do the individual modes blend into a broad spectrum.

Propagation speeds near  $C_s$  are a well-known feature of type-I echoes in the equatorial electrojet, despite the fact that linear theory (cf. Equation 5.2a) predicts propagation speeds near the relative electron drift speed,  $|\mathbf{u_d}|$ . However, the most robust prediction of linear theory has been that the FBI will develop when  $|\mathbf{u_d}| > C_s (1 + \psi_{\perp})$  – after that, the waves become turbulence and linear theory no longer applies. These simulation results suggest that FBI turbulence reduces the electric field to just above the threshold value, at which point the threshold wave propagation

velocity is roughly  $C_s$ . Therefore, the observation that type-I echoes propagate near  $C_s$  appears to go hand-in-hand with electric-field saturation.

The simulations presented here are subject to a number of assumptions and short-comings. First, they are two dimensional in the plane perpendicular to  $\mathbf{B}_0$ . The parallel direction provides a path for electrons to short out instabilities which is missing from these simulations. However, observations have established that the FBI is highly aspect sensitive, with  $k_{\parallel} \ll |\mathbf{k}_{\perp}|$ , and 2-D simulations still capture much of the crucial instability development.

Second, the constant electric field neither varies with altitude nor responds to the vertical flow. Rocket measurements reported by Pfaff et al. (1997) showed both the zonal and vertical electric fields varying with altitude at the magnetic equator and Kudeki et al. (1985) showed that asymmetric vertical currents develop to reduce the vertical electric field in the equatorial electrojet, thereby enforcing zero flux divergence. However, the fixed-field simulations presented in this paper provide a comparison point for future, more complex simulations.

Third, background plasma density does not vary with altitude, as it does in nature. However, the background plasma density does not factor into the FBI growth rate and therefore should not affect the conclusions significantly.

Fourth, this model assumes isothermal electrons. Anomalous electron heating produces anomalous conductivities which reduce the driving electric field at high latitude, during geomagnetically active conditions (Oppenheim and Dimant, 2013). The missing electron thermal equation is a significant drawback of the current model and will be the subject of future research. Anomalous electron heating would likely affect only the runs with the strongest total electric fields, and only then if the primary waves grow quickly enough to overcome shorting out due to the turbulent transport mechanism shown in these results.

Fifth, the simulation employs periodic boundary conditions. Periodic boundary conditions on the large-scale wave potential may produce non-physical effects by preventing the polarization field from vanishing outside the wave. However, as the GDI develops in nature, there will be many individual waves that are bounded by similar waves on all sides, mimicking the simulated situation. Development of non-periodic boundary conditions will be another subject of future work.

Finally, the sinusoidal initial density distribution, while designed to approximate a single period of a large-scale wave, is nonetheless an idealized case. It does not grow directly due to the GDI but is an imposed initial condition. In nature, the actual feedback processes between large-scale growth and meter-scale saturation will necessarily be more complex than the model results presented here. As km-scale waves grow out of the GDI, they may reach an amplitude that triggers the FBI in a particular region, initiating the negative feedback process illustrated by these simulations. An electrojet developing GDI will be a turbulent mix with a range of wavelengths, each producing polarization electric fields of varying magnitude and direction. The lack of periodic boundary conditions, as described above, preclude simulations with a zeroth-order density gradient, thereby precluding the fully self-consistent development of km-scale GDI waves. This work simply provides another piece to a complex puzzle.

#### 5.6 Conclusion

This chapter presents the first hybrid plasma simulations of meter-scale secondary wave growth driven by a kilometer-scale primary wave. They assume inertialess, isothermal, fluid electrons in quasineutrality with particle ions at four different altitudes in the lower equatorial electrojet. The simulations impose the primary wave as an initial condition but evolve self-consistently thereafter, without recourse to pa-

rameterized turbulent effects. The background electric field is not large enough to drive meter-scale turbulence via the Farley-Buneman instability (FBI), but the total electric field, including the polarization electric field of the primary wave, exceeds the FBI threshold. The FBI produces turbulent density and electric field structures that propagate at an intermediate angle between horizontal and vertical, the direction of which is largely determined by the direction of Hall drift in the total electric field. As density turbulence develops, nonlinear currents transport plasma along meter-scale wave fronts. This anomalous transport shorts out the primary-wave polarization electric field, leading to flat-top fields with average magnitude just above the FBI threshold value. The reduced electric field causes meter-scale waves to propagate near the plasma acoustic speed, corresponding to the near-threshold condition and matching observations of equatorial type-I radar spectra. The results presented here may also have applications to auroral density structures produced by convection, auroral precipitation, and ionospheric cavitation (Zettergren et al., 2015; Mrak et al., 2018).

# Chapter 6

# Variation of the Farley-Buneman Spectrum with Altitude

#### 6.1 Introduction

Observations of coherent, spectrally narrow echoes at high latitudes, where they often get the name "radar aurora", predate the large body of equatorial type-I and type-II observations. Haldoupis et al. (1984) used the bi-static Scandinavian Twin Auroral Radar Experiment (STARE) to make observations of a common volume in the high-latitude E-region. The bi-static setup allowed that author to derive the electron drift direction from the mean Doppler shift in both radars, and to make measurements of irregularity propagation at a range of angles from the electron drift. The angle that the radar LOS makes with the electron drift is the "flow angle". Haldoupis et al. (1984) observed narrow and broad Doppler spectra in the same volume, with narrow spectra coming from flow angles within  $-60^{\circ}$  to  $0^{\circ}$  and broad spectra coming from flow angles within  $-90^{\circ}$  to  $-65^{\circ}$ .

Uspensky et al. (2003) reported a study of joint STARE and European Incoherent Scatter (EISCAT) radar data from a single event during a moderate geomagnetic disturbance. That work emphasized the importance of accounting for non-negligible ion drifts, and the resultant deflection of the phase velocity from  $\mathbf{E}_0 \times \mathbf{B}_0$  by 5°-15°, in VHF observations.

Oppenheim and Dimant (2004) presented results of 2-D PIC simulations that appeared to show the effects of an ion thermal instability, as theoretically explained by Dimant and Oppenheim (2004). The effective altitude of those simulations was 103 km in the high-latitude ionosphere. One important aspect of their simulations, which they attributed to ion thermal effects, was the tendency for ion waves to turn clockwise away from  $\mathbf{E}_0 \times \mathbf{B}_0$ . They observed elevated ion temperatures, especially in regions of reduced density, and suggested that such thermal effects could explain wave turning in earlier simulations by Janhunen (1994b) and Oppenheim et al. (1996). However, they noted that excluding a simulation component parallel to  $\mathbf{B}_0$  may over-emphasize thermal effects.

Oppenheim et al. (2008) presented results from 2-D PIC simulations with improved resolution that allowed those authors to make much more precise statements about the spectral characteristics of ion perturbations than in previous simulations. They claimed that elevated electron and ion temperatures explained the phase velocity of simulated perturbations in terms of an elevated ion acoustic speed. Hysell et al. (2008) presented radar and rocket observations showing that the Doppler shift and spectral width of ion perturbations are related in a relatively simple way to the flow angle, in qualitative agreement with the simulations presented by Oppenheim et al. (2008).

Hysell et al. (2012) reported results from VHF coherent-scatter radar observations during a geomagnetic substorm over Alaska, with an emphasis on aspects of the radar aurora revealed through VHF radar imaging. One goal of that work was to establish a relationship between coherent backscatter from FAI – ultimately caused by the FBI – and F-region incoherent scatter from ion  $\mathbf{E}_0 \times \mathbf{B}_0$  drifts, so that future research could use the former to predict the latter. In order to compare E-region coherent-scatter measurements to F-region incoherent-scatter measurements, they first assumed that

the F-region electric field maps perfectly down magnetic field lines into the E region. They also assumed that the coherent-scatter Doppler velocity and spectral width followed empirical formulas involving the electron drift speed, the ion acoustic speed, the LOS E-region ion drift speed, the LOS flow angle, and an angular correction for wave turning. The final parameter accounts for wave turning effects as seen in Oppenheim and Dimant (2004); Oppenheim et al. (2008). Hysell et al. (2012) set the angular correction to 10° for their analysis and assumed that the observed coherent echoes came from 110 km.

#### 6.2 Simulation Methods and Limitations

This chapter follows radar convention by defining flow angle as the angle between zeroth-order electron drift and LOS. Since electrons drift predominantly in the  $\mathbf{E}_0 \times \mathbf{B}_0$  direction and radars can only observe Doppler shift from echoes propagating parallel or anti-parallel to their LOS, the flow angle is equivalently the angle between  $\mathbf{E}_0 \times \mathbf{B}_0$  and the direction of wave propagation. Where the sign of flow angle is unspecified, the reader may assume that it is negative in a couner-clockwise sense – in terms of physical quantities, it points in a direction between  $\mathbf{E}_0 \times \mathbf{B}_0$  and  $-\mathbf{E}_0$ .

Chapters 4 and 5 described the interaction of meter-scale waves with what many in the aeronomy community would call meso-scale and large-scale waves. This chapter focuses only on the dynamics of meter-scale waves driven by a constant electric field in a small patch of plasma. Whereas Chapters 4 and 5 assumed that thermal effects did not play an appreciable role in meter-scale irregularity development, this chapter allows thermal effects to alter the dynamics of meter-scale waves. To carry out this small-scale, non-isothermal analysis, the simulations described in this chapter used the pure-PIC version of EPPIC in both 2D (perpendicular to  $\mathbf{B}_0$ ) and 3D. See Oppenheim and Dimant (2004) for a description of the advantages and disad-

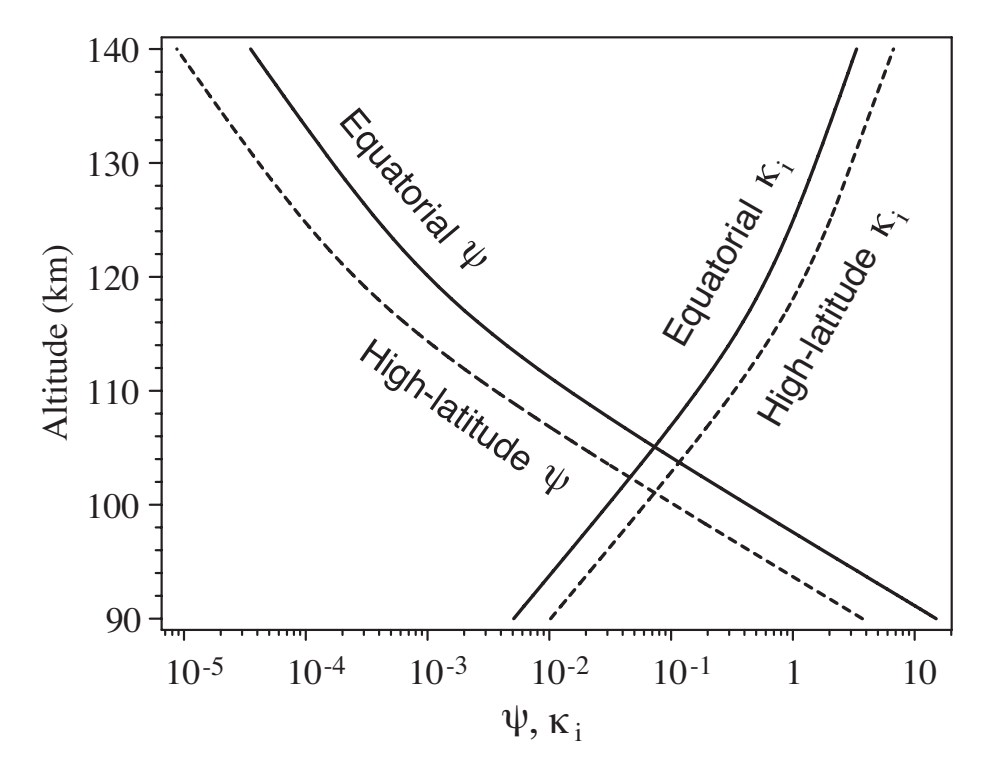


Figure 6.1: Figure 2 from Dimant and Oppenheim (2004), showing theoretical altitudinal profiles of  $\psi$  and  $\kappa_i$  at equatorial and high magnetic latitudes.

vantages of the pure-PIC version of the code. See Oppenheim et al. (2008) for a description of an improvement in parallelizing the 2-D version, and see Oppenheim and Dimant (2013) for a description of the 3-D version.

One major goal of the research presented in this chapter was to determine the change in FBI spectrum with altitude. Neutral density is a good proxy for altitude in the atmosphere, but EPPIC does not use neutral density as a simulation parameter, so the ion and electron collision frequencies,  $\nu_i$  and  $\nu_e$ , specify the equivalent altitude. As Oppenheim and Dimant (2013) explain, the effective collision frequency during a simulation run differs, in general, from the input value. Selecting an input value that will produce an appropriate simulated value requires some care.

Figure 2 in Dimant and Oppenheim (2004), reproduced here in Figure 6·1, provides a way to select collision frequencies corresponding to a desired altitude. The

first step is to identify an appropriate value of  $\psi_{\perp:sim}$  for the desired altitude. Next, we identify the corresponding value of  $\kappa_{i:sim} = \Omega_i/\nu_{i:sim}$  from which we calculate  $\nu_{i:sim}$ . We then use the definition  $\psi_{\perp} \equiv \nu_e \nu_i/\Omega_e \Omega_i$ , to calculate a value for  $\nu_{e:sim}$ :

$$\nu_{e:sim} = \psi_{\perp:sim} \left( \frac{\Omega_i \Omega_{e:sim}}{\nu_{i:sim}} \right)$$
$$= \psi_{\perp:sim} \left( \frac{q_i q_e B_0^2}{m_i m_{e:sim} \nu_{i:sim}} \right)$$

Often,  $\nu_{e:sim} \approx \nu_{i:sim}$ , whereas  $\nu_e \approx 10\nu_i$  in the real E region. With these candidate values for  $\nu_{i:sim}$  and  $\nu_{e:sim}$  in hand, we run two types of simulations with sub-threshold electric fields to validate their values.

The process for validating  $\nu_{i:sim}$  consists of running the simulator with a subthreshold driving electric field,  $E_{y0}$ , and calculating the effective ion collision frequency from the ion Pedersen drift,  $u_{iP}$ , via the zeroth-order drift relation  $\nu_{i:sim} = q_i E_{y0}/m_i u_{iP}$ . The process for validating  $\nu_{e:sim}$  consists of running the simulator with a small parallel electric field,  $E_{\parallel 0}$ , and calculating the effective electron collision frequency from the electron parallel drift,  $u_{e\parallel}$ :  $\nu_{e:sim} = |q_e|E_{\parallel 0}/m_e u_{e\parallel}$ . The resulting collision frequencies are  $\nu_i = 1022 \text{ s}^{-1}$  and  $\nu_e = 965 \text{ s}^{-1}$ , corresponding to 107 km;  $\nu_i = 610 \text{ s}^{-1}$  and  $\nu_e = 671 \text{ s}^{-1}$ , corresponding to 110 km;  $\nu_i = 369 \text{ s}^{-1}$  and  $\nu_e = 491 \text{ s}^{-1}$ , corresponding to 113 km. Many observations of FBI associated with the visible aurora – often called the "radar aurora" – assume that the echoes originate in a volume centered on 110 km. The effectively altitudes of the simulations presented here encompass that altitude to facilitate comparison to observations. Note that this chapter differs from Chapters 4 and 5, which used a constant value of  $\nu_e$  for the electron fluid approximation in hybrid EPPIC. Table 6.1 lists the other parameters used in these simulations.

The ratio of ion mass to electron mass was artificially small for these simulation runs – a common practice in PIC simulations (cf. Chapter 3). Oppenheim and

**Table 6.1:** Simulation Parameters for Chapter 6

Symbol	Value	Unit	Name
$m_{i}$	$5.0 \times 10^{-26}$	kg	ion mass
$m_i/m_e$	1250		mass ratio
$m_n$	$4.6 \times 10^{-26}$	$_{ m K}^{ m kg}$	neutral mass
$egin{array}{c} m_n \ T_i \ T_e \ T_n \end{array}$	600		initial ion temperature
$T_e$	1200	K	initial electron temperature
$T_n$	300	$\mathbf{K}_{\mathbf{k}}$	neutral temperature
$n_0$	$2 \times 10^{8}$	$\mathrm{m}^{-3}$	plasma density
$ u_i$	1022, 611, 369	$s^{-1}$	ion-neutral coll. freq.
$ u_e$	965, 671, 491	$s^{-1}$	electron-neutral coll. freq.
$\psi_{\perp}$	$0.030, 0.013, 5.6 \times 10^{-3}$		anisotropy factor
$\overset{\psi_{\perp}}{h}$	107,110,113	${ m km}$	effective altitude
$B_{y0}$	$5.0 \times 10^{-5}$	${ m T}$	magnetic field
$ B_{y0} \\ E_{z0} \\ L_x \\ dx \\ L_y \\ dy \\ L_t $	50.0	$\mathrm{mV/m}$	vertical electric field
$L_x$	40.96	m m	box length in X direction
dx	0.04,  0.08	$\mathbf{m}$	2D, 3D cell size in X direction
$L_y$	40.96	$\mathbf{m}$	box length in Y direction
$d\mathring{y}$	0.04,  0.08	$\mathbf{m}$	2D, 3D cell size in Y direction
	$\approx 460, \approx 115$	${ m ms}$	2D, 3D time span
$\underline{}$ $dt$	$1.75 \times 10^{-6}, 3.0 \times 10^{-6}$	S	2D, 3D time step

Dimant (2004) noted that the simulation can use an artificially inflated electron mass as long as it maintains the electron and ion Hall and Pedersen drift rates, and the collision and thermalization rates. It must also keep the electron collision frequency large compared to the ion collision frequency, so that electron Landau damping does not become important.

## 6.3 Irregularity growth at meter and decameter scales

The simulations presented in this Chapter have no background density gradients, meaning G=0 in Equation 2.7, and they occur high enough in the E region for ions to have a non-negligible Hall drift, so  $k_x u_{e0} \to \mathbf{k} \cdot \mathbf{u}_D$  in Equation 2.6 (cf. Chapter 2). Finally, they cover both 2-D and 3-D cases, so the following equations for the real frequency and growth rate apply with the caveat that  $k_z=0$  and  $\psi \to \psi_{\perp}$  in

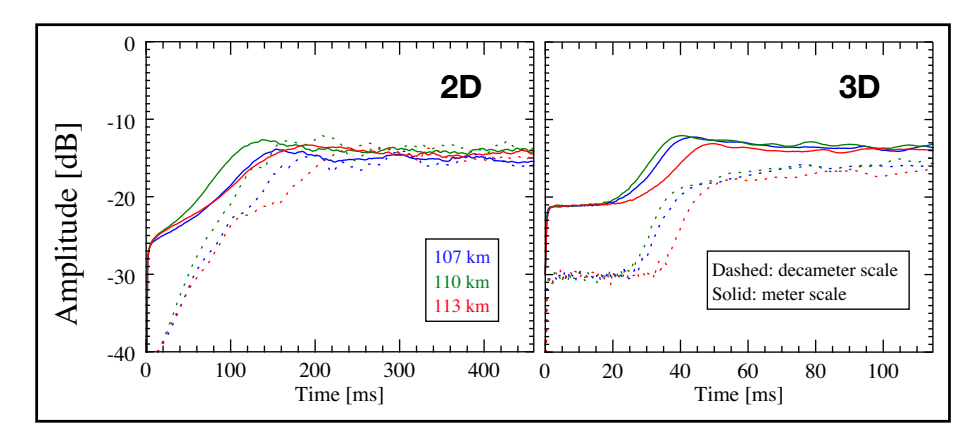


Figure 6.2: Comparison of amplitude in meter-scale density perturbations (solid lines) to amplitude in decameter-scale density perturbations (dashed lines), in both 2-D and 3-D runs. The meter-scale amplitude comprises amplitude in all available modes with 1 m  $\leq \lambda \leq$  4 m. The decameter-scale amplitude comprises amplitude in all available modes with 10 m  $\leq \lambda \leq$  40.96 m. In both panels, the blue trace corresponds to the 107-km run, the green trace to the 110-km run, and the red trace to the 113-km run. Note the difference in time ranges between 2-D and 3-D runs.

2-D runs.

$$\omega_r = \frac{\mathbf{k} \cdot \mathbf{u}_d}{1 + \psi} \tag{6.1a}$$

$$\omega_i = \frac{\psi}{1+\psi} \left( \frac{\omega_r^2 - k^2 C_s^2}{\nu_i} \right) \tag{6.1b}$$

Figure 6·2 shows development of spatially averaged spectral amplitude in meterscale and decameter-scale density perturbations in the plane perpendicular to  $\mathbf{B}_0$ . The 3-D plot contains only strictly perpendicular modes because calculating the full 3-D FFT for all time steps proved prohibitively time-consuming. As such, it misses power in oblique modes, which would cause the growth stage to start slightly earlier than 20 ms.

The analysis routine first interpolated relative perturbed ion density,  $\delta n_i/n_0$ , from the Cartesian simulation grid to a polar grid:  $\delta n_i(k_x, k_y, t) \rightarrow \delta n_i(k, \theta, t)$ , where  $k = \sqrt{k_x^2 + k_y^2}$  and  $\theta = \tan^{-1}(k_y/k_x)$ . Next, it calculates the RMS amplitude as shown in Figure 6.2 via the formula

Amplitude = 
$$\sum_{k=k_{lo}}^{k_{hi}} \left\langle \left| \frac{\delta n(k,\theta,t)}{n_0} \right| \right\rangle_{\theta},$$

where  $\langle \cdots \rangle_{\theta}$  denotes an RMS over  $\theta$ ,  $k_{lo}$  is the wave number corresponding to the longest wavelength in the band, and  $k_{hi}$  is the wave number corresponding to the shortest wavelength in the band. For the meter-scale wave band,  $k_{lo} = (2\pi/4) \text{ m}^{-1}$  and  $k_{hi} = (2\pi/1) \text{ m}^{-1}$ . For the decameter-scale wave band,  $k_{lo} = (2\pi/10) \text{ m}^{-1}$  and  $k_{hi} = (2\pi/40.96) \text{ m}^{-1}$ . All traces exhibit a growth stage, associated with linear behavior, followed by a saturated stage, associated with nonlinear behavior. The zeroth time step in all runs contains isotropic noise from randomly placed particles, and is therefore a few orders of magnitude lower than the first simulation output step; the initial jump does not correspond to instability growth.

In the 2-D runs, both meter-scale amplitude and decameter-scale amplitude begin growing early. The growth rate of decameter-scale waves is about twice that of meter-scale waves so that decameter-scale amplitude reaches saturation soon after meter-scale amplitude despite starting lower. The growth trends in meter-scale and decameter-scale amplitude are similar among altitudes – amplitude at 110 km grows initially fastest, then amplitude at the other two altitudes catches up. In both wavelength bands, amplitude at 107 km saturates at a slightly lower value than at the other two altitudes. Both wave bands saturate at the same amplitude.

The 3-D runs exhibit an initial flat period, with no instability, that the 2-D runs do not. This is not merely a sampling artifact due to the longer 2-D runs – images of just the first twenty seconds (not shown) confirm the the 2-D instability growth starts almost immediately. Meter-scale amplitude in 3-D runs begins growing around 10 ms at 107 km and 110 km, and around 15 ms at 113 km. The run at 110-km run

peaks first, followed after about 5 ms by the run at 107 km, then after about 20 ms by the run at 113 km. The peak meter-scale amplitude varies with altitude but the difference between the highest and lower values is only a factor of two or three.

Decameter-scale amplitude in the 3-D runs begins its growth roughly ten seconds after meter-scale amplitude and again grows faster than meter-scale amplitude, though not as fast as in 2D. Decameter-scale amplitude saturates at approximately the same time that meter-scale growth does, though the peak is not as drastic. Unlike the 2-D case, decameter-scale amplitude saturates at a slightly lower value than meter-scale amplitude.

## 6.4 Average Temperatures

Figure 6·3 shows spatially averaged electron temperature,  $T_e$ , and ion temperature,  $T_i$ , in the Hall, Pedersen, and parallel directions, as functions of time. Temperature is defined as the average kinetic energy of the particle distribution, which is proportional to the second velocity moment of the distribution. This is appropriate for particles with little to no internal energy.

All three components of  $T_e$  during the 3-D runs remain nearly identical, indicating isotropic electron temperature. The 2-D runs show increased  $T_e$  anisotropy with increasing altitude, but the difference is only a few degrees in the parallel component at 113 km. The relative isotropy in  $T_e$  is due to the fact that, though many collisions between electrons and neutrals can cause a significant change to an individual electron's momentum, that net scattering in velocity space occurs much more quickly than the change in kinetic energy. That effect does not change with the values of electric field considered here. The 3-D  $T_e$  recovers after initially cooling, then heats during the growth phase of meter-scale perturbations shown in Figure 6·2. The initial drop in  $T_e$  is a non-physical artifact produced by starting the simulation with

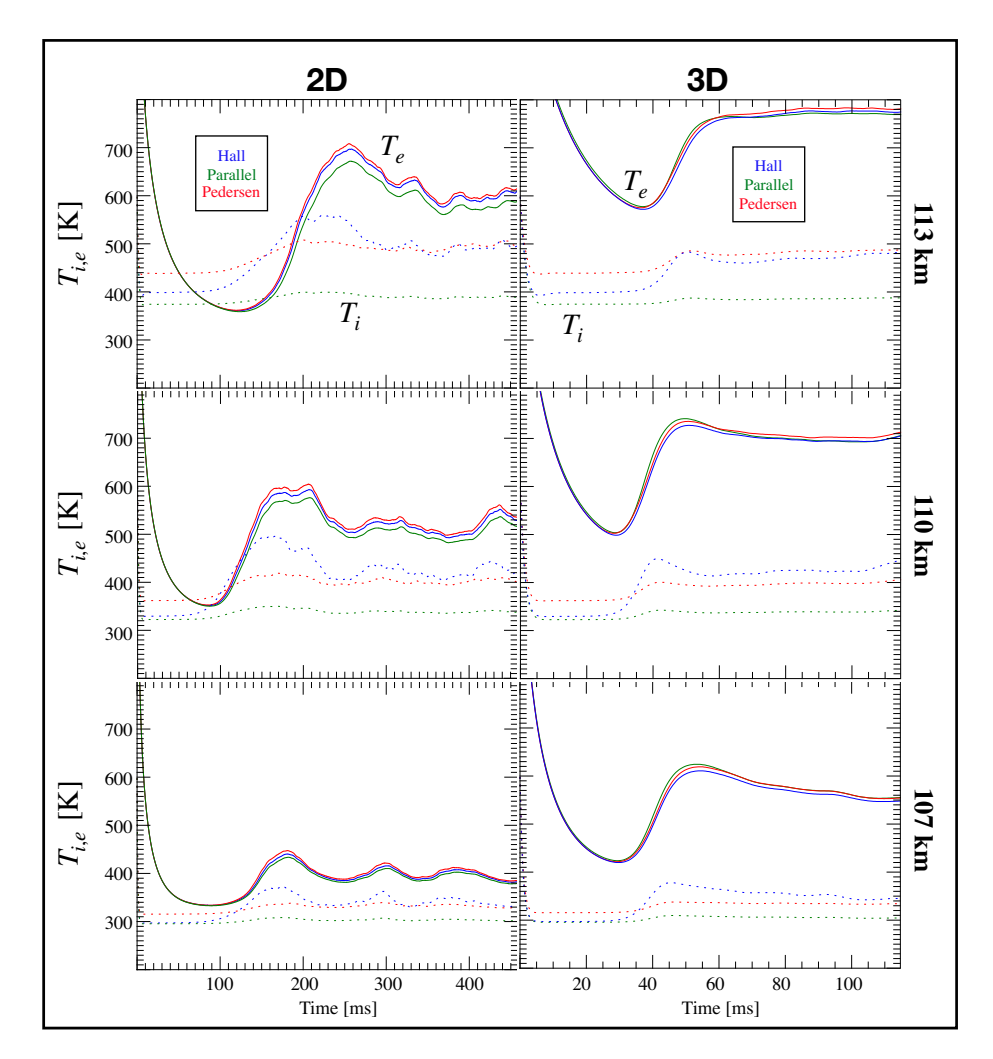


Figure 6.3: Average electron and ion temperatures, computed as functions of time from the respective velocity distributions, for each run. Rows correspond to altitude, from 107 km (bottom) to 113 km (top). The left column shows temperatures in 2-D runs and the right column shows temperatures in 3-D runs. In each panel, the solid traces correspond to electron temperature and the dotted traces correspond to ion temperature. For each species, the blue trace gives the Hall temperature (aligned with  $\mathbf{E}_0 \times \mathbf{B}_0$ ), the green trace gives the parallel temperature (aligned with  $\mathbf{E}_0$ ) and the red trace gives the Pedersen temperature (aligned with  $\mathbf{E}_0$ ). As in Figure 6.2, the time ranges significantly differ between 2-D and 3-D runs.

a relatively hot electron population. The collision routines used in this work check the ratio of the particle velocity to a reference velocity against a normalized random number to calculate the probability of collision. The reference velocity depends on the species' initial thermal velocity, so starting a population with relatively high temperature ensures that the collision model behaves more accurately as the population heats up.

The 2-D  $T_e$  shows a looser correlation to meter-scale perturbation growth but nonetheless undergoes a similar cooling-heating sequence. Both 2-D and 3-D  $T_i$  contain more anisotropy overall, with anisotropy clearly increasing with altitude. The Hall component of  $T_i$  increases abruptly around the time when meter-scale density perturbations reach their peak amplitude and the Pedersen component experiences a smaller temperature increase. These are due to the instability-enhanced Hall and Pedersen mobilities. In 3-D,  $T_e > T_i$  always holds, whereas  $T_e > T_i$  only at 107 km in 2-D. In the real (3-D) ionosphere, we should expect  $T_e > T_i$ . Both 2-D  $T_i$  and  $T_e$  show more amplitude variation after saturation than do their 3-D counterparts, especially at 110 km and 113 km.

# 6.5 Ion Density Perturbations

The FBI is an ion-scale instability. It grows on the ion collisional time scale and the wavelength of peak growth is a few times the ion MFP. The following figures show  $\delta n_i/n_0$  in a slice perpendicular to  $\mathbf{B}_0$  at fiducial points throughout each simulation run.

Figures 6.4, 6.5, and 6.6 show  $\delta n_i/n_0$  in the plane perpendicular to  $\mathbf{B}_0$  at sixteen equally spaced snapshots throughout the 2-D runs at 107 km, 110 km, and 113 km, respectively. The first panel of each figure captures roughly the beginning of the growth stage and the final panel comes from the final time step. Images from time

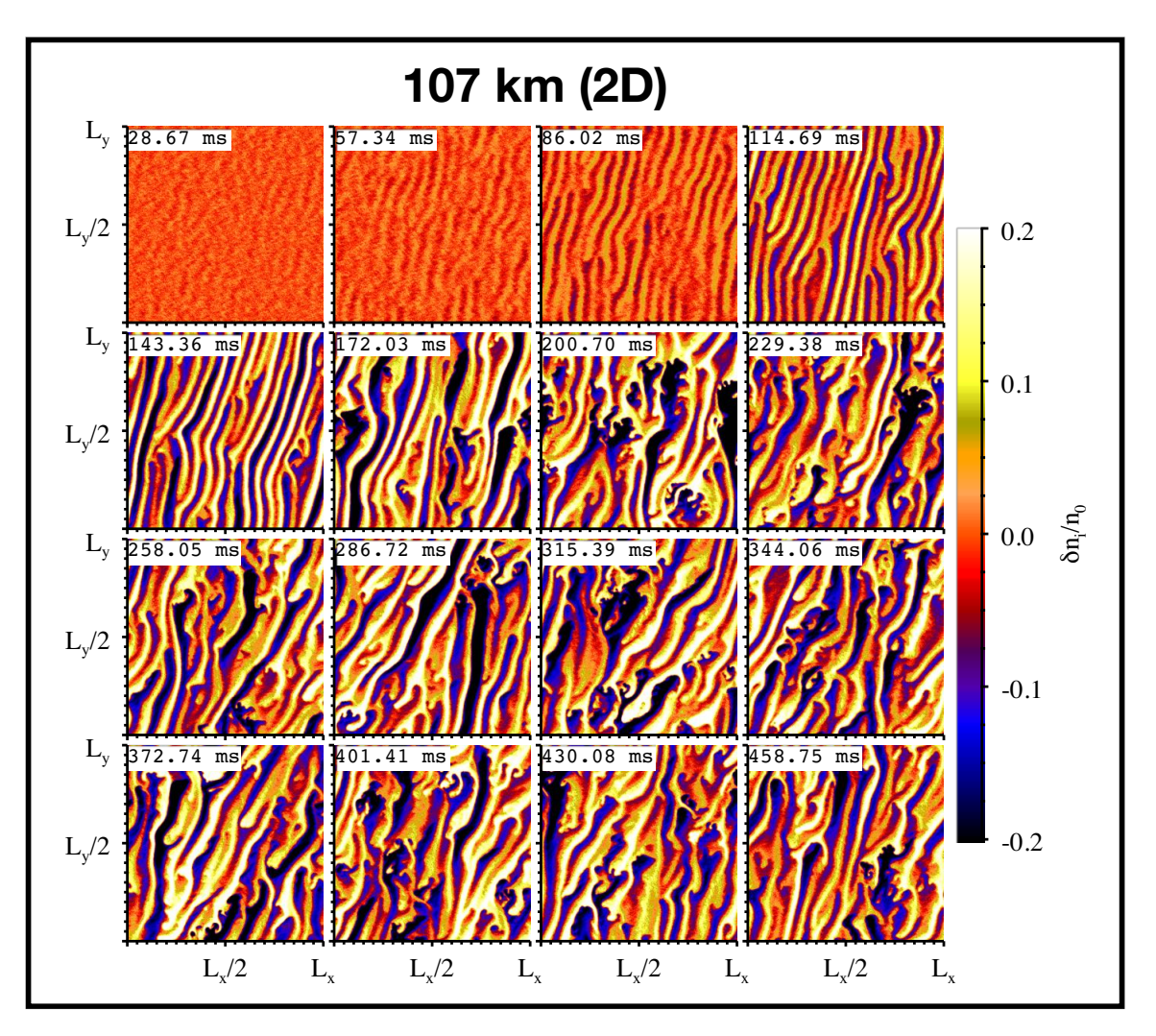
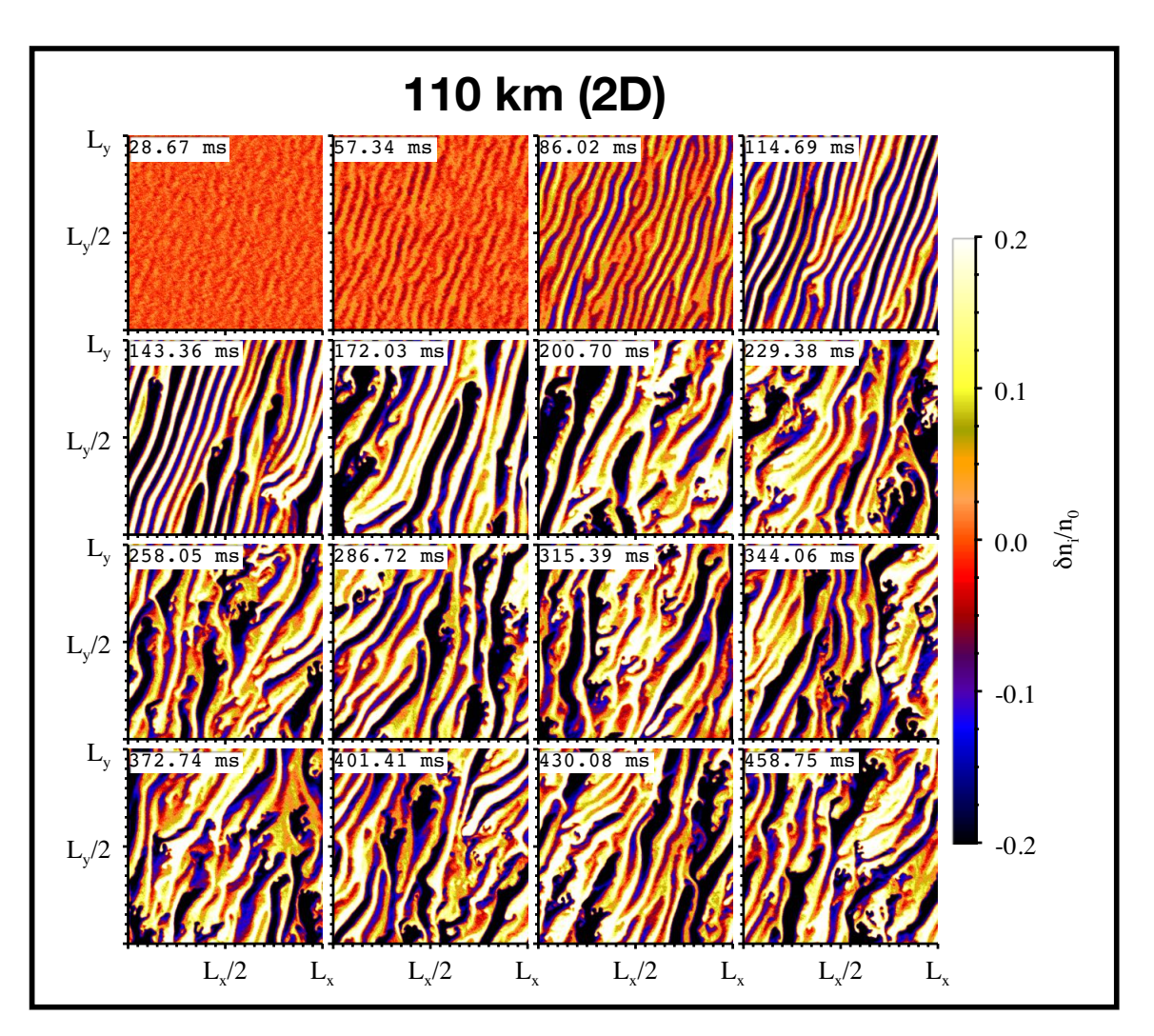


Figure 6.4: Relative perturbed ion density,  $\delta n_i/n_0$ , at sixteen time steps throughout the 2-D run at 107 km. The time stamp of each panel is in the upper left corner. Each panel spans 40.96 m× 40.96 m, covering the entire physical area perpendicular to  $\mathbf{B}_0$ . The color scale for all panels ranges from -0.2 to +0.2, or -20% of  $n_0$  to +20% of  $n_0$ 



**Figure 6.5:** Relative perturbed ion density,  $\delta n_i/n_0$ , at sixteen time steps throughout the 2-D run at 110 km. The layout is identical to that of Figure 6.4.

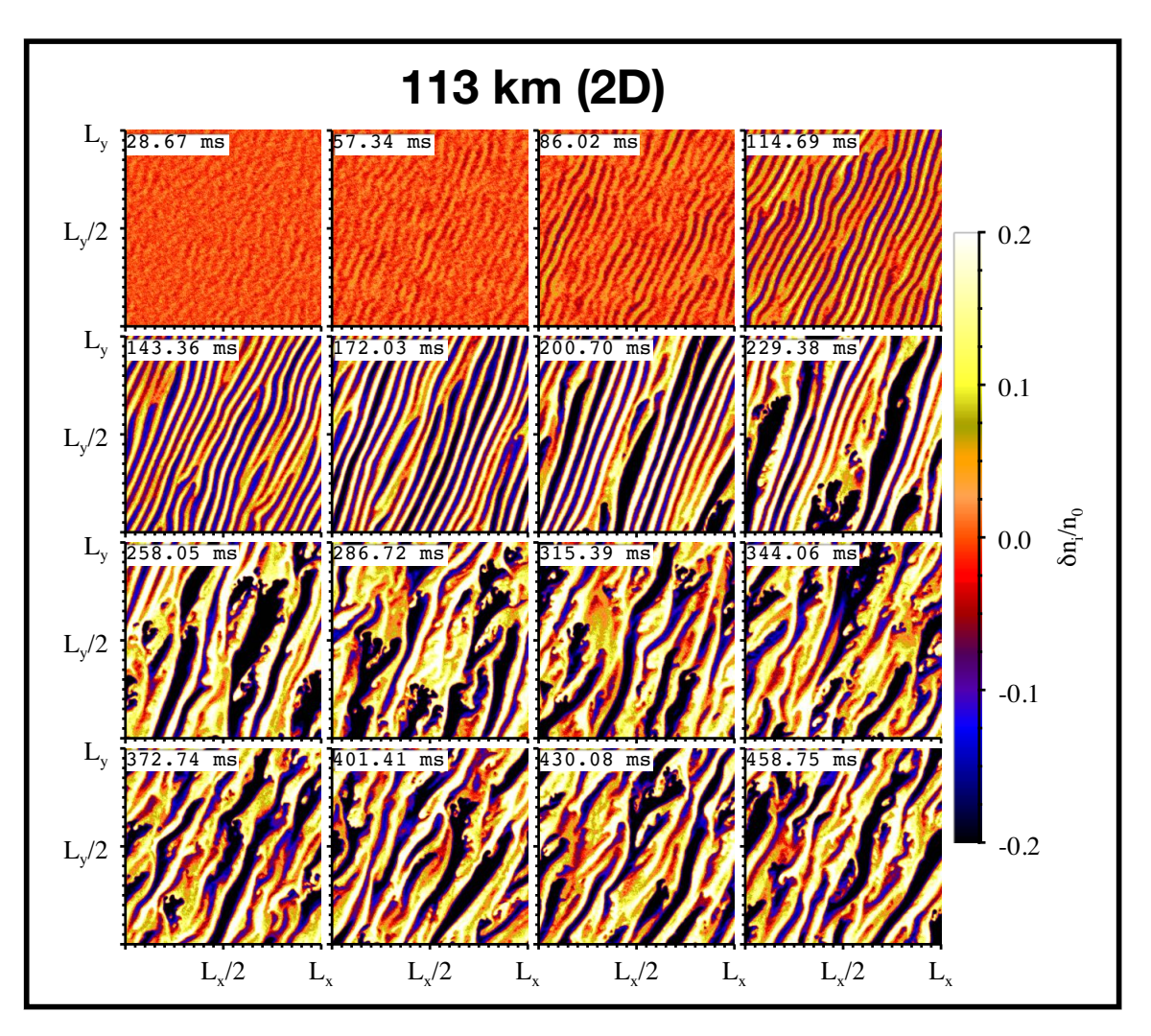


Figure 6.6: Relative perturbed ion density,  $\delta n_i/n_0$ , at sixteen time steps throughout the 2-D run at 113 km. The layout is identical to that of Figure 6.4.

steps before the first panel show isotropic noise.

The thin, elongated structures that grow out of noise in the first four panels (up to t = 114.69 ms) of Figures 6.4 and 6.5 are a good example of linearly growing FBI waves. Spatial spectra, shown in later figures, indicate that these structures have wavelengths between two and three meters. By the fifth panel (t = 143.36ms) of those two figures, the linear-stage structures have begun to bend and mix together, so that by the next panel (t = 172.03 ms), they have lost their thin, roughly monochromatic form. Movies of density evolution show an inverse cascade – the instability grows at a wavelength of a few meters, then those meter-scale waves merge to form a range of longer wavelength waves. Figure 6.2 2D shows that meterscale perturbations saturate at approximately 140 ms at 107 km and at approximately 160 ms at 110 km, meaning that the fifth and sixth panels in Figures 6.4 and 6.5 show the transition from the linear instability growth phase to the non-linear saturated phase. Figure 6.6 contains similar linear-stage structures that transition to non-linear structures but the transition comes around t = 200.70 ms. Again, this transition in the shape of density irregularities is consistent with the fact that meter-scale perturbations peak around 180 ms in Figure 6.2 2D. By the final panel at each altitude,  $\delta n_i/n_0$  is fully non-linear.

Figures 6·7, 6·8, and 6·9 show  $\delta n_i/n_0$  at sixteen equally spaced snapshots throughout the 3-D runs at 107 km, 110 km, and 113 km, respectively. All 3-D runs show the same linear growth followed by a saturated non-linear stage as the 2-D runs showed, and the progression illustrated by Figures 6·7 through 6·9 again follows the corresponding traces in Figure 6·2.

In Figures 6.4 through 6.9,  $\delta n_i/n_0$  displays a characteristic tilt that develops as soon as perturbations rise above the noise level. The tilt is relatively consistent during the linear growth stage of a given run but it varies among all runs. The most

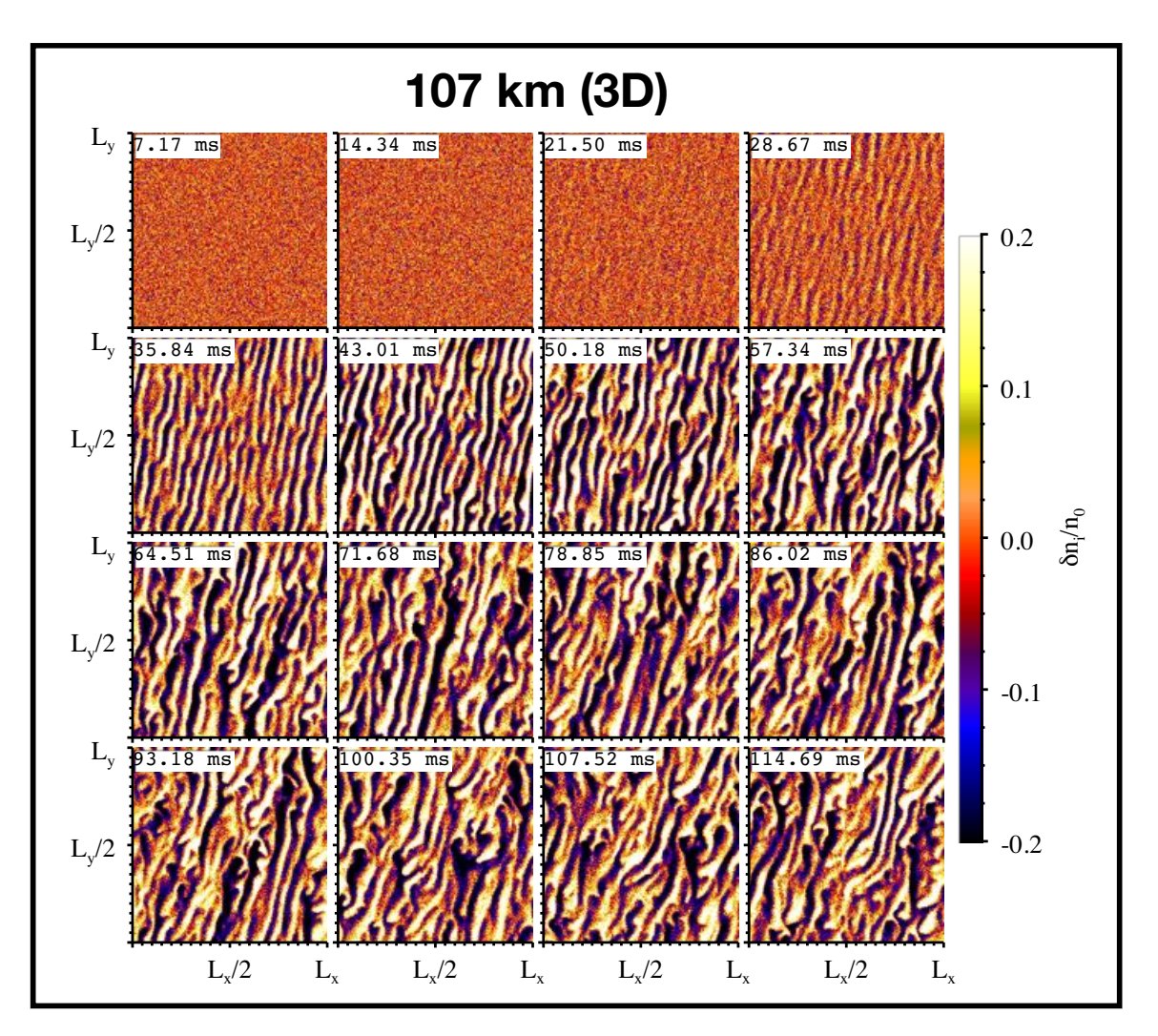
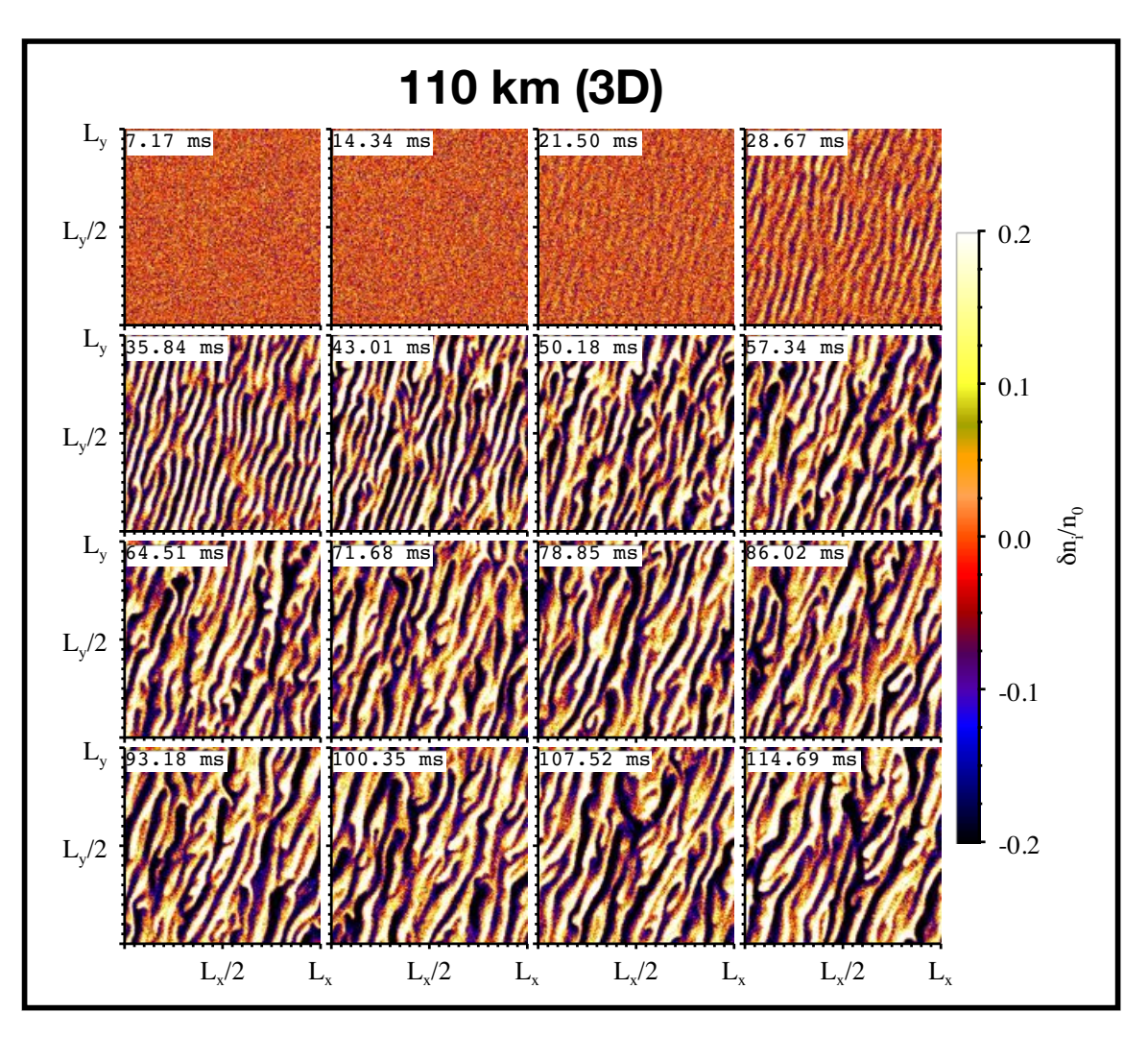


Figure 6.7: Relative perturbed ion density,  $\delta n_i/n_0$ , at sixteen time steps throughout the 3-D run at 107 km. The layout is identical to that of Figure 6.4 except that the time steps are different, since the 3-D runs cover a quarter as much time as do the 2-D runs.



**Figure 6.8:** Relative perturbed ion density,  $\delta n_i/n_0$ , at sixteen time steps throughout the 3-D run at 110 km. The layout is identical to that of Figure 6.7.

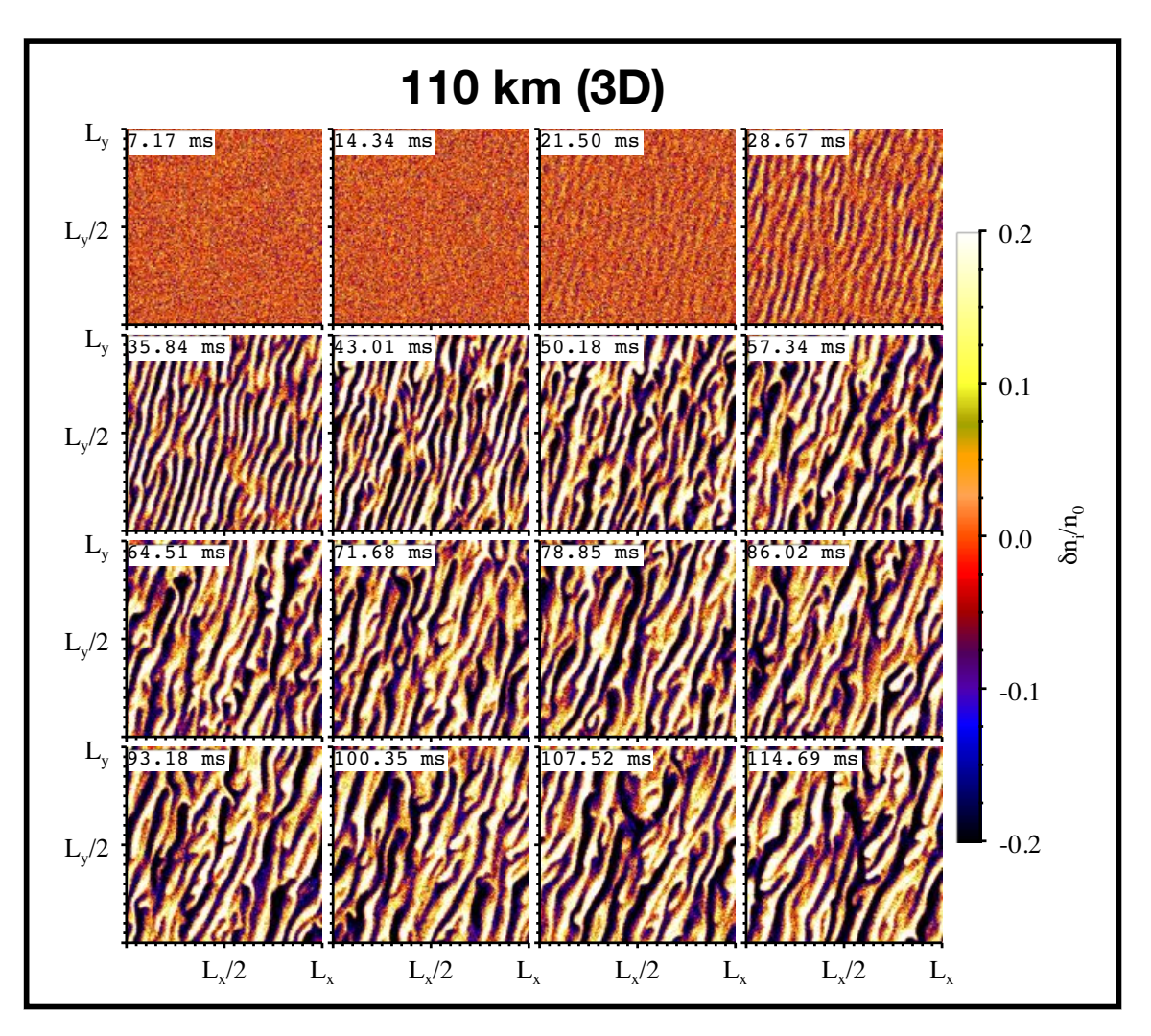


Figure 6.9: Relative perturbed ion density,  $\delta n_i/n_0$ , at sixteen time steps throughout the 3-D run at 113 km. The layout is identical to that of Figure 6.7.

noticeable variation is between altitudes in either the 2-D or 3-D set, but there is also some difference between the 2-D and 3-D runs at a given altitude. Naturally, this linear-stage tilt is more difficult to define for non-linear waves – that is, for  $\delta n_i/n_0$  after saturation. Section 6.6 will show that it exists and section 6.8 will quantify it with respect to the directions of  $\mathbf{E}_0 \times \mathbf{B}_0$ , relative drift, and the theoretical optimal flow angle after accounting for ion thermal effects.

## 6.6 Perturbed Ion Density Spectra

Figures 6·10, 6·11, and 6·12 show  $\delta n_i/n_0$  squared spectral amplitude in the plane perpendicular to  $\mathbf{B}_0$  in 2-D runs, at the same sixteen snapshots as shown in Figure 6·4. The analysis routine produced each panel by computing the Fast Fourier Transform (FFT) of the  $\delta n_i/n_0$  data shown in the corresponding panel in Figure 6·4, Figure 6·5, or Figure 6·6, then normalizing that FFT image to its peak value.

Each run begins with two concentrations of power: One near  $k_x = +\pi$  with  $k_y < 0$ , and the same feature reflected about the origin. Because density is a real quantity, it should be symmetric with respect to a sign reversal in both  $k_x$  and  $k_y$ . In the first panel, spectral noise surrounds the regions of relatively high power, consistent with the presence of only very low-amplitude perturbations in the first panel of each of the  $\delta n_i/n_0$  figures. The concentrations in spectral power move toward the origin slightly as the signal-to-noise ratio (SNR) increases but remain near k values equivalent to few-meter wavelengths. They are the spectral signatures of the thin, elongated structures in images of  $\delta n_i/n_0$  during the linear growth stage.

As each run progresses, power spreads from the meter-scale peaks toward longer wavelengths (lower k) and the isolated concentrations give way to a single structure. The spreading of spectral power represents an inverse cascade during the transition from linear growth to non-linear saturation as the linear modes described by Equa-

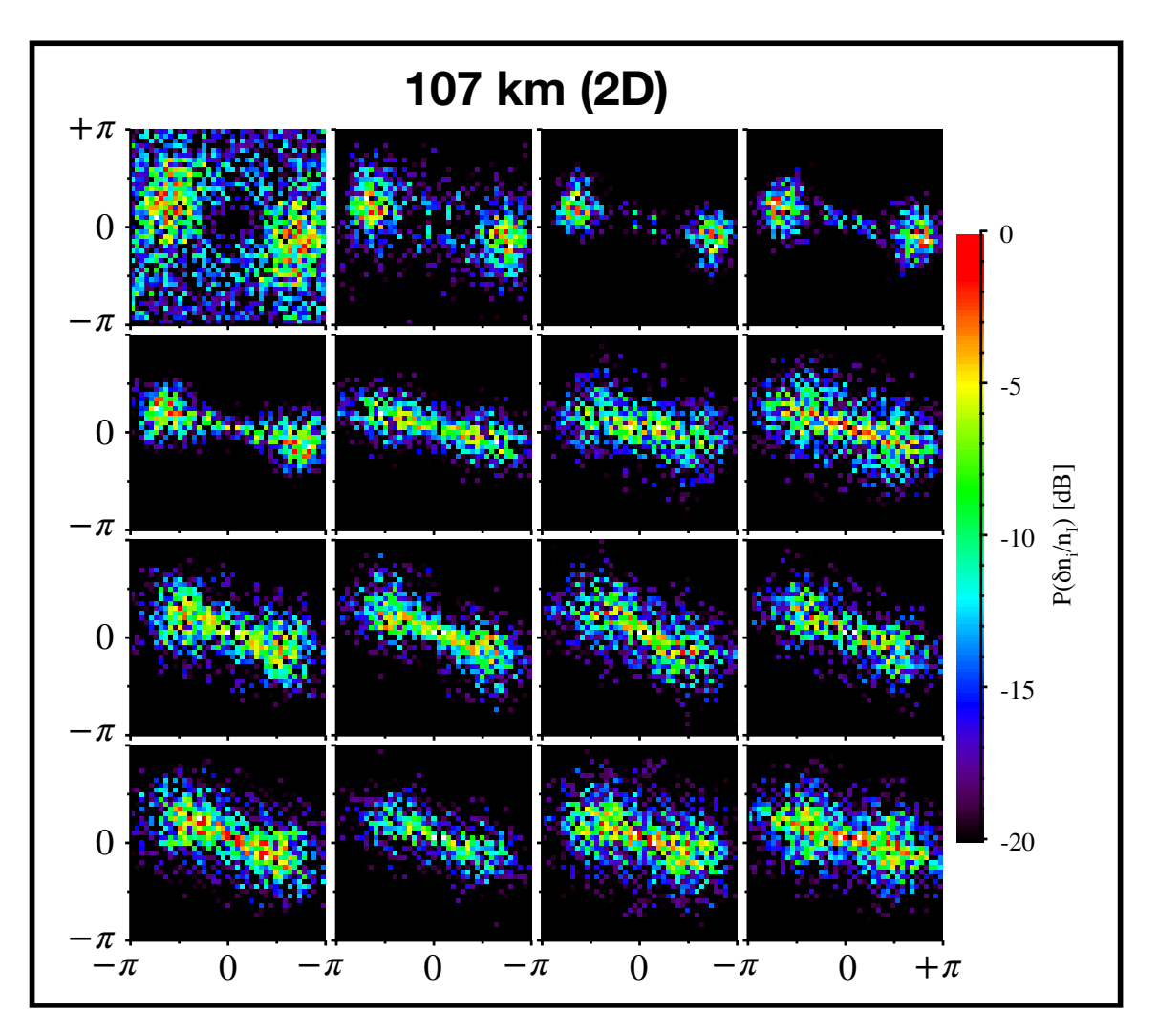
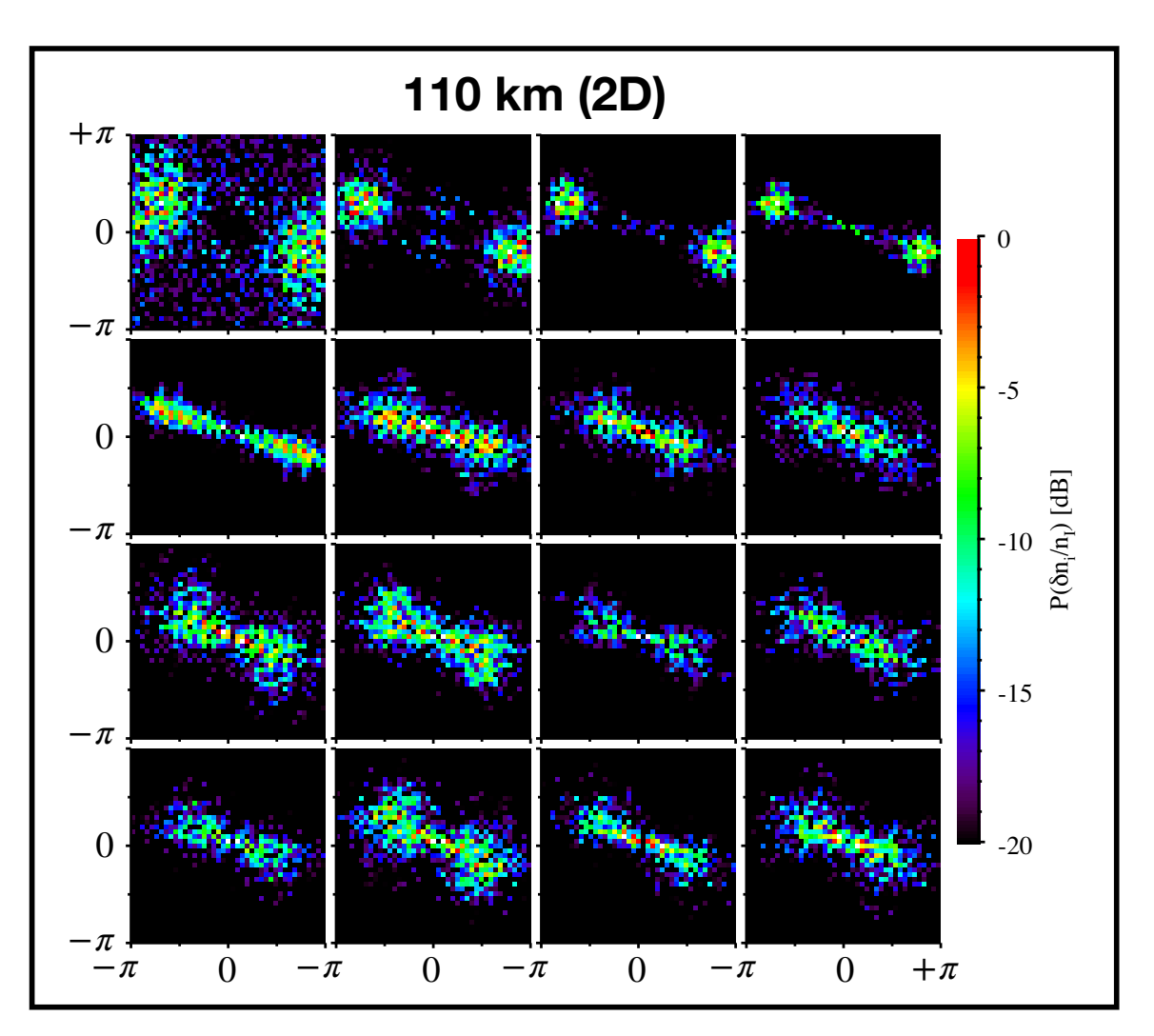
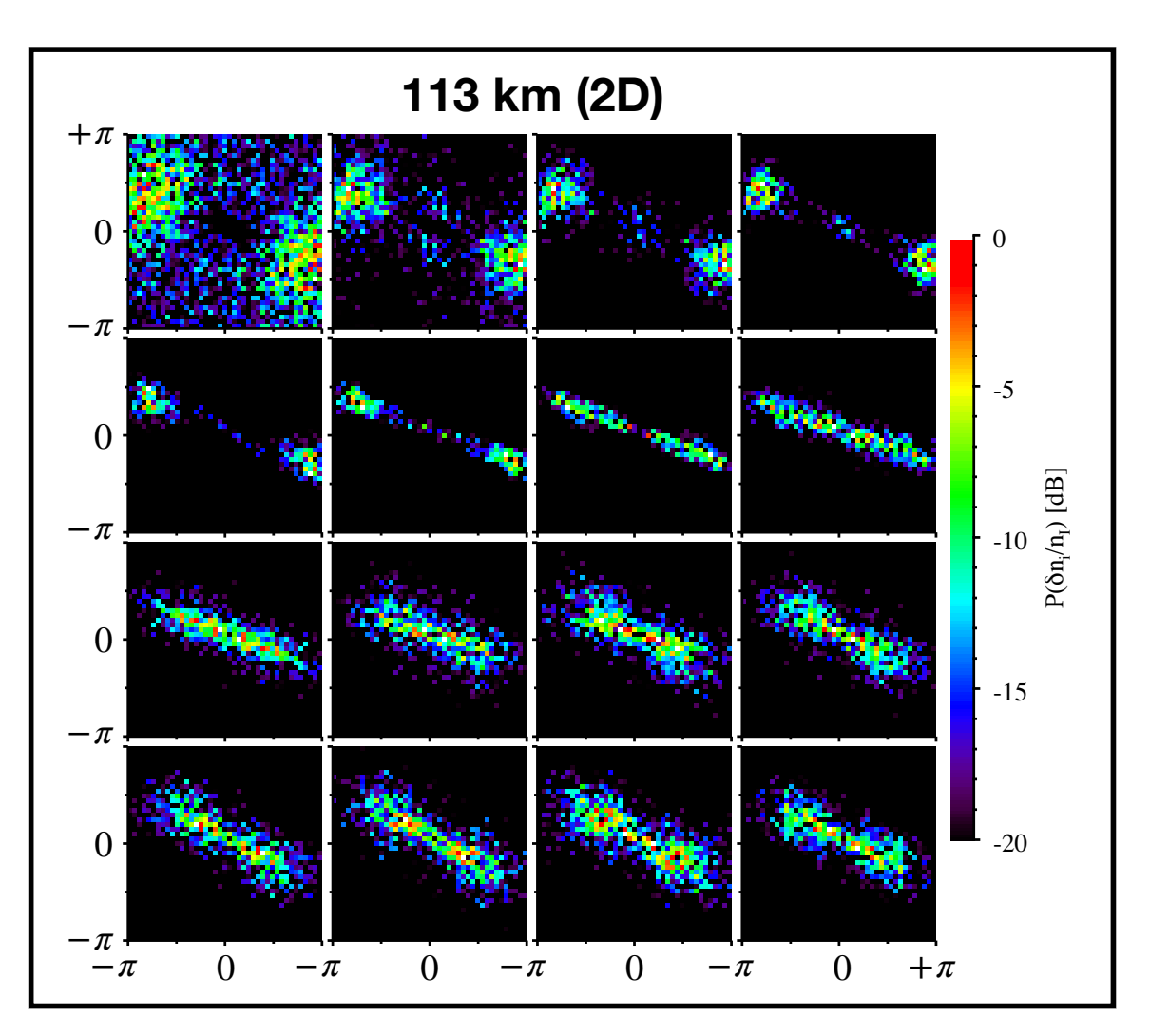


Figure 6·10: Self-normalized log squared spectral amplitude in relative ion density perturbation,  $\langle \delta n_i/n_0 \rangle^2$ , during the 2-D run at 107 km. Panel times correspond to the sixteen time steps shown in Figure 6·4. Each panel spans slightly more than  $-\pi$  to  $+\pi$  in  $k_x$  and  $k_y$ . The color scale for all panels ranges from -20 dB to 0 dB, or two orders of magnitude in power.



**Figure 6.11:** Self-normalized log squared spectral amplitude in relative ion density perturbation,  $\langle \delta n_i/n_0 \rangle^2$ , during the 2-D run at 110 km. The layout is identical to that of Figure 6.10.



**Figure 6·12:** Self-normalized log squared spectral amplitude in relative ion density perturbation,  $\langle \delta n_i/n_0 \rangle^2$ , during the 2-D run at 113 km. The layout is identical to that of Figure 6·10.

tions 6.1a and 6.1b couple energy into each other.

Figures 6·13, 6·14, and 6·15 show  $\delta n_i/n_0$  squared spectral amplitude in the plane perpendicular to  $\mathbf{B}_0$  in the 3-D runs, at the same sixteen snapshots as shown in Figure 6·7. In 3D, oblique modes with a nonzero, albeit small, component parallel to  $\mathbf{B}_0$  dominate the FBI spectrum during growth whereas the saturated spectrum is essentially isotropic in the plane perpendicular to  $\mathbf{B}_0$  (see, for example, Oppenheim and Dimant (2013) Figure 9). In order the capture the important growth-stage oblique modes, the FFT analysis procedure computed the mean value over five pixels in  $k_{\parallel}$ . This range corresponds to an aspect angle of roughly 2°. The true FBI grows at a much smaller aspect angle but the elevated electron mass in our simulations artificially increases the angle of peak growth. Furthermore, limitations on 3-D box size make the parallel resolution too poor to properly resolve aspect sensitivity. The five-pixel mean captures all the growth-stage power in oblique modes without unnecessarily introducing noise. It also increases the SNR of 3-D spectra.

Each 3-D run begins similar to its 2-D counterpart, with oblique modes contributing to the growth-stage spectrum via the five-pixel mean. Images of purely perpendicular modes (not shown) contain very little power in the meter-scale clumps so evident in the first few frames in both 2D and 3D.

The tilt of  $\delta n_i/n_0$  structures during the linear stage of Figures 6·4 through 6·6 is clear in Figures 6·13 through 6·15. In each panel of all spectral figures, a straight line through the middle of relatively high power would extend from the  $(k_x < 0, k_y > 0)$  quadrant to the  $(k_x > 0, k_y < 0)$ , quadrant. This indicates a universal negative angular deflection from  $\mathbf{E}_0 \times \mathbf{B}_0$  – in other words, a non-zero flow angle in all runs. Moreover, the angular deflection after saturation is much clearer in  $\delta n_i/n_0$  spectra than in the raw  $\delta n_i/n_0$  images.

Before proceeding to a quantitative analysis of the flow-angle deflection of meter-

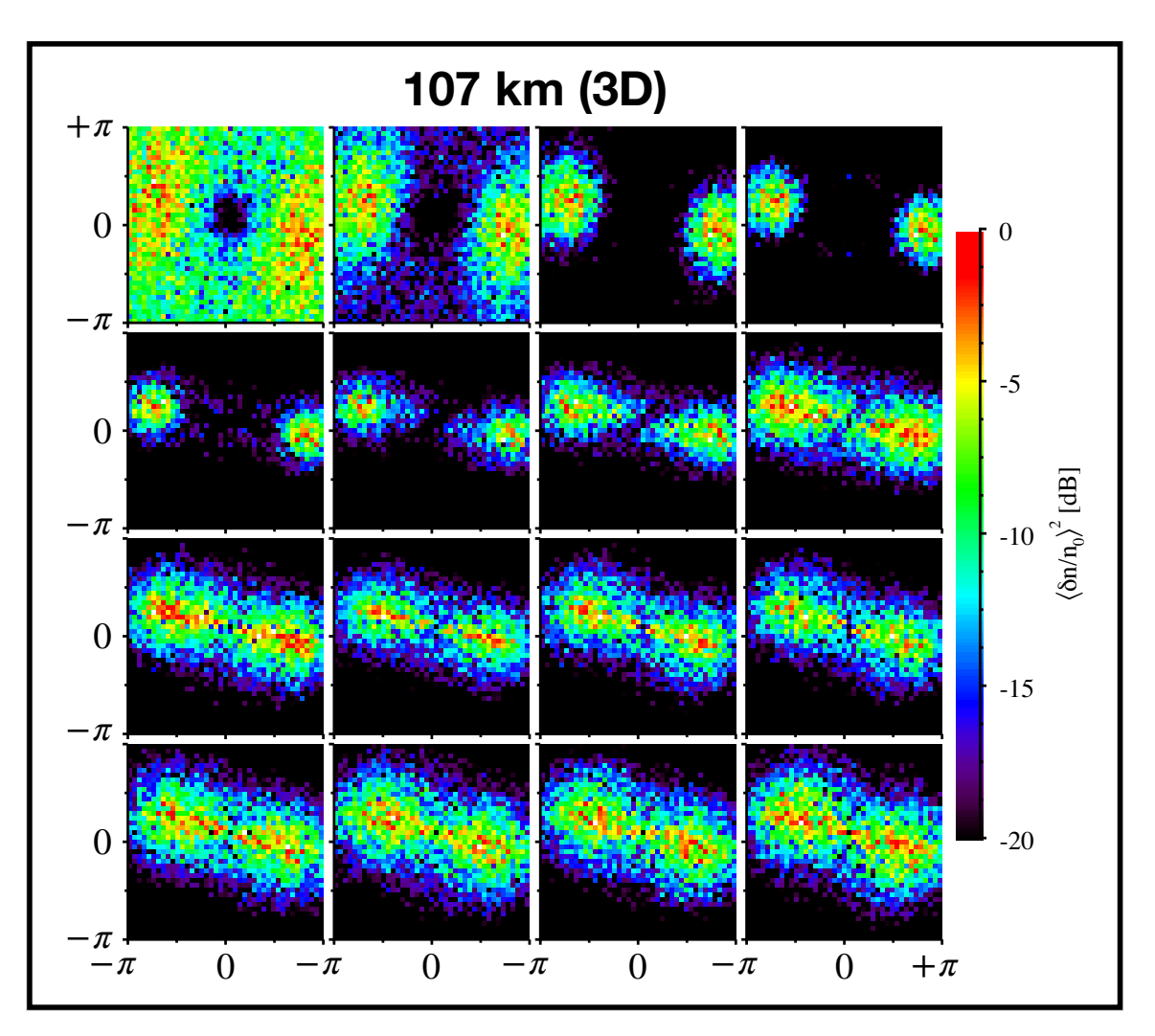


**Figure 6·13:** Self-normalized log squared spectral amplitude in relative ion density perturbation,  $\langle \delta n_i/n_0 \rangle^2$ , during the 3-D run at 107 km. Panel times correspond to the sixteen time steps shown in Figure 6·7. The layout is otherwise identical to that of Figure 6·10.

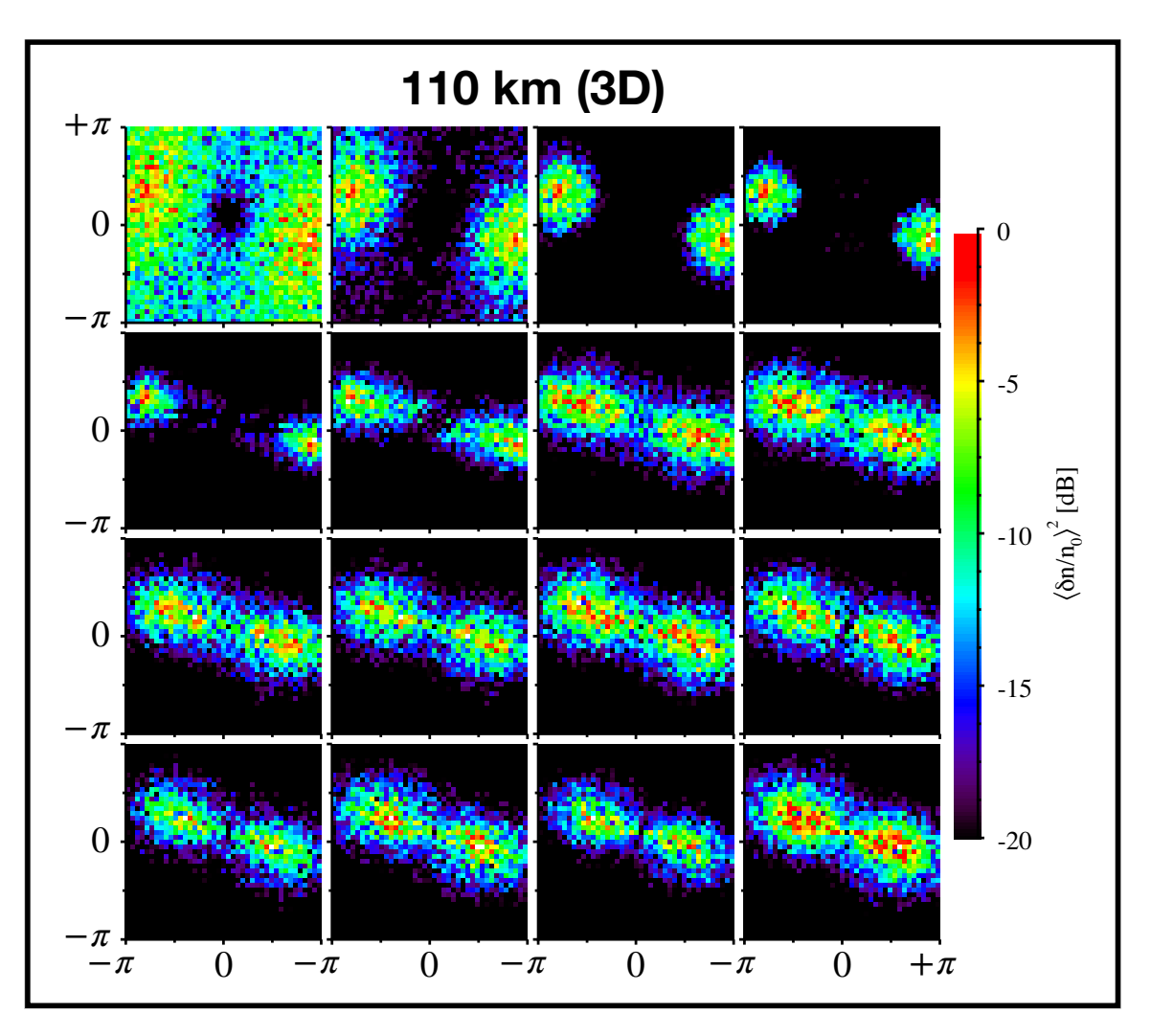


**Figure 6.14:** Self-normalized log squared spectral amplitude in relative ion density perturbation,  $\langle \delta n_i/n_0 \rangle^2$ , during the 3-D run at 110 km. The layout is identical to that of Figure 6.13.

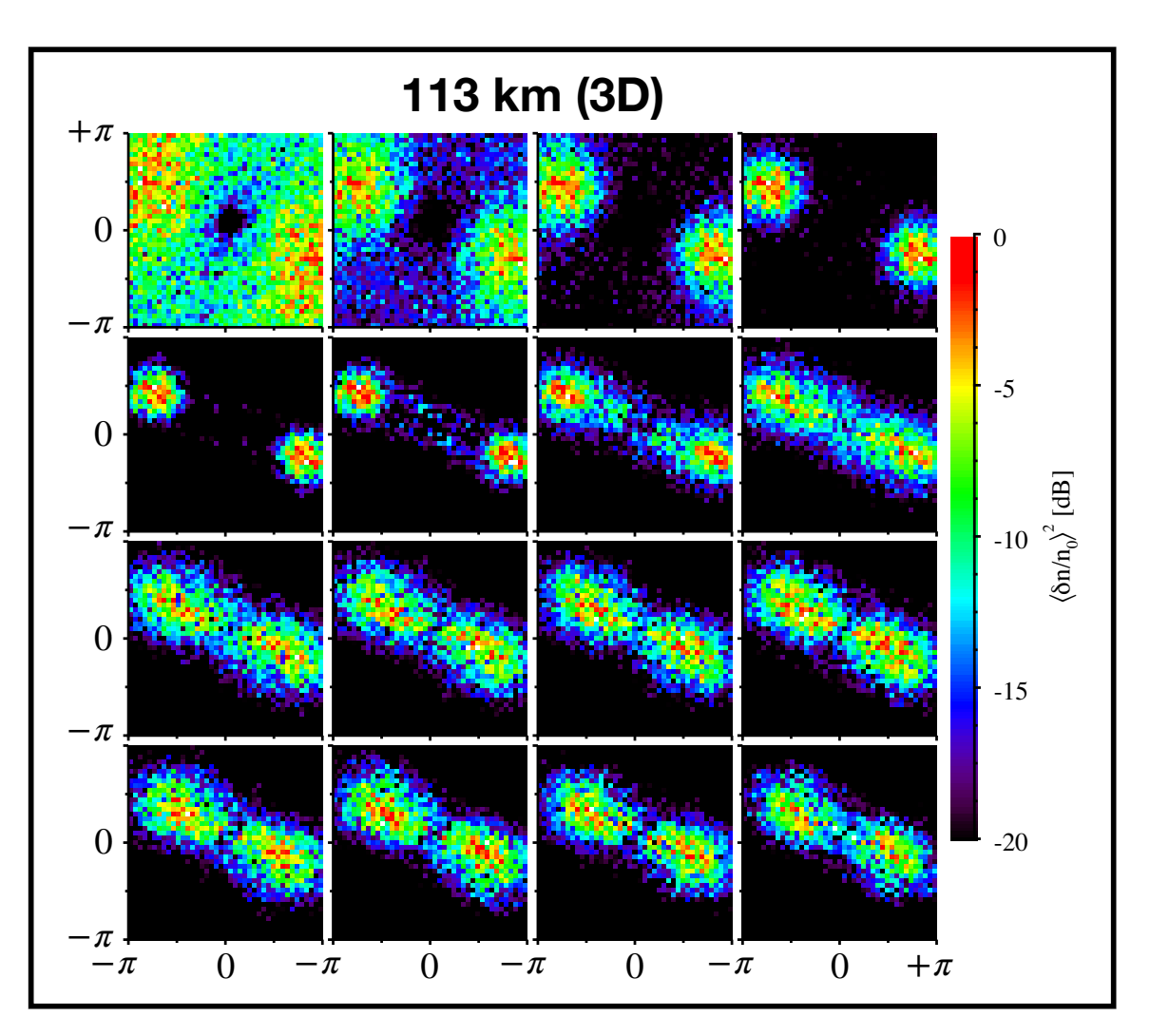


**Figure 6.15:** Self-normalized log squared spectral amplitude in relative ion density perturbation,  $\langle \delta n_i/n_0 \rangle^2$ , during the 3-D run at 113 km. The layout is identical to that of Figure 6.13.

scale perturbations, §6.7 will describe effects introduced by a relatively recently proposed instability due to non-isothermal ion perturbations. These thermal effects likely contribute to observed wave turning under certain conditions.

## 6.7 Thermal Instability Effects

Dimant and Sudan (1995a,b,c) predicted, with a rigorous kinetic analysis, the existence of a theretofore unknown electron thermal instability (ETI) that should arise in the upper-D/lower-E region ionosphere, and grow at wavelengths around ten meters. Blix et al. (1996) presented evidence of the ETI in rocket data and Dimant and Sudan (1997) presented a simplified physical model that connected the rocket observations to their earlier kinetic analysis. Kagan and Kelley (2000) developed a theory of ion thermal perturbations driven by ion-neutral frictional heating in the electrostatic field produced by the dynamo effect of a neutral wind, which they used to explain type-2 echoes at midlatitude. Similar to the Dimant and Sudan (1997) electron thermal instability, it heats regions of relatively low plasma density and cools regions of relatively high plasma density.

Dimant and Oppenheim (2004) extended the Dimant and Sudan (1997) theory of the ETI to ions in 2D and discovered that an analogous ion thermal instability (ITI) should exist in the electrojet, roughly coincident with the FBI. Furthermore, they predicted that the ITI should grow at wavelengths of a few meters, similar to the FBI, resulting in a combined instability. Both the ETI and ITI growth rates peak at  $-45^{\circ}$  from  $\mathbf{E}_0 \times \mathbf{B}_0$ . In the case of the combined FBI+ITI, this can cause an angular deflection from the zeroth-order Hall direction in addition to that produced simply by the deviation of  $\mathbf{u}_d$ .

This work will follow Dimant and Oppenheim (2004) in representing the angle between the zeroth order drift and perturbation flow as  $\chi$ . At the altitudes of interest

for this study, the optimal deviation of k from  $\mathbf{u}_d$  (toward  $-\mathbf{E}_0$ ) for the combined instability,  $\chi_{\mathrm{opt}}^{\mathrm{CI}}$ , is only a few degrees, while the optimal angle between k and  $\mathbf{E}_0 \times \mathbf{B}_0$  falls in the range  $-10 \le \theta_{\mathrm{opt}}^{\mathrm{CI}} \le -30$ . Due to the small predicted value of  $\chi_{\mathrm{opt}}^{\mathrm{CI}}$ , the effects of the ITI can be difficult to isolate from the combined instability.

Both thermal instabilities arise due to  $\mathbf{J} \cdot \delta \mathbf{E}$  heating of density depletions when  $\delta \mathbf{E}$  has a component parallel to  $-\mathbf{E}_0$  that results in a phase offset between temperature and density perturbations. In an isothermal plasma with an electric field below the FBI threshold, temperature perturbations in phase with density perturbations cause the former to smooth out the later. For thermal instabilities, the tandem effects of the background electric field,  $\mathbf{E}_0$ , and the wave polarization electric field,  $\delta \mathbf{E}$ , produce temperature modulations via collisional friction. In the optimal case, the temperature perturbations are  $180^{\circ}$  out of phase with density perturbations, reversing the usual stabilizing effect. The destabilization comes about when regions of high temperature are in phase with regions of low density, leading the pressure increase from the relatively high temperature to drive additional plasma out of the already depleted regions. Likewise, regions of low temperature in phase with high density reduce the pressure locally, allowing additional plasma to flow into those regions and increase the already high density.

Equation 40 in Dimant and Oppenheim (2004) gives an expression for the complex ratio of Fourier-transformed perturbations in ion temperature,  $\tau_i \equiv \delta T_{i\mathbf{k}}/T_{i0}$ , to Fourier-transformed perturbations in ion density,  $\eta_i \equiv \delta n_i/n_0$ , in the plane perpendicular to  $\mathbf{B}_0$ :

$$\frac{\tau_i}{\eta_i} = \frac{2}{3} \frac{\kappa_i \nu_i \left( u_d / v_{i,th} \right)^2 \sin \chi \cos \chi - ik u_d \cos \chi}{\nu_i - ik u_d \cos \chi}$$

The real and imaginary parts of this equation are

$$\Re\left[\frac{\tau_i}{\eta}\right] = \frac{2}{3} \frac{\kappa_i \left(\nu_i u_d / v_{ith}\right)^2 \sin \chi \cos \chi + (k u_d \cos \chi)^2}{\nu_i^2 + (k u_d \cos \chi)^2}$$

$$\Im\left[\frac{\tau_i}{\eta}\right] = \frac{2}{3} \frac{\nu_i k u_d \cos \chi \left[\kappa_i \left(u_d / v_{ith}\right)^2 \sin \chi \cos \chi - 1\right]}{\nu_i^2 + (k u_d \cos \chi)^2}$$

Defining  $\rho \equiv \tau_i/\eta$ , the phase relationship between temperature and density perturbations is

$$\varphi(k,\chi) = \tan^{-1} \left[ \frac{\Im(\rho)}{\Re(\rho)} \right]$$
$$= \tan^{-1} \left[ \frac{\nu_i k u_d \cos \chi \left[ \kappa_i \left( u_d / v_{ith} \right)^2 \sin \chi \cos \chi - 1 \right]}{\kappa_i \left( \nu_i u_d / v_{ith} \right)^2 \sin \chi \cos \chi + (k u_d \cos \chi)^2} \right]$$

This expression in terms of  $\chi$  becomes an expression in terms of  $\theta$  via the relation  $\chi = \theta - \beta$ , where  $\beta$  is the angle that  $\mathbf{u}_d$  makes with the  $\mathbf{E}_0 \times \mathbf{B}_0$  direction. The expression in terms of  $\tan \varphi(k, \theta)$  is

$$\tan \varphi(k,\theta) = \frac{\nu_i k u_d \cos(\theta - \beta) \left[\kappa_i \left(u_d / v_{ith}\right)^2 \sin(\theta - \beta) \cos(\theta - \beta) - 1\right]}{\kappa_i \left(\nu_i u_d / v_{ith}\right)^2 \sin(\theta - \beta) \cos(\theta - \beta) + \left[k u_d \cos(\theta - \beta)\right]^2}$$

$$= \frac{\nu_i k u_d \left(C_\theta C_\beta + S_\theta S_\beta\right) \left[\kappa_i \left(u_d / v_{ith}\right)^2 \left(S_\theta C_\beta - C_\theta S_\beta\right) \left(C_\theta C_\beta + S_\theta S_\beta\right) - 1\right]}{\kappa_i \left(\nu_i u_d / v_{ith}\right)^2 \left(S_\theta C_\beta - C_\theta S_\beta\right) \left(C_\theta C_\beta + S_\theta S_\beta\right) + \left(k u_d\right)^2 \left(C_\theta C_\beta + S_\theta S_\beta\right)^2}$$

In the final line,  $C_{\theta} \equiv \cos \theta$ ,  $C_{\beta} \equiv \cos \beta$ ,  $S_{\theta} \equiv \sin \theta$ , and  $S_{\theta} \equiv \sin \theta$  to make the expression readable. One more step makes this expression amenable to graphical representation: converting  $\tan \varphi(k, \theta) \to \tan \varphi(k_x, k_y)$  via the relations  $C_{\theta} = k_x/k$  and  $S_{\theta} = k_y/k$ . Since  $\beta$  is fixed for a given altitude,  $C_{\beta}$  and  $S_{\beta}$  are constant parameters. That yields

$$\tan \varphi(k_x, k_y) = \frac{\nu_i u_d (k_x C_\beta + k_y S_\beta) \left[ \kappa_i (u_d / k v_{ith})^2 (k_y C_\beta - k_x S_\beta) (k_x C_\beta + k_y S_\beta) - 1 \right]}{\kappa_i (\nu_i u_d / k v_{ith})^2 (k_y C_\beta - k_x S_\beta) (k_x C_\beta + k_y S_\beta) + (u_d)^2 (k_x C_\beta + k_y S_\beta)^2}.$$

Figures 6·16, 6·17, and 6·18 show  $\varphi(k_x, k_y)$  in the plane perpendicular to  $\mathbf{B}_0$  in 2-D runs, at the same sixteen snapshots as shown in Figure 6·4. All panels show broad

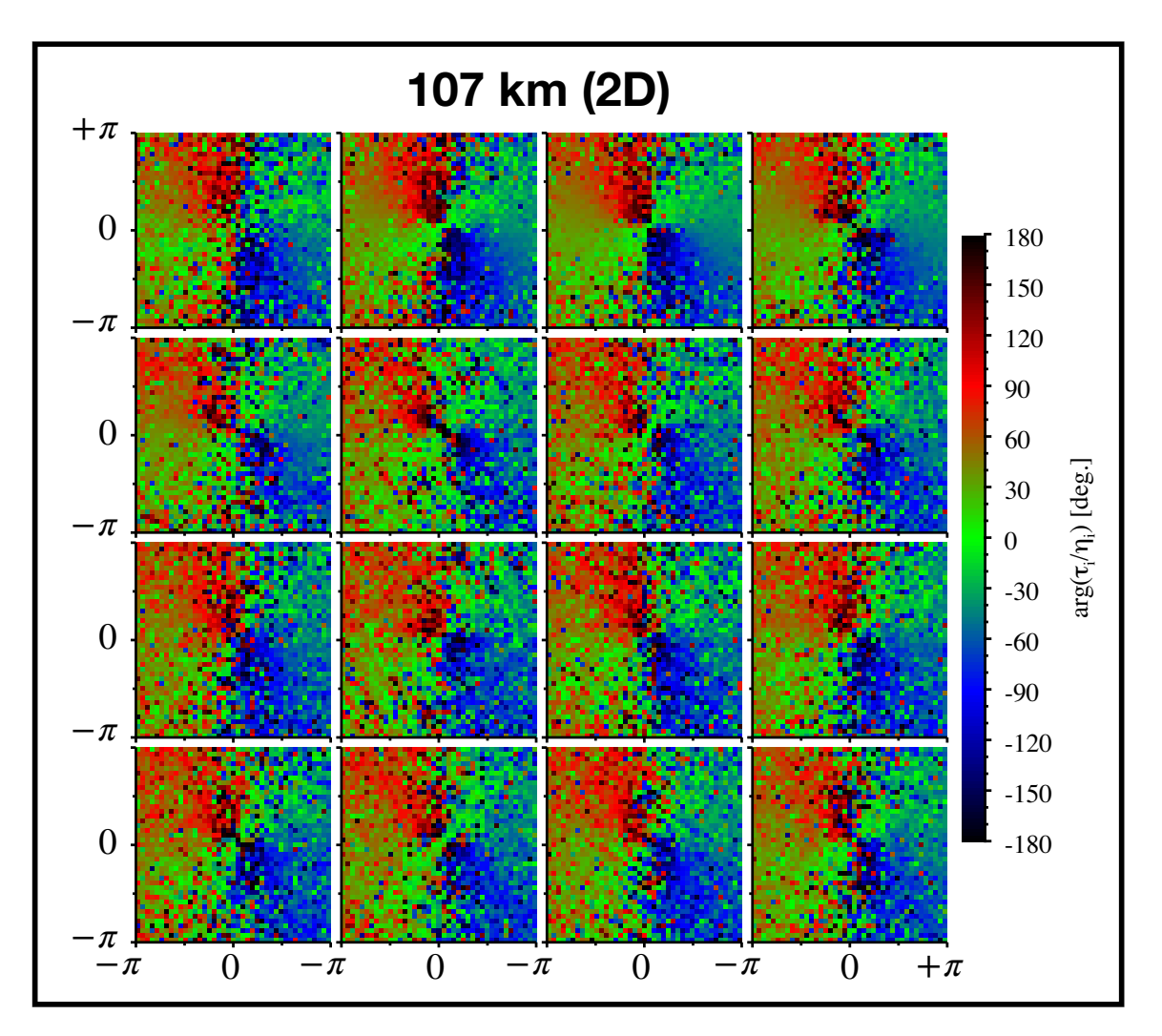


Figure 6·16: Phase offset of relative ion temperature perturbations,  $\delta T_{i\mathbf{k}}/T_{i0}$ , from relative ion density perturbations,  $\delta n_i/n_0$ , during the 2-D run at 107 km. Panel times correspond to the sixteen time steps shown in Figure 6·4. Each panel spans slightly more than  $-\pi$  to  $+\pi$  in both  $k_x$  and  $k_y$ . The color scale for all panels is periodic and ranges from  $-180^{\circ}$  to  $+180^{\circ}$ .

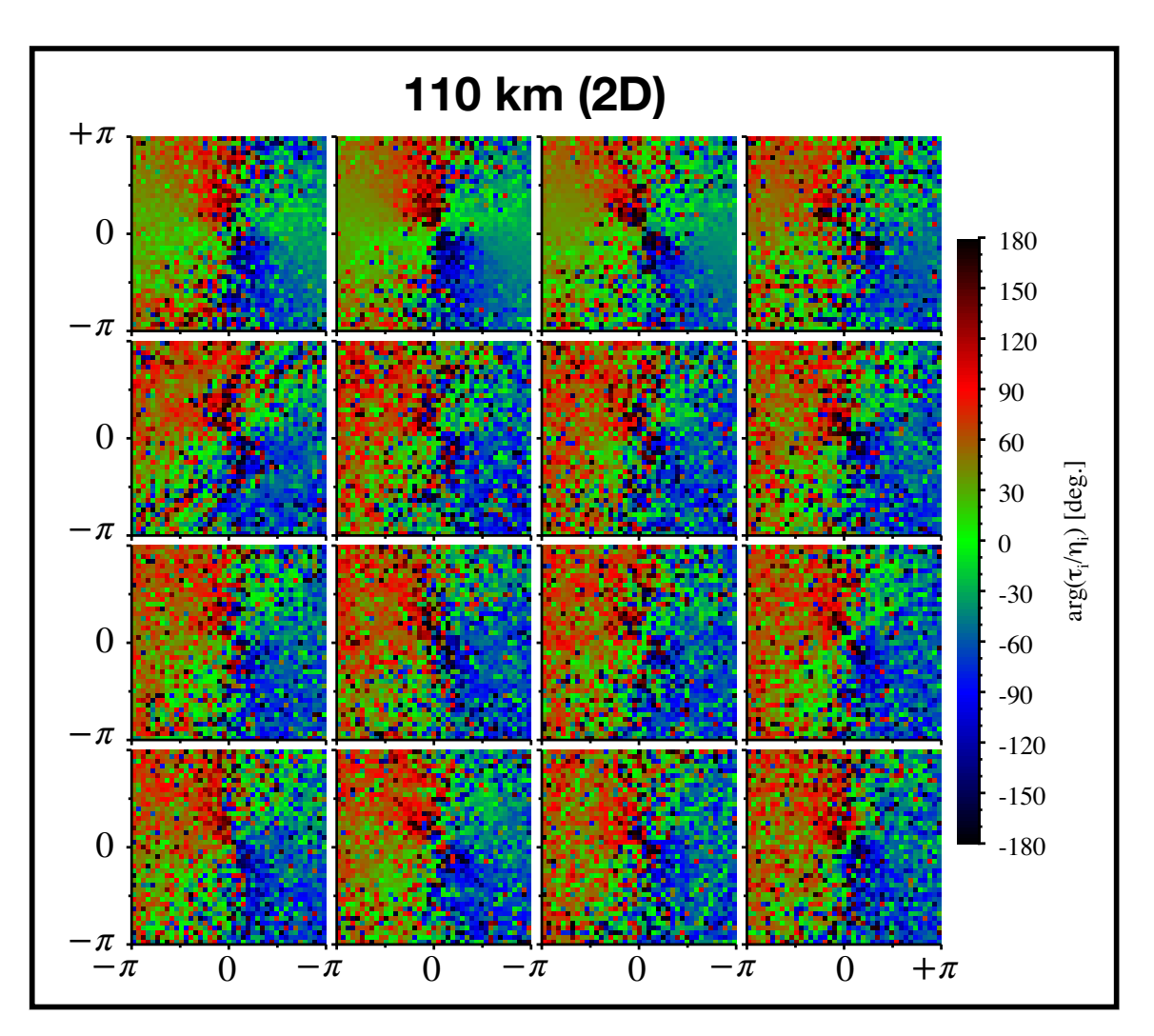


Figure 6·17: Phase offset of relative ion temperature perturbations,  $\delta T_{i\mathbf{k}}/T_{i0}$ , from relative ion density perturbations,  $\delta n_i/n_0$ , during the 2-D run at 110 km. The layout is identical to that of Figure 6·16.

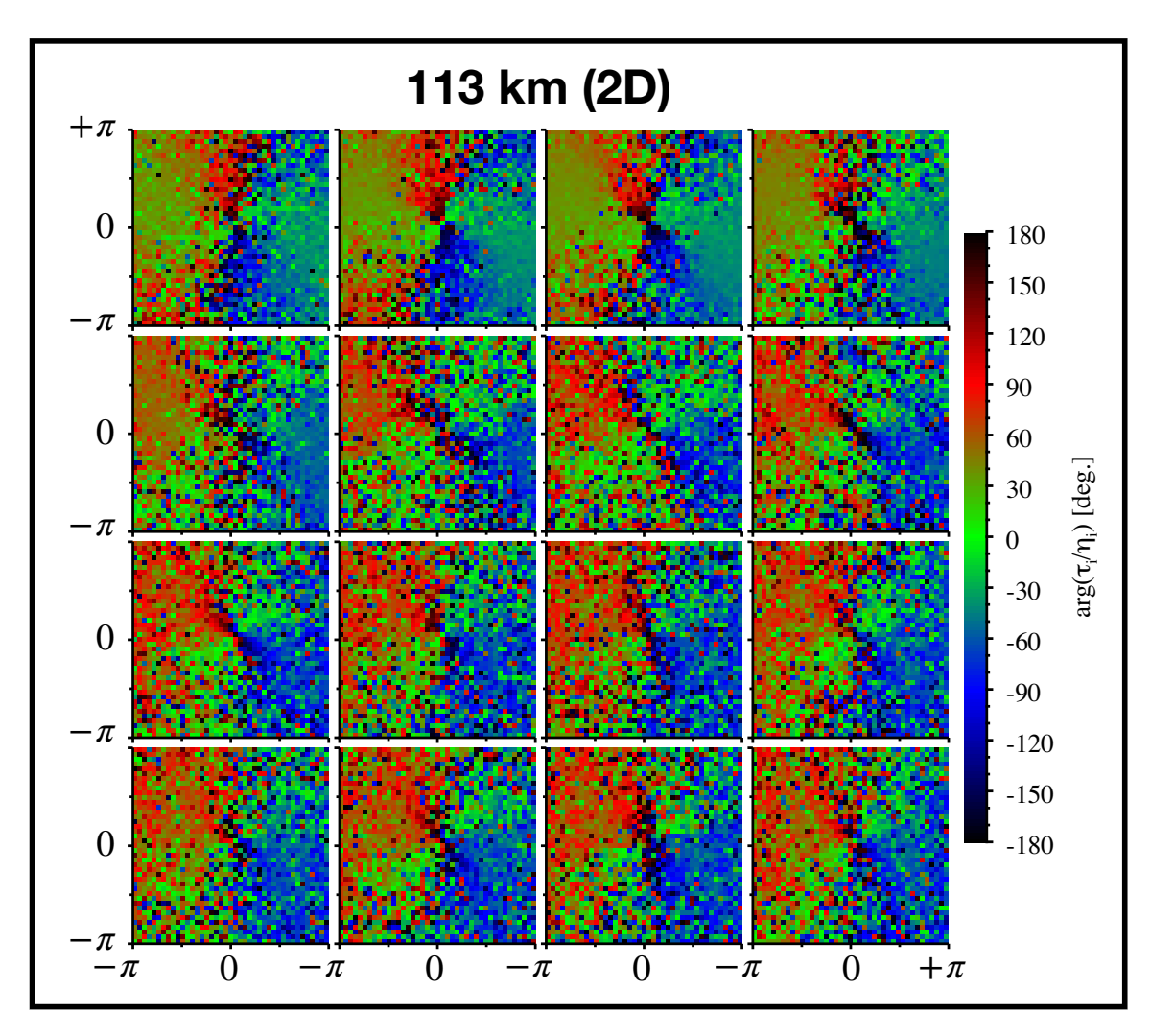


Figure 6.18: Phase offset of relative ion temperature perturbations,  $\delta T_{i\mathbf{k}}/T_{i0}$ , from relative ion density perturbations,  $\delta n_i/n_0$ , during the 2-D run at 113 km. The layout is identical to that of Figure 6.16.

regions of  $-180^{\circ} < \varphi < 0$  in the  $(k_x > 0, k_y < 0)$  quadrant,  $0^{\circ} < \varphi < +180$  in the  $(k_x < 0, k_y > 0)$  quadrant, and regions of  $\varphi \approx 0$  in the other two quadrants. There is a predominance of  $\varphi \approx \pm 90^{\circ}$  in the regions of significant  $\varphi > 0^{\circ}$ , indicating that ion thermal perturbations should enhance density perturbations in those regions, as opposed to acting to suppress density perturbations in the regions where  $\varphi \approx 0^{\circ}$ .

In the linear stage of each 2-D run,  $\varphi$  develops regions of  $\varphi \approx \pm 45^{\circ}$  colocated with concentrations of  $\langle \delta n_i/n_0 \rangle^2$  in Figures 6·10 through 6·12. Portions of these regions overlap with the  $\varphi \approx \pm 90^{\circ}$  regions, meaning that the ITI is less active in the linear-stage concentrations of  $\langle \delta n_i/n_0 \rangle^2$ . The  $\varphi \approx \pm 45^{\circ}$  regions are more prominent in the first panel as altitude increases, suggesting that ITI effects are less relevant as altitude approaches the magnetization boundary, and they fade during the transition from linear to non-linear instability, suggesting that ITI effects should be more important to non-linear behavior. Note that the  $\varphi \approx \pm 45^{\circ}$  regions fade earlier in the run at 110 km, consistent with the earlier transition from linear to non-linear behavior seen in Figures 6·2, 6·5, and 6·11.

Figures 6·19, 6·20, and 6·21 show  $\varphi(k_x, k_y)$  in the plane perpendicular to  $\mathbf{B}_0$  in 3-D runs, at the same sixteen snapshots as shown in Figure 6·7. The analysis routine again used five-pixel averages of temperature and density spectra to compute 3-D  $\varphi$ . The images have a structure similar to their 2-D counterparts, which is again due to the inclusion of oblique modes, especially during instability growth. As with Figures 6·13, 6·14, and 6·15, computing  $\varphi$  by using only perpendicular temperature and density spectral modes dramatically changes the growth-stage images. The other point of note regarding Figures 6·19 through 6·21 is that the regions of  $|\varphi| \approx 90^{\circ}$  during growth are smaller and less clearly defined than in Figures 6·16 through 6·18, suggesting that the ITI plays a smaller role in 3D.

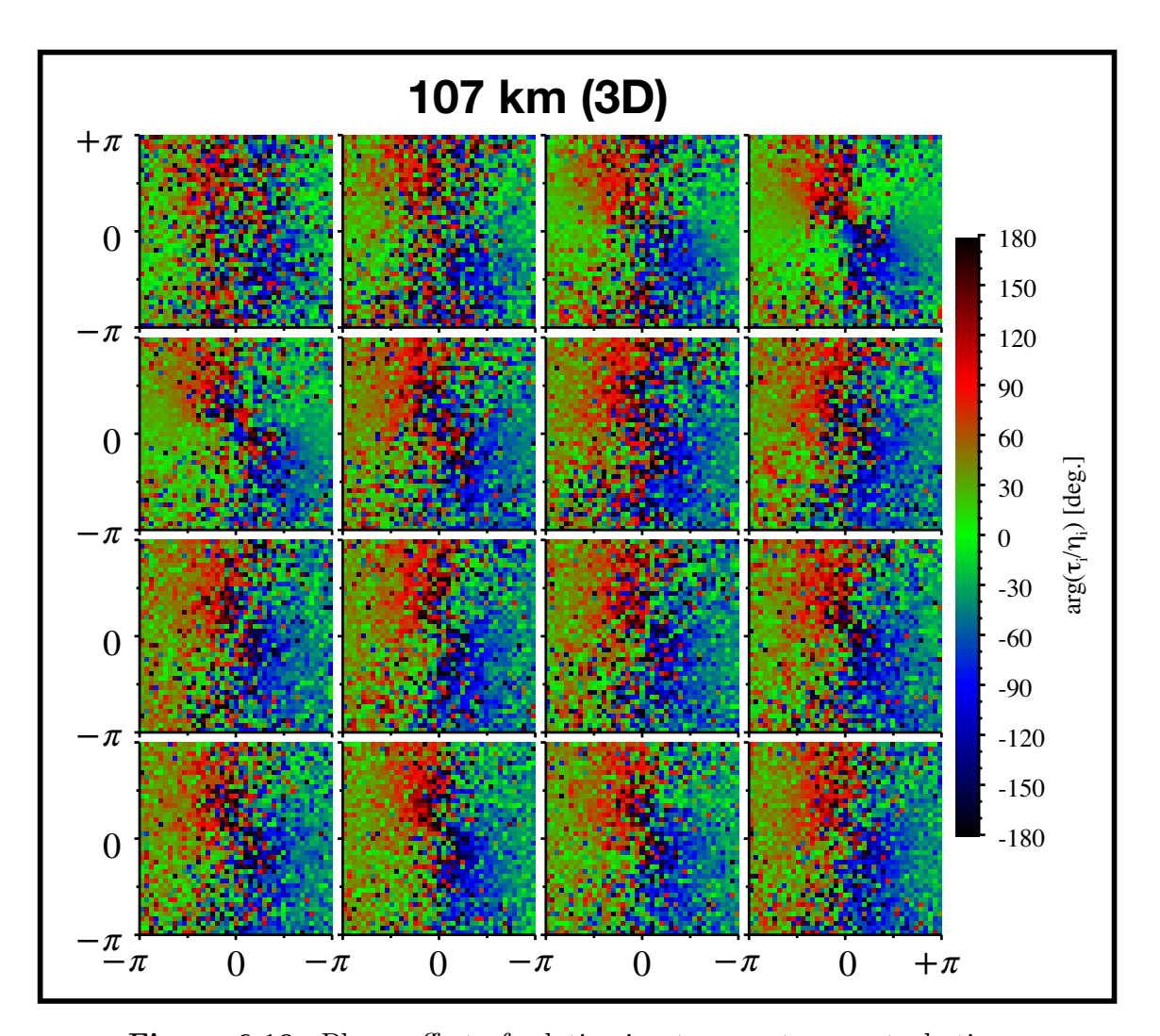


Figure 6·19: Phase offset of relative ion temperature perturbations,  $\delta T_{i\mathbf{k}}/T_{i0}$ , from relative ion density perturbations,  $\delta n_i/n_0$ , during the 3-D run at 107 km. Panel times correspond to the sixteen time steps shown in Figure 6·7. The layout is otherwise identical to that of Figure 6·16.

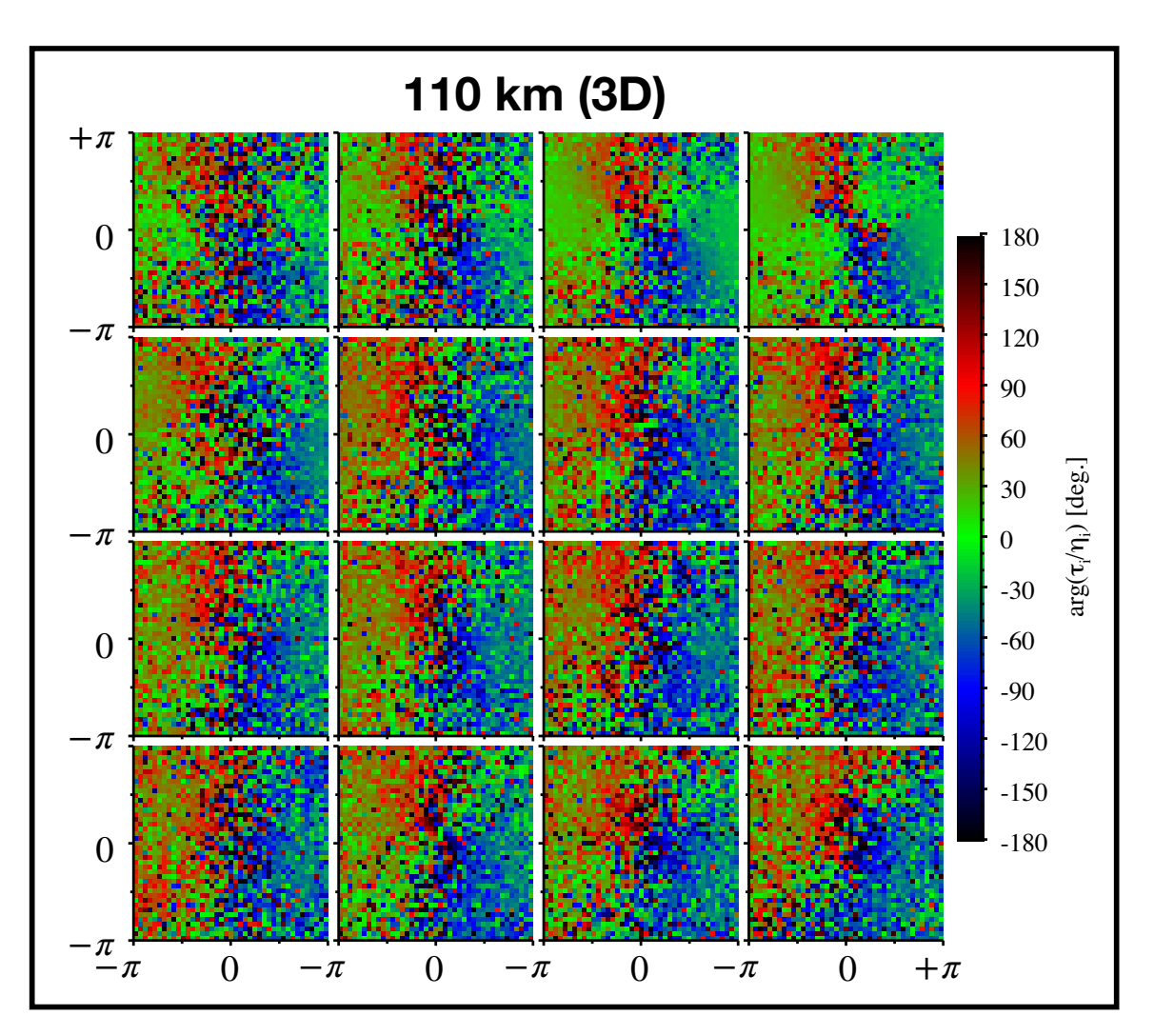


Figure 6.20: Phase offset of relative ion temperature perturbations,  $\delta T_{i\mathbf{k}}/T_{i0}$ , from relative ion density perturbations,  $\delta n_i/n_0$ , during the 3-D run at 110 km. The layout is identical to that of Figure 6.19.

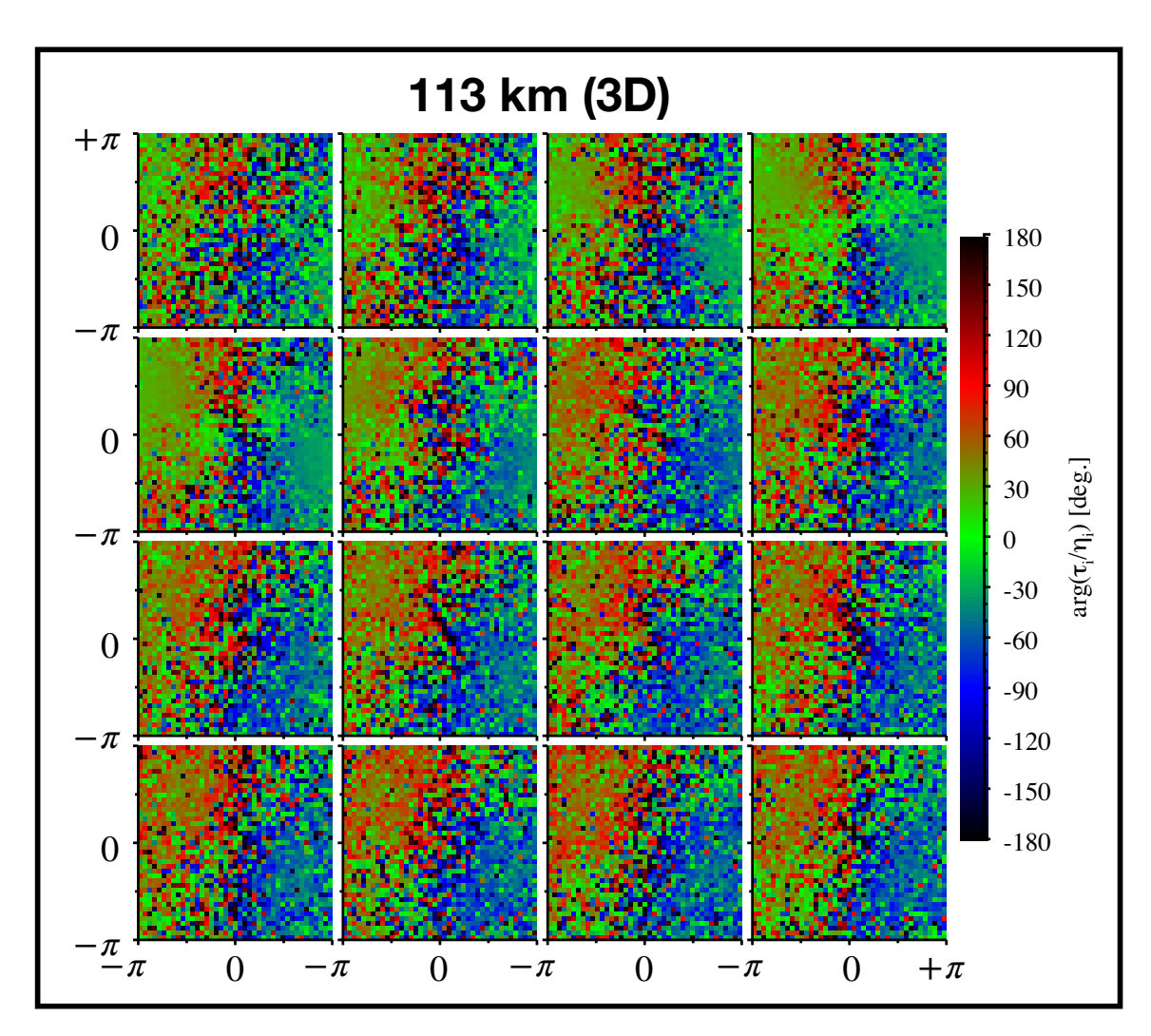


Figure 6.21: Phase offset of relative ion temperature perturbations,  $\delta T_{i\mathbf{k}}/T_{i0}$ , from relative ion density perturbations,  $\delta n_i/n_0$ , during the 3-D run at 113 km. The layout is identical to that of Figure 6.19.

## 6.8 Instability Flow Angle

The following set of figures show spectra of ion density perturbations in the plane perpendicular to  $\mathbf{B}_0$  after computing the RMS over an appropriate time range. Each panel includes color-coded lines which aid in answering two questions fundamental to this chapter: 1) How does the flow angle of ion perturbations change with altitude? 2) Do thermal effects from the ITI significantly alter the flow angle beyond isothermal FBI? All five lines represent angles with respect to  $\mathbf{E}_0 \times \mathbf{B}_0$ .

The first line, shown in magenta, gives the angle of relative drift velocity between electrons and ions,  $\mathbf{u}_d = \mathbf{u}_e - \mathbf{u}_i$ . Theory predicts that the isothermal FBI growth rate should peak at the drift-velocity angle. In the absence of pressure gradients and inertia, assuming  $\mathbf{E}_0 = E_0 \hat{y}$  and  $\mathbf{B}_0 = B_0 \hat{z}$ , the electron and ion drift components are

$$u_{ey} = -\frac{eE_0}{\nu_e m_e (1 + \kappa_e^2)}$$

$$u_{ex} = -\kappa_e u_{ey} = +\frac{\kappa_e eE_0}{\nu_e m_e (1 + \kappa_e^2)}$$

$$u_{iy} = +\frac{eE_0}{\nu_i m_i (1 + \kappa_i^2)}$$

$$u_{ix} = +\kappa_i u_{iy} = +\frac{\kappa_i eE_0}{\nu_i m_i (1 + \kappa_i^2)}$$

The drift-velocity components are thus

$$u_{dx} = u_{ex} - u_{ix}$$

$$= +eE_0 \left[ \frac{\kappa_e}{m_e \nu_e \left( 1 + \kappa_e^2 \right)} - \frac{\kappa_i}{m_i \nu_i \left( 1 + \kappa_i^2 \right)} \right]$$

$$u_{dy} = u_{ey} - u_{iy}$$

$$= -eE_0 \left[ \frac{1}{m_e \nu_e \left( 1 + \kappa_e^2 \right)} + \frac{1}{m_i \nu_i \left( 1 + \kappa_i^2 \right)} \right]$$

These components make an angle  $\beta = \tan^{-1}(u_{dy}/u_{dx})$  with the  $\mathbf{E}_0 \times \mathbf{B}_0$  (i.e.,  $\hat{x}$ )

direction. Plugging in the above expressions yields

$$\beta = \tan^{-1} \left[ -\frac{(1 + \kappa_i^2) + \Theta_0^2 (1 + \kappa_e^2)}{\kappa_e (1 + \kappa_i^2) - \Theta_0^2 (1 + \kappa_e^2) \kappa_i} \right]$$
(6.2)

where  $\Theta_0 \equiv \sqrt{m_e \nu_e/m_i \nu_i}$  as in Dimant and Oppenheim (2004). To be relevant to a simulation run,  $\Theta_0$  must use the simulated values of its parameters. The ion mass,  $m_i$ , is the physical ion mass but the electron mass,  $m_e$ , is inflated. Both ion and electron collision frequencies are as described in section 6.1. We also set  $\nu_e$  to maintain the appropriate value of  $\psi$  for a given altitude, accounting for the artificial electron mass. At 107 km,  $\beta \approx -9^\circ$ ; at 110 km,  $\beta \approx -15^\circ$ ; at 113 km,  $\beta \approx -24^\circ$ . Plots of  $\beta$  made directly from  $u_{dx:sim}$ ,  $u_{dy:sim}$ , and  $u_{dz:sim}$  in the sub-threshold run with  $E_{y0} = 10$  mV/m at each altitude (not shown) give these values directly.

The second line, shown in cyan, gives the predicted deflection of FBI+ITI perturbations. Equation 34 of Oppenheim and Dimant (2004) is

$$\tan 2\chi_{\text{opt}} = -\frac{2\kappa_i \left(1 + \psi\right)}{3 - \kappa_i^2}$$

Solving this equation for  $\chi_{\text{opt}}$  and using the relation  $\theta = \chi + \beta$  yields an equation for  $\theta_{\text{opt}}$  at a given altitude:

$$\theta_{\text{opt}} = \frac{1}{2} \tan^{-1} \left[ -\frac{2\kappa_i (1 + \psi)}{3 - \kappa_i^2} \right] + \beta$$

This angle represents the predicted angle of maximum growth of FBI+ITI perturbations. The values are  $\theta_{\rm opt} = -12^{\circ}$  at 107 km,  $\theta_{\rm opt} = -20^{\circ}$  at 110 km, and  $\theta_{\rm opt} = -32^{\circ}$  at 113 km. Note that, graphically,  $\chi_{\rm opt}$  is the difference between the magenta and cyan lines.

The third line, shown in white, actually represents three lines: the centroid of spectral power, with plus and minus one- $\sigma$  uncertainty. The centroid of a 2-D distribution of points is a quantity familiar to most people. Calling it by its more colloquial

name, the center of mass, evokes an intuitive sense of the point at which the surface would balance on the head of a pin. Since spectral power is spread over a range of angles, the angular deflection of the centroid of spectral power represents flow angle between the wave vector, k, and  $\mathbf{E}_0 \times \mathbf{B}_0$ .

Consider a 2-D discrete distribution,  $f(x_i, y_j)$ , with  $x_i = i\Delta x$ ,  $y_j = j\Delta y$  and  $(i, j) \in \{0..N_x - 1\} \otimes \{0..N_y - 1\}$ . The coordinates of the center of mass,  $(\langle x \rangle, \langle y \rangle)$ , are

$$\langle x \rangle = \frac{\sum_{j} \sum_{i} x_{i} f(x_{i}, y_{j})}{\sum_{j} \sum_{i} f(x_{i}, y_{j})} = \frac{1}{M} \sum_{j} \sum_{i} x_{i} f_{ij}$$
$$\langle y \rangle = \frac{\sum_{i} \sum_{j} y_{j} f(x_{i}, y_{j})}{\sum_{i} \sum_{j} f(x_{i}, y_{j})} = \frac{1}{M} \sum_{i} \sum_{j} y_{j} f_{ij}$$

where  $f_{ij} \equiv f(x_i, y_j)$  and  $M \equiv \sum_j \sum_i f_{ij}$  is the total mass. These are just the components of the first moment of the distribution with respect to the radial coordinate  $r \equiv (x, y)$ . The conversion from Cartesian to polar coordinates is simple:  $\langle k \rangle = \sqrt{\langle x \rangle^2 + \langle y \rangle^2}$  and  $\langle \theta \rangle = \tan^{-1}(\langle y \rangle / \langle x \rangle)$ .

In order to reduce the uncertainty in the centroid location, the analysis routine calculated the centroid for each image in the RMS time frame, calculated  $\langle \theta \rangle$  as the mean centroid from that distribution, and calculated  $\delta \langle \theta \rangle$  as the standard deviation of that distribution. The standard deviation is so small in all cases as to be imperceptible in the images.

It is worth noting that the centroid is a better measure of flow angle during growth than in saturation. During the growth stage, spectral amplitude is relatively isolated in both wavelength and angle, and the two peaks on either side of  $k_x = 0$  are distinct. This means that the centroid of one of the peaks – the  $k_x > 0$  peak in the following – represents the peak  $(k_x, k_y)$  value of linear growth. After saturation,

there is no longer a single peak wavelength that characterizes the instability. The centroid algorithm can still find the spectral center of mass but its value as a measure of flow angle is diminished. Nonetheless, it will serve as a visual guide.

Figure 6·22 shows RMS squared spectral amplitude in the plane perpendicular to  $\mathbf{B}_0$  during the growth stage and after saturation in 2-D runs. Each panel also shows the drift angle,  $\beta$ , the optimum FBI+ITI flow angle,  $\theta_{\rm opt}$ , and the flow-angle of the centroid,  $\langle \theta \rangle$ .

The run at 107 km matches FBI+ITI theory well during growth: Despite the fact that  $\chi_{\rm opt}$  is only a few degrees at this altitude,  $\langle \theta \rangle$  is within a few degrees of  $\theta_{\rm opt}$ . After saturation, the flow-angle magnitude increases by 1° so that it sits clearly below both  $\beta$  and  $\theta_{\rm opt}$ . This increase is probably associated with the presence, then fading, of the  $\varphi \approx -45^{\circ}$  region in Figure 6·16.

At 110 km,  $\langle \theta \rangle$  value sits approximately equidistant from  $\beta$  and  $\theta_{\rm opt}$ , indicating the possibility of some thermal effects but less than predicted. The magnitude of  $\varphi$  during growth in Figure 6·17 at angles near  $\langle \theta \rangle$  is smaller, which suggests that the ITI simply does not enhance the FBI as much as in the run at 107 km. The transition from growth to saturation again carries an increase in flow-angle magnitude and the deviation from  $\theta_{\rm opt}$  is more extreme. Similarly to the run at 107 km, thermal effects appear to play a role in determining the saturated  $\langle \theta \rangle$  value at 110 km. Unlike at 107 km, they increase the flow angle magnitude from less than  $\theta_{\rm opt}$  to greater than  $\theta_{\rm opt}$ .

At 113 km,  $\langle \theta \rangle$  is approximately equal to  $\beta$  during growth but increases toward  $\theta_{\rm opt}$  in saturation. Physically, this implies that ion density perturbations at 113 km propagate at the angle from  $\mathbf{E}_0 \times \mathbf{B}_0$  predicted by isothermal FBI theory during the growth stage but become non-isothermal during the transition to saturation.

Figure 6.23 shows RMS spectral power in the plane perpendicular to  $\mathbf{B}_0$  during

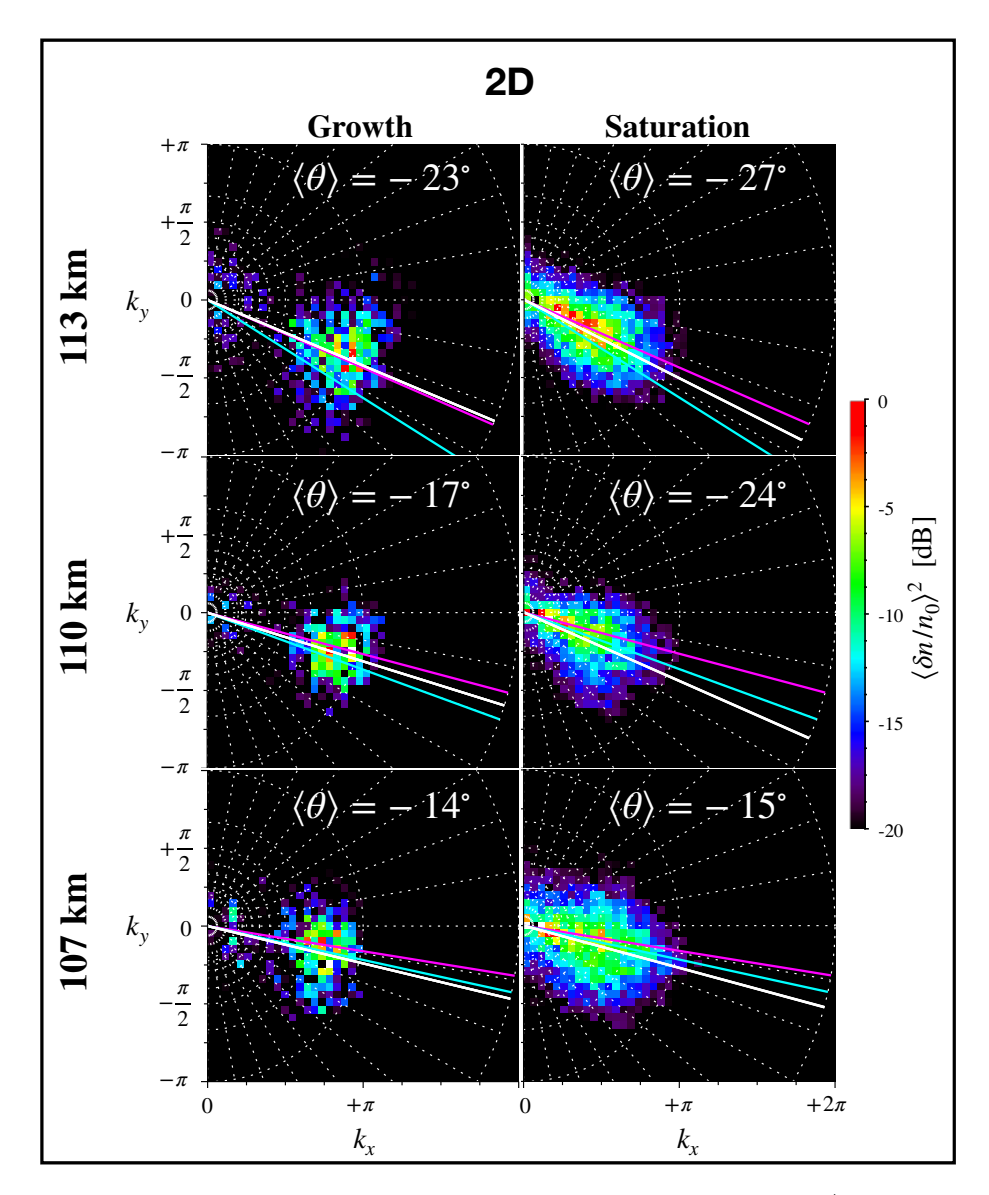


Figure 6.22: RMS squared spectral amplitude in  $\delta n_i/n_0$  during growth and after saturation in 2-D runs. Each panel spans 0 to  $+2\pi$  in  $k_x$  and  $-\pi$  to  $+\pi$  in  $k_y$ . Rows correspond to altitude, from 107 km (bottom) to 113 km (top). The left column shows the growth stage and the right column shows the saturation stage. In each panel, a magenta line indicates the drift angle,  $\beta$ , a cyan line indicates the optimal flow angle for the combined FBI+ITI,  $\theta_{\rm opt}$ , and white lines indicate the centroid angle,  $\langle \theta \rangle$ , with  $\pm \sigma$  uncertainties. The top of each panel lists the centroid angle. The color scale is identical to Figures 6·10 through 6·15.

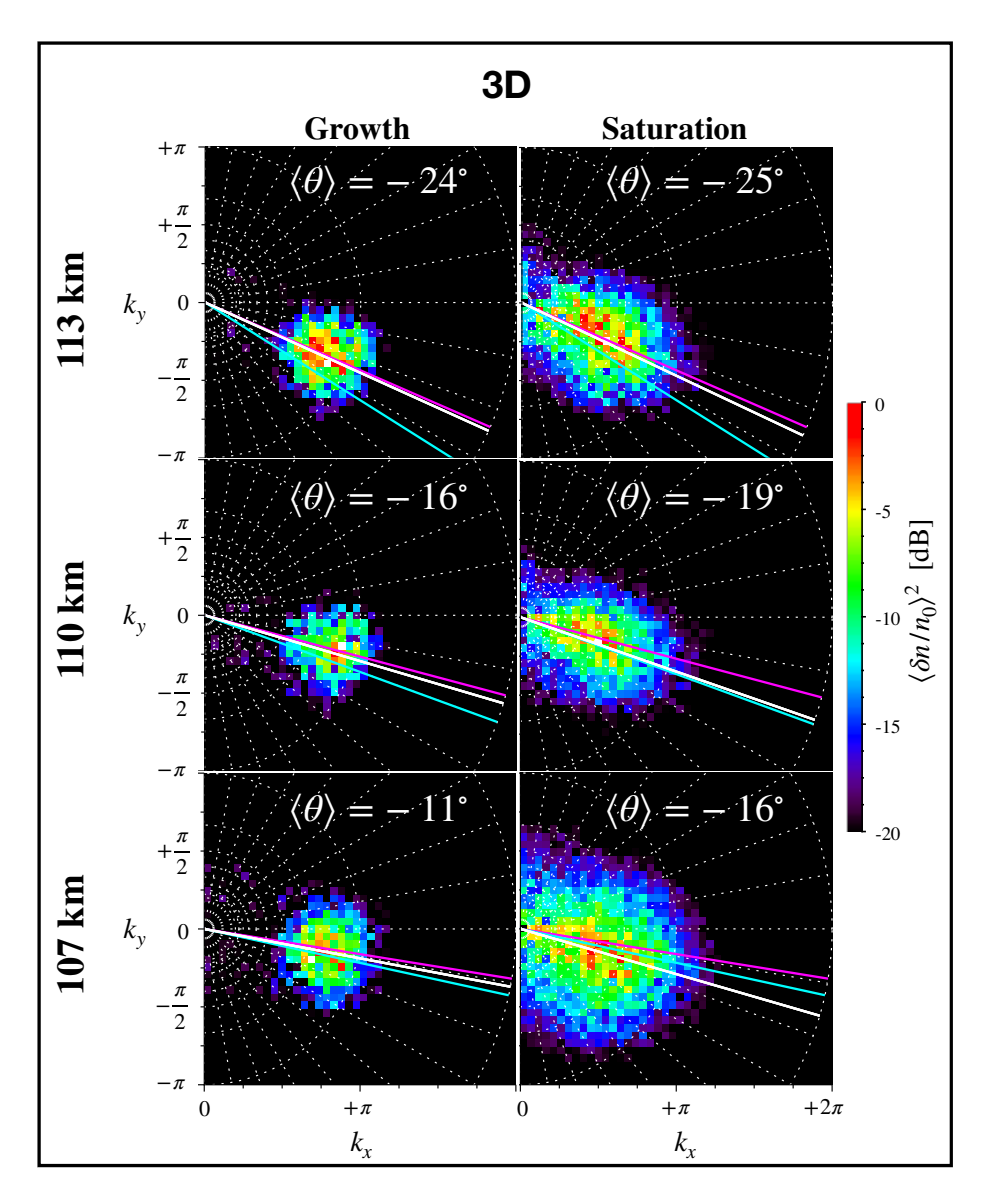


Figure 6.23: RMS squared spectral amplitude in  $\delta n_i/n_0$  during growth and after saturation in 3-D runs. The figure layout is identical to that of Figure 6.22.

the growth stage and after saturation in 3-D runs. Overall, thermal effects appear to produce less deviation from  $\beta$  than in 2-D runs.

At 107 km,  $\langle \theta \rangle$  sits between  $\beta$  and  $\theta_{\rm opt}$  during growth, suggesting some thermal effects but not as much as in the 2-D case. The shallower growth-stage value of  $\langle \theta \rangle$  in 3D, combined with a saturated-stage value closer to the 2-D value, suggest that the modest thermal effects associated with the weaker  $\varphi$  regions in Figure 6-19 require more time to build up. There is also appreciable spectral amplitude in the ranges  $4 \text{ m} < \lambda < 6 \text{ m}$  and  $-30^{\circ} < \theta < -20^{\circ}$  that the centroid-finding algorithm does not capture, as described above. This patch of relatively high amplitude likely represents perturbations of the combined FBI+ITI.

At 110 km,  $\langle \theta \rangle$  is closer to  $\beta$  while its value after saturation is very close to  $\theta_{\rm opt}$ . In Figure 6·19, regions of  $-90^{\circ} < \varphi < -60^{\circ}$  are less prevalent than at 107 km and are weaker diffuse than in 2D, consistent with the difference in  $\langle \theta \rangle$ .

At 113 km,  $\langle \theta \rangle$  does not differ much from  $\beta$  during growth but is about 1° larger after saturation. In both Figures 6·18 and 6·21 the regions of significant  $\varphi$  are aligned with larger flow angles than the regions of high amplitude at 113 km, especially during the linear phase, compared to runs at 107 km and 110 km. Thus it appears that the ITI has less effect on the runs at 113 km.

Figures 6·22 and 6·23 show that, over the range of altitudes that this chapter considers, the ITI make a significant contribution to the flow angle at 107 km and less contribution as altitude increases, to the point where the angle of relative drift effectively determines the flow at 113 km, especially in the 3-D runs. In general, the flow angle is shallower in 3-D runs, indicating that the presence of wave modes with a component parallel to  $\mathbf{B}_0$  reduces the ITI effect. The theoretical basis presented in Dimant and Oppenheim (2004) for predicting ion thermal effects applies to 2-D perturbations in the long-wavelength limit  $ku_d \ll \nu_i$  and does not account for kinetic

effects. The shortest long-wavelength limit relevant to the simulations presented in this chapter is 6 m, corresponding to 107 km (assuming  $|\mathbf{E}_0| = 50 \text{ mV/m}$ ). Therefore, the formal theory does not strictly apply to any of the simulations presented in this chapter. Development of a theory that describes the apparent thermal effects presented here represents an intriguing avenue of research.

### 6.9 Conclusion

This chapter analyzes how the spectrum of meter-scale irregularities in the upper auroral E region varies with altitude. The magnitude of the flow angle with respect to  $\mathbf{E}_0 \times \mathbf{B}_0$ ,  $\langle \theta \rangle$ , increases with increasing altitude in both 2-D and 3-D simulations. In both 2-D and 3-D runs at 107 km and 110 km, the increase in flow angle results in part from the thermal effects of the ITI enhancing wave growth in a direction offset from the direction predicted by isothermal theory. However, the change in angle of relative drift velocity,  $\mathbf{u}_d$ , plays the dominant role in turning waves away from  $\mathbf{E}_0 \times \mathbf{B}_0$  at upper-electrojet altitudes. In both 2-D and 3-D runs at 113 km, the direction of  $\mathbf{u}_d$  largely determines the flow angle with less contribution from thermal effects in 3D than in 2D. In all the cases presented in this chapter, the flow angle is never smaller than the drift angle.

The magnitude of the background electric field,  $E_{y0} = 50 \text{ mV/m}$  represents the E-region response to a modest geomagnetic storm. Simulations with a 30-mV/m driving field failed to develop ion instabilities in the same time as their 2-D and 3-D 50-mV/m counterparts. The threshold electric field at auroral latitudes is  $E_{th} \approx 21 \text{ mV/m}$ , so it is likely that the 30-mV/m runs needed more time to develop turbulence. Simulations with a 70-mV/m driving field developed ion instabilities that behaved very similarly to the 50-mV/m case, though instability growth was faster for the higher electric field, as expected. The 70-mV/m run at 107 km produced the largest flow angle of

any run, consistent with a large region of  $-180^{\circ} < \varphi < -90^{\circ}$ . The ITI arises because the total electric field due to the background field and wave polarization field drive enhanced Joule heating, so it is no surprise that increasing  $E_{y0}$  had an effect on flow angle. The 70-mV/m results simply reinforce the conclusions drawn from the 50-mV/m case.

This chapter also identifies differences between 2-D and 3-D simulations of ion instabilities in the upper auroral electrojet. All 3-D runs evolve more quickly than do 2-D runs because allowing a component not strictly perpendicular to  $\mathbf{B}_0$  introduces additional unstable modes. Figure 6-2 showed that 3-D runs display an initial noisy period, roughly twenty seconds long, before instability growth starts, whereas 2-D runs show instability growth almost immediately. The 3-D runs appear to complete their initial growth phase much more quickly than 2-D runs – a span of roughly twenty seconds in 3D compared to over 100 seconds in 2D – but the non-linear amplitude of decameter-scale waves in 3D appears to be trending toward the meterscale amplitude at the end of each run. Considering that the 2-D runs ran for four times as long, the asymptotic behavior in both 2D and 3D may be the same.

Figure 6·3 showed that average electron temperatures differ over the course of a 2-D run compared to a 3-D run at a given altitude. All 2-D runs showed more erratic  $T_e$  than their 3-D counterparts – likely a result of the 3-D runs having many more modes into which the FBI can couple energy. Overall,  $T_e$  is much higher in 3-D runs than in 2-D runs and the value of  $T_e$  after instability saturation increases with altitude. Although this chapter focused on the contribution of ion thermal effects to the FBI, the difference in  $T_e$  is notable. Average temperatures in the 70-mV/m runs displayed similar trends, with saturated-state  $T_e$  values 300 to 400 K hotter at each altitude than in the 50-mV/m runs. Similarly to the average amplitude of density perturbations, 3-D average temperature dynamics evolve approximately four times

more quickly than do 2-D temperature dynamics. However, average 3-D temperatures do not appear to mimic the long-term behavior of average 2-D temperatures, unlike the similar asymptotic behavior of average density amplitudes.

The structure of the phase offset between ion temperature and density perturbations,  $\varphi(k_x, k_y)$ , is similar between 2-D and 3-D runs after accounting for oblique wave modes. The slower instability evolution in 2-D runs means that Figures 6·16 through 6·18 do not sample the pre-growth stage as well as Figures 6·19 through 6·21 do. However, even the saturated stages of 2-D runs show larger values of  $|\varphi|$  than their 3-D counterparts, suggesting that thermal effects play a larger role in 2-D simulations. Despite the sampling difference, the 2-D and 3-D growth stages are clearly different, especially at long wavelengths along the bisector between  $\mathbf{u}_d$  and  $\mathbf{u}_d \times \mathbf{B}_0$ .

Finally, the difference in  $\varphi(k_x, k_y)$  manifests as a difference in flow angle between 2-D and 3-D runs at all altitudes, but less so at 113 km than at 107 km and 110 km. The flow angle in 3-D runs is consistently a few degrees shallower in 3-D runs than in 2-D runs, except during growth at 113 km, where it follows the relative drift. The ITI appears to have a smaller effect on flow angle with increasing altitude, at least for the simulations presented here. The growth stages of these simulations are so short that a radar pulse would average over them and the saturate states would dominate the return signal. In light of this fact, the saturation column in Figure 6·23 predicts that the flow angles at 107 km, 110 km, and 113 km should be  $-16^{\circ}$ ,  $-19^{\circ}$ , and  $-25^{\circ}$ , respectively.

The influence of including wave modes with a component parallel to  $\mathbf{B}_0$  on meterscale ion instabilities has noticeable effects beyond allowing them to propagate at a small non-zero aspect angle. In addition to increasing the growth rates, suppressing direct excitation of decameter-scale waves, and stabilizing average temperatures, it may suppress the effects of the ion thermal instability, leading to less flow-angle

deviation from  $\mathbf{E}_0 \times \mathbf{B}_0$ . Any future simulations that attempts to approximate the naturally 3-D auroral electrojet as a 2-D phenomenon must account for these discrepancies.

# Chapter 7

# Conclusion

## 7.1 Summary of the Dissertation

The over-arching theme of this dissertation was the non-linear behavior of meter-scale density irregularities as they evolve in the terrestrial E-region ionosphere. Chapter 1 provided an introduction to the ionosphere, a summary of research into E-region plasma instabilities, and a primer on two relevant instabilities: the Farley-Buneman instability (FBI) and the gradient-drift instability (GDI). Chapter 2 provided the theoretical background necessary for understanding plasma instability research. Chapter 3 provided a primer on numerical modeling as a tool in plasma instability research.

The main body of this dissertation presented my research into density irregularities produced by the FBI in various ionospheric contexts: Chapter 4 described its co-evolution with the GDI on small scales, Chapter 5 demonstrated how the GDI on large scales drives the FBI on small scales, and Chapter 6 elucidated the effects of the ion thermal instability (ITI) on FBI evolution. Short summaries of the three research chapters follow.

#### 7.1.1 Summary of Chapter 4

Chapter 4 presented the first results from a parallelized hybrid quasi-neutral plasma simulation with particle ions and fluid electrons. Those simulations employed a numerical model that is well suited to studying meter- and decameter-scale turbulence in the presence of hundred-meter- to kilometer-scale density waves. The simula-

tions modeled the development of meter-scale plasma instabilities in the presence of ionization layers perturbed by an approximately half-kilometer wave. Density gradients along the perturbed ionization layers drive broad-spectrum (Type-II) plasma instabilities and the electric field between perturbed layers drives narrow-spectrum (Type-I) plasma instabilities. The main results of Chapter 4 were: 1) Simulations with zeroth-order vertical electric fields of varying strength produce gradient-drift turbulence in regions that satisfy the GDI condition. 2) The total electric field in the density minimum is large enough to drive the FBI even when the zeroth-order vertical field is below the threshold. 3) Waves traveling below the plasma acoustic speed develop in all runs. 4) Wave power spectra show characteristics of Type-II irregularities in all runs. 5) Wave power spectra show a mix of Type-I and Type-II irregularities when the background electric field is 12 mV/m. 6) Wave with Type-I spectra travel at the plasma acoustic speed and are confined to a 30° range in elevation.

#### 7.1.2 Summary of Chapter 5

Chapter 5 presented the first hybrid plasma simulations of meter-scale secondary wave growth driven by a kilometer-scale primary wave. This chapter directly addressed the problem of secondary FBI generation, originally considered by Balsley and Farley (1973) and contemporaries, on a realistic spatial scale. The simulations presented in Chapter 5 required significant code development, which Chapter 3 describes. These simulations imposed a one-kilometer wave, then evolved self-consistently under the influence of background electric and magnetic fields, with field strengths and plasma parameters typical of 100 km at the magnetic equator. The large-scale wave developed a polarization electric field which produced FBI in the crest and trough, aligning nicely with observations of vertically propagating meterscale density irregularities, such as those observed by Hysell et al. (2007). The FBI,

in turn, transported plasma across the magnetic field and shorted out the wave polarization electric field in the regions of strongest wave growth. The shorting-out effect produced flat-top electric fields that are similar to those observed by Pfaff et al. (1987a,b), and represents a feedback mechanism that appears to explain why the irregularities that produce Type-I spectra travel at the plasma acoustic speed.

#### 7.1.3 Summary of Chapter 6

Chapter 6 presented pure particle-in-cell (PIC) simulations of FBI waves in the high-latitude ionosphere, under conditions typical of a moderate geomagnetic storm. It showed that the angle that ion perturbations make with  $\mathbf{E}_0 \times \mathbf{B}_0$ , called the flow angle, increases with increasing altitude in both 2-D and 3-D simulations. It showed that the flow angle is non-zero due to a combination of the FBI and the ITI at 107 km and 110 km, especially after instability saturation, but that the angle of relative drift between electrons and ions determines the flow angle at 113 km. It also showed that the magnitude of the flow angle is smaller in 3-D than in 2-D at 107 km and 110 km, indicating a difference in behavior of the ITI in 2-D simulations versus 3-D simulations. Spectra of ion perturbations at all altitudes also differ between 2-D and 3-D simulations in the growth of decameter-scale waves versus growth of meter-scale waves, meaning that attempts to simulate the auroral electrojet as a 2-D system must account for possibly non-physical wave growth at large scales.

### 7.2 Future Work

Development of the 2-D hybrid version of EPPIC was the cornerstone of my graduate research. Despite the years I have spent developing hybrid EPPIC, not to mention the time other members of out research group have spent developing other aspects of EPPIC, there are many ways it can improve.

One way is the development of a thermal equation for fluid electrons. The isothermal simulations presented in Chapters 4 and 5 are sufficient for simulating interacting FBI and GDI in the equatorial ionosphere but Chapter 6 showed that thermal effects may alter FBI evolution, especially at high latitudes. While the pure-PIC version of EPPIC provided results for that chapter, the spectral resolution of ion modes was poor because the need to resolve the Debye length forced the simulation box size to be relatively small. The aeronomy community will benefit from simulations of FBI+ITI dynamics driven by density gradients at high latitudes that provide parameterizations of sub-kilometer turbulent effects such as plasma heating, plasma transport, and electric field saturation, which larger-scale models can incorporate into their physics.

Another way to improve hybrid EPPIC is the extension to 3D. Again, the pure-PIC simulations of Chapter 6 identify a short-coming in hybrid EPPIC by illustrating differences between 2-D and 3-D instability evolution. In addition to substantial electron heating, which Oppenheim and Dimant (2013) previously described, the dimension parallel to  $\mathbf{B}_0$  changes the nature of the combined FBI+ITI and affects the flow angle. These effects will clearly matter at high latitudes, but even in equatorial simulations, a change in flow angle would change the obliquity of secondary FBI waves and may contribute to up-down/east-west asymmetries.

With these two improvements, hybrid EPPIC or a similar code developed from scratch would be poised to self-consistently simulate the growth of GDI waves which develop electric fields strong enough to drive the FBI, which in turn transports plasma, leads to species-specific thermal effects, and shorts out the GDI-wave electric field. Such a tool would not only contribute substantial insight into E-region plasma processes but also plasma processes in the solar system and beyond.

#### 7.3 Final Remarks

This dissertation represents original scientific research into ionospheric plasma instabilities that contributes substantially to the advancement of the field of aeronomy. Chapter 1 asked three questions that guided the research presented in this dissertation. Those questions, and their answers, are:

- 1. How do density irregularities from co-evolving Farley-Buneman (FBI) and gradient drift instabilities (GDI) relate to historical classifications of radar spectra? Meter-scale Type-II spectra develop in the presence of a density gradient for a range of electric fields, even in the absence of Type-I spectra. Type-I spectra appear when the total electric field exceeds the FBI threshold, and a portion of energy previously in Type-II spectra moves into Type-I spectra. Attempting to classify radar echoes as one type or the other is less fruitful than studying how echo amplitude, Doppler shift, and spectra width evolve over minutes or hours, and using those quantities to infer the presence of gradients, strengths of electric fields, and other plasma parameters.
- 2. How does a kilometer-scale wave give rise to vertically propagating meter-scale waves and how do those meter-scale waves feed back to their kilometer-scale driver?

A kilometer-scale wave, such as those produced by the GDI, develops a polarization electric field that points parallel to its propagation in the crest and antiparallel in the trough. If the magnitude of that polarization electric field and the ambient electric field exceeds the FBI threshold, meter-scale waves will grow in the crest and trough, propagating with some vertical component. As the meter-scale waves grow, they transport plasma through the crest and trough, shorting out the polarization electric field to just above the FBI thresh-

old.

3. How does the spectrum of FBI turbulence change with altitude and how well do 2-D simulations model the 3-D dynamics?

FBI waves turn from the  $\mathbf{E}_0 \times \mathbf{B}_0$  direction for two reasons:1) their growth peaks in the direction of relative electron-ion drift; 2) ion thermal effects further tilt meter-scale waves toward  $-\mathbf{E}_0$ . The major difference between 2-D and 3-D spectra is that flow angles in 2D are almost always larger than in 3D, especially after saturation, which is when radars are likely to observe meter-scale echoes. Thermal effects appear to decrease significantly above 110 km and the addition of wave modes parallel to  $\mathbf{B}_0$  appear to partially suppress the ion thermal instability (ITI).

This dissertation has answered some fundamental questions about plasma instabilities in the E-region ionosphere, has placed those physical results in the context of observations and broader processes, and has proposed additional avenues for future research.

# List of Journal Abbreviations

Ann. Geophys.
Astron. Astrophys.
Astrophys. J.
Geophys. Res. Lett.
J. Atmos. Terr. Phys.

J. Geophys. Res.Phys. Rev. Lett.Rev. Geophys. Space Phys.

Annales Geophysicae
Astronomy and Astrophysics
Astrophysical Journal
Geophysical Research Letters
Journal of Atmospheric and
Terrestrial Physics
Journal of Geophysical Research
Physical Review Letters
Reviews of Geophysics and
Space Physics

# References

- Amestoy, P. R., Duff, I. S., L'Excellent, J.-Y., and Koster, J. (2001). A fully asynchronous multifrontal solver using distributed dynamic scheduling. *SIAM Journal on Matrix Analysis and Applications*, 23(1):15–41.
- Amestoy, P. R., Guermouche, A., L'Excellent, J.-Y., and Pralet, S. (2006). Hybrid scheduling for the parallel solution of linear systems. *Parallel Computing*, 32(2):136–156.
- Balay, S., Abhyankar, S., Adams, M. F., Brown, J., Brune, P., Buschelman, K., Dalcin, L., Eijkhout, V., Gropp, W. D., Kaushik, D., Knepley, M. G., May, D. A., McInnes, L. C., Mills, R. T., Munson, T., Rupp, K., Sanan, P., Smith, B. F., Zampini, S., Zhang, H., and Zhang, H. (2018). PETSc Web page. http://www.mcs.anl.gov/petsc.
- Balay, S., Abhyankar, S., Adams, M. F., Brown, J., Brune, P., Buschelman, K., Dalcin, L., Eijkhout, V., Gropp, W. D., Kaushik, D., Knepley, M. G., McInnes, L. C., Rupp, K., Smith, B. F., Zampini, S., and Zhang, H. (2015). PETSc users manual. Technical Report ANL-95/11 Revision 3.6, Argonne National Laboratory.
- Balay, S., Gropp, W. D., McInnes, L. C., and Smith, B. F. (1997). Efficient management of parallelism in object oriented numerical software libraries. In Arge, E., Bruaset, A. M., and Langtangen, H. P., editors, *Modern Software Tools in Scientific Computing*, pages 163–202. Birkhäuser Press.
- Balsley, B. B. (1965). Some Additional Features of Radar Returns from the Equatorial Electrojet. *J. Geophys. Res.*, 70:3175–3182.
- Balsley, B. B. (1969). Some characteristics of non-two-stream irregularities in the equatorial electrojet. *J. Geophys. Res.*, 74:2333–2347.
- Balsley, B. B. and Farley, D. T. (1971). Radar studies of the equatorial electrojet at three frequencies. *J. Geophys. Res.*, 76:8341–8351.
- Balsley, B. B. and Farley, D. T. (1973). Radar observations of two-dimensional turbulence in the equatorial electrojet. *J. Geophys. Res.*, 78:7471–7479.

- Bhatnagar, P. L., Gross, E. P., and Krook, M. (1954). A Model for Collision Processes in Gases. I. Small Amplitude Processes in Charged and Neutral One-Component Systems. *Physical Review*, 94:511–525.
- Bilitza, D., Altadill, D., Truhlik, V., Shubin, V., Galkin, I., Reinisch, B., and Huang, X. (2017). International Reference Ionosphere 2016: From ionospheric climate to real-time weather predictions. *Space Weather*, 15:418–429.
- Birdsall, C. K. and Langdon, A. B. (1991). Plasma Physics via Computer Simulation. Taylor & Francis.
- Blix, T. A., Thrane, E. V., Kirkwood, S., Dimant, Y. S., and Sudan, R. N. (1996). Experimental evidence for unstable waves in the lower E/Upper D-region excited near the bisector between the electric field and the drift velocity. *Geophys. Res. Lett.*, 23:2137–2140.
- Booker, H. G. (1956). A theory of scattering by nonisotropic irregularities with application to radar reflections from the aurora. *J. Atmos. Terr. Phys.*, 8:204–221.
- Bowles, K. L. (1954). Doppler shifted radio echoes from aurora. *J. Geophys. Res.*, 59:553–555.
- Bowles, K. L., Balsley, B. B., and Cohen, R. (1963). Field-aligned e-region irregularities identified with acoustic plasma waves. *J. Geophys. Res.*, 68(9):2485–2501.
- Bowles, K. L., Cohen, R., Ochs, G. R., and Balsley, B. B. (1960). Radio echoes from field-aligned ionization above the magnetic equator and their resemblance to auroral echoes. *J. Geophys. Res.*, 65(6):1853–1855.
- Briggs, W., Henson, V., and McCormick, S. (2000). A Multigrid Tutorial, Second Edition. Society for Industrial and Applied Mathematics, second edition.
- Buneman, O. (1963). Excitation of field aligned sound waves by electron streams. *Phys. Rev. Lett.*, 10:285.
- Cohen, R. and Bowles, K. (1963). The association of planewave electrondensity irregularities with the equatorial electrojet. *J Geophys Res*, 68(9):2503–2525.
- Cohen, R. and Bowles, K. L. (1967). Secondary irregularities in the equatorial electrojet. *J. Geophys. Res.*, 72:885–894.
- Crochet, M., Broche, P., and Hanuise, C. (1979a). High frequency radar observations of horizontal plasma waves in the equatorial ionosphere. *Nature*, 277:203.

- Crochet, M. and Hanuise, C. (1981). On a method of extended observations of the spectrum of plasma instabilities in the electrojet. *J. Atmos. Terr. Phys.*, 43:829–834.
- Crochet, M., Hanuise, C., and Broche, P. (1979b). HF radar studies of two-stream instability during an equatorial counter-electrojet. *J. Geophys. Res.*, 84:5223–5233.
- Dimant, Y. S. and Oppenheim, M. M. (2004). Ion thermal effects on E-region instabilities: linear theory. J. Atmos. Solar Terr. Phys., 66:1639–1654.
- Dimant, Y. S. and Oppenheim, M. M. (2011a). Magnetosphere-ionosphere coupling through E-region turbulence: 1. Energy budget. *J. Geophys. Res.*, 116(A09):A09303.
- Dimant, Y. S. and Oppenheim, M. M. (2011b). Magnetosphere-ionosphere coupling through E-region turbulence: 2. Anomalous conductivities and frictional heating. *J. Geophys. Res.*, 116(A09):A09304.
- Dimant, Y. S. and Sudan, R. N. (1995a). Kinetic theory of low-frequency cross-field instability in a weakly ionized plasma. I. *Physics of Plasmas*, 2:1157–1168.
- Dimant, Y. S. and Sudan, R. N. (1995b). Kinetic theory of low-frequency cross-field instability in a weakly ionized plasma. II. *Physics of Plasmas*, 2:1169–1181.
- Dimant, Y. S. and Sudan, R. N. (1995c). Kinetic theory of the Farley-Buneman instability in the E region of the ionosphere. *J. Geophys. Res.*, 100:14605–14624.
- Dimant, Y. S. and Sudan, R. N. (1997). Physical nature of a new cross-field current-driven instability in the lower ionosphere. *J. Geophys. Res.*, 102:2551–2564.
- Dougherty, J. P. and Farley, D. T. (1967). Ionospheric E-region irregularities produced by nonlinear coupling of unstable plasma waves. *J. Geophys. Res.*, 72:895–901.
- Drexler, J., St.-Maurice, J.-P., Chen, D., and Moorcroft, D. R. (2002). New insights from a nonlocal generalization of the Farley-Buneman instability problem at high latitudes. *Ann. Geophys.*, 20:2003–2025.
- Eckersley, T. L. (1937). Irregular Ionic Clouds in the E Layer of the Ionosphere. *Nature*, 140:846–847.
- Erickson, P. J., Foster, J. C., and Holt, J. M. (2002). Inferred electric field variability in the polarization jet from Millstone Hill E region coherent scatter observations. *Radio Science*, 37:1027.

- Falgout, R. D. and Yang, U. M. (2002). hypre: A library of high performance preconditioners. In Sloot, P. M. A., Hoekstra, A. G., Tan, C. J. K., and Dongarra, J. J., editors, Computational Science ICCS 2002: International Conference Amsterdam, The Netherlands, April 21–24, 2002 Proceedings, Part III, pages 632–641. Springer Berlin Heidelberg, Berlin, Heidelberg.
- Farley, D. T. (1963a). A plasma instability resulting in field-aligned irregularities in the ionosphere. *J. Geophys. Res.*, 68:6083.
- Farley, D. T. (1963b). Two-stream plasma instability as a source of irregularities in the ionosphere. *Phys. Rev. Lett.*, 10(7):279–282.
- Farley, D. T. (1985). Theory of equatorial electrojet plasma waves New developments and current status. *J. Atmos. Terr. Phys.*, 47:729–744.
- Farley, D. T. (2009). The equatorial E-region and its plasma instabilities: a tutorial. *Ann. Geophys.*, 27:1509–1520.
- Farley, D. T. and Balsley, B. B. (1973). Instabilities in the equatorial electrojet. *J. Geophys. Res.*, 78:227–239.
- Farley, D. T. and Fejer, B. G. (1975). The effect of the gradient drift term on type 1 electrojet irregularities. *J. Geophys. Res.*, 80:3087–3090.
- Farley, D. T., Fejer, B. G., and Balsley, B. B. (1978). Radar observations of two-dimensional turbulence in the equatorial electrojet. III Nighttime observations of type 1 waves. *J. Geophys. Res.*, 83:5625–5632.
- Fejer, B., Farley, D., Balsley, B., and Woodman, R. (1976). Radar observations of two dimensional turbulence in the equatorial electrojet, 2. *J. Geophys. Res.*, 81(1):130–134.
- Fejer, B. G., Farley, D. T., Balsley, B. B., and Woodman, R. F. (1975a). Oblique VHF radar spectral studies of the equatorial electrojet. *J. Geophys. Res.*, 80:1307–1312.
- Fejer, B. G., Farley, D. T., Balsley, B. B., and Woodman, R. F. (1975b). Vertical structure of the VHF backscattering region in the equatorial electrojet and the gradient drift instability. *J. Geophys. Res.*, 80:1313–1324.
- Fejer, B. G. and Kelley, M. C. (1980). Ionospheric irregularities. Rev. Geophys. Space Phys., 18:401–454.
- Fejer, B. G., Providakes, J., and Farley, D. T. (1984). Theory of plasma waves in the auroral E region. *J. Geophys. Res.*, 89:7487–7494.

- Fejer, J. A. (1979). Ionospheric instabilities and fine structure. *J. Atmos. Terr. Phys.*, 41:895–903.
- Fletcher, A. C., Dimant, Y. S., Oppenheim, M. M., and Fontenla, J. M. (2018). Effects of Ion Magnetization on the Farley-Buneman Instability in the Solar Chromosphere. *Astrophys. J.*, 857:129.
- Fontenla, J. M. (2005). Chromospheric plasma and the Farley-Buneman instability in solar magnetic regions. *Astron. Astrophys.*, 442:1099–1103.
- Fontenla, J. M., Peterson, W. K., and Harder, J. (2008). Chromospheric heating by the Farley-Buneman instability. *Astron. Astrophys.*, 480:839–846.
- Forbes, J. M. (1981). The equatorial electrojet. Rev. Geophys. Space Phys., 19:469–504.
- Foster, J. and Erickson, P. (2000). Simultaneous observations of eregion coherent backscatter and electric field amplitude at fregion heights with the millstone hill UHF radar. *Geophys Res Lett*, 27(19):3177–3180.
- Foster, J. C. and Tetenbaum, D. (1991). High-resolution backscatter power observations of 440-MHz E region coherent echoes at Millstone Hill. *J. Geophys. Res.*, 96:1251–1261.
- Foster, J. C. and Tetenbaum, D. (1992). Phase velocity studies of 34-cm E-region irregularities observed at Millstone Hill. *J. Atmos. Terr. Phys.*, 54:759–768.
- Haldoupis, C., Nielsen, E., and Ierkic, H. M. (1984). STARE Doppler spectral studies of westward electrojet radar aurora. *Planet. Space Sci.*, 32:1291–1300.
- Hanuise, C. and Crochet, M. (1977). Multifrequency HF radar studies of plasma instabilities in Africa. J. Atmos. Terr. Phys., 39:1097–1101.
- Hanuise, C. and Crochet, M. (1981a). 5- to 50-m wavelength plasma instabilities in the equatorial electrojet. III Counter-electrojet conditions. *J. Geophys. Res.*, 86:7761–7766.
- Hanuise, C. and Crochet, M. (1981b). 5-50-m wavelength plasma instabilities in the equatorial electrojet. 1. Cross-field conditions. *J. Geophys. Res.*, 86:3561–3572.
- Hanuise, C. and Crochet, M. (1981c). 5-50-m wavelength plasma instabilities in the equatorial electrojet 2. Two-stream conditions. *J. Geophys. Res.*, 86:3567–3572.
- Hassan, E., Horton, W., Smolyakov, A. I., Hatch, D. R., and Litt, S. K. (2015). Multiscale equatorial electrojet turbulence:Baseline 2-D model. J. Geophys. Res. Space Physics, 120:1460–1477.

- Hoh, F. C. (1963). Instability of Penning-Type Discharges. *Physics of Fluids*, 6:1184–1191.
- Hysell, D., Miceli, R., Munk, J., Hampton, D., Heinselman, C., Nicolls, M., Powell, S., Lynch, K., and Lessard, M. (2012). Comparing VHF coherent scatter from the radar aurora with incoherent scatter and all-sky auroral imagery. J. Geophys. Res. Space Physics, 117(A16):A10313.
- Hysell, D. L. and Chau, J. L. (2006). Optimal aperture synthesis radar imaging. *Radio Science*, 41:RS2003.
- Hysell, D. L., Drexler, J., Shume, E. B., Chau, J. L., Scipion, D. E., Vlasov, M., Cuevas, R., and Heinselman, C. (2007). Combined radar observations of equatorial electrojet irregularities at Jicamarca. *Ann. Geophys.*, 25:457–473.
- Hysell, D. L., Michhue, G., Larsen, M. F., Pfaff, R., Nicolls, M., Heinselman, C., and Bahcivan, H. (2008). Imaging radar observations of Farley Buneman waves during the JOULE II experiment. *Ann. Geophys.*, 26:1837–1850.
- Hysell, D. L., Munk, J., and McCarrick, M. (2018). VHF Radar Images of Artificial Field-Aligned Ionospheric Irregularities in the Subauroral E Region. *Radio Science*, 53:334–343.
- Janhunen, P. (1994a). Implications of flow angle stabilization on coherent E region spectra. *J. Geophys. Res.*, 99:13.
- Janhunen, P. (1994b). Perpendicular particle simulation of the E region Farley-Buneman instability. J. Geophys. Res., 99:11461–11474.
- Kagan, L. M. and Kelley, M. C. (2000). A thermal mechanism for generation of small-scale irregularities in the ionospheric E region. *J. Geophys. Res.*, 105:5291–5302.
- Kelley, M. C. (2009). The Earth's Ionosphere: plasma physics and electrodynamics. Academic Press.
- Kudeki, E., Farley, D. T., and Fejer, B. G. (1982). Long wavelength irregularities in the equatorial electrojet. *Geophys. Res. Lett.*, 9:684–687.
- Kudeki, E., Farley, D. T., and Fejer, B. G. (1985). Theory of spectral asymmetries and nonlinear currents in the equatorial electrojet. *J. Geophys. Res.*, 90:429–436.
- Kudeki, E., Fejer, B. G., Farley, D. T., and Hanuise, C. (1987). The Condor equatorial electrojet campaign Radar results. *J. Geophys. Res.*, 92:13561–13577.

- Li, X., Demmel, J., Gilbert, J., iL. Grigori, Shao, M., and Yamazaki, I. (1999). SuperLU Users' Guide. Technical Report LBNL-44289, Lawrence Berkeley National Laboratory. http://crd.lbl.gov/~xiaoye/SuperLU/. Last update: August 2011.
- Liu, J. (1992). The multifrontal method for sparse matrix solution: Theory and practice. SIAM Review, 34(1):82–109.
- Madsen, C. A., Dimant, Y. S., Oppenheim, M. M., and Fontenla, J. M. (2014). The Multi-species Farley-Buneman Instability in the Solar Chromosphere. *Astrophys. J.*, 783:128.
- Maeda, K., Tsuda, T., and Maeda, H. (1963). Theoretical interpretation of the equatorial sporadic *e* layers. *Phys. Rev. Lett.*, 11:406–407.
- Makarevich, R. A. (2016). Toward an integrated view of ionospheric plasma instabilities: Altitudinal transitions and strong gradient case. *J. Geophys. Res. Space Physics*, 121:3634–3647.
- Moro, J., Denardini, C. M., Resende, L. C. A., Chen, S. S., and Schuch, N. J. (2016). Influence of uncertainties of the empirical models for inferring the E-region electric fields at the dip equator. *Earth, Planets, and Space*, 68.
- Mrak, S., Semeter, J., Hirsch, M., Starr, G., Hampton, D., Varney, R. H., Reimer, A. S., Swoboda, J., Erickson, P. J., Lind, F., Coster, A. J., and Pankratius, V. (2018). Field-Aligned GPS Scintillation: Multisensor Data Fusion. *J. Geophys. Res. Space Physics*, 123:974–992.
- Newman, A. L. and Ott, E. (1981). Nonlinear simulations of type 1 irregularities in the equatorial electrojet. *J. Geophys. Res.*, 86:6879–6891.
- Oppenheim, M. (1996). A wave-driven nonlinear current in the E-region ionosphere. *Geophys. Res. Lett.*, 23:3333–3336.
- Oppenheim, M. (1997). Evidence and effects of a wave-driven nonlinear current in the equatorial electrojet. *Ann. Geophys.*, 15:899–907.
- Oppenheim, M. and Otani, N. (1996). Spectral characteristics of the Farley-Buneman instability: Simulations versus observations. *J. Geophys. Res.*, 101:24573–24582.
- Oppenheim, M., Otani, N., and Ronchi, C. (1995). Hybrid simulations of the saturated Farley-Buneman instability in the ionosphere. *Geophys. Res. Lett.*, 22:353–356.
- Oppenheim, M., Otani, N., and Ronchi, C. (1996). Saturation of the Farley-Buneman instability via nonlinear electron  $E \times B$  drifts. J. Geophys. Res., 101:17273-17286.

- Oppenheim, M. M., Dimant, Y., and Dyrud, L. P. (2008). Large-scale simulations of 2-D fully kinetic Farley-Buneman turbulence. *Ann. Geophys.*, 26:543–553.
- Oppenheim, M. M. and Dimant, Y. S. (2004). Ion thermal effects on E-region instabilities: 2D kinetic simulations. J. Atmos. Solar Terr. Phys., 66:1655–1668.
- Oppenheim, M. M. and Dimant, Y. S. (2013). Kinetic simulations of 3-D Farley-Buneman turbulence and anomalous electron heating. *J. Geophys. Res. Space Physics*, 118:1306–1318.
- Patra, A. K., Tiwari, D., Devasia, C. V., Pant, T. K., and Sridharan, R. (2005). East-west asymmetries of the equatorial electrojet 8.3 m type-2 echoes observed over Trivandrum and a possible explanation. *J. Geophys. Res. Space Physics*, 110(A9):A11305.
- Pfaff, R. F., Kelley, M. C., Fejer, B. G., Maynard, N. C., and Baker, K. D. (1982). In-situ measurements of wave electric fields in the equatorial electrojet. *Geophys. Res. Lett.*, 9:688–691.
- Pfaff, R. F., Kelley, M. C., Kudeki, E., Fejer, B. G., and Baker, K. D. (1987a). Electric field and plasma density measurements in the strongly driven daytime equatorial electrojet. 1 The unstable layer and gradient drift waves. *J. Geophys. Res.*, 92:13578–13596.
- Pfaff, R. F., Kelley, M. C., Kudeki, E., Fejer, B. G., and Baker, K. D. (1987b). Electric field and plasma density measurements in the strongly driven daytime equatorial electrojet. 2 Two-stream waves. *J. Geophys. Res.*, 92:13597–13612.
- Pfaff, Jr., R. F., Acuña, M. H., Marionni, P. A., and Trivedi, N. B. (1997). DC polarization electric field, current density, and plasma density measurements in the daytime equatorial electrojet. *Geophys. Res. Lett.*, 24:1667–1670.
- Picone, J. M., Hedin, A. E., Drob, D. P., and Aikin, A. C. (2002). NRLMSISE-00 empirical model of the atmosphere: Statistical comparisons and scientific issues. *J. Geophys. Res. Space Physics*, 107:1468.
- Prakash, S., Gupta, S. P., and Subbaraya, B. H. (1969). Irregularities in the Equatorial E Region Over Thumba. *Radio Science*, 4:791–796.
- Prakash, S., Gupta, S. P., and Subbaraya, B. H. (1970). A study of the irregularities in the night time equatorial E-region using a Langmuir probe and plasma noise probe. *Planet. Space Sci.*, 18:1307–1318.
- Press, W. H., Teukolsky, S. A., Vetterling, W. T., and Flannery, B. P. (2007). *Numerical Recipes 3rd Edition: The Art of Scientific Computing*. Cambridge University Press, New York, NY, USA, 3 edition.

- Prölls, G. W. (2004). Physics of the Earth's Space Environment. Springer.
- Rishbeth, H. and Garriott, O. K. (1969). *Introduction to Ionospheric Physics*. Academic Press.
- Rogister, A. (1972). Nonlinear theory of cross-field instability with application to the equatorial electrojet. *J. Geophys. Res.*, 77:2975–2981.
- Rogister, A. and D'Angelo, N. (1970). Type II irregularities in the equatorial electrojet. J. Geophys. Res., 75:3879–3887.
- Ronchi, C., Similon, P. L., and Sudan, R. N. (1989). A nonlocal linear theory of the gradient drift instability in the equatorial electrojet. *J. Geophys. Res.*, 94:1317–1326.
- Ronchi, C., Sudan, R. N., and Farley, D. T. (1991). Numerical simulations of large-scale plasma turbulence in the daytime equatorial electrojet. *J. Geophys. Res.*, 96:21263.
- Rosenberg, M. and Chow, V. W. (1998). Farley-Buneman instability in a dusty plasma. *Planet. Space Sci.*, 46:103–108.
- Saad, Y. and Schultz, M. H. (1986). GMRES: A generalized minimal residual algorithm for solving nonsymmetric linear systems. SIAM J. Sci. Stat. Comput., 7(3):856–869.
- Schlegel, K. and St.-Maurice, J. P. (1981). Anomalous heating of the polar E region by unstable plasma waves. I Observations. *J. Geophys. Res.*, 86:1447–1452.
- Schmidt, M. J. and Gary, S. P. (1973). Density gradients and the Farley-Buneman instability. *J. Geophys. Res.*, 78:8261–8265.
- Schunk, R. W. and Nagy, A. F. (2004). *Ionospheres*. Cambridge University Press.
- Simon, A. (1963). Instability of a Partially Ionized Plasma in Crossed Electric and Magnetic Fields. *Physics of Fluids*, 6:382–388.
- St.-Maurice, J.-P., Foster, J. C., Holt, J. M., and del Pozo, C. (1989). First results on the observation of 440-MHz high-latitude coherent echoes from the E region with the Millstone Hill radar. *J. Geophys. Res.*, 94:6771–6798.
- St.-Maurice, J.-P. and Hamza, A. M. (2001). A new nonlinear approach to the theory of E region irregularities. J. Geophys. Res., 106:1751–1760.
- St.-Maurice, J. P., Schlegel, K., and Banks, P. M. (1981). Anomalous heating of the polar E region by unstable plasma waves. II Theory. *J. Geophys. Res.*, 86:1453–1462.

- Sudan, R. N. (1983). Unified theory of type I and type II irregularities in the equatorial electrojet. *J. Geophys. Res.*, 88:4853–4860.
- Sudan, R. N., Akinrimisi, J., and Farley, D. T. (1973). Generation of small-scale irregularities in the equatorial electrojet. *J. Geophys. Res.*, 78:240–248.
- Sudan, R. N. and Keskinen, M. J. (1984). Unified theory of the power spectrum of intermediate wavelength ionospheric electron density fluctuations. *J. Geophys. Res.*, 89:9840–9844.
- Untiedt, J. (1967). A model of the equatorial electrojet involving meridional currents. J. Geophys. Res., 72:5799–5810.
- Uspensky, M., Koustov, A., Janhunen, P., Pellinen, R., Danskin, D., and Nozawa, S. (2003). STARE velocities: the importance of off-orthogonality and ion motions. *Annales Geophysicae*, 21:729–743.
- Woodman, R. F. and Chau, J. L. (2002). First Jicamarca radar observations of two-stream E region irregularities under daytime counter equatorial electrojet conditions. J. Geophys. Res. Space Physics, 107:1482.
- Xie, H.-S. (2013). Generalized plasma dispersion function: One-solve-all treatment, visualizations, and application to Landau damping. *Physics of Plasmas*, 20(9):092125.
- Young, M. A., Oppenheim, M. M., and Dimant, Y. S. (2017). Hybrid simulations of coupled Farley-Buneman/gradient drift instabilities in the equatorial E region ionosphere. J. Geophys. Res. Space Physics, 122:5768–5781.
- Zettergren, M. D., Semeter, J. L., and Dahlgren, H. (2015). Dynamics of density cavities generated by frictional heating: Formation, distortion, and instability. *Geophys. Res. Lett.*, 42:10.

# Curriculum Vitae

## Matthew A. Young

Astronomy Department 725 Commonwealth Avenue Boston, MA, 02215

### Education

B.S. Physics, University of New Hampshire

May 2012

B.A. Anthropology, University of New Hampshire

May 2004

# Research Experience

BU Center for Space Physics

June 2012 - present

Research Assistant (Dr. Meers Oppenheim, advisor)

UNH Magnetosphere-Ionosphere Research Lab

October 2008-June 2012

Research Assistant (Dr. Marc Lessard, advisor)

# Teaching Experience

Boston University

Fall 2012

Teaching Fellow, AS 105: Alien Worlds (Dr. Andrew West, instructor)

#### Outreach

Guest lecture, Spaulding High School Honors Astronomy, 14 December 2017

Presenter, Kearsarge Regional High School Career Day, 19 April 2017

Presenter, Kingswood Regional High School Science Week, 18 April 2017

Volunteer, Science By the Pint, Aeronaut Brewing Company, 20 October 2016

Presenter, Kingswood Regional High School Science Week, 20 April 2015

Volunteer, Science By the Pint, The Burren, 11 January 2015

Presenter, Kingswood Regional High School Science Week, 15 April 2013

Presenter, Tuesday Night Lecture Series, BU Graduate School of Visual Arts, 3 February 2015

## Professional Development

Reviewer: Journal of Geophysical Research (Space Physics), 2016.

Incoherent Scatter Radar Summer School, MIT Haystack Observatory, 28 July-2 August 2013.

### Journal Articles

**Young, M. A.**, M. M. Oppenheim, and Y. S. Dimant. (submitted) "Simulations of Secondary Farley-Buneman Instability Driven by a Kilometer-Scale Primary Wave: Anomalous Transport and Formation of Flat-Topped Electric Fields," *J. Geophys. Res. Space Phys.* 

**Young, M. A.**, M. M. Oppenheim, and Y. S. Dimant. (2017) "Hybrid simulations of coupled Farley-Buneman/gradient drift instabilities in the equatorial E region ionosphere," J. Geophys. Res. Space Phys. doi: 10.1002/2017JA024161.

Fritz, B. A., J. Heavisides, M. A. Young, H. Kim, and M. R. Lessard, (2018) "ELF Whistler Dependence on a Sunlit Ionosphere," *J. Geophys. Res. Space Phys.* doi: 10.1029/2017JA024912.

Rojas, E. L., M. A. Young, and D. L. Hysell, (2016) "Phase speed saturation of Farley-Buneman waves due to stochastic, self-induced fluctuations in the background flow," *J. Geophys. Res. Space Phys.* doi: 10.1002/2016JA022710.

Young, M. A., M. R. Lessard, M. J. Engebretson, J. R. Woodroffe, and K. Oksavik. (2012) "Spectral enhancements associated with Pi1B events observed at high latitude," *J. Geophys. Res. Space Phys.* doi:10.1029/2011JA017127.

Young, M. A., M. R. Lessard, and M. J. Engebretson. (2012) "Pi1B propagation in the high-latitude ionosphere," *J. Geophys. Res. Space Phys.* doi:10.1029/2011JA017127.

Kim, H., M. R. Lessard, M. J. Engebretson, and M. A. Young. (2011) "Statistical study of Pc 1-2 wave propagation characteristics in the high-latitude ionospheric waveguide," *J. Geophys. Res. Space Phys.* doi: 10.1029/2010JA016355.

### Conference Presentations

Presenting author in **BOLD** 

- **Young, M.**, "Gradient-driven E-region Turbulence," *Oral Presentation*, Coupling, Energetics, and Dynamics of Atmospheric Regions Workshop, 25-29 June 2018.
- Young, M., M. Oppenheim, and Y. Dimant, "Simulations of Secondary Farley-Buneman Instability," *Poster Presentation*, Coupling, Energetics, and Dynamics of Atmospheric Regions Workshop, 25-29 June 2018.
- **Young, M.**, M. Oppenheim, and Y. Dimant, "A Simulation of Plasma Turbulence from Dust Gradients," *Poster Presentation*, Coupling, Energetics, and Dynamics of Atmospheric Regions Workshop, 18-23 June 2017.
- **Young, M.**, M. Oppenheim, and Y. Dimant, "Wave Turning and Flow Angle in the E-Region Ionosphere," *Poster Presentation*, American Geophysical Union Fall Meeting, 11-15 December 2016
- **Young, M.**, M. Oppenheim, and Y. Dimant, "Parametric Wave Growth in a Hybrid PIC/Fluid Simulation of the Equatorial E Region," *Poster Presentation*, Coupling, Energetics, and Dynamics of Atmospheric Regions Workshop, 19-24 June 2016.
- **Young, M.** and M. Oppenheim, "Simulation of Ionospheric E-Region Plasma Turbulence with a Massively Parallel Hybrid PIC/Fluid Code," *Poster Presentation*, American Geophysical Union Fall Meeting, 14-18 December 2015.
- **Young, M.**, M. Oppenheim, and Y. Dimant, "Development of a Parallel PIC/Fluid Simulation of E-region Farley-Buneman Turbulence," *Poster Presentation*, Coupling, Energetics, and Dynamics of Atmospheric Regions Workshop, 21-25 June 2015.
- **Young, M.**, M. Oppenheim, R. Cuevas, and Y. Dimant, "Using Simulations to Quantify High-Latitude Type-I Radar Backscatter Spectra as a Function of Flow Angle," *Poster Presentation*, American Geophysical Union Fall Meeting, 15-19 December 2014.
- Young, M., M. Lessard, I. Cohen, D. Wright, and L. Baddeley. "Experimental Evidence of Resonant Cavities in the High-Latitude Ionosphere Above Svalbard," *Poster Presentation*, American Geophysical Union Fall Meeting, 5-9 December 2011.

- Young, M., M. Lessard, M. Engebretson, J. Woodroffe, and K. Oksavik. "Observed Characteristics of Ducted ULF Pi1B Pulsations," *Poster Presentation*, Geospace Environment Modeling Summer Workshop, 20-25 June 2010.
- Young, M., M. Lessard, C. Weaver, A. Weatherwax, and E. Lindgren. "A Statistical Study of Narrow-Band ELF Events Observed at the South Pole," *Poster Presentation* American Geophysical Union Fall Meeting, 13-17 December 2010.
- Young, M., M. Lessard, and M. Engebretson. "Statistical Study of Ducted Propagation Characteristics of ULF Pi1B Pulsations," *Poster Presentation* American Geophysical Union Fall Meeting, 14-18 December 2009.

Updated: December 10, 2018